UNIVERSITA'

CAMPUS BIO-MEDICO DI ROMA

School of Biomedical Engineering

PhD Course in Biomedical Engineering

(XXVI-2011/2013)

INTERACTION BETWEEN PANCREATIC TISSUE AND Nd:YAG LASER FOR LASER ABLATION PURPOSE: THERMOMETRY AND OPTICAL CHARACTERIZATION

Paola Saccomandi

Supervisor:

Prof. Sergio Silvestri

PhD Program Coordinator:

Prof. Giulio Iannello

March 2014

INTERACTION BETWEEN PANCREATIC TISSUE AND ND:YAG LASER FOR LASER ABLATION PURPOSE: THERMOMETRY AND OPTICAL CHARACTERIZATION

A thesis submitted by

Paola Saccomandi

in partial fulfillment of the requirements of the degree of

Doctor of Philosophy

in Biomedical Engineering

at Università Campus Bio-Medico di Roma

Supervisor:

Prof. Sergio Silvestri

PhD Program Coordinator:

Prof. Giulio Iannello

March 2014

Index

Abstract

The aim of this study is to assess the effects of Nd:YAG laser light on pancreatic tissue. The final goal is to investigate the feasibility of Laser Ablation (LA) for the removal of pancreatic cancer.

Besides the high mortality and the poor diagnosis of pancreatic tumor, treatments for inoperable patients are limited, and consist mainly in palliative methods aimed to reduce the pain and to slightly improve the life quality of the patient. The social and economic impacts of the traditional surgery, the Whipple procedure, for pancreatic cancer removal is high, considering the strong invasivity and the reduced life expectancy, the use of many resources of the hospital (i.e., a expert surgeon, a complete and experienced team, the operating theatre available for many hours) and the long recovery times, among other factors.

Since an adjuvant solution is desirable, the Endoscopic Ultrasound guided-LA represents a minimally-invasive solution for removal of pancreatic cancer: it is an alternative to the traditional surgery, and can be employed also in patients who cannot undergone operation. Laser light is carried inside the deep seated neoplasia through an optical fiber applicator, guided in the target site trough an endoscope, and images can be acquired by an ultrasound probe placed on the tip of the endoscope, avoiding percutaneous entry. Positive outcomes in EUS guided-LA *in vivo* procedure have been preliminary carried out in our Hospital (Endoscopy Unit of University Campus Bio-Medico di Roma) on human liver neoplasia and on pancreases of eight healthy pigs with a Nd:YAG laser. EUS guided-LA was applied on porcine pancreases, with different laser power settings, showing no post-procedure complications within 24 hours after treatment.

The promising results of the first trials on animal models encourage to pursue the research on LA application on pancreas. In order to plan a safe and effective therapy, a mathematical model of the thermal effects caused by pancreas absorption of laser light is useful. The prediction of injured tissue volume size and temperature rise during treatment may allow to optimize the dosimetry of LA.

In the present study, I implemented a theoretical model to predict the temperature distribution within pancreas undergoing LA, and several experimental trials have been

performed, aiming to assess capability prediction of theoretical model and outcome on pancreas.

The interaction between pancreatic tissue and Nd:YAG laser has been assessed from two perspectives: the measurement of temperature distribution within pancreas undergoing LA, and the estimation of optical properties of tissue.

Thermometry trials have been carried out considering two modalities: invasive one, using temperature sensors (Fiber Bragg Gratings, thermocouples, Fluoroptic probes), and non-invasive one, based on CT-scan and MRI images.

Although the drawback of invasivity, Fiber Bragg gratings have the advantages to be MRI compatible, and the small size (diameter of 250 µm) allows performing quasi-punctual measurement. Furthermore, they are not affected by measurement artifact, if compared with thermocouples and Fluoroptic probes, due to direct light absorption, and do not present artifacts on CT images during CT-thermometry. All these features make FBG the most appropriate sensors for LA thermometry.

As far as it concerns non-invasive thermometry, images-based thermometry aims to provide real time images with acceptable temperature resolution: both CT-scan and MRI-based approach are suitable for temperature monitoring during LA on pancreas. Results obtained during trials show a thermal sensitivity of methods comparable with the results reported in current literature for other tissue (e.g., liver). Also the performances of Dual-Source CT (DSCT) scanner have been evaluated for thermotherapy purposes, in collaboration with Radiology Department in Klinikum of Goethe Universität (Frankfurt am Main, Germany). Three fusion factors, corresponding at three kVp settings (80 kV, 110 kVp and 140 kVp), have been analyzed, and their thermal sensitivity has been assessed.

On the other hand, the investigation of laser-pancreas interaction included also the study of pancreas optical properties, absent in the currently literature, since this project represents the first study about laser irradiated pancreas. Biological tissue are highly scattering media, and the phenomenon of conversion of laser light into heat is related to the capability of tissue to absorb and to scatter laser light. Two experimental approaches have been employed to estimate tissue optical properties: the first one is based on a double integrating sphere system, and the second one on goniometric and spectrophotometric measurements, in collaboration with Biophysik Institute of Goethe Universität (Frankfurt am Main, Germany). Although still under investigation, preliminary results are comparable with data of other tissues: e.g., for native porcine liver at 850 nm I measured an anisotropy factor of

0.947, comparable with the range of values between 0.93 and 0.95 reported by some authors.

Part I. Laser Ablation: background and clinical applications

Chapter 1. Laser Ablation

1.1 Interaction map

The application of laser light on biological tissue results on several effects, depending on laser settings, such as the power density, the energy density, as well as the exposure time. The log-log plot of power density versus exposure time with the basic interaction mechanisms is shown in Fig. 1.1 [1]:

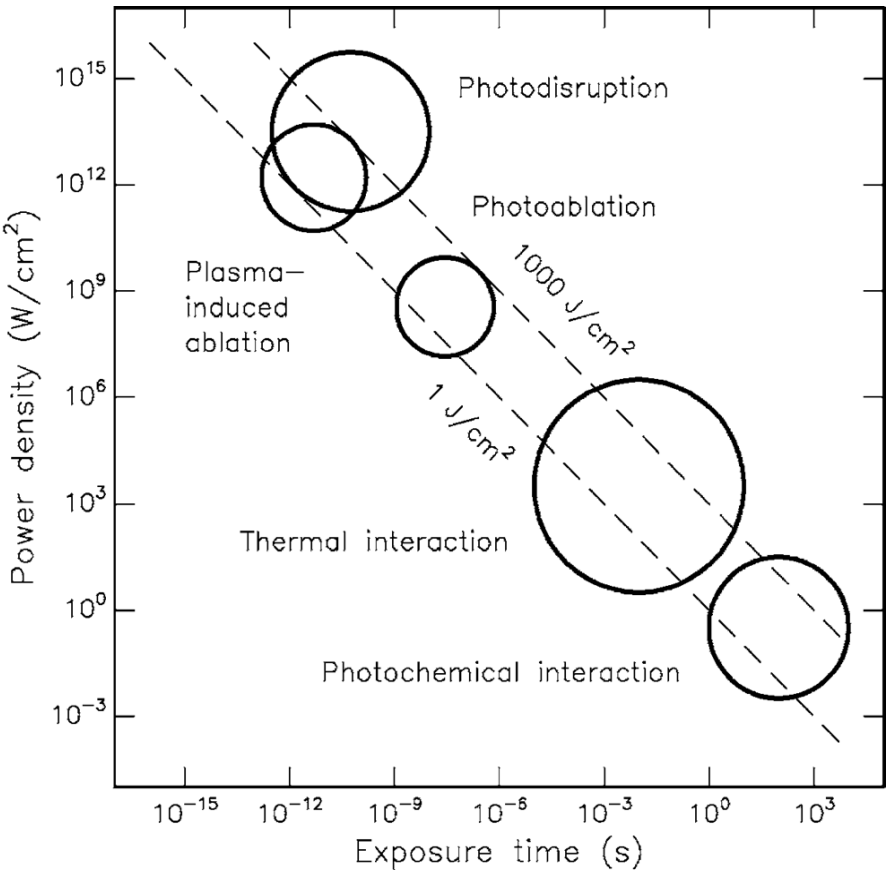

Figure 1.1 Laser-tissue interaction map [1].

As observable in Fig. 1.1, different laser-tissue interactions can be divided into five main classes: photochemical interaction, thermal interaction, photoablation, plasma-induced ablation and photodisruption.

Photochemical ablation is based on the chemical effects induced by light on macromolecules and tissues. The interaction is chemical, since the energy causes a mutation of the molecules which could result into an isomer or into a new molecule. This process occurs thanks to the presence of photosensible elements in human tissues, such as chromophore and pigments. It occurs at low power density (around 1 W/cm^2) and with

long exposure times. In general, wavelength in visible range is preferred, because of its high optical penetration depth. One of the most diffused techniques is the Photo Dynamic Therapy (PDT).

Thermal interaction regards a large number of mechanisms, based on the increase of local temperature within the laser-irradiated tissue. Thermal effects can be induced either by continuous wave or pulsed laser radiation but, depending on the duration and peak value of temperature achieved within tissue, different effects, such as coagulation, vaporization, carbonization and melting, can occur. A temperature above 60 °C is required to induce tissue coagulation, and, consequently, tissue necrosis. Vaporization is defined as a thermo-mechanical effect, since, when the water contained inside the cells vaporizes, it expands its volume and causes microexplosions. At temperature above 100 °C, carbonization occurs: the carbon is released, leading to a blackening in color. In general, carbonization should be avoided, since necrosis can be achieved with lower temperatures, and it reduces the visibility during surgery. Finally, at temperature higher than 300 °C, melting occurs. During treatment, in general all these phenomena occur, since the precise control of tissue temperature is a big deal. Typical wavelengths for thermal interaction are in the range between 400 nm and 1 mm, and the power density ranges from 10 to 10^6 $W \cdot cm^{-2}$. Laser Ablation (also known as Laser-induced Interstitial Thermotherapy) is classified as thermal interaction, since it is a treatment able to deposit a precise amount of laser energy within localized tissues. The features of Laser Ablation (LA) will be deeply discussed in the following.

Photoablative interaction is a variant of the above-mentioned photochemical interaction. A large amount of biologic molecules have a high absorption coefficient in the UV band (λ=200÷320 nm) and, if they are struck by pulses of a duration in the range from 10 ns to 10 µs, they dissociate in two sub-molecules. The process of the interaction is the following:

- Laser UV pulse focused on the tissue
- High absorption of the pulse by proteins and peptides
- Macromolecules excitation
- Dissociation of the macromolecules

The laser used to exploit this type of interaction are required to emit UV radiation and are widely used in refractive surgery due to its high precision.

Plasma induced ablation and Photo-disruption are classified as techniques for Laser-Induced Optical Breakdown (LIOB). LIOB requires strong electric fields (in the order of megawatt) and short exposure time (or laser pulse) to be used in surgery; in particular, ultra-short pulses (in the range of 10^{-15} s and 10^{-12} s) are well suited for high-precision microsurgery. When the radiation hits the tissue an electric field is generated, whose magnitude varies from 10^{6} V·cm^{-1} up to 10^{7} V·cm^{-1}. These electric fields provide energy, comparable to ionization energy of the molecules, electrons are stripped from their host atoms, forming free electrons that are further accelerated by the laser-induced electrical field. This results in an electron avalanche and the subsequent ionization of atoms in the focal volume, leading to the formation of plasma. Plasma absorbs most of the energy from the laser beam. As a result, the temperature of the plasma rises rapidly, causing the newly formed plasma bubble to expand at high speed. The plasma expansion generates a rupture where its pressure overcomes the cohesion forces holding the tissue. This type of interaction, known as photodisruption, is used in ophthalmic surgery because it is possible to remove part of a tissue without cutting it.

1.2 Laser: principle of working

All these effects are achieved thanks to interaction of laser light with biological matter.

The description of LASER (Light Amplification by Stimulated Emission Radiation) principle was performed in 1917 by Albert Einstein, and only about thirty years later it was introduced in medical field. In 1961 Chamber and Koestler used the laser light for removal of retinal tumor, and two years later laser was used in dermatology and cardiovascular surgery.

The interaction of light with matter can be distinguished into three phenomena: the absorption, the spontaneous emission and the stimulated emission. Under the hypothesis that the atom is described according to Bohr model, and that each orbital is a stationary state characterized by a specific energy value, when a photon is incident on a atom, the following processes happen simultaneously:

a) stimulated absorption: an incident photon with energy $h\nu = E_1 - E_0$ excites an electron, which transits from its elementary state E_0 to the higher energy state E_1;

b) spontaneous emission: an electron at excited state with energy E_1 drops to the fundamental state E_0, emitting a photon with energy $E=E_1-E_0$;

c) stimulated emission: the electron is in the excited state E_1, and when an incident photon with energy $h\nu = E_1 - E_0$ stimulates the excited electron to drop from E_1 to E_0, another photon with same energy of incident photon is emitted.

These phenomena are represented in Fig. 1.2.

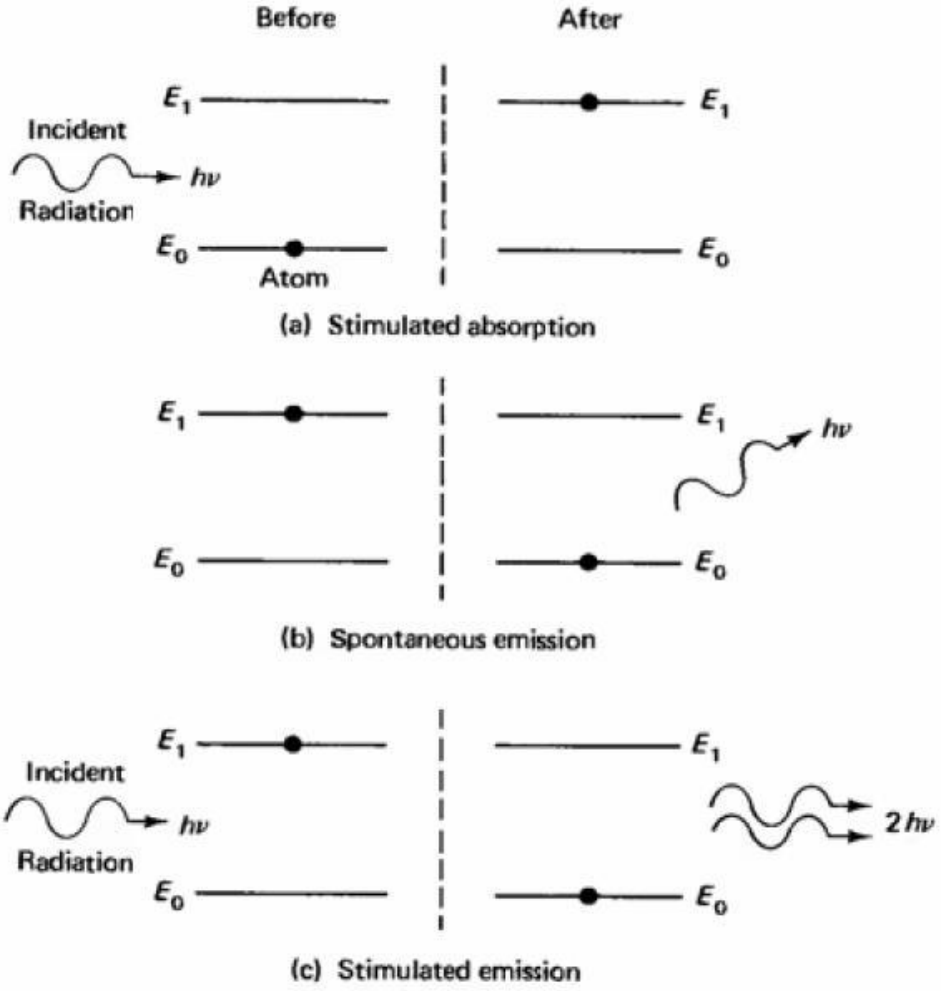

Figure 1.2 Matter-photons interaction

Two identical photons generate from the stimulated emission, and the emitted one has not only the same energy, also the same phase, direction and polarization of the incident photon, resulting in the phenomenon of amplification.

Since all the above described phenomena occur contemporarily, it is fundamental that stimulated emission outnumbers other two processes in order to realize the amplification and, consequently, to produce laser light.

Each process is characterized by a coefficient (Einstein coefficient, A_{21}, B_{21} and B_{12}, in Fig. 1.3), indicating the probability that each phenomenon occurs, and is accounted in Equation of thermodynamic balance.

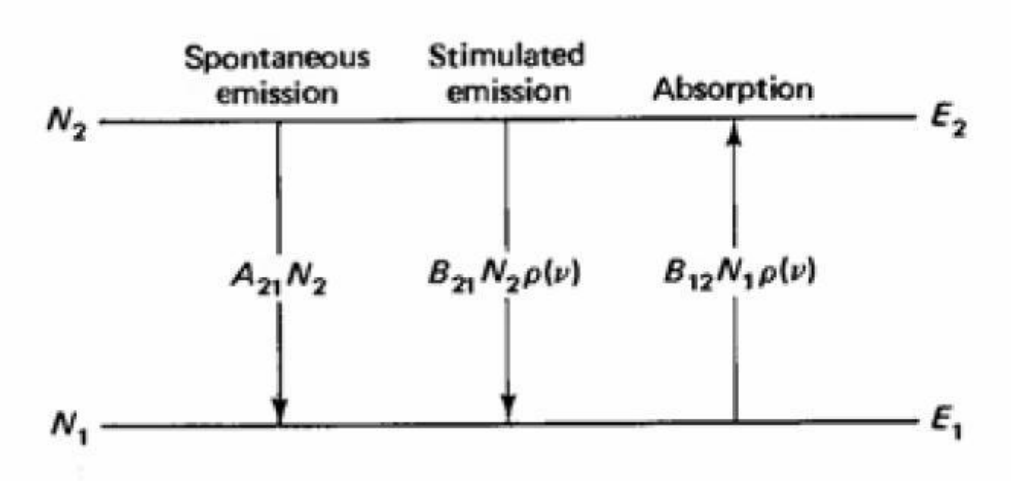

Figure 1.3 Thermodynamic equilibrium: N_1 and N_2 are the population of electrons in fundamental and excited state, respectively; E_1 and E_2 are the energy of fundamental and excited state, respectively; lastly, A_{21}, B_{21} and B_{12} are the Einstein coefficients.

At equilibrium condition, the number of electrons N_2 on the level with energy E_2 is constant, such as the number of electrons N_1 on the level with energy E_1.

In case of spontaneous emission, the number of electrons N_2 decreases to N_1, with a probability A_{21}. The absorption causes a transition from E_1 to E_2, causing a decrement of N_1 and an increment of N_2: this temporal variation is function of N_1, B_{12} and the density of photon $\rho(\nu)$ with frequency $\nu_{1\to2}$ required for the transition. The stimulated emission is described as the process opposite to the absorption, which can cause the increment of N_1, and therefore proportional to B_{21}, N_2 and $\rho(\nu)$.

With reference to Fig. 1.3, the three processes are described by the following Equations:

$$\begin{aligned} \frac{dN_2}{dt} &= -A_{21}N_2 \\ \frac{dN_1}{dt} &= -B_{12}N_1\rho(\nu) \\ \frac{dN_2}{dt} &= -B_{21}N_2\rho(\nu) \end{aligned} \tag{1.1}$$

and the thermodynamic equilibrium allows obtaining:

$$B_{12}N_1\rho(\nu) = A_{21}N_2 + B_{21}N_2\rho(\nu) \tag{1.2}$$

From Equations 1.1 and 1.2 results that, in order to induce stimulated emission prevalent on other two processes, two conditions have to be realized:

1) population inversion, i.e., $N_2>N_1$, achieved by means of *pumping* of electrons in excited state;

2) resonant cavity, to increase the density of photons, $\rho(\nu)$, incident on the medium to be stimulated (known as *laser medium*).

A typical laser consists of an optical cavity, also called tube, laser medium and two mirrors (Fig. 1.4). The laser medium contains the atoms to be stimulated by photons that are reflected back and forth through this medium, thanks to the mirrors (one of them is semitransparent). External energy source is needed to pump the electrons of laser medium in excited state. Lasing is possible when more than one half of the photons in laser medium is in exited state, i.e., when population inversion is achieved.

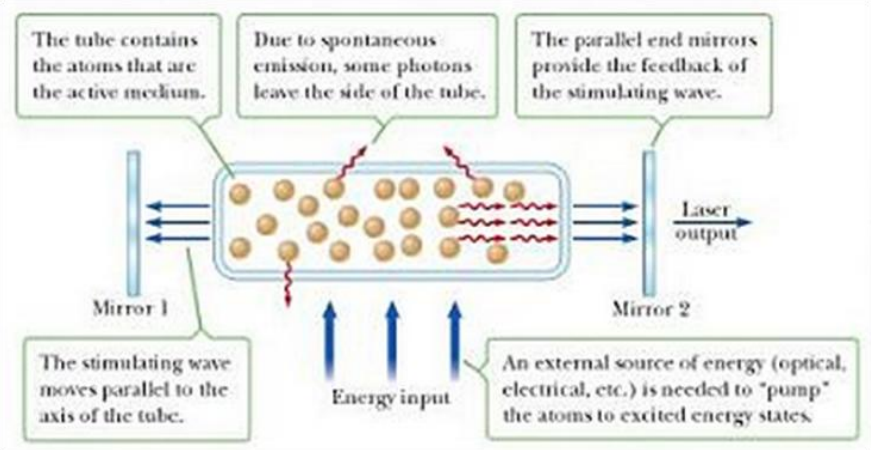

Figure 1.4 Steps of lasing process, and principal laser device components [2].

Hints about laser working principle are useful to introduce its features, which are appreciable in medicine: the *monochromatic emission*, *collimation* and *coherence*. Laser light is monochromatic, being characterized by a single wavelength. The laser beam presents also the feature of collimation, or low divergence, i.e., differently from a conventional light source, it does not emit light in all directions, and allows concentrating high energy in limited surfaces. Finally, the coherence, both temporal either spatial, characterizes the laser light because all the photons are in phase.

1.3 Nd:YAG laser: principle of working and medical applications

Nd:YAG laser is an optically pumped solid state laser, whose lasing medium is 1–2% neodymium (Nd^{3+}) doped into an yttrium–aluminium–garnet crystal. The laser can emit at

several wavelengths in the near infrared, and the most frequently used wavelength is 1064 nm [3, 4].

Nd:YAG laser is defined "the most important surgical laser" by Philipp [5], since the adequate choice of applicator and laser settings allows obtaining several effects on tissues. Advantages can be summarized as following: hemostatis, high precision, reduced instrumentation at treatment site, minimal risk of infection and trauma at surrounding structures.

With an *ad hoc* focusing handpiece, can be induced small coagulation seam, broad coagulation seam for hemostasis, and cutting/vaporization. For example, a focus of 30 mm, and a laser pulse from 0.1 s to 0.5 s with a power of 30 W can induce a precise coagulation seam, while a focus of 0.1 mm and a power of 60-100 W can induce a broad coagulation seam, in continuous mode. Bare fibers allow also achieving the effect of cutting, when used in contact mode, with laser power of about 50 W [5].

1.3.1 Working principle of Nd:YAG laser

Nd:YAG laser operation was demonstrated by Geusic et al. at Bell Laboratories in 1964.

The laser medium is a colorless isotropic crystal $Y_2Al_5O_{12}$ (Yttrium-Aluminum-Garnet, YAG), where 1-2% of Yttrium is replaced by Neodimium, since the Nd^{3+} are the active particles in the amplification process [6]. Nd^{3+} ions lend the crystal appreciable features, such as good mechanical stability and optical properties, and high thermal conductivity, in comparisons with other laser medium.

The laser medium operates as a four-level system, as shown in Fig. 1.5:

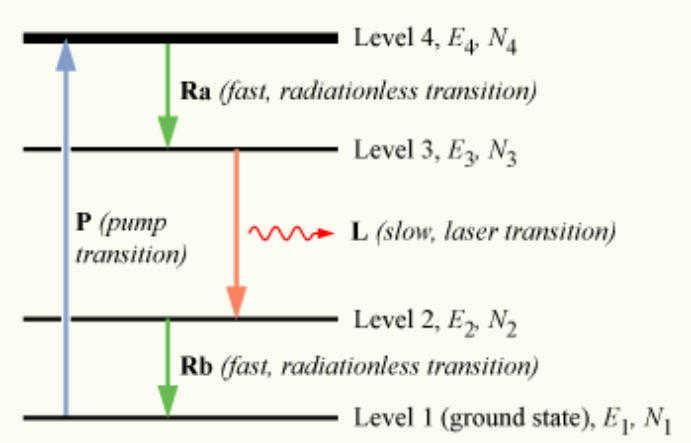

Figure 1.5 Principle of working of Nd:YAG aser

$E_1<E_2<E_3<E_4$ are the energy values of four levels, with population of N_1, N_2, N_3 and N_4, respectively. The population inversion, which is required in order to emit laser light, occurs when $N_3>N_2$: since level 2 is not the ground state, at the beginning of process can have a small population. An important requirement is that the transition from level 3 to level 2 is slower than decays $E_4 \rightarrow E_3$ and $E_2 \rightarrow E_1$.

The medium is excited by continuous or flashed Xe lamps or, more recently, by diode lasers.

1.3.2 Nd:YAG in gastroenterology

Gastroenterology was one of the earliest specialties to apply lasers in the early 1970s for the arrest of gastrointestinal haemorrhage. Because of the developments in gastrointestinal endoscopic techniques and the optic fibres inserted through the instrument channels of endoscopes, laser light can be easily delivered to the upper and lower gastrointestinal tracts in a safe and relatively non-invasive modality [7]. The most important laser used today in gastroenterology is Nd:YAG. Short shots from this laser obtain good hemostasis due to thermal contraction of soft tissue. Longer shots at high powers can vaporize tissue and coagulate the underlying layers for effective debulking of advanced tumors; whereas those with lower power can coagulate a larger volume of tissue without vaporization. Thermal lasers in current practice are used for palliation of advanced, inoperable cancers of the upper and lower gastrointestinal tract [4]. Under direct vision with the laser fiber held away from the surface of the target, nodules of exophytic tumour can be vaporized and the underlying tumor coagulated either to relieve obstruction or to reduce blood loss. Laser therapy can improve dysphagia in patients with cancers of the esophagus and gastric cardia, but several treatments and the introduction of expanding stents are often needed to achieve optimum recanalization. The tip of the laser fibre can also be directly inserted into a targeted tissue with a much lower power to induce increment of temperature in the targeted area over a period of several minutes.

1.4 Laser Ablation

Laser Ablation (also known as Laser-induced interstitial thermotherapy) is a minimally invasive surgical procedure used to treat neoplasia of several organs, such as the brain, liver and kidneys. Laser radiation is guided within a fiber-optic applicator, with the tip placed in contact with the tumoral region requiring treatment. The therapy is based on the photothermal effects related to the transformation of the absorbed light energy into heat,

which results in tissue hyperthermia around the applicator. The optimal outcome for Laser Ablation (LA) is determined by the complete and controlled removal of the tumor volume and the absence of thermal damage to healthy surrounding tissue. The removal of tissue mass is due to several mechanisms, such as: plasma formation, tissue vaporization, combustion and explosive tissue fragmentation.

The efficacy of therapy is related to several parameters:

- laser settings (power, energy, time of exposition)
- laser wavelength
- applicator shape and size, as well as working principle
- tissue characteristics
- the chance to monitor and control temperature increase during therapy

1.4.1 Laser settings

As mentioned, laser settings are power (P [W]), energy (E [J]) and time of exposition (t_L [s]).

The laser power is the output optical power of laser, and it can be emitted both in continuous and pulsed wave mode. It represents the amount of energy delivered during a certain period of time, and the time represents the period of irradiation. A difference should be highlighted between continuous wave and pulsed wave mode. In particular, in the second case, a power value peak and a laser pulse duration are defined.

Common laser powers for LA purposes range between 2 W and 40 W, depending above all on the device used to guide laser radiation within the tissue to be treated. (this will be better explained in the part dedicated to laser applicators, cfr Paragraph 1.4.3).

1.4.2 Laser wavelength: absorption and applications

Laser wavelength is a fundamental parameter to be taken into account for LA. As previously mentioned, one of the advantages of laser light is the monochromaticity, and the capability of a specific tissue to transform laser light into heat mainly depends by the laser wavelength, since it is strongly related to the *absorption properties* of tissue (this concept will be better explained in physical terms in Chapter 3). Laser emits optical radiation, i.e., light in the wavelength range of ultraviolet, visible and infrared, which has the feature to be nonionizing. The modulation of light by a specific medium or tissue component results in the absorption spectrum: the pattern is unique and can be used to identify the material.

Fig. 1.6 shows the absorption spectrum of some biological materials, such as pure water, melanin, hemoglobin and oxy-hemoglobin:

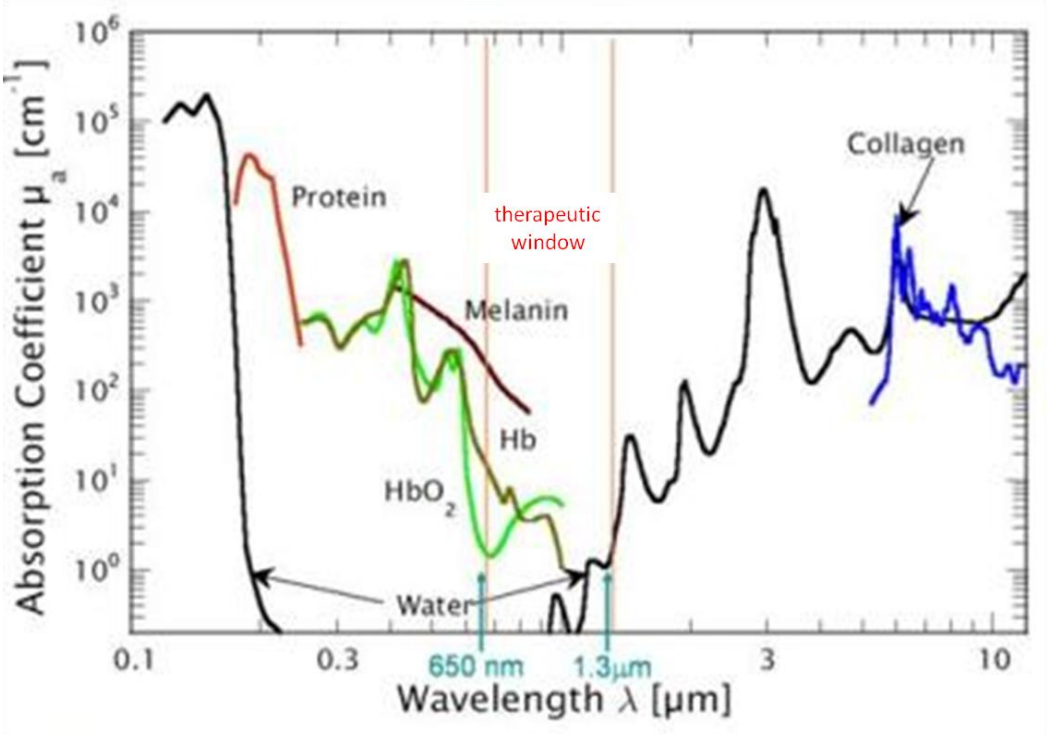

Figure 1.6 Absorption spectra of pure water, protein, melanin, hemoglobin, oxy-hemoglobin and collagen.

All these materials present a selective absorption, i.e., their capability to absorb light depends on the wavelength of light itself. The absorption (represented with *absorption coefficient* in the spectrum) is the propriety of medium to attenuate the incident radiation passing through it: the attenuation is achieved after a partial conversion of electromagnetic energy into heat motion of particles of medium. The spectral band between 650 nm and 1300 nm is defined "therapeutic window", since both most biological components and water reveal a combined low absorption, allowing therefore a deeper penetration of light within tissue (the penetration depth of light in a tissue is inversely related to the absorption coefficient).

Typical laser for coagulation purposes are Nd:YAG and diode laser. Although the first experimentations of LA were carried out using CO_2 laser source, this is more suitable for cutting and vaporization. CO_2 laser is widely spread in surgical field: its most used wavelength in medicine field is 10600 nm (far infrared spectrum), in correspondence of that water shows a peak of absorption (about $5 \cdot 10^3$ cm^{-1}), and as consequence allows a low penetration depth of 0.1 mm, making it suitable as a scalpel [8].

Nd:YAG laser emits light at different wavelength (i.e., 1064 nm, 532 nm, 266 nm and 1320 nm), although the most used wavelength for thermotherapy purposes is 1064 nm, since it belongs to "therapeutic window". It is a very versatile light source because easily transportable within optical fibers.

Diode lasers have been introduced more recently in the field of LA. They are portable, compact, silent and efficient. Diode lasers traditionally emit radiation in near infrared spectrum (800-980 nm), but modern diode laser can emit radiation in the spectrum between 600 nm and 1300 nm.

Although both Nd:YAG and diode lasers are considered efficient sources for LA, they have different optical penetration length within biological tissues such as liver, prostate, kidney, among others [9, 10]. As a matter of fact, diode lasers achieve a higher lesion size, since they are characterized by lower tissue penetration: for example, at the same laser power and energy, diameter of lesion performed by Nd:YAG reaches 4 mm, *vs* about 6 mm obtained with diode laser (980 nm). This behavior is demonstrated by the values of optical properties of all the investigated tissues, at 850 nm and 1064 nm [11]: for liver, prostate and white matter brain, absorption and scattering coefficients at 850 nm are higher than the ones at 1064 nm (e.g., for native porcine liver, absorption coefficient is 0.14 mm^{-1} at 850 nm and 0.05 mm^{-1} at 1064 nm).

Another important effect of absorption at different wavelength is on the exposition time, and on the laser power to be employed in the treatment. In fact, as discussed by Rohde *et al.* [12], since the difference of penetration depths of liver and muscle porcine tissues are respectively 3.8 mm and 5.9 mm at 940 nm and 7.2 mm and 9.1 mm at 1064 nm, the absorption of laser light at 940 nm is higher than absorption at 1064 nm. This finding results in the following: at the same laser settings and with a bare fiber applicator, treatment performed with 940 nm achieved in both liver and muscle tissues a coagulation lesion with higher volumes with respect the treatment at 1064 nm (e.g., increment of 20 % in liver). It means that to obtain a similar damage volume with Nd:YAG, a higher exposition time and laser power are required, as demonstrated by Nikfarjam et al. [13]: LA on animal liver performed with 980 nm laser with laser power of 2 W for 20 s provides a similar coagulation volume of treatment with 1064 nm with same laser power, but exposition time of 40 s.

Anyway, because the penetration depth is inversely correlated to absorption coefficient, one of the drawbacks in the use of a diode laser is that it produces tissue heating closer to the applicator compared to that with Nd:YAG devices. Therefore, Nd:YAG is still the most employed source for LA.

Is results useful to introduce here some hints about the optical response of tissue, although these concepts will be deeply examined in Chapter 3. Within the "therapeutic window" the maximum light penetration depth in tissue is achieved. Biological tissues are defined as turbid media, because the phenomenon of scattering is predominant with respect to the absorption, of around one or two orders of magnitude higher. In simple words, scattering increases the probability of absorption of photons by tissue, but because of the weak dependence of scattering on wavelength in this "therapeutic window", the heating properties of tissue and the different effects induced by different laser sources are strongly related to the absorption. Predominant tissue component responsible for absorption are hemoglobin, oxy-hemoglobin and water, which present a local maximum of absorption coefficient at 980 nm. Besides 980 nm, the absorption for the three abovementioned components drops, leading to reduce rate of heating and to increment the penetration depth of light travelling through tissue [14].

1.4.3 Fiber optic applicators for Laser Ablation

LA was originally introduced in medicine thanks to the feasibility to guide the laser light within an optical fiber. Optical fibers were introduced in biomedical field in sixties, with the development of endoscopes, and they became essential for medical imaging and surgery. Fiber optics have a lot of appreciable features for medical purposes, such as the electromagnetic immunity, the reduced dimensions, the inertness of materials (glass, quartz, acrylate polymer) which they are made of, the intrinsic safety due to the absence of electrical connection with the body.

Originally, LA was performed by using a simple optical fiber to transport a Nd:YAG laser beam [15], but during the following years many more sophisticated devices and systems were developed to achieve a more efficient treatment. Anyway, all of these novel system include optical fibers in their working principle, therefore a brief description of the working principle of an optical fiber is useful.

1.4.3.1 Optical fiber: working principle

Optical fibers are dielectric optical waveguides, used to transport light along long distances with minimal energy light losses. They are fundamentally made up of two coaxial materials: the internal one is known as *core*, and the external one as *cladding*. In most applications, especially in industrial field, other materials are common: the cladding could be clad by a buffer, which can be itself covered by an external jacket. While buffer and jacket are mostly used to increase the robustness of the fiber, core and cladding are assigned to let the light travelling efficiently through the fiber. Core has a higher index of refraction (n_1) than cladding (n_2), in order to satisfy the following relationship (from the Snell's law):

$$\theta_c = a\sin\left(\frac{n_2}{n_1}\right) \tag{1.3}$$

where θ_c, defined as critical angle, is the limit value for the angle of the incident light ray on the interface core-cladding (α_L) in order to be totally reflected inside the core, avoiding refraction into the cladding (angle of refraction, β, is 90°). This phenomenon, known as *total internal reflection*, is clarified in Fig. 1.7, where θ_a is the angle of the ray coming from the source, and n_0 is the refractive index of the surrounding medium:

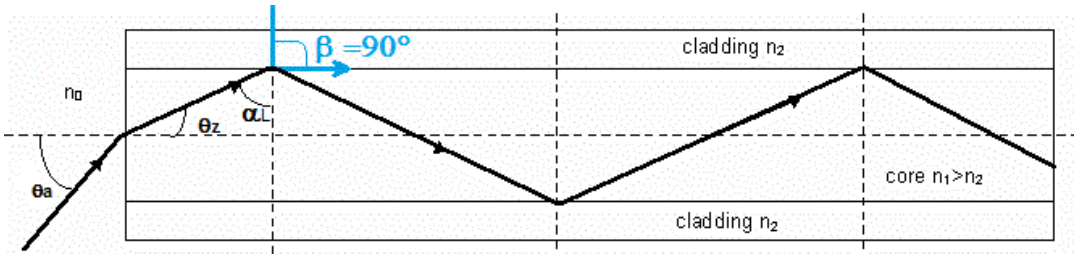

Figure 1.7 Working principle of light transmission of an optical fiber, based on the phenomenon of total internal reflection.

If $\alpha_L > \theta_c$, no refraction occurs, and the ray light travels along the fiber with negligible energy loss [16].

Optical fibers are distinguished into two fundamental categories: single-mode and multi-mode. Single-mode fibers (SMF) are designed to support only a single propagation mode per polarization direction for a given wavelength. They usually have a diameter core of a few micrometers (e.g., around 10 μm) and a small refractive index difference between core and cladding. SMF are commonly used for communication purposes, since the absence of intermodal dispersion (i.e., group velocity of multi-mode light depends not only

on the optical frequency, but also on the propagation mode involved) makes them suitable to transport data for long distances.

Multi-mode fibers (MMF) support multiple transverse guided modes for a given optical frequency and polarization. The number of guided modes depends on the wavelength and on the difference of refractive index between core and cladding. MMF are characterized by a core diameter larger than SFM, e.g., typical values are 50 µm or 62.5 µm. When core diameter reaches values between 100 µm and 400 µm, these MMF are classified as large-core mode. The acceptation of many modes of light weakens the performances of MMF, in terms of intermodal dispersion and shorter distance transmission. Nevertheless, MMF are suitable for the guide of laser light, especially of high power, and, considering the surgical and endoscopic applications, the distances (some meters) are considerably shorter than the distances covered for communication purposes (hundreds of kilometers) [17].

1.4.3.2 Applicators for Laser Ablation

A panoramic of the most known LA applicators is provided by Müller and Roggan [11], and here reported in Fig. 1.8.

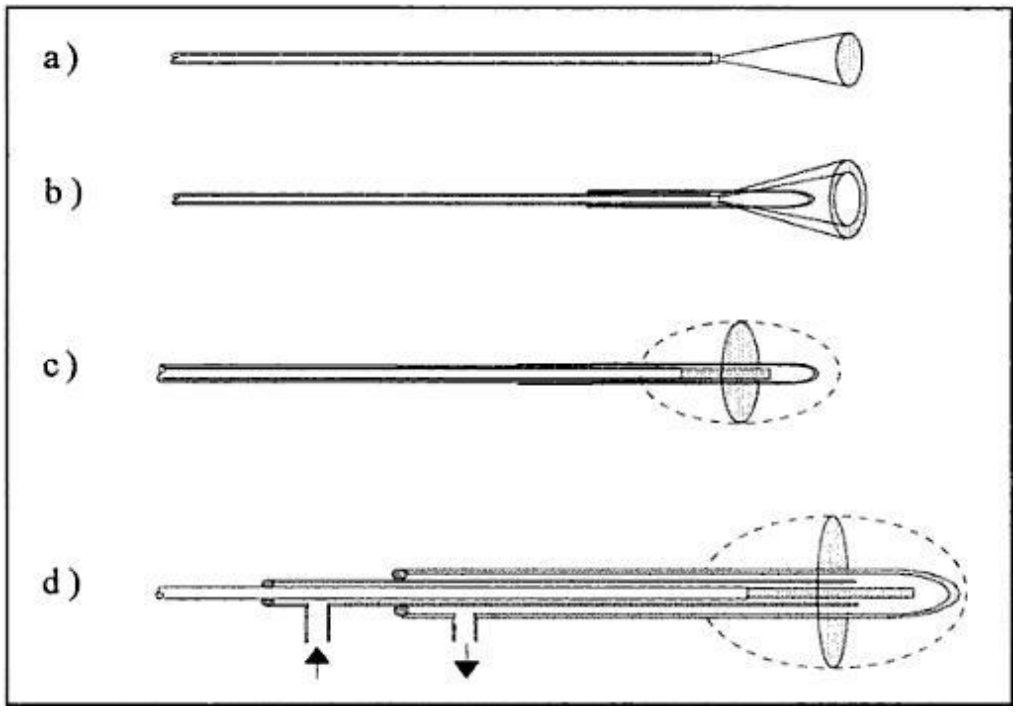

Figure 1.8 Optical fiber applicators for LA: a) bare fiber, b) ring-mode fiber, c) scattering fiber and d) water-cooled scattering fiber.

A *bare fiber* (Fig. 1.8A and 1.9B) is an optical fiber without any external protection, characterized by a core diameter larger than the cladding one. The tip of an optical fiber is

realized by cutting the free termination of the fiber parallel to the axis of light propagation. Besides its simplicity and the easy availability, bare fiber has the property to concentrate the high laser power on its small surface placed in contact with the tissue: considering a diameter of 400 µm and a laser power of 3 W, the power density at the fiber tip is 2400 W/cm^2. This feature is appreciable in case of treatment of small tumoral lesions, but presents the drawback of induce a high thermal gradient close to its tip which, for high laser power, can damage the tip. Bare fiber was the first applicator employed to perform LA in eighties [18, 15].

A modification of the bare fiber resulted in the conic fiber: the emitting surface of a bare fiber is modeled in order to concentrate all the radiation on the tip, as shown in the Fig. 1.9A. The comparison of thermal effect induced in the tissue (liver tissue, in this case) by bare fiber and conic fiber is also presented in Fig. 1.9C:

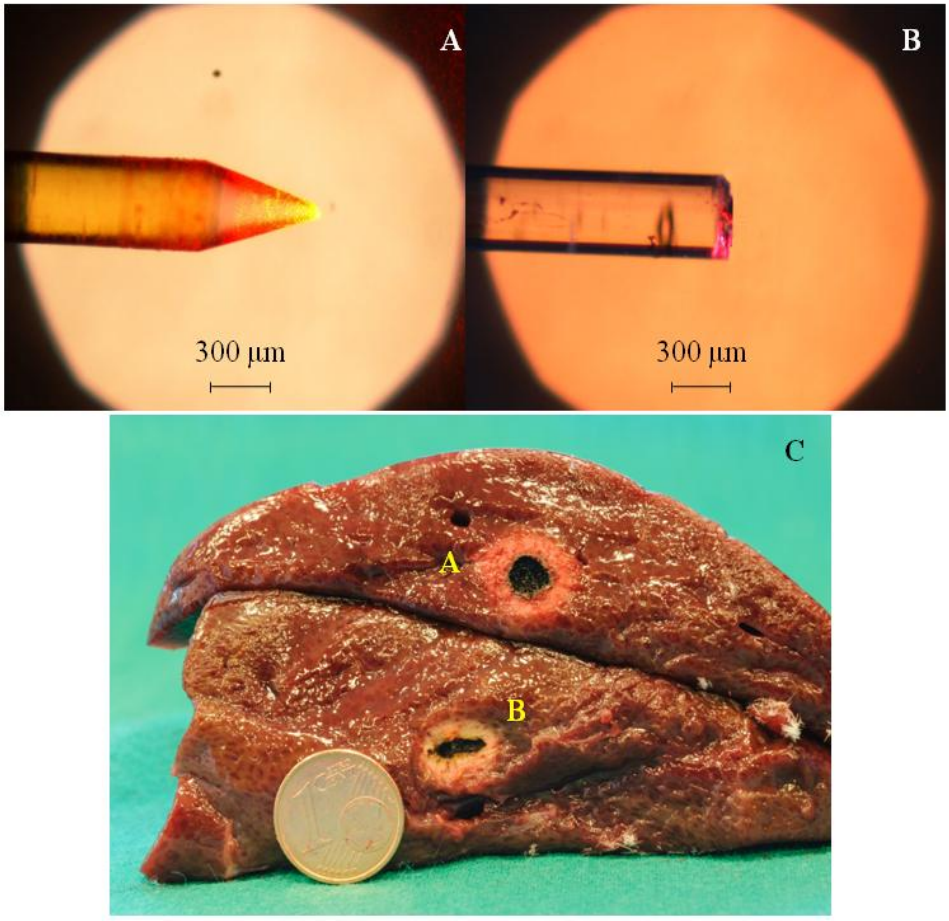

Figure 1.9 Optical fiber applicators for LA: A) conic fiber, B) bare fiber, C) comparison of thermal damage on liver tissue performed by conic fiber (A) and bare fiber (B).

With the development of LA, the interest in the increment of outcome of therapy grew, and many researchers investigated novel manufactures of bare fiber, focusing on the design of new tips, namely, the part of the fiber in direct contact with the tissue undergoing treatment.

A modified form is the *ring-mode fiber* (Fig. 1.8B), which has a circumferential radiation characteristic, but, such as the bare fiber, emits light in forward direction.

Aiming to obtain a more homogeneous radiation pattern, also useful to have a larger contact surface with tissue, surface-emitting applicators were introduced, under the name of scattering -or diffusing- emitters (Fig. 1.8C and D). To realize this kind of applicator, the cladding is partially removed by the surface of core in correspondence of the active length of the applicator, by means of etching techniques. Since after the etching, the surface of the fiber core is frosted and breakable, usually the fiber is housed within a glass dome transparent to the wavelength of laser light, to prevent mechanical stress on it [19].

A detail of applicator in Fig. 1.8C is shown below:

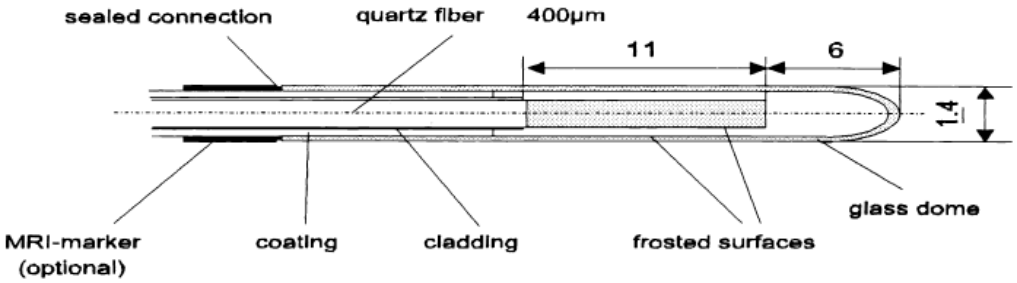

Figure 1.10 Diffusing cylindrical fiber for LA. Lengths are expressed in mm [19].

MRI-marker is used to control the positioning of the applicator in the lesion under MRI-guide.

An alternative to the *diffusing cylindrical fiber* is the *zebra-like applicator* (Fig. 1.11), where emitting regions are alternate to not-emitting regions, in order to increase the active surface, since the etching technique does not allow obtaining frosted core longer than 2 cm.

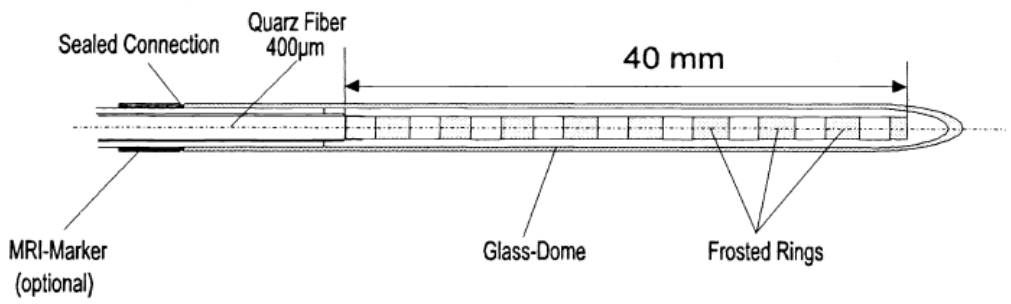

Figure 1.11 Zebra-like fiber for LA [19].

A further step in the panorama of applicators was the introduction of a liquid-cooler system. A diffusing fiber is housed within a catheter transparent to the wavelength of laser light, and during the irradiation, a liquid (saline solution, lipid solution, or pure water) circulating into the catheter at room temperature is forced to cool the surface of applicator. This technical solution allows to preventing the damage of external surface of applicator during the procedures, and to increase the volume of thermal damage induced within tissue. The different extent of thermal lesion depends on the feasibility to supply higher laser power (around 20 W, vs the common 5 W used with bare fiber), or to increase the duration of treatment.

A schematic of the liquid-cooler applicator is shown in Fig. 1.12:

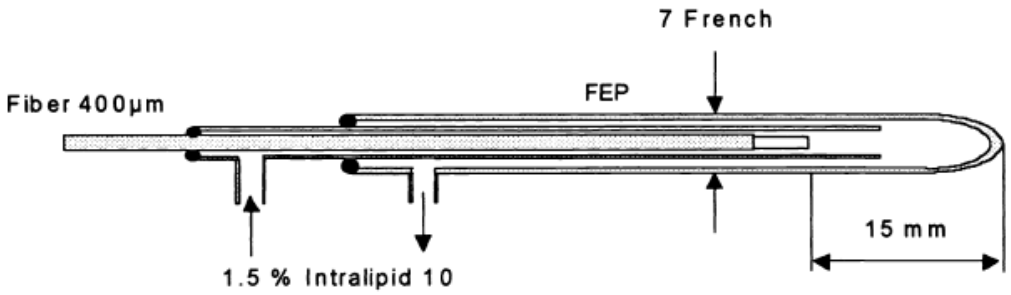

Figure 1.12 Internally-flushed laser applicator for LA [19].

Authors proposed also a comparison of effects on porcine liver tissue induced by different applicators, predicted by a theoretical model (Fig. 1.13).

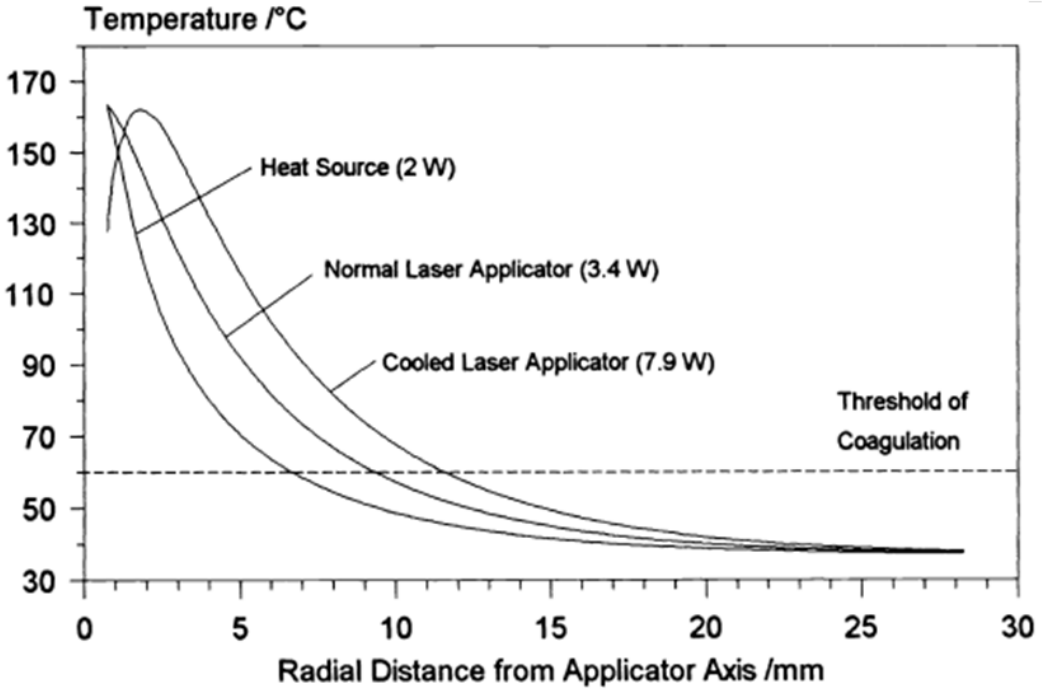

Figure 1.13 Comparison of computed temperature profiles achieved by a heat source with laser power of 2 W, a bare fiber emitting laser power of 3.4 W, and a liquid-cooler applicator with a laser power of 7.9 W The threshold of coagulation at reference temperature of 60 °C is also shown [19].

1.4.4 Tissue characteristics

Each tissue has own physical properties and, since LA is achieved by the mechanism induced by laser-tissue interactions, tissue properties involved in the physical process are thermal, mechanical and optical ones.

Some hints about the role of optical properties have been mentioned in previous paragraph (cfr. 1.4.2): absorption and scattering properties account for the ability of tissue to transform laser energy into heat and to diffuse the light penetrating within medium, respectively, and allow modulating the component (such as water, pigments, chromophore, as well as others), and are function of the light wavelength. Each tissue is, therefore, characterized by an absorption and a scattering spectrum. The analysis of tissues optical properties is deeply described in Chapter 3.

Once the light energy is converted into heat, accumulated in the volume surrounding the region of energy conversion, heat is transferred within tissue by conduction phenomenon. Actually, if the laser applicator is not inserted within the tissue, and blood vessels are close to the treatment region, also phenomena of radiation and convection are involved in heat transfer. Considering only the phenomenon of conduction, the thermal tissue parameters

involved are the thermal conductivity, the thermal diffusivity and the specific heat capacity [20].

- Thermal conductivity, k [$W \cdot K^{-1} \cdot m^{-1}$], is defined as the steady-state ability of an object to conduct heat when subject to a temperature gradient between its surfaces. Considering the 1-dimensional heat flow through a homogeneous wall (e.g., skin), of thickness ΔL and surface A, with gradient of temperature $\Delta T/\Delta L$ between two faces, the relationship from Fourier's law is the following:

$$q = \frac{dQ}{dt} = -kA \cdot \frac{\Delta T}{\Delta L} \tag{1.4}$$

  where Q is the thermal energy and q is the heat flow.

- Thermal diffusivity, α [$W \cdot K^{-1} \cdot m^{-1}$], is the transient ability of the medium to conduct heat when subjected to spatial gradient of temperature. The general expression is derivable from the conduction Equation:

$$\frac{\partial}{\partial x}\left(k\frac{\partial T}{\partial x}\right)+\frac{\partial}{\partial y}\left(k\frac{\partial T}{\partial y}\right)+\frac{\partial}{\partial z}\left(k\frac{\partial T}{\partial z}\right)+S=\rho c\cdot\frac{dT}{dt} \tag{1.5}$$

  where S is the internal heat generation [$W \cdot m^{-3}$], ρ is the tissue density and c the specific heat capacity at constant pressure. If k is assumed to be constant, Equation 1.5 changes in:

$$\frac{\partial^2 T}{\partial x^2}+\frac{\partial^2 T}{\partial y^2}+\frac{\partial^2 T}{\partial z^2}+\frac{S}{k}=\frac{1}{\alpha}\cdot\frac{dT}{dt} \tag{1.6}$$

  where $\alpha = \frac{k}{\rho c}$.

  Considering a semi-infinite medium with initial temperature of T_i, and a temperature T_s at time zero fixed on one flat surface, the solution of Equation 1.5 in 1 dimension and under these simplifying hypothesis is the following:

$$\frac{T(x,t)-T_s}{T_i-T_s}=erf\left(\frac{x}{\sqrt{4\alpha t}}\right) \tag{1.7}$$

  where x is the spatial coordinate, and erf(·) is the error function, defined as:

$$erf(x)=\frac{2}{\sqrt{\pi}}\cdot\int_0^x e^{-u^2}du \tag{1.8}$$

From Equation 1.7 the characteristic length of the tissue, or "penetration thermal depth", is defined as $z_{therm}(t) = \sqrt{4\alpha t}$, that represents the distance within tissue where the temperature reaches the value of 1/e of its peak value.

- The specific heat capacity, c [$kJ \cdot kg^{-1} \cdot K^{-1}$], determines the amount of thermal energy stored in a material at a certain temperature. It represents the variation of enthalpy, h, with respect to temperature, T, at fixed pressure, P:

$$c \equiv \left.\frac{dh}{dT}\right|_P = \frac{k}{\rho\alpha} \tag{1.9}$$

1.4.5 Temperature monitoring during treatment

Temperature is the crucial parameter to control during LA, since the efficacy of treatment depends on it. Some factors make the measurement challenging: the high spatial temperature gradient, that can exceed 50 °C/mm, the high temperature reached within tissue (up to around 300 °C), the direct optical absorption of laser energy into the sensor [21].

The techniques of temperature measuring can be split into two main methodologies: invasive and non-invasive techniques.

Invasive techniques require the use of a sensor, placed in direct contact with the tissue region under temperature monitoring. Although the new technologies lead to small-size sensors, also with inertness and intrinsically safe features, the main drawback of these probes is the insertion, despite their elevate metrological characteristics, such as, among others, high sensitivity and resolution. The most used sensors for invasive tissue temperature monitoring are firstly the thermocouples, followed by optical sensors.

Thermocouples are cheap and easily available, but the main issue is related to the self-heating because of the direct absorption of laser light during LA. This concern is well known in the scenario of LA thermometry, and many authors are working on the correction of measurement artifacts. This theme is analyzed in Chapter IV.

Optical sensors mostly include two kind of probes, both based on fiber optic technology: fluoroptic sensors and fiber Bragg grating sensors The principal advantage of optic sensors is the electromagnetic immunity, which make them suitable to be employed during MRI-guided LA. Nevertheless, fluoroptic probes show also the drawback of artifact, but particularly close to the laser applicator, where the temperature gradient is

high. Some authors recommend to use them when inserted within tissue at a minimum distance of 1 cm, where artifacts are negligible. Despite the above mentioned concern, fluoroptic sensor are largely employed because of their simplicity of use, and the commercial availability of a module that converts in real time the optical output of sensors in temperature value.

Lastly, fiber Bragg grating are spreading in the last decade in the scenario of LA thermometry. Beside the electromagnetic immunity, fiber Bragg gratings do not present the issue related to self-heating and, as consequence, measurement artifact. They can be fabricated to allow temperature measurement in several tissue regions by using only one optical fiber, minimizing therefore the issue related to the insertion

Anyway, sensors are mostly suitable to perform thermometry experiments in *ex vivo* models.

Non-invasive thermometry is based on imaging techniques, and the research in this field is encouraged because it allows overcoming the issues related to the invasivity of sensors, and also because LA is usually performed under imaging guide. In particular, infrared, ultrasound, CT and MR-based thermometry has been carried out. The basic idea of each image-based thermometry approach is that some physical or chemical properties of tissue undergoing LA are temperature-dependent, and it is possible to visualize their change on images, in terms of variation of specific image properties. Beyond the advantage of non-requiring sensors insertion within the organ, a relevant benefit of image-based thermometry is the possibility of obtaining the temperature distribution pixel by pixel in the whole volume of interest.

Infrared modality, performed with infrared thermo-camera, is the simplest technique, but poor, since it allows monitoring only surface tissue temperature. Therefore, it is available for thermometry during superficial laser treatment (e.g., dermatology), but not for interstitial thermotherapy.

Ultrasound thermometry is still debated, and only a few studies were performed during LA. The principal concern of this method is the presence of physiological motion or unexpected variation in acoustic tissue properties, which could cause artifacts in ultrasound thermal imaging. Nevertheless, artifacts can be removed and compensated by image post-processing. The main advantages of ultrasound thermal imaging are: 1) the employment of non-electromagnetic and non-ionizing waves, 2) the non-invasiveness of the method, 3) the

widespread availability of ultrasound technology that could be a valid alternative to the high costs related to other established techniques (e.g., MRI or CT thermometry).

CT- and MRI-based thermometry are nowadays the principal non-invasive techniques, although the idea of use MRI for temperature monitoring saw the light almost contemporary to the development of LA, because of the compatibility of laser light guided by optical fibers with magnetic fields. Such as for ultrasound, the dependence of some tissue properties on temperature modifies other image parameters, therefore the temperature change during LA is observable in real time in the images. A big research effort is dedicated to CT- and MRI-based thermometry because of the valuable resources provided by these tools, and of the importance to optimize image parameter, in order to achieve the maximum performances of the techniques, destined to the control of LA outcome during human treatments.

Concepts of CT- and MRI-thermometry are analyzed in detail in Chapter V and VI, were experimental trials on *ex vivo* tissue are presented.

1.5 Laser Ablation: clinical background

Laser Ablation (or Laser-induced Interstitial Thermotherapy, LITT) was introduced in the first time in clinical scenario by Bown for treatment of liver metastasis [15], and by Ascher for brain tumor ablation [18] in 1983. During the following years, Laser Ablation found application also in the management of isolated metastasis, benign prostatic (LA) hyperplasia metastasis of colorectal cancer of liver, breast and brain, as well as thyroid nodules [22]. In 1989 Bown and his team documented the first cases of five treated patients with four different malignancies (tumor breast, subcutaneous secondary tumor, recurrent pancreatic tumor, and secondary liver tumors): in most cases, tumor was partially reduced and no particular complications after operations with Nd:YAG laser were found [23]. The team of Dachman worked since 1989 in the assessment of LA for treatment of liver metastasis, focusing on one hand on the correlation between laser power and necrosis size, on the other hand on the assessment of tissue temperature during procedure, both in animal model and patient [24].

Nowadays, the largest experience in clinical practice regards the use of LA for metastasis of liver, lung and breast.

As far as it concerns LA for liver tumor, a big experience can be found in Universitätsklinikum in Frankfurt am Main (Germany), where Prof. Vogl and Prof. Mack

performed for years this kind of therapy. About 1400 patients with liver metastasis underwent LA in a large-scale study 14-years long, until 2008. The inclusion criteria were the following: not more than 5 lesions, maximum diameter of 50 cm, residual metastases in patients who have already undergone liver resection, progress of metastases despite chemotherapy, bilobar metastases (involvement of both lobes of liver), patients who are contraindicated for operation, patients who are primarily inoperable can be brought to an operable situation with LA (metastases in both liver lobes), LA as alternative therapy for patients who refuse surgical resection and systemic or local chemotherapy. Exclusion criteria were extraepatic metastatic spread, controindication for MRI and coagulation status more than 50% below normal status [25]. MRI- and ultrasound-guided LA were performed with Nd:YAG laser source, whose radiation is transported by means of a water cooled optical applicator within the lesion to be treated. A mean laser power of 25 W (water-cooled applicator) for about 25 minutes were employed, and treatment was performed under local anesthesia, well tolerated by patients. In 95% of cases the complete tumor necrosis was achieved, and safety margins of 5 mm avoiding recurrences, although frequent complications such as pleural effusion and intrahepatic or subcapsular hematoma [26, 27].

Different group are performing LA for treatment of lung metastasis: among them, Mensel *et al.* treated 42 patients since 2001, with 80% of success [28], Rosenberg *et al.* used a multi-applicator approach to ablate lung tumor on 64 patients with tumor diameter between 0.4 cm and 8.5 cm. survival rate at 1, 2, 3, 4 and 5 years was of 81%, 59%, 45%, 44% and 27% [29]. In both cases complicances like pneumothorax occurred.

1.6 Human pancreas and cancer

1.6.1 Anatomy and physiology of human pancreas

Pancreas is a gland of digestive system. It is mainly composed by two type of glands: exocrine glands, deputed to the secretion of digestive enzymes in pancreatic juice, which reach the duodenum through pancreatic duct, for digestion of carbohydrates, fat, proteins and acids, such as the production of bicarbonate to neutralize acid; endocrine glands, i.e, islets of Langerhans, which secret hormones like insulin and glucagon (which regulate the level of glucose in the blood), and somatostatin (which prevents the release of the other two hormones).

Pancreas lies transversely in the retroperitoneal sac, between the duodenum on the right, the spleen. It is related to the omental bursa above, the transverse mesocolon anteriorly, the greater sac below. Pancreas is composed of the following parts: the head lies within the concavity of the duodenum; the uncinate process emerges from the lower part of head, and lies deep to superior mesenteric vessels; the neck is the constricted part between the head and the body; the body lies behind the stomach, the tail is on the left end of the pancreas. It lies in contact with the spleen and runs in the lienorenal ligament.

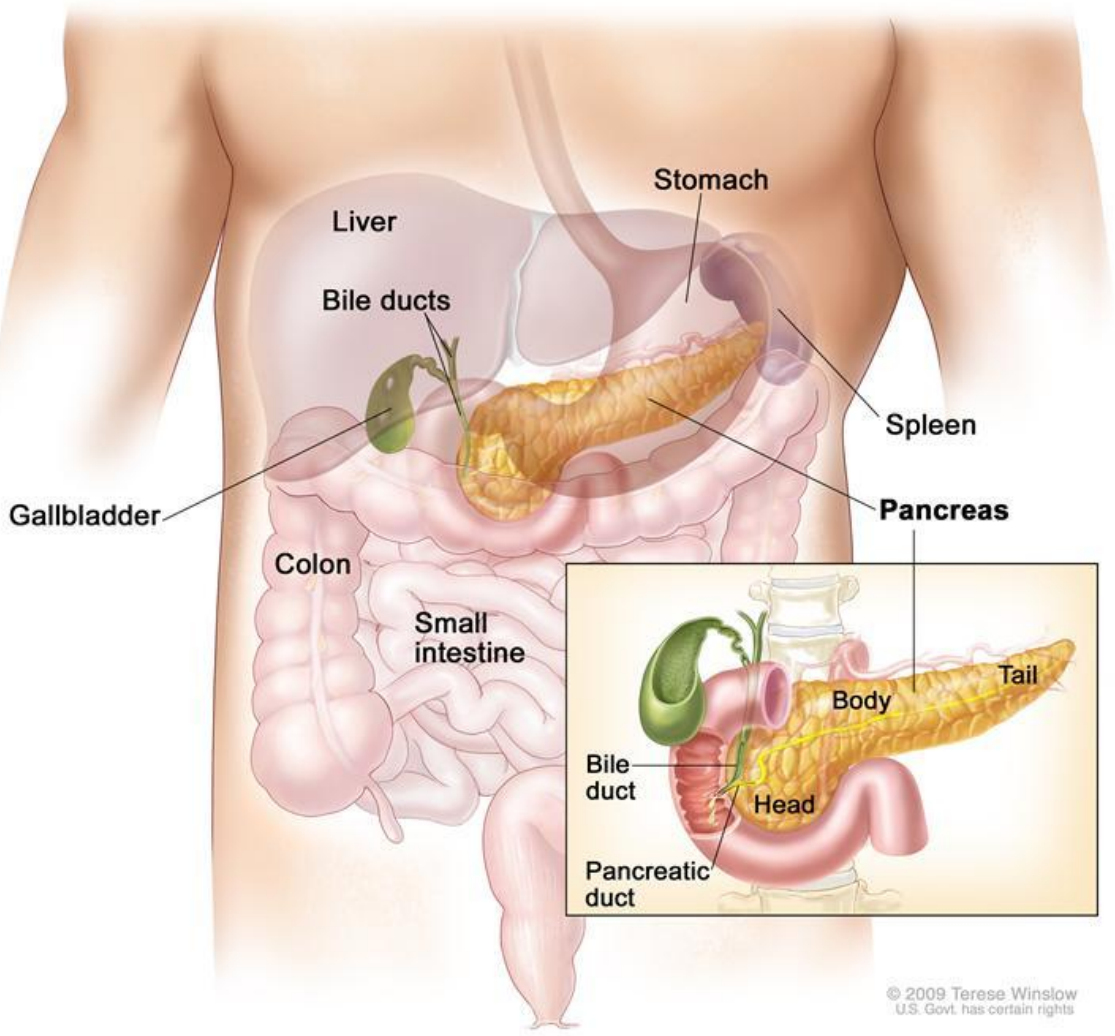

Figure 1.14 Anatomy of gastrointestinal system and normal pancreas.

1.6.2 Pancreatic cancer

The poor prognosis of pancreatic cancer is a hard challenge for the medical community. Radical resection is currently the only treatment able to improve long-term survival in

pancreatic cancer. Pancreatic cancer is the fourth most frequent cause of death from cancer in most developed countries (more than 290000 new cases of cancer in digestive system are estimated in US in 2013 [30]), and strategies for its diagnosis and resection are strongly limited. The traditional surgical treatment, known as Whipple procedure, is high risk, strongly operator-dependent and invasive: in fact, it requires a complex open surgical access to reach the gland, the removal and subsequent anastomosis of different parts of digestive apparatus. Surgeon usually removes 95% of the pancreas, including tumor, and leaves the 5% for the insulin production. The procedure takes more than 6 hours, with extended pre-hospital and post-hospital recovery (i.e., currently from 1 to 3 weeks), characterized by a poor life quality. The Whipple procedure leads to about a 20% 5-year survival, but because of the presence of widespread local disease or metastasis, only 10–20% of patients undergo pancreatic resection. This issue is related to the delayed diagnosis of pancreatic cancer, because symptoms usually appear after the tumor reaches a significant size. Treatments for inoperable patients are limited, and consist mainly in palliative methods, based on chemotherapy and radiotherapy, aimed to reduce the pain and to slightly improve the life quality of the patient [31]. Furthermore, the economic impact of the traditional surgery for pancreatic cancer removal is high, considering the use of many resources of the hospital (i.e., a expert surgeon, a complete and experienced team, the operating theatre available for many hours) and the long recovery times, among other factors.

Treatment options for unresectable pancreatic cancer are limited and new therapeutic measures should be advocated. Recently, there has been a growing interest about the possibility to administer local ablative methods by thermal coagulation and protein denaturation to locally advanced pancreatic cancer. The main limiting factor for the diffusion of ablative techniques are the delicate parenchyma of pancreas predisposing to pancreatitis, such as the closeness to important anatomical structures, i.e., duodenum, common bile duct, important veins and arteries [32]. Nevertheless, current preclinical studies documented the feasibility, safety and efficacy of ablative methods for pancreatic cancer treatment, but nowadays only a few clinical studies have been carried out. The most diffused technique is the Radiofrequency Ablation (RFA), together with High Intensity Focalised Ultrasound (HIFU). The feasibility of Microwave Ablation and Photodynamic Therapy (PDT) have also been investigated in several trials for the palliative treatment of pancreatic cancer.

1.7 Ablative techniques for pancreatic cancer removal

Before to proceed with the description of LA for pancreatic cancer removal, it would be useful to briefly deal with other ablative techniques, proposed during the last decades for the treatment of pancreatic tumor. Since eighties the concept of minimally invasive surgery spread in the treatment of locally advanced malignancies. Open surgery is usually associated with morbidity and mortality, causes significant suppression of immune system, leading to a risk of perioperative metastatic tumor dissemination. Laparotomy can slightly reduce the contraindications of traditional surgery, but minimally invasive procedures are more suitable for localized tumors. In general terms, minimally invasive surgery utilizes a range of energy-based methods for *in situ* tumor destruction. The most known techniques employ laser (LA, photodynamic therapy), radiofrequency and microwave energy, cryoablation and high intensity focused ultrasound.

The first proposal of new techniques for pancreatic cancer treatment is dated 1981, when Holyokes discussed the benefit of adjuvant therapies (particularly, thermal and photodynamic therapies), also in combination with traditional surgery [33].

The concept of ablation is related to the increase of temperature within the tumoral mass, caused by the introduction of a heat source inside the lesion, and the thermal conduction through the tissue itself (with exception of Photodynamic Therapy, where the interaction is chemical). The outcome of therapy are related to the temperature reached within the tissue to be treated, but the choice of the adequate source is related to the size of the thermal damage the physician wants to achieve, and also to the tool used to guide the procedure (MRI, CT, ultrasound).

In the following the most commonly accepted ablative techniques for pancreatic cancer removal are discussed.

1.7.1 Radiofrequency ablation

The Radiofrequency (RF) ablation requires a RF electrode which releases the RF current generated by a RF generator to the tissue. The RF electrode is composed by a metal shaft, which is insulated, with exception of the exposed conductive tip, as well as a wide grounding pad placed on the patients skin. The RF generator produces RF voltage between electrode tip and grounding pad, establishing lines of electrical field within patients body between two electrodes. The typical RF frequency used for this treatment is less than 1 MHz: it allows the oscillation of electric field and, consequently, the oscillatory

movements of ions of tissue, with a velocity proportional to the field intensity. The mechanism of tissue heating with RF ablation is frictional (or resistive) energy loss associated with this ionic current [34]. The strength point of RF ablation is the feasibility to easily adapt the geometry of RF electrode to the shape of tumor to be treated, such as the introduction of many strategies, like: the internally cooling electrodes to decrease the temperature increase at the center of the tumor and provide heat conduction towards the boundary; the use of pulsed RF with the aim to increase the mean intensity of energy deposition; the use of multiprobe and bipolar arrays. Goldberg *et al.* proposed the RF ablation for resection of pancreatic malignancies in a porcine model since 1999 [35], but the first clinical experimentation saw the light in 2005, with the studies of Date [36] and of Varshney [37]. Three patients underwent RF ablation during open operation, a necrosis with a diameter of about 3 cm was achieved in each candidate, and no major morbidity neither mortality occurred, such as pancreatitis was avoided, since healthy parenchyma was not thermally injured. A study performed in 2007 on 25 patients demonstrated that the combined use of RF ablation and palliative therapy can increase the mean survival from a value of 13 months (patients undergoing only palliative therapy) to 30 months (RF ablation and palliative therapy).

Although under investigation, clinicians still debate about the safety of RF ablation for pancreatic cancer removal, because of the frequent recurrence of complications, such as, pancreatitis when the thermal damage occurs in normal parenchyma [32]. Nevertheless, a recent study demonstrates that RF ablation is feasible in tumors located in the body and tail of pancreas, but not in those placed in the head, because the closeness to portal vein [38].

1.7.2 Microwave ablation

Microwave (MW) ablation is an almost new ablative technique in the field of tumor ablation. MW radiations represent the region of spectrum between 900 MHz and 2450 MHz. The interaction between polar water molecules and the oscillating electrical charges (at particular frequency of 9.2×10^8 Hz) causes the flip of water molecules, about 2-5 billion times for seconds. The movement of water molecules raises the temperature of medium, up to cellular death via coagulation necrosis [39]. As with RF ablation, MW ablation allows percutaneous, laparoscopic and open-surgical access. After an imaging guide, the microwave antenna (around 14 gauge) is placed within the tumor, and the antenna is connected by coaxial cable to the MW generator, able to produce a power of 60 W, with frequency of 915 MHz. Because of the inherent properties of electromagnetic waves, the

device is not required to be grounded, avoiding therefore drawbacks related to grounding pads burn. MW offers many of the benefit of RF, with some improvements: for example, during RF ablation, the zone of active tissue heating is limited to few millimeters around the applicator, and the increase of temperature at higher distances is caused by heat conduction, whereas the broad field up to 2 cm around MW antenna results in an larger treatment volume; furthermore, RF is also limited by the increase of electrical impedance of boiling and charring tissue, while this phenomenon seems to not affect MW procedures. Other advantages are related to the shorter treatment time, the optimal outcomes for mass close to vessels and less procedural pain. MW ablation is currently used for the treatment of lung and liver tumor, and some information are available about pancreatic cancer. In 2007 Lygidakis *et al.* performed the first clinical study of MW ablation feasibility on 15 patients affected by unresectable locally advanced pancreatic carcinoma. A MW antenna was inserted through laparotomic access, and tumoral masses had a mean diameter of 6 cm (from 4 to 8 cm). Minor complications (e.g., mild pancreatitis and asymptomatic hyperamylasemia) occurred only in 6 of 15 patients, and the longest survivor patient had a follow up of 22 months. Authors consider MW ablation feasible and safe for treatment of pancreas cancer [40].

1.7.3 High Intensity Focused Ultrasound ablation

An ultrasound wave produced by an oscillating piezoelectric crystal in the generator outside the body is guided by means of an *ad hoc* device that focalizes the beam in the target region. Although diagnostic ultrasound uses frequencies in the range 1-20 MHz, frequencies ranging from 0.8 MHz up to 3.5 MHz are employed in High Intensity Focused Ultrasound (HIFU) ablation [41]. Furthermore, typical diagnostic ultrasound transducers deliver ultrasound with time-averaged intensities of approximately 0.1–100 $mW \cdot cm^{-2}$ or compression and rarefaction pressures of 0.001–0.003 MPa, depending on the imaging mode. In contrast, HIFU transducers deliver ultrasound with intensities in the range of 100–10000 $W \cdot cm^{-2}$ to the focal region, with peak compression pressures of up to 30 MPa and peak rarefaction pressures up to 10 MPa [42]. Two predominant mechanisms of tissue damage are related to the conversion of mechanical energy into heat and to inertial cavitation, the last one caused by the alternating compression and decompression of tissue due to the US wave traveling through it. If compression and rarefaction pressure has sufficient magnitude, the gas stored into cells can be released in form of bubbles and produce *inertial cavitation*: the exposure of the bubble to the acoustic field results in

violent oscillations of the bubble and rapid growth of the bubble during the rarefaction phase, eventually leading to the violent collapse and destruction of the bubble.

Some studies concerning the application of HIFU for solid tumor ablation have been carried out, particularly on liver, prostate, breast and kidney. Some authors considered also the use of this new techniques for ablation of pancreatic cancer. Clinical trials on 250 patients have been performed in China between 2000 and 2002: no major complication were found after ablation procedure, and an interesting finding was related to the disappearing of pain due to pancreatic cancer after HIFU treatment, in 84 % of patients [43].

1.7.4 Cryoablation

The use of cold in medicine is as ancient as medicine itself. It is defined as the therapeutic destruction of tumor by freezing, and it is performed percutaneously under imaging guidance. During freezing, ice formation within extracellular space causes an osmotic gradient, responsible of tissue dehydratation. Ice crystals forming within cells cause the rupture of membranes and, as consequence, cellular death, while vascular stasis and thrombosis induce local tissue ischemia. Tissue temperature should be maintained between -50 °C and -20 °C. The procedure is realized by means of a cryoprobe and cryogenic freezing unity: the unity (for example, argon-based) allows a high-pressure gas (e.g. argon) to circulate within the lumen of the cryoprobe. The low pressure within the lumen causes a rapid expansion of gas, which results in decrease of temperature and in the formation of an ice-ball around the probe tip. The process of thaw is passive, and is accelerated thanks a gas like helium which circulates at the tip, to allow the removal of probe from the treatment volume. At the boundary of ice-ball the temperature is 0 °C, and the letal values between -50 °C and -20 °C are achieved within 5 mm inside the iceball edge, therefore the iceball should be extended beyond the tumor region. Unlike thermoablation, image-based monitoring during cryoablation is feasible, particularly with CT and MR images. First use of cryoablation for treatment of pancreatic cancer is dated 1991, when Patiutko *et al.* performed the therapy on 30 patients, with positive outcomes and alleviation of the pain [44]. Further studies have been carried out combining cryoablation with implantation of ^{125}Iodine seed, used to destroy residual cancer cells after treatment [45], or exploring the feasibility of ultrasound-guided percutaneous access for cryoprobe [46].

1.7.5 Photodynamic therapy

The last discussed minimally-invasive surgical technique for pancreatic cancer treatment is the Photodynamic Therapy (PDT). Differently from the techniques described above, PDT involves a chemical effect to induce cancer destruction, rather than a thermal interaction: a photosensitive element (photosensitizer) is pre-administered in the tissue undergoing treatment, and then activated by light at known wavelength, which matches with the absorption characteristic of photosensitizer. The activated photosensitizer is responsible for the production of reactive oxygen species, such as cytotoxic singlet oxygen and free radicals. These species mediate cellular toxicity [47]. Effects of PDT on tumor are related not only to the direct toxicity of oxygen in the cells, but also to the tumor-associate vasculature infraction induced by PDT, and can activate an immune response against tumor cells. Advantages of PDT are the high tumor selectivity behavior, since the tumor retains photosensitizer more than normal tissue, and the drug is cytotoxic only when activated by light [48]. One of the first *in vivo* study (Phase I) was carried out by Bown and his team [49] on sixteen patients. The median survival time after photodynamic therapy was 9.5 months (range 4–30). Seven of 16 patients (44%) were alive one year after therapy. Authors conclude that PDT can produce necrosis in pancreatic cancers with an acceptable morbidity, although care is required for tumours invading the duodenal wall or involving the gastroduodenal artery, because of the risk of bleeding.

4.8 EUS-guided LA for pancreatic cancer removal

PDT has shown some safety limitations in the ablation of medium-large size pancreatic masses, while RF ablation for locally advanced pancreatic cancer has been performed under ultrasound guidance in open surgery during laparotomy. Only few studies have focused on the feasibility and complications of RF ablation with encouraging results about survival rate improvement. However, this ablative method, such as MW ablation, cryoablation and HIFU has been currently described only during laparotomy for two main reasons: the size of the probe and the difficult anatomical approach to the pancreas.

In order to individuate an alternative mini-invasive approach, the LA has been proposed by Di Matteo *et al* [50]. LA can achieve a high rate of complete tissue necrosis with the application into the neoplastic mass of thin optic fibre (diameter between 300 μm and 600 μm) that can pass through a small calibre needle: these needles are already used during endoscopic procedures as the linear-array endosonography (EUS). EUS is a technique which integrates the potentialities of echography and endoscopy, and it is performed on

patients undergoing sedation, on the superior digestive tract. It is performed by means of an endoscope, for the visualization of gastro-intestinal tract, with an echo probe at its extremity, which allows visualization of images with high resolution (1-2 mm). In the last decade, a technique known as Endosonography-guided fine-needle aspiration biopsy (EUS-FNA) spread in the field of diagnosis and staging of pancreatic cancer [51]. The position of the echoendoscopic transducer within the stomach or duodenum allows for unparalleled access to the pancreas. With a curvilinear echoendoscope, a needle can be passed through the working channel under ultrasound guidance directly into a tumour to obtain tissue for diagnosis (Fig. 1.14). Fine needle aspiration (FNA) increases the diagnostic accuracy of EUS to 95%. Fine needle injection (FNI) has naturally emerged from this technique, enabling therapeutic modalities of injected agents under real time EUS guidance [52].

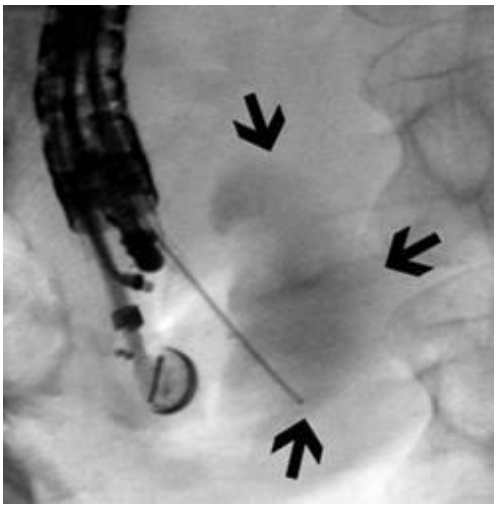

Figure 1.14 EUS-FNA for pancreatitis diagnosis (CT-image) [53].

EUS has become a popular diagnostic and therapeutic tool because of its ability to visualize pancreas with great accuracy and to allows the puncture of the target lesions under real-time imaging with more accurate positioning, minimal injury and reduced puncture distance. Actually, the pancreas is a retroperitoneal gland easier to reach from the stomach and/or duodenum than from trans-abdominal percutaneous approach.

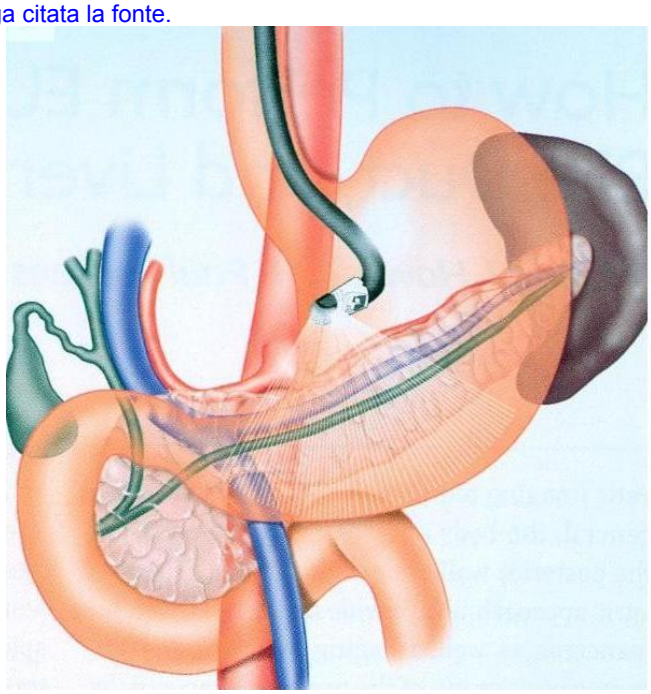

Figure 1.15 EUS-guided approach for pancreas.

At the best of my knowledge, the use of LA for the removal of pancreatic cancer is almost absent in clinical practice.

The main novelty of the proposed study is the integration of the minimally invasive features offered by both EUS methodology and LA. A small optical fiber can be introduced within the operative channel of the echo-endoscope and reach the pancreatic head trough the duodenal access.

The clinical procedure requires the support of a theoretical model, useful to predict the effect of the interaction between Nd:YAG and pancreatic tissue in different conditions, and with several laser settings, and the feedback information of effective outcome during LA. The last one is provided by the monitoring of temperature distribution during the procedure.

Therefore, during my research program, I focalized on the development of the predictive model, on its experimental validation, and on the principles and different techniques of thermometry during LA.

Bibliography Chapter 1

[1] M. Niemz, Laser tissue interaction. Foundamental and applications, Springer, 2005.

[2] R. A. Serway and C. Vuille, College physics, vol 2, 2012.

[3] H. P. Berlien and G. J. Müller, Applied laser in medicine, Springer, 2003.

[4] Q. Peng et al, "Laser in Medicine," *Rep. Prog. Phys.*, vol. 71, p. 056701, 2008.

[5] C. M. Philipp, Rohde and B. H. P. E, "Nd:YAG laser procedures in tumor treatment," *Seminars in surgical oncology*, vol. 11, pp. 290-198, 1995.

[6] W. Koechner, Solid-state laser engineering, Springer, 6th edition.

[7] N. S. Nishloka, "Application of lasers in gastroenterology," *Laser Surg Med*, vol. 16, no. 205, 1995.

[8] R. Tranfaglia, "Laser in medicina e riabilitazione. Appunti del corso di Bioingegneria.," 2009.

[9] M. Nikfarjam, C. Malcontenti-Wilson and C. Christophi, "M. Nikfarjam, C. Malcontenti-Wilson, C. Christophi Comparison of 980- and 1064-nm Wavelengths for Interstitial Laser Thermotherapy of the Liver," *Photomedicine and Laser Surgery*, vol. 23, no. 3, p. 284–288, 2005.

[10] E. Rohde, I. Mesecke-Vonrheinbaben, A. Roggan, H. Podbielska, M. Hopf and G. Müller, "Interstitial Laser-Induced Thermotherapy (LITT): Comparison of In-Vitro Irradiation Effects of Nd:YAG (1064 nm) and Diode (940 nm) Laser," *Medical Laser Application*, vol. 16, p. 81–90, 2001.

[11] G. J. Müller and A. Roggan, Laser-induced interstitial thermotherapy, SPIE, 1995.

[12] E. Rohde, I. Mesecke-von Rheinbaben, A. Roggan, H. Podbielska, M. Hopf and G. Müller, "Interstitial laser-induced thermotherapy (LITT): comparison of in-vitro irradiation effects of Nd: YAG (1064 nm) and diode (940 nm) laser.,"

Medical Laser Appl, vol. 16, pp. 81-90, 2001.

[13] M. Nikfarjam, C. Malcontenti-Wilson and C. Christophi, "Comparison of 980- and 1064-nm wavelengths for interstitial laser thermotherapy of the liver.," *Photomedicine and Laser Therapy,* vol. 23, no. 3, pp. 284-288, 2005.

[14] R. J. Stafford, D. Fuentes, A. A. Elliott, J. S. Weinberg and K. Ahrar, "Laser-induced thermal therapy for tumor ablation.," *Critical Reviews™ in Biomedical Engineering,* vol. 38, no. 1, pp. 79-100, 2010.

[15] S. G. Bown, "Phototherapy of tumors," *World J Surg,* vol. 7, p. 700, 1983.

[16] O. S. o. Ameica, Fiber Optics Handbook: Fiber, Devices, and Systems for Optical Communications, Bass, M; Van Stryland, E W;, 2002.

[17] [Online]. Available: http://www.rp-photonics.com/.

[18] P. W. Ascher, "Interstitial thermotherapy of brain tumors with Nd:YAG laser under real time MRI control," *SPIE 1200 Lasersurgery, Advanced characterization therapeutics and system II,* p. 242, 1990.

[19] A. Roggan, D. Albrecht, H. P. Berlien, J. Beuthan, C. T. K. H. Germer, W. Wodrich and G. J. Mueller, "Development of an application- set for intraoperative and percutaneous laser induced interstitial thermotherapy (LITT)," *SPIE, Medical Applications of Lasers II,* vol. 2327, pp. 253-260, 1994.

[20] J. W. Valvano, "Tissue thermal properties and perfusion," in *Optical-thermal response of laser-irradiated tissue,* Springer Netherlands, 2011, pp. 455-485.

[21] J. A. Pearce, J. W. Valvano and S. Emelianov, "Temperature Measurements," in *Optical-Thermal Response of Laser-Irradiated Tissue,* Springer Netherlands, 2011, pp. 399-453.

[22] C. M. Pacella and al., "Thyroid Tissue: US-guided Percutaneous Laser Thermal Ablation," *Radiology,* vol. 232 , pp. 272-280, 2004.

[23] A. C. Steger, W. R. Lees, K. Walmsley and S. G. Bown, "Interstitial laser hyperthermia: a new approach to local destruction of tumors," *British Medical Journal,* vol. 299, p. 362–365, 1989.

[24] A. H. Dachman et al, "Interstitial laser ablation in experimental models and in clinical use," *Seminars in interventional radiology,* vol. 10, no. 2, 1993.

[25] [Online]. Available: http://radiologie-uni-frankfurt.de/content/e4864/e27/e35/e1702/e1973/index_eng.html.

[26] T. J. Vogl et al, "Laser-induced thermotherapy of malignant liver tumors: general principals, equipment (s), procedure (s)–side effects, complications and results," *European journal of ultrasound,* vol. 13, no. 1, pp. 117-127, 2001.

[27] T. J. Vogl et al., "MR-guided laser-induced thermotherapy (LITT) of liver tumours: experimental and clinical data," *International journal of hyperthermia,* vol. 20, no. 7, pp. 713-724, 2004.

[28] C. Stroszczynski, Minimally Invasive Tumor Therapies, Springer, 2006.

[29] C. Rosenberg, "Laser ablation of metastatic lesions of the lung: long-term outcome," *American Journal of Roentgenology,* vol. 192, pp. 785-792, 2009.

[30] R. Siegel, D. Naishadham and A. Jem, "Cancer statistics, 2013.," *CA: a cancer journal for clinicians,* vol. 63, no. 1, pp. 11-30, 2013.

[31] M. Vulfovich and C. Rocha-Lima, "Novel advances in pancreatic cancer treatment," *Expert Rev Anticancer The,* vol. 8, p. 993–1002, 2008.

[32] F. Orsi, M. Bezzi and G. Orgera, "Local ablative techniques in the treatment of locally advanced pancreatic cancer," in *New Concepts in Diagnosis and Therapy of Pancreatic Adenocarcinoma*, Berlin Heidelberg, Springer, 2010, pp. 167-173.

[33] E. D. Holyoke, "New Surgical Approaches to Pancreatic Cancer," *Cancer,* vol. 47, pp. 1919-23, 1981.

[34] S. N. Goldberg, "Radiofrequency tumor ablation: principles and techniques," *European Journal of Ultrasound,* vol. 3, no. 2, pp. 129-147, 2001.

[35] S. N. Goldberg, S. Mallery, G. S. Gazelle and W. R. Brugge, "EUS-guided radiofrequency ablation in the pancreas: results in a porcine model," *Gastrointest Endosc,* vol. 50, pp. 392-401, 1999.

[36] R. S. Date and A. K. Siriwardena, "Radiofrequency ablation of the pancreas II:

Intra-operative ablation of non-resectable pancreas cancer: a description of technique and initial outcome.," *J Pancreas,* vol. 6, pp. 588-92, 2005.

[37] S. Varshney *et al*, "Radiofrequency ablation of unresectable pancreatic carcinoma: feasibility, efficacy and safety," *J Pancreas,* vol. 7, pp. 74-78, 2006.

[38] G. Carrafiello, A. M. Ierardi, F. Piacentino, N. Lucchina, G. Dionigi, S. Cuffari and C. Fugazzola, "Microwave Ablation with Percutaneous Approach for the Treatment of Pancreatic Adenocarcinoma.," *Cardiovascular and interventional radiology,* vol. 35, no. 2, pp. 439-442, 2012.

[39] C. J. Simon, D. E. Dupuy and W. W. Mayo-Smith, "Microwave Ablation: Principles and Applications," *Radiographics,* vol. 25, no. 1, pp. S69-S83, 2005.

[40] N. J. Lygidakis *et al.*, "Microwave ablation in locally advanced pancreatic carcinoma: A new look," *Hepato-gastroenterology,* vol. 54, pp. 1305-1310, 2007.

[41] J. E. Kennedy, "High-intensity focused ultrasound in the treatment of solid tumours," *Nature reviews cancer,* vol. 5, no. 4, pp. 321-327, 2005.

[42] T. J. Dubinsky, C. Cuevas, M. K. Dighe, O. Kolokythas and J. H. Hwang, "High-intensity focused ultrasound: current potential and oncologic applications.," *American journal of roentgenology,* vol. 190, no. 1, pp. 191-199, 2008.

[43] S. X. He *et al*, "The noninvasive treatment of 251 cases of advanced pancreatic cancer with focused ultrasound surgery," in *2nd International Symposium on Therapeutic Ultrasound,* Seattle, 2002.

[44] I. Patiutko *et al*, "The combined treatment of locally disseminated pancreatic cancer using cryosurgery," *Vopr Onkol.,* vol. 37, no. 6, pp. 695-700, 1991.

[45] K. C. Xu *et al*, "A pilot study on combination of cryosurgery and 125iodine seed implantation for treatment of locally advanced pancreatic cancer," *World journal of gastroenterology,* vol. 14, no. 10, p. 1603, 2008.

[46] L. Niu *et al*, "T1389 A Novel Percutaneous Approach to Deliver Cryotherapy for the Treatment of Advanced Pancreatic Cancer," *Gastroenterology,* vol. 5, p. 138, 2010.

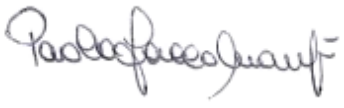

[47] D. E. Dolmans, D. Fukumura and R. K. Jain, "Photodynamic therapy for cancer," *Nature Reviews Cance*, vol. 3, no. 5, pp. 380-387, 2003.

[48] K. T. Moesta, P. Schlag, H. O. Douglass and T. S. Mang, "Evaluating the role of photodynamic therapy in the management of pancreatic cancer," *Lasers in surgery and medicine*, vol. 16, no. 1, pp. 84-92, 1995.

[49] S. G. Bown *et al*, "Photodynamic therapy for cancer of the pancreas," *Gut*, vol. 50, pp. 549-557, 2002.

[50] F. M. Di Matteo *et al*, "EUS-guided Nd: YAG laser ablation of normal pancreatic tissue: a pilot study in a pig model," *Gastrointestinal Endoscopy*, vol. 72, no. 2, pp. 358-363, 2010.

[51] M. Al-Haddad and M. A. Eloubeidi, "Interventional EUS for the Diagnosis and Treatment of Locally Advanced Pancreatic Cancer," *Journal of the Pancreas*, vol. 11, no. 1, pp. 1-7, 2011.

[52] B. M. Yan and J. Van Dam, "Endoscopic ultrasound-guided intratumoural therapy for pancreatic cancer," *Canadian Journal of Gastroenterology*, vol. 22, no. 4, pp. 405-10, 2008.

[53] D. I. Gheonea *et al*, "The Differential Diagnosis of Chronic Pancreatitis," *Current health sciences journal*, vol. 35, no. 3, pp. 159-64, 2009.

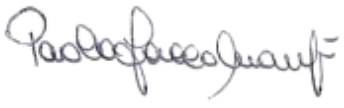

Chapter 2. Principles and theoretical model

2.1 Principles

Laser Ablation (or Laser induced Interstitial ThermoTherapy, LITT) is classified in the group of thermal interactions, where the increase of temperature is a pivotal parameter to be monitored for the efficacy of treatment [1]. Change of temperature within the organ depends on the time of irradiation and on the power value of the laser beam; therefore, it can be induced by either CW or pulsed laser radiation. At microscopic level, thermal effects can be described as follows: the photon with energy $h\nu$ interacts with a target molecule A, which changes in its excited state A*. Afterwards, the inelastic collisions of A* with the surrounding particles M cause the deactivation of A* and the simultaneous increase of the kinetic energy of M. The transfer of photon energy into kinetic one results in the local increment of temperature. These two steps can be summarized as follows:

$$A+h\nu \rightarrow A^*$$

$$A^*+M(E_{kinetic}) \rightarrow A+M(E_{kinetic}+\Delta E_{kinetic})$$

The efficiency of this process depends on the efficiency of two steps, separately. As far as it concerns the first step, the large number of accessible vibrational states of biological molecules facilitates the absorption; regarding the second one, thermal decay is also possible because energy of laser photons (e.g., Nd:YAG laser: 1.2 eV) is largely higher than kinetic energy of a molecule at room temperature (i.e., 0.025 eV).

The distribution of temperature in a laser-irradiated tissue is depends on many factors: most of them are related to the laser source (i.e., the wavelength, the power, the energy and the duration of irradiation), to the modality of emission of photons (i.e., the geometric characteristics of applicator), to the physical properties of tissue itself, in terms of optical and thermal parameters, and to the modalities of heat removal, due to blood flow, liquid evaporation and heat exchange with external environment.

The abovementioned pivotal parameters participate at different phases of the phenomenon of laser-tissue interaction, as schematized in the following flowchart (Fig. 2.1):

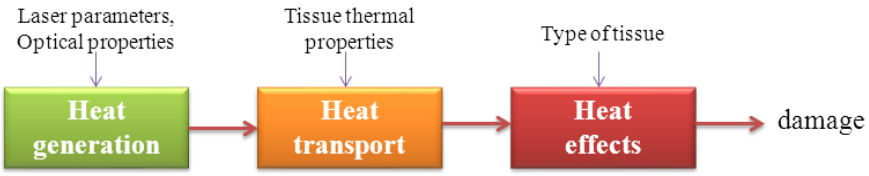

Figure 2.1: Flowchart of fundamental parameter for modeling laser thermal interaction.

Heat generation: we can consider a Gaussian-shape laser beam irradiating a slab of cylindrical tissue (coordinates system *r,z*) in *z*-direction, with an irradiance *I(r,z,t)* [$W \cdot m^{-2}$], at time *t*. The local heat deposit for time unit and area in thickness Δz, *S(r,z,t)* [$W \cdot m^{-3}$], can be expressed as:

$$S(r,z,t) = \frac{I(r,z,t) - I(r,z+\Delta z,t)}{\Delta z}$$

When Δz approaches to zero,

$$S(r,z,t) = -\frac{\partial I(r,z,t)}{\partial z}$$

and, since $I=f(-\mu_a \cdot z,r,t)$, we can express:

$$S(r,z,t) = \mu_a I(r,z,t)$$

Therefore, *S(r,z,t)* is strictly related to the absorption coefficient μ_a [m^{-1}], which depends on the wavelength of laser source and on the tissue. If no tissue alteration and phase transitions occur, the change of local heat content *dQ* causes a linear increase of temperature *dT*, according to the following:

$$dQ = mc \cdot dT$$

where *m* is the mass of tissue, and *c* is the specific heat capacity [$kJ \cdot kg^{-1} \cdot K^{-1}$].

Heat transport: if the applicator is in contact with tissue, the transport of heat occurs in terms of heat conduction and heat convection. The heat conduction takes place within the tissue, while the heat convection occurs when the heat transfer is due to blood flow, which plays a crucial role during Laser Ablation.

Heat conduction is the primary mechanism of heat transfer to the unexposed tissue; the heat flow j_Q is proportional to the temperature gradient ∇T, by means of the conductivity of tissue, k, i.e., $j_Q = -k\nabla T$.

A useful parameters for the modeling of spatial extent of heat transfer is the "thermal penetration depth", *z(t)*, defined as:

$$z_{therm}(t) = \sqrt{4kt} \tag{2.1}$$

and represents the distance where the temperature reaches the value of 1/e of its peak value. The choice of laser pulse -related to the time *t* in eq. (1)- during the therapy is pivotal for its efficacy and, in particular, to avoid thermal damage to surrounding structures. Hayes and Wolbarsht [2] introduced the parameter „thermal relaxation time", τ_{therm}, in the Equation 2.2, derived from Equation 2.1:

$$L = \frac{1}{\mu_a} = \sqrt{4k\tau_{therm}} \tag{2.2}$$

where L is the optical penetration depth.

If pulse duration $\tau < \tau_{therm}$, heat does not diffuse to a distance longer than L, otherwise thermal damage can occur. In this particular case, if $\tau_{therm} < 1$ ns, then heat diffusion during the laser pulse is negligible; otherwise, if $\tau_{therm} > 1$ ns, the heat diffusion becomes considerable, and the whole process shown in Fig. 2.1 and based on heat conduction equation, requires a numerical solution, for example by means of finite element method (as described in detail in 2.2).

The heat convection in *in vivo* biological tissue is mostly driven by blood perfusion. This phenomenon, besides the role in Laser Ablation (LA), is crucial also in many biological processes, such as the thermoregulation, or inflammation [3]. The blood perfusion has been modeled by Pennes [4] in 1948 considering a linear relationship with the temperature (Equation 2.4 in 2.2).

Heat effects: assuming a body temperature of 37 °C, no measurable effects are observed up to 42 °C. The first mechanism by which tissue is thermally affected can be attributed to conformational changes of molecules, that, with bond destruction and membrane alterations, cause **hyperthermia** (42-50 °C). If hyperthermia lasts for several minutes, a significant percentage of the tissue undergoes necrosis. Beyond 50 °C, a measurable decrease of enzyme activity is observed, resulting in reduced energy transfer within the cell and immobility of the cell. At 60 °C, denaturation of proteins and collagen occurs, leading to visible coagulation of tissue and necrosis of cells. Several treatment techniques, such as LA, produce temperatures above 60 °C. At temperatures higher than 80 °C, the membrane permeability is drastically increased, thereby destroying the otherwise maintained equilibrium of chemical concentrations. At 100 °C, water molecules contained in most tissues start to boil. The large vaporization heat of water (2253 kJ/kg) is advantageous,

since the vapor generated carries away excess heat and helps to prevent any further increase in the temperature of adjacent tissue. Due to the large increase in volume during this phase transition, gas bubbles are formed inducing mechanical ruptures and thermal decomposition of tissue fragments. Only if all water molecules have been vaporized, and laser exposure is still continuing, the increase in temperature proceeds. At temperatures exceeding 100 °C, carbonization takes place, as observable by the blackening of adjacent tissue and the escape of smoke. Finally, beyond 300 °C, melting can occur.

2.2 Theoretical model

A theoretical model has been implemented, with the aim to predict effects of laser light on pancreatic tissue. The predictions provided by the model have been afterwards compared with experimental results. In particular, the model provides an estimation of temperature distribution within pancreas during the therapy, and, as consequence, of volume of ablation and damage at the end of LA. These outcomes are strictly related to the laser settings (power, energy, time of irradiation), to the characteristic of emission of applicator(s), as well as to the properties of tissue. A schematic block diagram of the dominant parameters for thermal modeling is shown in Figure 2.2.

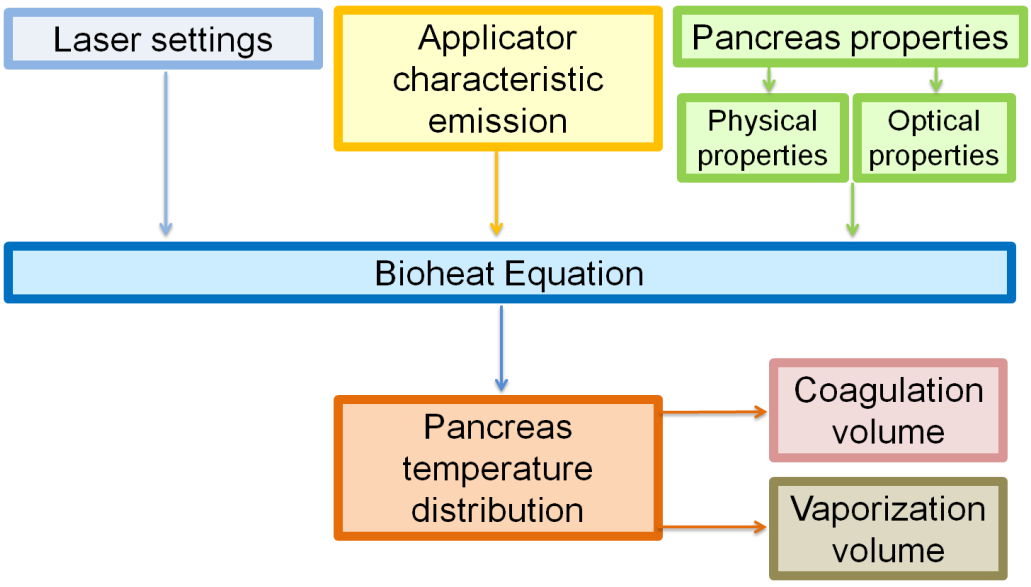

Figure 2.2: Block diagram of fundamental parameters for modeling thermal response of laser-irradiated pancreas.

The theoretical model, describing the thermal response of laser irradiated tissue [5, 6], is based on the Pennes Bioheat Equation [4] and assumes the form:

$$\rho \cdot c \frac{\partial T(x,y,z,t)}{\partial t} = \nabla(k \nabla T(x,y,z,t)) + Q_b + Q_m + Q_l - Q_e \quad (2.3)$$

where ρ is the tissue density [kg·m^{-3}], c is the tissue specific heat [J·kg^{-1}·K^{-1}] and k is the tissue heat conductivity [W·m^{-1}·K^{-1}]. $T(x,y,z,t)$ is the tissue temperature, expressed as a function of spatial coordinates, x, y, z, and of time, t. As simplifying hypothesis, tissue is assumed to be homogeneous and isotropic.

Other terms in Equation 2.3 are:

- Q_b [W·m^{-3}], the heat contribution due to blood perfusion per volume unit, which can be expressed by:

$$Q_b = \rho_b \cdot c_b \cdot w_b (T(x,y,z,t) - T_b) \quad (2.4)$$

where ρ_b is the blood density [kg·m^{-3}], c_b the blood specific heat [J·kg^{-1}·K^{-1}], w_b the blood perfusion rate per volume unit [s^{-1}] and T_b the blood temperature outside the treatment site;

- Q_m [W·m^{-3}], the metabolic heat generation due to oxidative process of lipids, proteins and carbohydrates;

- Q_l [W·m^{-3}], the heat source term due to photon absorption caused by laser-tissue interaction, expressed as:

$$Q_l = \mu_\alpha \cdot I(x,y) \cdot e^{-\mu_\alpha z} \quad (2.5)$$

being $I(x,y)$ the laser irradiance [W·m^{-2}], represented by a two-dimensional Gaussian distribution with $\sigma = r_f/3$ in order to obtain the 99% of the output laser power contained in the fiber core cross-section (r_f is the radius of bare fiber laser applicator):

$$I(x,y) = I_0 \cdot e^{-\frac{x^2+y^2}{2\sigma^2}} \quad (2.6)$$

where $I_0 = \frac{P}{2 \cdot \pi \cdot \sigma^2}$, and P is the output laser power [W] operating in continuous mode.

With reference to Equation 2.5, Lambert-Beer law accounts for the absorption of electromagnetic monochromatic radiation (1064 nm in this case) in an irradiated medium along the z-direction; μ_α is the linear absorption coefficient [m^{-1}] and depends on laser wavelength and on tissue properties.

The phenomenon of scattering, occurring in biological soft tissues which are normally classified as turbid media, has been taken into account. In fact, by defining the coefficient

known as optical albedo $a = \frac{\mu_s}{\mu_\alpha + \mu_s}$, where μ_s is the scattering coefficient [m^{-1}], most biological tissues have a close to unity in the therapeutic window, ranging from 600 nm to 1200 nm thus, the scattering phenomenon is not negligible if compared to the linear absorption. Therefore, according to the Diffusion Approximation by Ishimaru [7], scattering and absorption phenomena are modeled by the effective attenuation coefficient μ_{eff} [m^{-1}]:

$$\mu_{eff} = \sqrt{3\mu_\alpha(\mu_\alpha + \mu_s(1-g))} \tag{2.7}$$

where g is the anisotropy coefficient. Thus, in present study, Equation 2.5 has been modified by replacing μ_α with $\mu_{eff.}$

- Q_e represents the power density due to water evaporation [8]:

$$Q_e = -\lambda \cdot \frac{d\rho_w}{dt} \tag{2.8}$$

where λ is the water's latent heat [$J \cdot kg^{-1}$] and ρ_w is water density [$kg \cdot m^{-3}$]. Parameter ρ_w is assumed to be temperature dependent only, and expressed as follows:

$$\rho_w(T) = \begin{cases} 0.778 \cdot \left(1 - e^{\frac{T-106}{3.42}}\right) & T \le 103\,°C \\ 0.0289 \cdot T^3 - 8.924 \cdot T^2 + 919.6 \cdot T - 31573 & 103\,°C < T < 104\,°C \\ 0.778 \cdot e^{\left(\frac{T-80}{34.37}\right)} & T \ge 104\,°C \end{cases} \tag{2.9}$$

At 100 °C water boils and induces lysis, causing necrosis and, obviously, the loss of cellular physiological activity [9]. Equation 2.8 is applied under the hypothesis that the whole water steam does not leave the system (closed system), that steam fills the tissue region at lower temperature and condenses uniformly.

Equation 2.3 has been solved using Finite Element Modeling, with the initial condition of $T(x,y,z,0)$=T_{0t}=37 °C and also considering T=37 °C at the boundary of the domain. The theoretical model has been implemented on Comsol Multiphysics® 3.5a. Pancreatic tissue has been designed as a 3D geometry, and the origin of the coordinate system has been placed at the center of the emitting fiber cross section (Fig. 2.3A). The module called "Heat Transfer Module" has been used for the implementation of the Application Mode "Bioheat Equation", with a transient analysis and Lagrange-Quadratic element type. The mesh is constituted by $33 \cdot 10^5$ tetrahedral elements, with a number of degrees of freedom of

$45 \cdot 10^5$. The size of mesh has been optimized for the solution: as a matter of fact, in proximity of the applicator tip, where a higher thermal gradient is expected (Fig. 2.3B), the maximum mesh size has been set to 0.00099 m, whereas, elsewhere it has been set to "coarse".

The Geometrical Multigrid was used, with the Linear System solver. Computational time is 43233 s. The workstation HP Z400 has been used for the implementation of simulations. It has an Intel(R) Xeon(R) W3565 processor (3.20 GHz) and 4 GB of RAM.

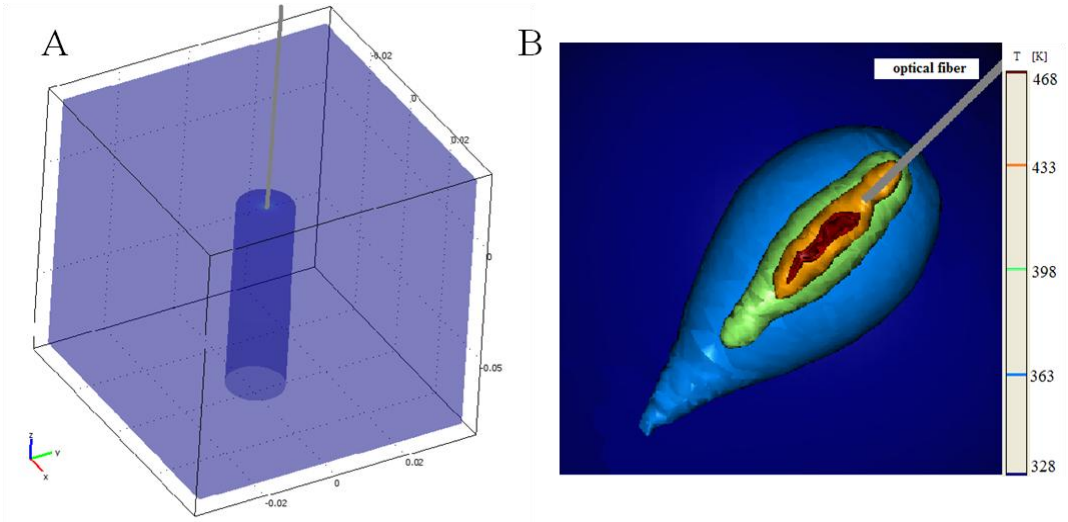

Figure 2.3: A) Design in Comsol Multiphysics® 3.5a; B) Simulated temperature distribution.

Constant values are: for pancreas, ρ=1040 kg·m^{-3}, c=3590 J·kg^{-1}·K^{-1}, k=0.5417 W·m^{-1}·K^{-1}, α=20-30 m^{-1}, α_{eff}=331 m^{-1}; for blood, ρ_b=1060 kg·m^{-3}, w_b=0.0253 s^{-1}, c_b=3640 J·kg^{-1}·K^{-1}, λ=2260000 J·kg^{-1}; Q_{met}=33800 W·m^{-3}; for the quartz fiber: ρ=2600 kg·m^{-3}, c=820 J·kg^{-1}·K^{-1}, k=3 W·m^{-1}·K^{-1}. For some constants, e.g., for c and for the optical properties, pancreas values have been replaced with liver ones [10], being this the first study about the thermal response of pancreas to laser Nd:YAG radiation. Optical property values for pancreas lack in published literature, and are currently under investigation in our research center [cfr Chapter 3].

2.2.1 Theoretical assessment of temperature distribution

In order to illustrate the temperature dynamic on laser irradiated pancreas, numerical simulations are performed to obtain the trend of T(t) at the applicator tip, and for six points at distances (y) ranging from 1 mm to 15 mm. Fig. 2.4A shows T dynamic during laser treatment at 1.5 W: the smaller is y, the more steeply T increases. The dynamic response of the system was described by means of the time constant of the heating phenomenon (τ).

The estimation of τ was performed by considering the temperature change magnitude defined as the difference between the tissue steady-state temperature ($T\infty$) and the initial temperature T_{0t} (37 °C). In particular, we considered τ as the time required to achieve 63.2% of the T increase ($T\infty$-T_{0t}). We obtained τ as follows:

$$T(\tau) = \left(1 - \frac{1}{e}\right) \cdot (T_\infty - T_{0t}) \cong 0.632 \cdot (T_\infty - T_{0t}) \qquad (2.10)$$

As shown in Figure 2.4B, τ increases with an approximately linear trend (e.g., at y=1 mm, τ =42 s, at y=10 mm, τ=750 s).

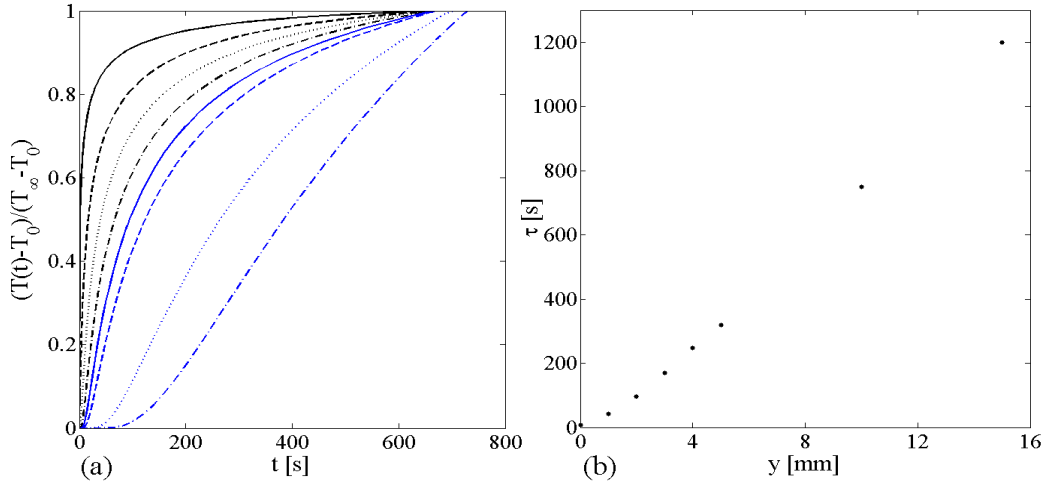

Figure 2.4: A) T dynamic of pancreas undergoing LA at 1.5 W, at applicator tip (black continuous line) and at different distances from it: 1 mm (dashed black line), 2 mm (dotted black line), 3 mm (dash-dotted black line), 4 mm (blue continuous line), 5 mm (blue dashed line), 10 mm (blue dotted line), 15 mm (blue dash-dotted line). ΔT has been normalized respect to the steady value, T_∞; B) τ of the phenomenon as a function of the distance from the applicator.

During treatment, T increases from T_{0t} up to a maximum value (T_{max}) reached in correspondence of the laser applicator (z=0) at the end of the procedure; when stopping laser treatment, the phenomenon of heat conduction entails the steep drop in T_{max}. The analysis has been performed simulating *ex vivo* tissue, i.e., Q_b=0 and Q_m=0 in Equation 2.3.

The cooling phenomenon occurring in pancreas has also been theoretically assessed by simulating Equation 2.3 with P=1.5 W. Figure 2.5 shows the ratio between temperature increase (ΔT) and its maximum increase (ΔT_{max}) as a function of z and t. At applicator tip, ΔT drops of about 45 % after 1 s since the laser treatment ends (dashed line), and of about 65 % after 4 s (dotted line). After 34 s LA effect on T is mostly negligible (gray continuous line), as shown in Fig. 2.5A. The dynamic of cooling phenomenon changes with z: the longer is z the slower is the decrease of T after the end of the procedure. This effect is due

to the heat flowing from the region close to the applicator to the peripheral region. For example at z=5 mm (Fig. 2.5B) ΔT drop is 19 % after 1 s, and 37 % after 4 s.

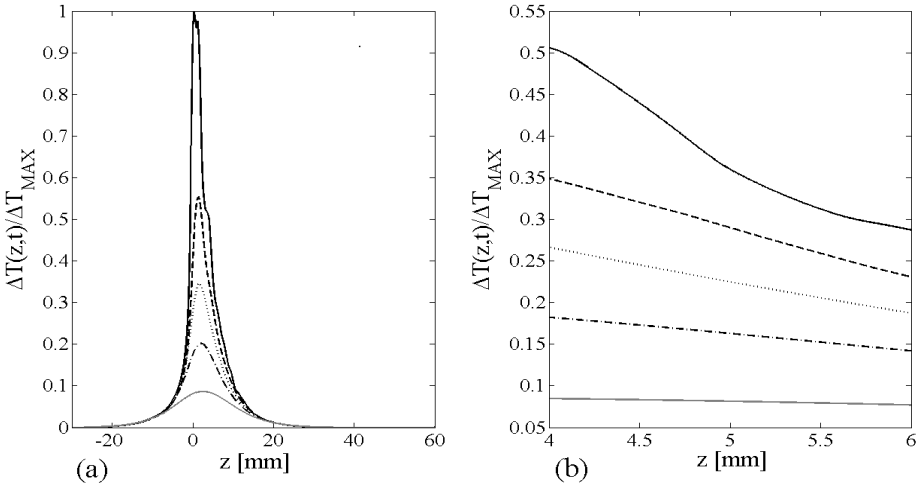

Figure 2.5: A) Ratio between ΔT and ΔT_{max} as a function of z by simulating *ex vivo* pancreas undergoing LA with P=1.5 W: at the end of laser irradiation (black continuous line) and after it (1 s, dashed line, 4 s, dotted line, 14 s, dash dotted line, 34 s gray line); B) zoom of simulation around z=5 mm.

2.2.2 Theoretical assessment of coagulation and vaporization volumes

The previously described analytical model allows to evaluate temperature distribution as a function of time and to calculate volume of coagulation (V_c) and volume of vaporized tissue (V_v) values. Equation 2.3 has been modified by posing Q_b=0 (being w_b=0) and Q_m=0 for *ex vivo* tissue.

From the centre of the emitting fibre cross section, three different regions are observable by analyzing a specimen of pancreatic tissue after LA: the vaporized region indicated as V, the coagulated region C, and the unaffected region H (Fig. 2.6A).

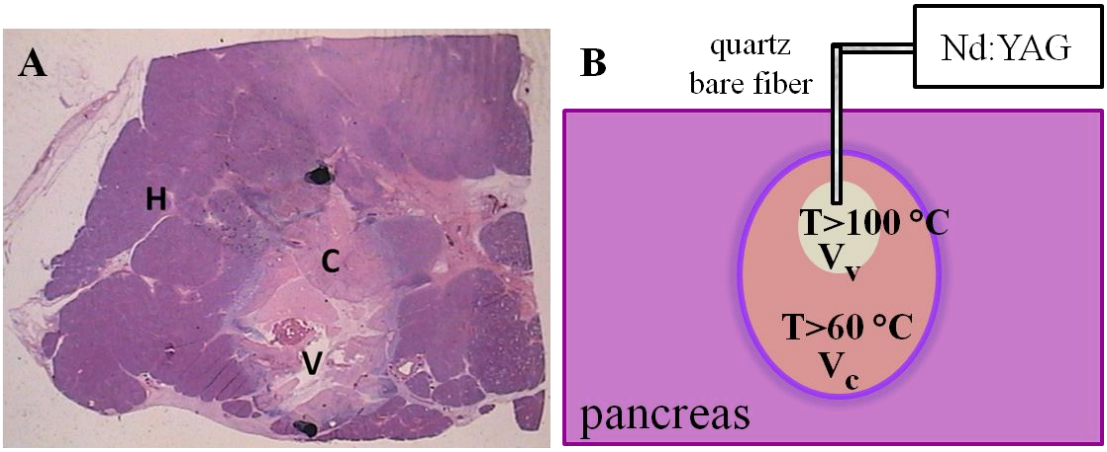

Figure 2.6: A) Specimen of pancreatic tissue undergone LA: C, V and H indicate the three regions observed in samples after treatment; B) Schematic of vaporized volume (V_v) and coagulation volume (V_c) and respective temperature.

The V region is the closest to the application point and tissue is vaporized: as also reported by McKenzie [9], for T>100 °C the cells water vaporization entails explosive expansion causing tissue removal. The tissue volume subjected to this phenomenon has been measured for each laser setting, and indicated with V_v (Fig. 2.6B).

The C region surrounds the V region; it shows a different colour respect to region H, and it has a sharp-cutting outline separating it from H. The volume where the condition 60 °C<T<100 °C [9] has been reached is indicated as V_c (Fig. 2.6B).

The H region is not damaged, so it is indicated as unaffected tissue.

Numerical simulations also allow to analyzing how V_v and V_c increase as a function of time. Fig. 2.7A shows the increase of V_c and Fig. 2.7B the increase of V_v as function of time. Energy (E) has been maintained at 1000 J during each LA treatment, whereas treatment time t_l value changes depending on P value, accordingly to the expression $E=P \cdot t_l$.

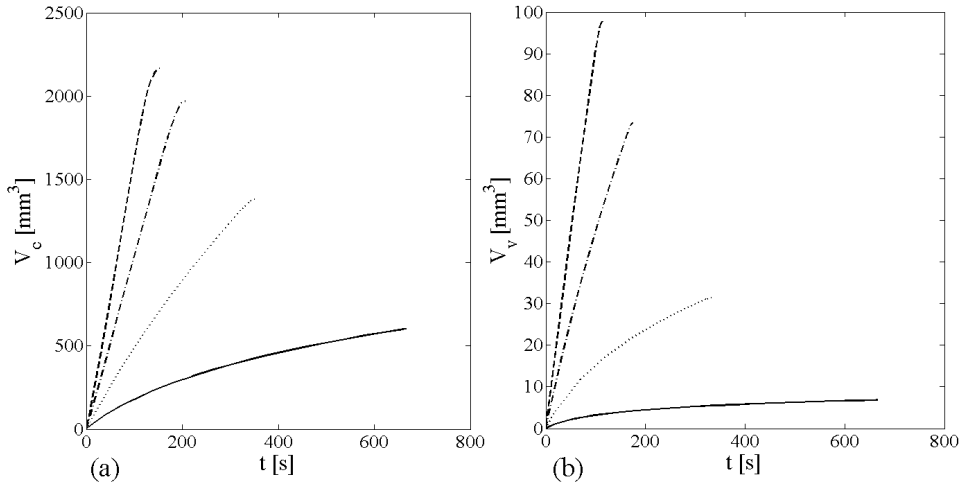

Figure 2.7: A) Trend of V_c and B) trend of V_v values during laser treatment, with different P: dashed line (P=10 W), dash-dotted line (P=6 W), dotted line (P=3 W), continuous line (P=1.5 W).

2.2.3 Theoretical assessment of principal factors influencing laser interstitial thermotherapy outcomes on pancreas

This theoretical study [11] investigates the thermal effects of LA on *in vivo* pancreas considering some relevant parameters: both P and E are changed in a range commonly utilized in LA; the influence of applicator size (radius, r_f) is also analyzed; this study

purposes also to investigate the effects of optical properties (μ_a, μ_s, g) on pancreas thermal distribution, in order to quantitatively evaluate tissue injury.

Thermal response of *in vivo* laser irradiated pancreas has been analyzed with a twofold approach: 1) evaluation of T rise in a point close to the laser applicator tip (e.g., distance of 3 mm) during treatment; 2) calculation of V_c and V_v using the abovementioned approach [cfr 2.2.2]. The *in vivo* case has been simulated by considering all the terms in Equation 2.3, with particular regard to Q_b -Equation 2.4- and Q_m.

Simulations have been performed at different P, E, r_f, and μ_{eff}, as reported in Table I.

Table I. Laser settings, applicator radius and effective attenuation coefficient values in simulations.

P [W]	**E [J]**	**r_f [µm]**	**μ_{eff} [m^{-1}]**
1.5	500	150	311
3	1000	300	331
6	1500	600	623

A. LA effects: P influence

Theoretical simulations have been conducted at different P values (Table I), and the effects on LA outcomes have been evaluated in terms of T, V_c, and V_v (Fig. 2.8).

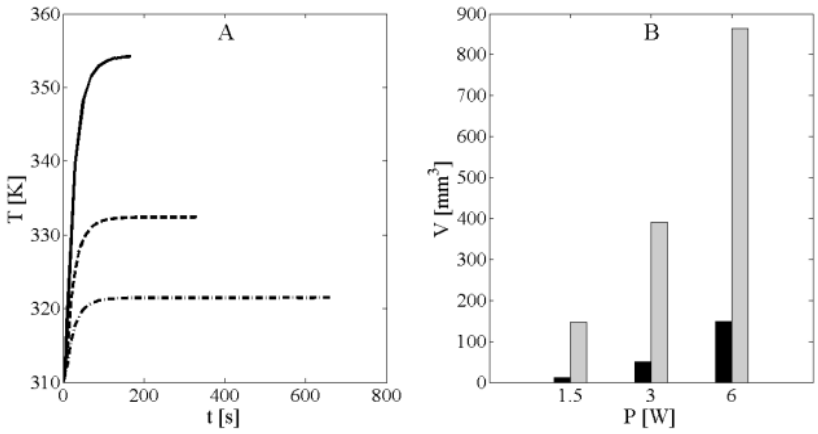

Figure 2.8: A) T rise, at 3 mm from fiber tip, vs t in pancreas during LA at 1.5 W (dash-dotted line), 3 W (dashed line) and 6 W (continuous line); B) V_v (black bar) and V_c (grey bar) at P from 1.5 W to 6 W.

As expected, the higher the P, the higher T rise in pancreatic tissue close to applicator (3 mm). For example, when E=1000 J, T reaches about 355 K at P=6 W, vs 321 K at 1.5 W (Fig 2.8A). Similar results are obtained for V_c and V_v (Fig 2.8B). In fact, the higher P, the higher V_v and V_c: increasing P from 1.5 W to 3 W, both V_v and V_c increase of about 2.8 times; from 3 W to 6 W, V_v triples (50 mm^3 vs 150 mm^3); on the other hand, V_c increases slightly more than double (391 mm^3 vs 867 mm^3). This trend quite agrees with *in vivo* trials on healthy pigs reported in a previous study by Di Matteo *et al.* [12]: at both E values (500 J and 1000 J), and r_f=150 µm, they found a V_c increase with P. When E=1000 J, they report V_c=483 mm^3 at 3 W vs V_c=460 mm^3 at 2 W. Definitively, P strongly influences T distribution and injured volumes on pancreas undergoing LA, and therefore should be carefully chosen by clinicians.

B. LA effects: E influence

Numerical simulations have been performed at different E values (Table I), and effects have been assessed (Fig. 2.9).

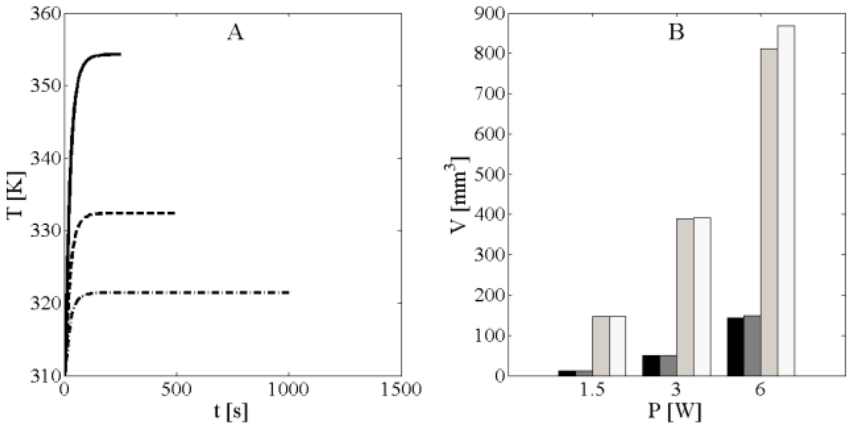

Figure 2.9: A) T rise, at 3 mm from fiber tip, vs t in pancreas during LA at 1.5 W (dash-dotted line), 3 W (dashed line) and 6 W (continuous line) when E=1500 J; B) V_v at 500 J (black bar) and 1500 J (dark grey bar), and V_c at 500 J (grey bar) and 1500 J (white bar), at P from 1.5 W to 6 W.

Fig. 2.9A shows that T_{max} is not influenced by E: T values at 1500 J (for three P values analyzed) are not subjected to variations respect to the treatment with 500 J (covered by black lines in the same picture), also V_v changes can be neglected. On the other hand, V_c is influenced by E: Fig. 2.9B shows that at 6 W, V_c increases from 799 mm^3 at 500 J to 884 mm^3 at 1500 J.

C. LA effects: r_f influence

Numerical simulations have been performed for different r_f values (Table I), and effects have been evaluated (Fig. 2.10).

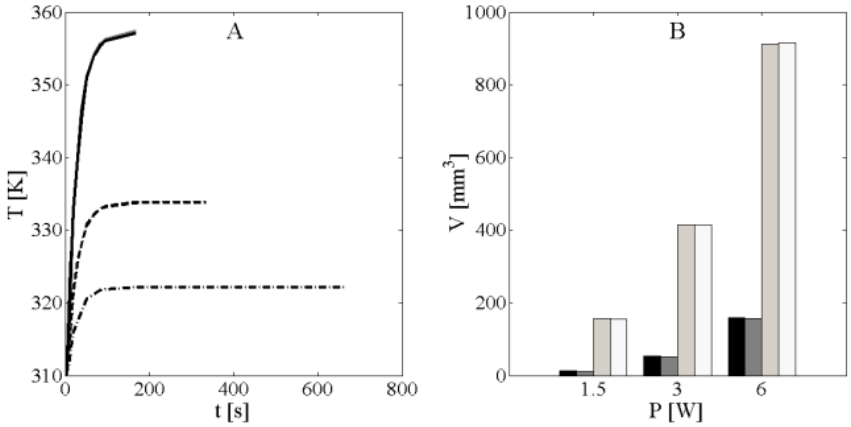

Figure 2.10: A) T rise, at 3 mm from fiber tip, vs t in pancreas undergoing LA at 1.5 W (dash-dotted line), 3 W (dashed line) and 6 W (continuous line); B) V_v at 300 µm (black bar) and 600 µm (dark grey bar), and V_c at 300 µm (grey bar) and 600 µm (white bar), at P from 1.5 W to 6 W.

The effects of r_f variation are not significant on T rise, as observable in Fig. 2.10A, where the T rise curve for r_f=300 µm and the same curve obtained with 600 µm are overlapped. In Fig. 2.10B it is shown a slight influence of r_f on V_v and V_c, decreasing with P: for example, at 3 W, increasing r_f from 300 µm to 600 µm, V_v decreases from about 51 mm^3 to about 30 mm^3 (decrement of 40%), and V_c drops from 425 mm^3 to 391 mm^3 (decrement of about 8%); on the other hand, at 6 W, V_v decreases from 159 mm^3 to 131 mm^3 (decrement of 19%), and V_c changes from 918 mm^3 to 884 mm^3 (decrement of about 4%).

D. LA effects: μ_{eff} influence

Optical information about pancreas lack and are still under investigation in our laboratory, but literature reports data about optical properties of biological tissues commonly undergoing LA for cancer removal, i.e., liver and prostate. Although evaluated at wavelength relevant for LA, optical properties are not known with great accuracy. For example, many Authors provide several values for liver properties (μ_a, μ_s, g and, consequently, μ_{eff}), that differentiate strongly each another, as observable in Table II:

Table II. Human Liver Optical Properties at 1064 nm.

μ_a [m^{-1}]	μ_s [m^{-1}]	g	μ_{eff} [m^{-1}]	reference
70	35600	0.95	623	[10]
30	15000	0.93	311	[13]
24	30000	0.95	331	[6]

In my study, values in Table II have been substituted in Equations 2.5 and 2.7. Simulations have been performed at μ_{eff} equal to 311 m^{-1} and 623 m^{-1} (Fig. 2.11).

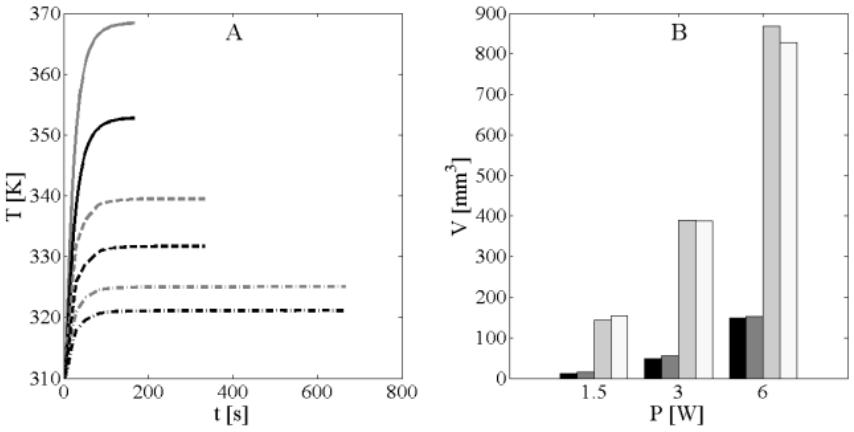

Figure 2.11: A) T rise, at 3 mm from fiber tip, vs t in pancreas undergoing LA at 1.5 W (dash-dotted line), 3 W (dashed line) and 6 W (continuous line); B) V_v at 311 m^{-1} (black bar) and 623 m^{-1} (dark grey bar), and V_c at 311 m^{-1} (grey bar) and 623 m^{-1} (white bar), at P from 1.5 W to 6 W.

Numerical calculations show that T_{max} increases with μ_{eff} (Fig. 2.11A): at 1.5 W, T_{max} raises from 320 K to 324 K (increment of about 1 %), at 3 W, from 330 K to 340 K (increment of 3 %), and at 6 W it increases from 351 K to 368 K, with an increment of 5 %. Therefore, the change in optical properties modifies the punctual T value reached at a fixed point from the quartz fiber tip (i.e., 3 mm), despite the influence on injured volumes. In fact, V_c and V_v are not subjected to a significant variation respect to T_{max}. Fig. 2.11B presents the increment of V_v reducing with P when μ_{eff} is 623 m^{-1}: for example, at 1.5 W, V_v values 9 mm^3 if μ_{eff}=311 m^{-1} and it doubles at 18 mm^3 if μ_{eff}=623 m^{-1}; *vice versa*, at 6 W V_v is about 150 mm^3 for both μ_{eff} values. V_c shows the same trend: at 1.5 W, V_c at 311

m^{-1} is less than V_c at 623 m^{-1} (136 mm^3 vs 153 mm^3), but at 6 W this trend changes, resulting 867 mm^3 at 311 m^{-1} vs 833 mm^3 at 623 m^{-1}.

In conclusion, as expected, P is the most influencing parameter on T rise, T_{max}, V_v and V_c. On the other hand, μ_{eff} mainly influences T rise and T_{max}; variations are also appreciable in V_c and V_v values, particularly at 1.5 W and 6 W. Lastly, simulations show negligible effects of E and r_f. As far as it concerns E, the no appreciable effects on V_c and V_v could be due to the simple approach in their estimation [9]. Further investigations could be carried out to analyze effects of time-temperature history on pancreatic tissue.

2.2.4 Theoretical modeling of laser applicators for LA

As previously reported, geometry of laser applicator strongly influences the shape and dimensions of the tissue lesion.

First applications of LA employed the applicator called "bare-fiber", i.e., an optical waveguide with an emitting distal end [14]. Its advantages are small diameter (e.g., 300 µm) and affordability, therefore it was extensively used in this field. Biological tissues strongly absorb Nd:YAG laser light, therefore the lesion dimension is quite limited and could be not sufficient for a quick treatment. Besides the employment of multiple applicators [15, 16], a wide and homogeneous initial distribution of the laser light can be achieved by diffusing applicators. Thanks to an appropriate manufacture of their emitting surface, diffusing applicators reduce the power density and the temperature on their surface, and model and control the shape of the tissue volume to be treated. In all ablation procedures (e.g., radiofrequency, microwave) efforts are made to design a robust device that can destroy more accurately as possible the whole neoplastic mass, without significant side effects and with predictable outcomes [17].

This study [18] aims to theoretically investigate the effects of geometry in different typologies of fiber optic applicators on *in vivo* liver tissue, considering both *T* and dimensions of coagulation volume at the end of the procedure. Simulations are performed at two *P* (i.e., 3 W and 5 W) and E=1650 J, according to typical settings of clinical LA procedures [19, 6].

2.2.4.1 Photon Propagation Modeling

Monte Carlo simulation has been employed for modeling the phenomenon of photons emission from the applicator surface and, consequently, propagation through a biological medium.

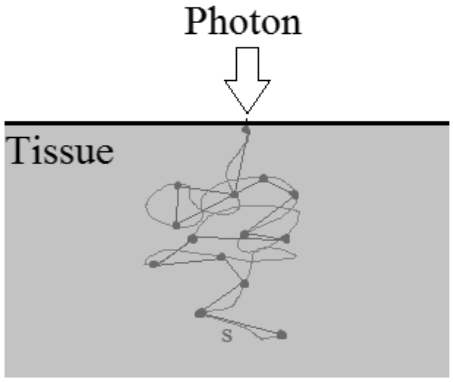

Figure 2.12: Photon trajectory within tissue, and step *s*.

Initially, a weight (*w*) equal to 1 is assigned to each photon. N photons are set into the tissue at a certain location, depending on the geometry and shape of the applicator, defined by *x*, *y*, *z* coordinates. Their trajectory is specified by the directional cosines (u_x, u_y, u_z), corresponding to the trajectories projection onto the corresponding axes. The random distance, traveled before the photon interacts with the tissue, depends on a random number ranging from 0 and 1, and on the total attenuation coefficient $\mu_t=\mu_a+\mu_s$, where μ_a and μ_s are the absorption and scattering coefficient of the tissue, respectively. After each photon step, *w* is reduced by absorption, and the remaining non-absorbed *w* is redirected according to a phase function, that describes the angular dependence of a single scattering. Once a new trajectory is defined, the photon is again moved on through the tissue. During the propagation, *w* drops until it reaches a threshold value, typically chosen as 10^{-4} [20, 21].

The tissue is modeled as a 3D grid of bins, each indexed with *ix*, *iy*, *iz*, according to the three spatial coordinates. The volume of each bin is V [cm^3]. The length of photon step, s [cm] (Fig. 2.12), is exponentially distributed, as expressed by the probability, *p(s)*, in Equation 2.11

$$p(s)=\frac{\exp(-\mu_t\cdot s)}{\mu_t} \tag{2.11}$$

By the integration of *p(s)*, evaluated at a particular s_1, the probability distribution function $F(s_1)$ is defined from (11):

$$F(s_1)=\int_0^{s_1} p(s)ds=1-\exp(-\mu_t\cdot s_1) \tag{2.12}$$

A random number rnd_1 is posed equal to $F(s_1)$, according to:

$$rnd_1=F(s_1)=1-\exp(-\mu_t\cdot s_1) \tag{2.13}$$

From Equation 2.13 we obtain:

$$s_1 = \frac{-\ln(rnd_1)}{\mu_t} \tag{2.14}$$

The position and trajectory of each photon at *i*-step of simulation is defined as follows:

$$\begin{cases} x_{i+1} = x_i + s \cdot u_{xi} \\ y_{i+1} = y_i + s \cdot u_{y_i} \\ z_{i+1} = z_i + s \cdot u_{z_i} \end{cases} \tag{2.15}$$

At each step, the photon is scattered into a new trajectory according to two scattering functions, used to establish the angles of scattering θ (defined by the Henyey-Greenstein phase function [20]) and φ, respectively the deflection and azimuthal scattering angles:

$$\begin{cases} \theta = \arccos\left\{ \frac{1}{2g} \cdot \left[1 + g^2 - \left(\frac{1-g^2}{1-g+2g \cdot rnd} \right)^2 \right] \right\} \\ \varphi = 2\pi \cdot rnd \end{cases} \tag{2.16}$$

At each step, the photon interacts with the tissue: a fraction $w \cdot (\mu_a/\mu_t)$ is absorbed by the tissue, whereas the remaining one, $w \cdot (\mu_s/\mu_t)$, keeps on propagating. The absorption process is described as follows:

$$A_{i+1} = A_i + w_i \cdot \frac{\mu_a}{\mu_t} \tag{2.17}$$

where A is the matrix that stores the absorption contribution of each photon, at each step. It is possible to define the fluence rate ψ, [$W \cdot cm^{-2}$] :

$$\Psi = P \cdot M \tag{2.18}$$

where *P* is the power emitted by the laser source, and

$$M = \frac{A}{V \cdot N \cdot \mu_a} \tag{2.19}$$

In the implementation of this model, the following variable values have been selected: $N=10^5$, μ_a= 0.24 cm^{-1}; μ_s=300 cm^{-1}, g =0.95 (liver tissue).

Finally, in the Bioheat Equation 2.3, the term related to the laser source, Q_l, is changed in:

$$Q_l = \mu_a \cdot \Psi$$

(2.20)

Two simulation environments were utilized: the Monte Carlo model for photon propagation through tissue was implemented in Matlab 2010a, whereas the thermal model based on Bioheat Equation was simulated in Comsol Multiphysics 3.5a.

Figure 2.13 reports the flowchart of simulation including the main blocks (i.e., Monte Carlo modeling and Bioheat Equation), and the respective input variables (i.e., applicator characteristics, optical and physical properties of tissue) and outputs (fluence rate and tissue temperature distribution).

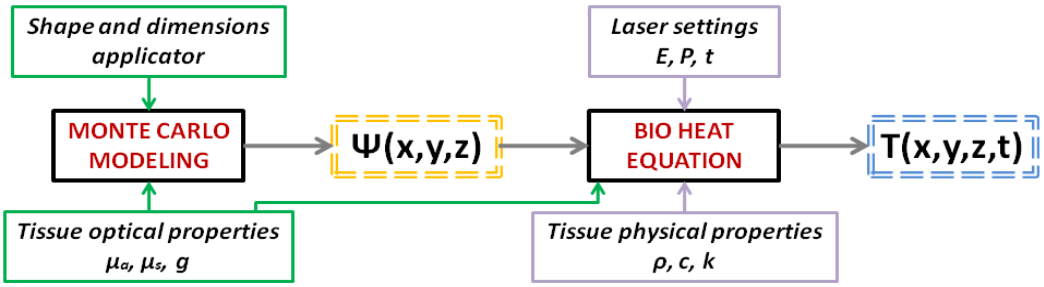

Figure 2.13: Flowchart of simulation

2.2.4.2 Fluence Rate Distribution

The initial position and direction of photons is specified for each typology of applicator (Table III):

Table III. Initial positions and directions of photons.

	Bare fiber	Cylindrical applicator	Zebra applicator	Hybrid applicator
	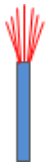	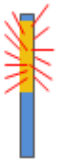	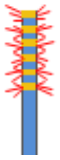	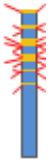
x_{in}	$\sigma\sqrt{-\ln(rand)}$	$r_a \cdot cos(t)$	$r_a \cdot cos(t)$	$r_a \cdot cos(t)$
y_{in}	$\sigma\sqrt{-\ln(rand)}$	$r_a \cdot sin(t)$	$r_a \cdot sin(t)$	$r_a \cdot sin(t)$
z_{in}	1	2+rand	$z=1+3 \cdot rand$ 10 emitting regions, each of length 1.5 mm, and equidistant (1.5 mm)	$z=1+3 \cdot rand$ 6 emitting regions with growing surface when directed to the applicator centre, and equidistant (1.5 mm)
ux_{in}	0	$cos(t) \cdot cos(\varphi)$	$cos(t) \cdot cos(\varphi)$	$cos(t) \cdot cos(\varphi)$
uy_{in}	0	$cos(t) \cdot sin(\varphi)$	$cos(t) \cdot sin(\varphi)$	$cos(t) \cdot sin(\varphi)$

	Bare fiber	Cylindrical applicator	Zebra applicator	Hybrid applicator
uz_{in}	*1*	*cos(t)*	*cos(t)*	*cos(t)*
-r_a: applicator radius [cm] -t=arcos(rand), where rand is a randomic value obtained from the standard uniform distribution on the open interval (0,1)				

The random number is used in the definition of initial position when photons are launched from a surface (Table III). In zebra and hybrid applicators, emitting regions are spaced out with non-emitting ones, in order to decrement ψ. Initial position of photons in bare fiber simulation is achieved considering that the laser beam guided by a bare fiber can be described with a Gaussian distribution; hence the probability density function of the radial position of launch is:

$$p(r) = \frac{\exp\left(-r^2/\sigma^2\right)\cdot 2\pi r}{\pi\sigma^2} \tag{2.21}$$

and the respective probability distribution function is:

$$F(r_1) = \int_0^{r_1} p(r)dr = \exp(-r_1^2/\sigma^2) \tag{2.22}$$

According to the Monte Carlo method described in Equations 2.11-2.14, is obtained:

$$r_1 = \sigma\sqrt{-\ln(rand)} \tag{2.23}$$

Figure 2.14 shows the distribution of ψ inside the tissue. Thanks to the cylindrical symmetry of the geometry, ψ is plotted in the *r*, *z* plane.

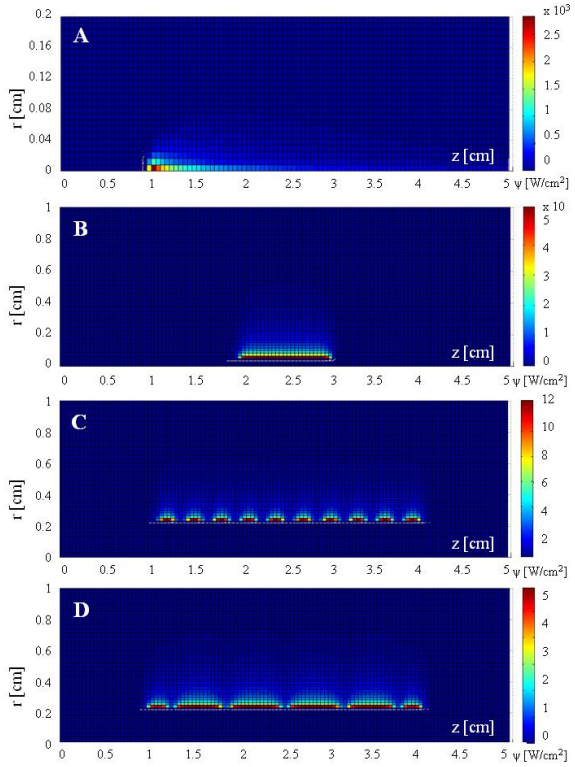

Figure 2.14: Fluence rate, ψ for A) bare fiber, B) cylindrical 1 cm-long, C) zebra and D) hybrid applicator.

As expected, ψ distribution varies with the geometry of the applicator: in particular, the highest ψ is obtained with a bare fiber (fig. 2.14A), with a maximum value of $3 \cdot 10^3$ W·cm^{-2}, it decreases in cylindrical and zebra applicator (50 W·cm^{-2} and 12 W·cm^{-2}, respectively), and in hybrid applicator (about 5 W·cm^{-2}). This behaviour is mainly due to the size of the emitting surface: in fact, the bare fiber emits N photons from its tip (diameter of 300 µm and surface of $7 \cdot 10^{-4}$ cm^2), where they are extremely concentrate, whereas in other applicators the emission surface increases, and, consequently, ψ decreases.

2.2.4.3 Thermal Distribution

Temperature distribution inside the tissue is obtained by solving Bioheat Equation 2.3. *E* was set at 1650 J and *P* was set at 3 W and 5 W. Results for *P*=3 W are shown in Fig. 2.15.

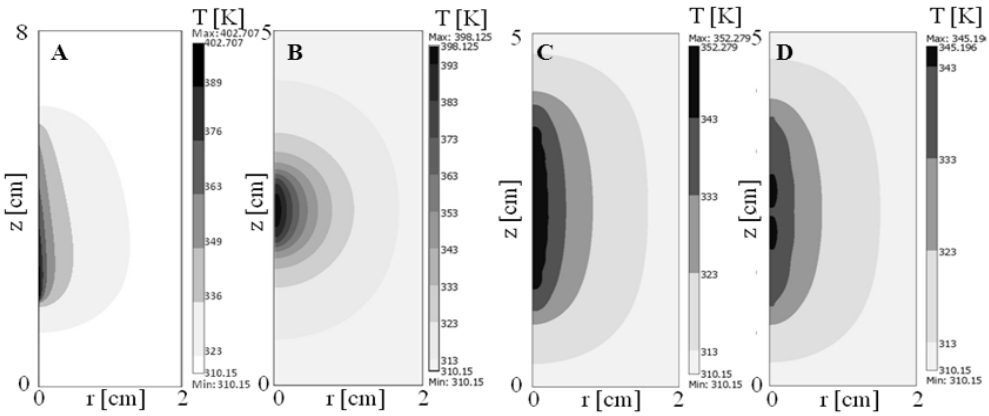

Figure 2.15: Temperature distribution at the end of LA (*P*=3 W) produced by A) bare fiber, B) cylindrical 1 cm-long, C) zebra and D) hybrid applicator.

Maximum *T* (*Tmax*) decreases from about 400 K for bare fiber and cylindrical applicator, to about 350 K for zebra and hybrid applicators. Besides the temperature distribution, the comparison of thermal effects of different applicators can be obtained by considering the isothermal surface at 333 K (60 °C), as described in previous sessions for prediction of coagulated and ablated volumes. Figure 2.16 shows the thermal damage ($T \geq 60$ °C) for the applicators, at 3 W and 5 W. The effects of cylindrical applicator were simulated for length of diffusing surface of: 1 cm (fig. 2.16D), 1.5 cm (fig. 2.16E) and 3 cm (fig. 2.16F).

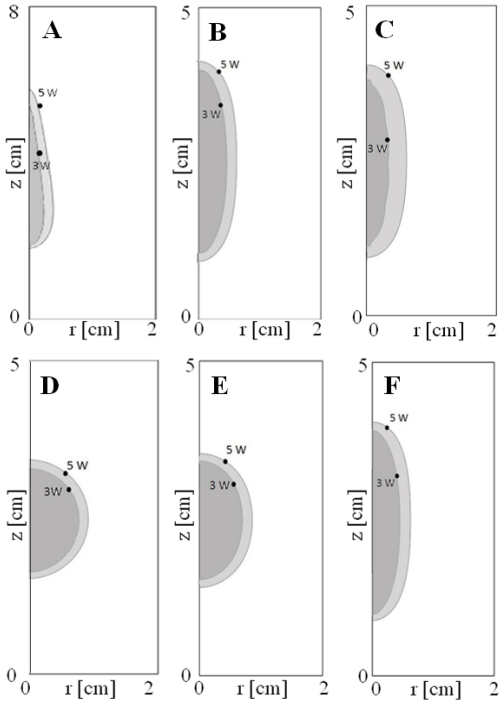

Figure 2.16: Temperature distribution at the end of LA (*P*=3 W and *P*=5 W) produced by A) bare fiber, B) zebra applicator, C) hybrid applicator, and cylindrical applicator D)1 cm, E) 1.5 cm and F) 3 cm-long.

Bare fiber causes an irregular coagulation shape (fig. 2.16A); zebra applicator 3 cm-long (fig. 2.16B), hybrid (fig. 2.16C) and cylindrical ones (fig. 2.16F) produce a similar damage region, for both volume (at 5 W it ranges between 4 cm^3 and 5 cm^3) and shape (ellipsoid), although the *Tmax* reached on the applicator surface is slightly different (fig. 2.15C and 2.15D). Cylindrical applicators with diffusing length of 1 cm (fig. 2.16D) and 1.5 cm (fig. 2.16E) obtain almost spherical volumes of damage, of about 3.5 cm^3 and 6 cm^3 at 5 W, respectively. Also, Ahrar *et al.* [22] employed a water-cooled applicator with diffusing surface of 1 cm, that although different laser settings and the drawback of the composed system, achieved similar results, in term of spherical shape of thermal damage. Benefit of a spherical lesion is the temperature distribution inside the tissue, that allows to easily perform a controlled and predictable amount of tissue removal. Furthermore, applicators with spaced out emitting regions entail low *T* on their surface, and preserve their integrity.

Bibliography Chapter 2

[1] M. Niemz, Laser tissue interaction. Foundamental and applications, Srpinger, 2005.

[2] J. Hayes and M. Wolbarsht, "Thermal model for retinal damage induced by pulsed lasers," *Aerospace Med.*, vol. 39, p. 474–480, 1968.

[3] Welch and van Gemert, "Laser generated Heat Transfer," in *Optical-Thermal Response of Laser-Irradiated Tissue*, Springer, II Ed., 2011.

[4] H. Pennes, "Analysis of tissue and arterial blood temperature in the resting human forearm," *J Appl Physiol*, vol. 1, pp. 93-122, Aug. 1948.

[5] P. Saccomandi, E. Schena, F. Di Matteo, M. Pandolfi, M. Martino, R. Rea and S. Silvestri, "Laser interstitial thermotherapy for pancreatic tumor," in *Proc. 33rd Annu. Int. Conf. IEEE Eng. Med. Biol. Soc. pp. 5585-8*, Boston, MA, Aug./Sep., 2011.

[6] P. Saccomandi, E. Schena, M. Caponero, F. Di Matteo, M. Martino, M. Pandolfi and S. Silvestri, "Theoretical Analysis and Experimental Evaluation of Laser Induced Thermotherapy in Ex Vivo Porcine Pancreas," *IEEE Trans Biomed Eng*, vol. 59, no. 10, pp. 2958-64, Oct. 2012.

[7] A. Ishimaru, "Diffusion of light in turbid material," *Appl Opt*, vol. 28, no. 12, pp. 2210-2215, Jun. 1989.

[8] D. Yang, M. Convesre, D. Mahvi and L. Webster, "Expanding the Bioheat Equation to include tissue internal water evaporation during heating," *IEEE Trans Bio-Med Eng*, vol. 54, no. 8, pp. 1382-1388, Aug. 2007.

[9] A. McKenzie, "Physics of thermal processes in laser-tissue interaction," *Phys Med Biol*, vol. 35, no. 9, pp. 1175-1209, Sep. 1990.

[10] G. Müller and A. Roggan, "Optical and thermal properties of biological tissue," in *Laser-Induced Interstitial Thermotherapy*, SPIE Press, 1995, pp. 9-82.

[11] P. Saccomandi, E. Schena, F.M. Di Matteo, M. Pandolfi, M. Martino, R. Rea, F. Panzera and F. Silvestri, "Theoretical assessment of principal factors influencing laser interstitial thermotherapy outcomes on pancreas," in *Proc. 34th Annu. International Conf. IEEE Eng. Med. Biol. Soc.*, San Diego, pp. 5687-5690, 2012.

[12] F. Di Matteo *et al*, "EUS-guided Nd:YAG laser ablation of normal pancreatic tissue: a pilot study in a pig model," *Gastrointest Endosc*, vol. 72, pp. 358-363, Aug. 2010.

[13] W. Gottschalk, «Ein Meβverfahren zur Bestimmung der optischen Parameter biologischer

Gewebe in vitro,» Dissertation 93 HA 8984, Universität Fridericiana Karlsruhe, 1992.

[14] C. Philipp, E. Rhode and H. Berlien , "Nd:YAG laser procedures in tumor treatment," *Semin Surg Oncol*, vol. 11, no. 4, pp. 290-298, Jul. 1995.

[15] L. Veenendaal, A. de Jager, G. Stapper, H. Borel Rinkes and R. van Hillegersberg, "Multiple fiber laser-induced thermotherapy for ablation of large intrahepatic tumors," *Photomed Laser Surg*, vol. 24, pp. 3-9, 2006.

[16] P. Saccomandi, E. Schena, F. Giurazza, R. Del vescovo, M. Caponero, L. Mortato, F. Panzera, R. Cazzato, F. Grasso, F. Di Matteo, S. Silvestri and B. Beomonte Zobel, "Temperature monitoring and lesion volume estimation during double-applicator laser-induced thermotherapy in ex vivo swine pancreas: a preliminary study.," *Lasers Med Sci.*, 2013.

[17] A. O'Rourke, D. Haemmerich, P. Prakash, M. Converse, D. Mahvi and J. Webster, "Current status of liver tumor ablation devices," *Expert Rev Med Devic*, vol. 4, no. 4, pp. 523-537, 2007.

[18] P. Saccomandi, E. Schena and S. Silvestri, "Design of fiber optic applicators for laser interstitial thermotherapy: theoretical evaluation of thermal outcomes," in 35th Edition *Proc.Conf. Eng. Biol. Med. Soc. EMBC*, Osaka, Japan, Jul. 2013, pp. 3733-6.

[19] G. Müller and A. Roggan, Laser-induced interstitial thermotherapy, SPIE Press, 1995.

[20] Welch and van Gemert, "Monte Carlo Modeling of Light Transport in Tissue (Steady State and Time of Flight)," in *Optical-Thermal Response of Laser-Irradiated Tissue*, Springer, II Ed., 2011.

[21] L. Wang and H. Wu, "Monte Carlo Modeling of Photon Transport in Biological Tissue," in *Biomedical Optics: Principles and Imaging*, John Wiley & Sons, 2007.

[22] K. Ahrar *et al*, "Preclinical assessment of a 980-nm diode laser ablation system in a large animal tumor model," *J Vasc Interv Radiol*, vol. 21, no. 4, pp. 555-561, 2010.

Chapter 3. Optical properties of biological tissues

3.1 Introduction

Laser light might have therapeutic effects on biological tissue, due to the conversion of light energy into heat. The energy of photons interacting with tissue depends on the wavelength (cfr. Plank Equation), and the conversion into heat is related to the *capability* of the tissue to absorb light. Thus, the interaction between tissue and laser is mostly described by three parameters (known as **tissue optical properties**): absorption, scattering and anisotropy. As briefly described in Chapter 1, tissue optical properties depend on the light wavelength, and on the composition of tissue, such as the presence of pigment, melanin, hemoglobin.

3.2 Light and matter

When a laser beam hits a slice of tissue, it is subjected to four phenomena: the reflection, the transmission, the absorption and the scattering (Fig. 3.1):

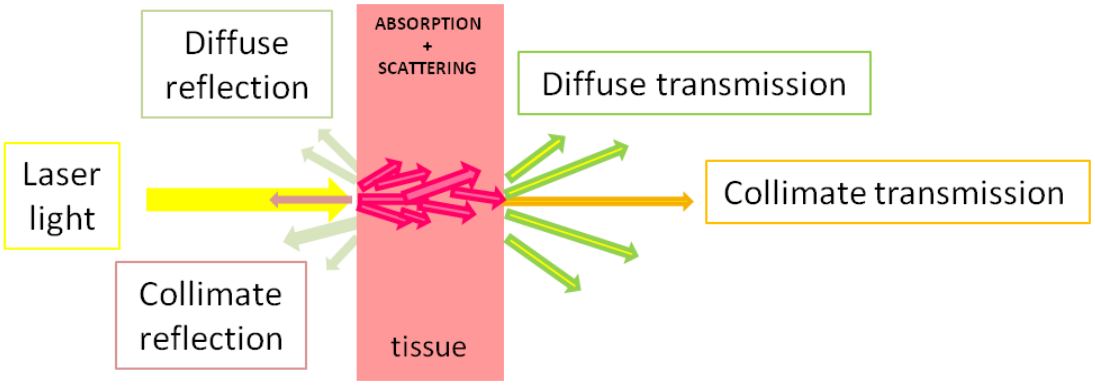

Figure 3.1 Laser light interacting with tissue subjected to phenomena of reflection, transmission, absorption and scattering.

Both reflected and transmitted light do not play role in the process of laser energy absorption and in the consequent conversion into heat, but are crucial in the assessment of optical response of a biological tissue, since they are the only quantities that can be directly measured.

Absorption: the electromagnetic radiation of incident light is attenuating by travelling through the medium. Biological tissues are defined as selective absorbent media, since their absorption properties depend on the light wavelength, λ (cfr. Chapter 1).

Scattering: when traveling through a biological tissue, the photons direction of propagation changes, because of the presence of particles with different dimensions. If the wavelength of light does not change, the scattering is called 'elastic scattering', otherwise it is called 'inelastic scattering' (i.e., Raman scattering), although the last one is usually negligible. Charged particles in a condensed material like tissue can be represented with a small element, having mass, bounded to the material by spring, which models the elastic bound. Therefore the movement of the charged particle is governed by the equation of motion of a mass-spring system (second-order system), with a proper natural frequency [1]. If the frequency of incident electromagnetic wave equals the natural frequency of system, the energy is absorbed (resonant case), whereas, in the other cases, scattering occurs. The oscillations, which take place when the frequency of the incident wave differs from the natural frequency, are caused by forced vibration. This vibration has the same direction and frequency of the incident electromagnetic wave, but a reduced amplitude, with respect to the resonant case. Furthermore, the phase of forced vibration differs from the phase of incident light, entailing a slowing down of photons during propagation through the medium. Dimension of particles is responsible of the type of elastic scattering: when the particle size is smaller than the wavelength of incident photons, Rayleigh scattering occurs; when the particle size is of the same order of magnitude or larger than the wavelength, Mie scattering occurs.

The general law for Rayleigh scattering is:

$$I_{s,Rayleigh}(\theta) \propto \frac{1+\cos^2(\theta)}{\lambda^4} \tag{3.1}$$

where $I_s(\theta)$ is the scattered light intensity, θ is the angle of scattering. When $\theta=0°$, forward scattering occurs.

Mie scattering is described by the following relationship:

$$I_{s,Mie}(x) \propto \lambda^{-x} \tag{3.2}$$

where $0.4<x<0.5$. Mie scattering shows a weaker dependence on λ than Rayleigh scattering. Furthermore, Rayleigh scattering is almost negligible in the therapeutic window, i.e., for $650\ nm<\lambda<1300\ nm$, where a high absorption is required (cfr. Chapter 1). Moreover, according to Equation 3.1, Rayleigh scattering is function of θ, and forward and

back scattering intensities are the same, while according to the Mie theory, only forward scattering is admitted. Nevertheless, in biological tissues, photons are preferably scattered in forward direction (not strongly described by Rayleigh) and with a dependence on λ stronger than the one described by Mie [2].

Therefore a probability function, p(θ), of a photon to be scattered with angle θ is presented for tissue.

3.3 Definition of optical properties

3.3.1 Anisotropy coefficient

The concept of anisotropy is strictly related to the phenomenon of scattering. Since for each tissue a probability function p(θ) - also known as phase function- is defined, the anisotropy coefficient g is expressed, in polar coordinates, as:

$$g = \frac{\int_{4\pi} p(\theta)\cdot\cos(\theta)d\omega}{\int_{4\pi} p(\theta)d\omega} \tag{3.3}$$

where dω is the elementary solid angle. When g=0, the scattering is isotropic, g=-1 means back-scattering and g=1 represents forward scattering. In biological tissues, 0.5<g<0.99, within the therapeutic window, as summarized in Fig. 3.2 [3]:

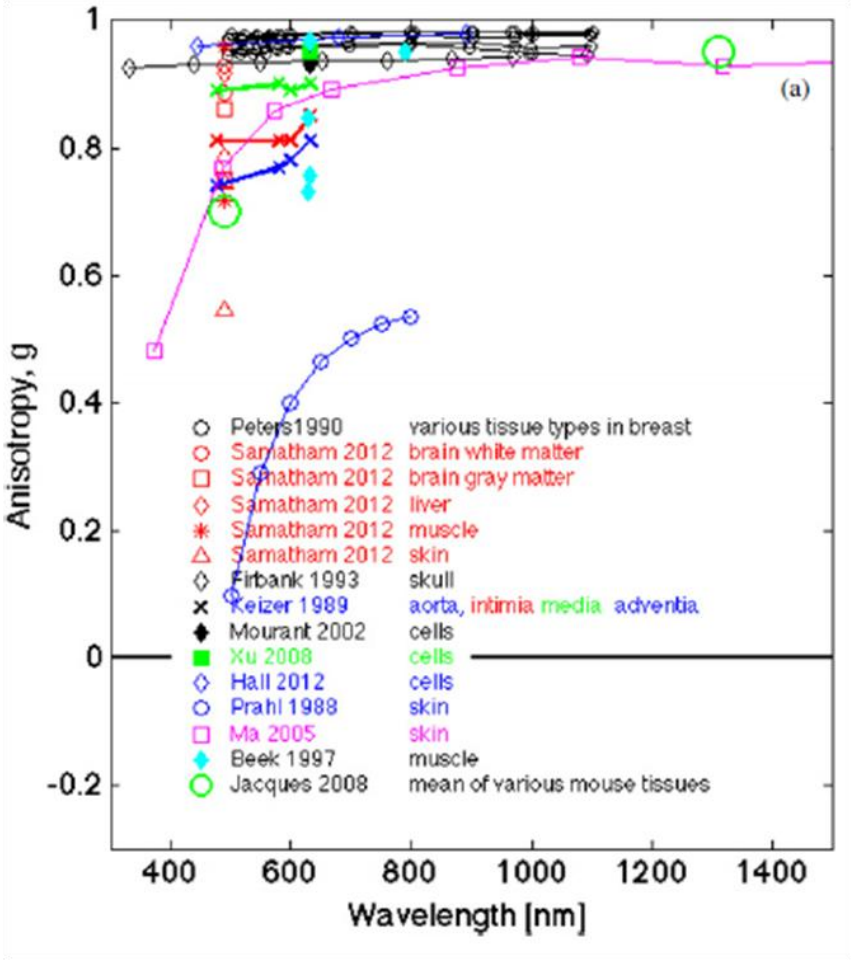

Figure 3.2 Anisotropy coefficient g *vs* wavelength, for different biological media [3].

The theoretical phase function p(θ), which can opportunely describe the anisotropy nature of tissue, is the Henyey-Greenstein function, implemented by these authors in 1941 and commonly used in the field of astrophysics:

$$p(\theta) = b \cdot \frac{1-g^2}{\left(1+g^2-2g\cos^2(\theta)\right)^{3/2}} \tag{3.4}$$

where *b* is a normalization coefficient.

A typical behavior of the equation 3.4 is shown in the Fig. 33A, for different values of g.

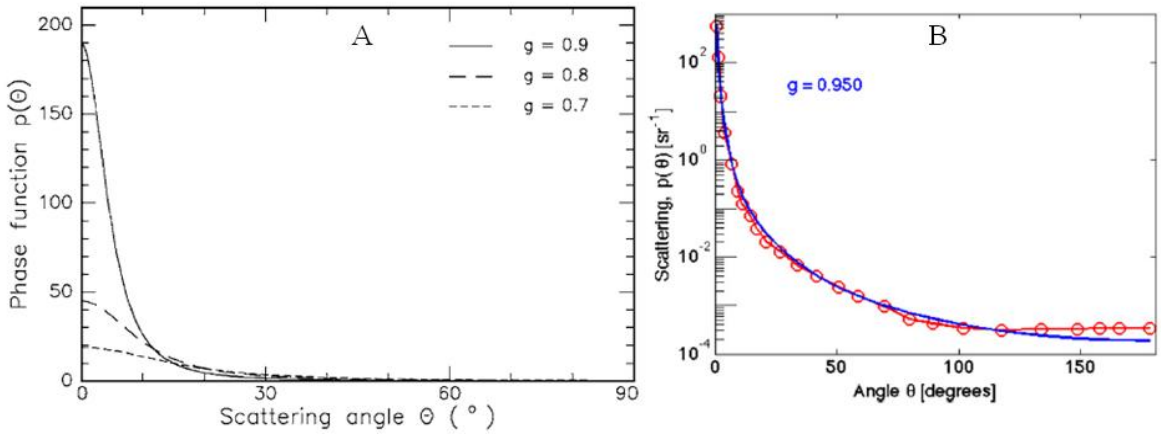

Figure 3.3 A) Phase function p(θ) for different values of anisotropy coefficient g (0.7, 0.8, 0.9), as a function of scattering angle θ [2] and B) p(θ) as function of θ for a suspension of cells at 633 nm: experimental data (red) are fitted by Equation 3.4, properly normalized [4].

Fig. 3.3B reports the comparison between the measurements of p(θ) and the fitting performed by Equation 3.4 on a suspension of cells, at 633 nm. The value of g=0.950 results from the fitting.

Equation 3.4 is an empirical model used to fit scattering behavior of media, and it is known as one-term Henvey-Greenstein (OTHG) phase function. As it is observable in Fig. 3.3B, and discussed by many authors [2, 3], OTHG is suitable for the fitting of phase function of biological tissues for angles smaller than 60°. To overcame this issue, a two-terms Henvey-Greenstein (TTHG) can be employed [5]:

$$p(\theta) = a\frac{1-g_{fs}^{\,2}}{\left(1+g_{fs}^{\,2}-2g_{fs}\cos^2(\theta)\right)^{3/2}} + c\frac{1-g_{bs}^{\,2}}{\left(1+g_{bs}^{\,2}-2g_{bs}\cos^2(\theta)\right)^{3/2}} \qquad (3.5)$$

where *a* and *c* represent the probability of a photon to be respectively forward and back scattered by the tissue, g_{fs} is the anisotropy coefficient describing the phenomenon of forward scattering, and g_{bs} represents the back scattering. The TTHG phase function was demonstrated to accurately describe anisotropy in biological tissues [6, 7].

3.3.2 Absorption coefficient

The relationship between the absorption of light in pure absorbent medium and its thickness was assessed by Bouguer in 1729, and the mathematical expression of absorption coefficient, μ_a [m^{-1}], was modeled some years later by Lambert (1760):

$$\frac{dI}{I} = \mu_a \cdot dl \tag{3.6}$$

describing how successive tissue layers of thickness *l* can absorb the same fraction of incident light d*I*/*I*, by means of the constant value represented by μ_a. The trivial solution of Equation 3.6 for the incident light intensity I_0 is the well known Lambert-Beer law:

$$I(z) = I_0 e^{-\mu_a \cdot z} \tag{3.7}$$

where z is the axis of light propagation (also defined as optical axis), I(z) is the light intensity at depth z.

3.3.3 Scattering coefficient

With a similar approach is possible to define the scattering coefficient, μ_s [m^{-1}] for a purely scattering medium:

$$I_s(z) = I_0 e^{-\mu_s \cdot z} \tag{3.8}$$

where $I_s(z)$ is the intensity of scattered light at depth z. μ_s represents the probability of a photon to be scattered, per unit of length.

3.3.4 Optical properties in turbid media

Equations 3.7 and 3.8 are very simple models, valid in case of pure absorption or pure scattering, respectively. In turbid media (as biological tissues are defined), the theory is more complicated, since phenomena of scattering and absorption are present simultaneously, and it is challenging to distinguish each contribute on the attenuation of laser light travelling through the tissue.

The simplest parameter which describes the macroscopic behavior of light attenuation of a *thin* slab of tissue is the total attenuation coefficient μ_t, defined as the sum of μ_a and μ_s.

Once defined a new parameter, the albedo *a* (in Equation 3.9),

$$a = \frac{\mu_s}{\mu_a + \mu_s} = \frac{\mu_s}{\mu_t} \tag{3.9}$$

is proved that in turbid media, *a* is close to unity, meaning that the contribution of scattering on the attenuation of light is high.

A relevant parameter is the extinction coefficient, also known as effective absorption, μ_{eff} [m^{-1}], derived from the theory of Ishimaru [8], defined as follows:

$$\mu_{eff} = \sqrt{3\mu_a[\mu_a + \mu_s(1-g)]} \tag{3.10}$$

Ishimaru developed the theory of Diffusion Approximation to solve the radiative transport equation [8, 2], useful to describe the behavior of *not optically thin tissue*, where the phenomenon of multiple scattering is dominant.

For the sake of completeness, the concept of *optical thickness*, τ, is defined according to the Equation 3.11:

$$\tau = (\mu_a + \mu_s) \cdot d \tag{3.11}$$

where *d* is the thickness of tissue sample.

For biological tissues, within the therapeutic window, τ is usually comprised between 0 and 10, and the value of the total attenuation $\mu_t=\mu_a+\mu_s$ ranges between 100 and 800 cm^{-1}. Therefore, the optimal value of tissue thickness to measure the total attenuation of tissue is 100 μm or less. Besides the theory, is it crucial to consider also the dimension of cells in the specific tissue under investigation. For example, hepatocytes, constituting the 80% of liver mass, have a diameter of 20-30 μm, and it is not recommendable to prepare sample with such thickness, or lower, since cellular membranes are destroyed, and no information about the integer morphology of the tissue can be provided.

3.4 Techniques of measurements of optical properties

3.4.1 State of the art

Nevertheless the field of measurement of tissue optical properties is still challenging, and it is difficult to realize the perfect measurement condition for each optical properties. This issue is particularly referred to the process of measurement of μ_a, that could be theoretically estimated with Equation 3.5 only under the strict hypotheses that the medium is purely and uniformly absorbing (absence of scattering), the incident light is monochromatic and highly collimated. Therefore, many authors proposed and investigated alternative methods to estimate tissue optical properties, requiring the use of model describing laser-tissue interaction, also adjuvant to the classic techniques. These techniques are commonly divided into two main families: direct and indirect methods.

- Direct methods

According to this modality, the optical properties are measured directly, without the need of any mathematical model simulating the propagation of photon within tissue. The

potentiality of these methods is limited, since they do not allow to measure μ_a, and the measurement of other coefficients cannot be performed simultaneously [2]. Nevertheless, they provide an immediate solution to obtain some parameters, such as the total absorption coefficient μ_t and the anisotropy factor g.

In Figure 3.4 an example of measuring chain for the estimation of μ_t is depicted.

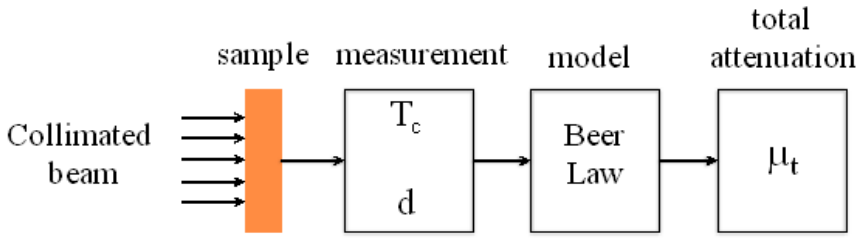

Figure 3.4 Direct method to estimate the total attenuation coefficient of biological tissue. A collimated beam hits a biological sample with thickness d, and the measurement of the fraction of collimated light transmitted by the tissue (T_c) is used to estimate the total attenuation coefficient (μ_t).

The sample, with thickness d (value of d is conveniently chosen in respect of the definition of optical thickness τ), attenuates the incident light of a collimated beam, and transmits a collimated fraction T_c. The adimensional parameter T_c represents the ratio between the collimated transmitted light intensity, measured by a photodetector, and the incident one. Through the application of Equation 3.7, where the coefficient μ_a is properly substituted with μ_t, is it possible to estimate the value of μ_t, as follows:

$$\mu_t = -\ln(T_c)/d \tag{3.12}$$

The typical measurement set up is shown in Fig. 3.5A: the source laser light is split into two beams by a beam splitter: one of them is directed to the sample, and the other one is directed to another detector, as reference. The incident light attenuated by the sample is measured by another detector, placed on the same axis of light source propagation. Once known the collimated transmitted light intensity, is it possible to calculate T_c and, through Equation 3.12, μ_t.

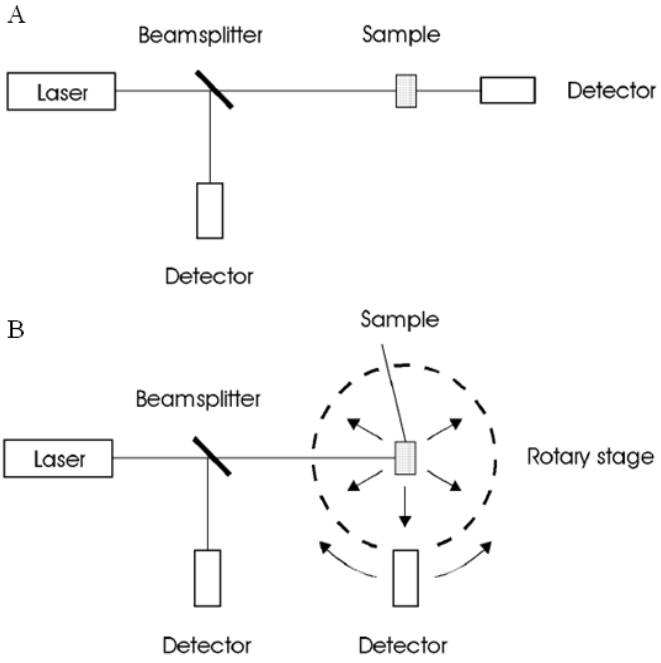

Figure 3.5 Typical experimental set up for direct measurement of A) collimated transmission (T_c) of a biological tissue, and B) scattering coefficient. Initial laser beam is split into two nominally identical beams, one directed through the tissue, the other one used as reference [2].

Also the measurement of anisotropy coefficient g can be performed by means of a direct method, commonly known as goniometric measurement.

Since a highly scattering medium diffuse the transmitted and reflected light in all the directions of the space, the detection of this light intensities at different angles can achieve the probability function p(θ) of the sample, index of the angular dependence of the scattering. The typical set up is similar to the one in Fig. 3.5A, with the exception of the moving photodetector mounted onto a rotary stage describing a circumference, around the sample (Fig. 3.5B). Once known p(θ), the estimation of g is achieved by using Equation 3.5 or 3.6.

- Indirect methods

These techniques employ a theoretical model of photon propagation inside the tissue to estimate the optical properties. They are, in turn, divided between non-iterative and iterative methods: the former allows obtaining optical properties from some parameters related to the experimental set up, and provided by a simplified model, known as Kubelka-Munk model; in the latter, the measurement of some tissue optical quantities leads to the calculation of some parameters, which are iteratively enumerated till parameters estimated

by the theoretical model match with the measurements. Inverse Monte Carlo simulation is an example of iterative indirect technique [9].

The typical experimental set up used to estimate tissue optical properties with indirect techniques is based on double integrating sphere system. This set up was used in 1990 by Derbyshire the first time [10] to evaluate the change of optical properties of myocardium during laser ablation, and it is now considered as the standard method for the estimation of tissue optical properties.

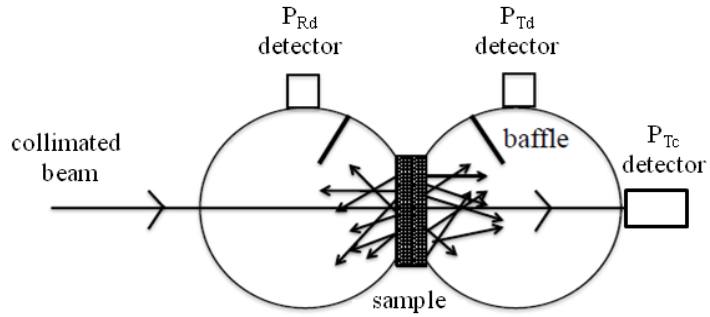

Figure 3.6 Double integrating spheres system: the tissue sample is placed between two spheres, which allocate three detectors, two for the measurement of diffused power of light, respectively reflected (P_{Rd}) and transmitted (P_{Td}), and one to measure the collimated transmitted power (P_{Tc}). Baffles are used to avoid that light reaches the detectors before being integrated.

Experimental set up, as shown in Fig. 3.6, is composed by two integrating spheres, three detectors, baffles and the tissue sample. Spheres are defined as "integrating", since they spatially integrate the flux of light reflected or transmitted by the sample, before to be measured. This feature is conferred by their behavior as *lambertian surfaces*, where the radiance (power per unit solid angle per unit projected source area) of the surface does not depend on the angle of view. Spheres are internally coated by a highly reflective coating (reflectivity higher that 90 %), which accounts for the internal multiple reflection of light

The sphere upward the sample is called *reflectance sphere*, since it integrates the flux of diffused reflected light, while the sphere downward the sample is known as *transmittance sphere*. The reflectance sphere houses the entrance port of the collimated laser light used to investigate the optical properties of the sample, and the detector of the diffused light reflected by the tissue (P_{Rd}). The sample is placed in correspondence of the exit port of the reflectance sphere and on the entry port of the transmittance sphere, which houses the detectors of light transmitted by the tissue, both diffused (P_{Td}) and collimated (P_{Tc}). Baffles avoid the first diffused reflection or transmission of the sample from reaching the correspondent detectors.

The relevant advantage of using a double integrating spheres system is the chance to perform the measurement of reflection and transmission simultaneously, avoiding possible degradation of tissue sample during the measurement process, with exposition to laser irradiation.

The theory of working principle of double integrating spheres system has been deeply investigated by several authors, such as Pickering [11, 12], and the system has been employed by a large number of researchers, to estimate optical properties of various biological tissue. For example, van Gemert *et al* employed the set up for the liver tissue, both animal and human, also considering the dependence of properties on coagulation temperature [13, 14, 15], Peters *et al* studied the properties of breast [16], Wei *et al* estimated the properties of human colon [17]. Many other results are reported by Beek *et al* [18] and Roggan and Müller [19].

3.5 Measurements of optical properties: experimental trials

3.5.1 Anisotropy coefficient of porcine liver

Measurement of anisotropy coefficient g of porcine liver have been carried out in the Institute of Biophysics of Goethe Universität in Frankfurt am Main. The choice of using porcine liver has been motivated by the necessity to validate the experimental set up before to employ it for measurements on pancreatic tissue, since current literature provides many information about liver tissue, and none about pancreas. I performed the measurement with a LED light source at wavelength of 850 nm, the closer to the wavelength of our clinical interest (1064 nm), at this time available in the laboratory. Anyway, future trials will be carried out at 1064 nm.

3.5.1.1 Liver samples preparations

Liver organ was collected and stored in freezer at -20 °C four hours after the swine was sacrificed. After 22 hours of storage, liver slices were cut by a traditional microtome for pathologic sample preparation: three porcine liver samples with thickness of 60 μm were arranged between two laboratory glass slides (Fig. 3.7A).

3.5.1.2 Experimental set up and method

Experimental set up adopted is shown in Fig. 3.7: liver samples were placed inside the goniometric holder shown in Fig. 3.7B which has been *ad hoc* designed in order to accurately control the angular distance between the position of the fiber guiding the source LED light, and the fiber collecting the light transmitted by the sample. The emitting fiber

has a fixed position, whereas the collecting fiber can be placed at different angles (0°, 30°, 45°, 60°, 120°, 135° and 150°) respect to the axis of emitting fiber.

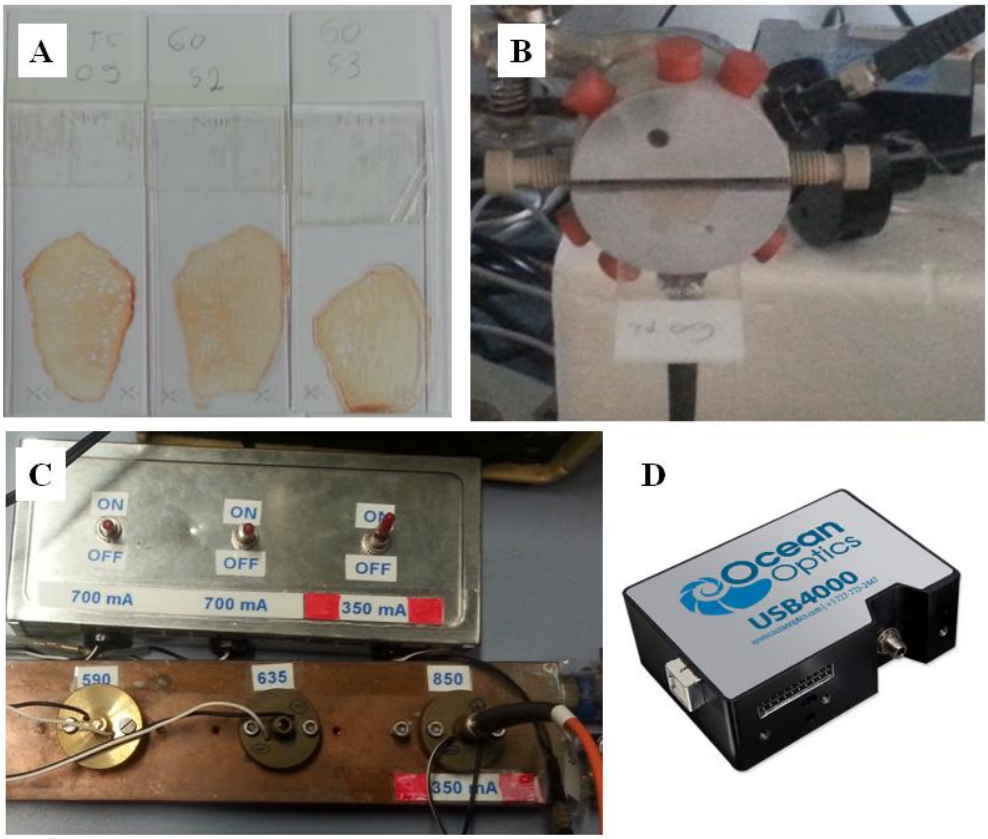

Figure 3.7 A) Three porcine liver samples with thickness of 60 μm, B) goniometric set up for the placement of the sample and the measurement of light intensity at angles of 0°, 30°, 45°, 60°, 120°, 135° and 150° respect to the axis of source light, C) LED source at 850 nm and D) portable spectrometer.

Collecting fiber guides the light to a portable spectrometer (Fig. 3.7D, Ocean Optics USB4000), and spectrum is visualized on a computer, through a dedicated software (Ocean Optics SpectraSuite). Wavelength of light source was 850 nm, and for each angular position the spectrum of the light was collected (Fig. 3.8), and the peak value of the spectrum was recorded for the estimation of g.

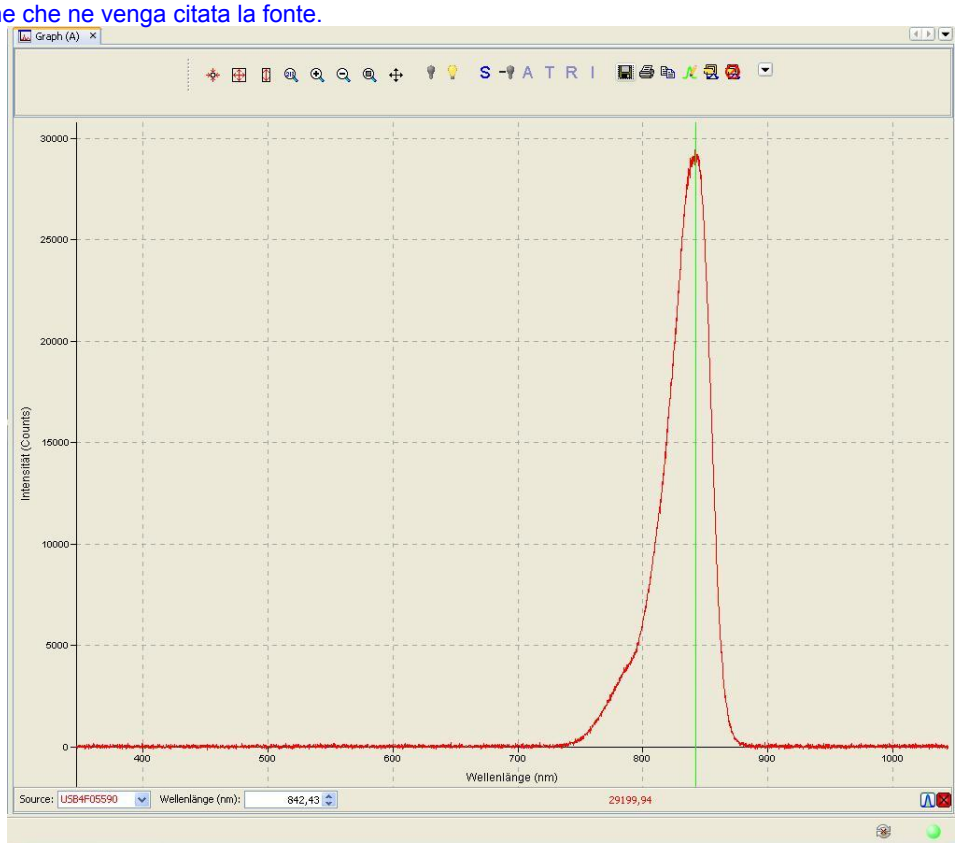

Figure 3.8 Spectrum of transmitted by liver sample laser light at 30°.

The measurement of scattered light at 0°, 30°, 45°, 60° (defined transmittance angles) account for the forward scattering of the tissue, whereas the measurements performed at 120°, 135° and 150° (defined reflectance angles) refer to the back scattering, as shown in the following schematic, where the ideal distribution of transmitted and reflected light is also represented:

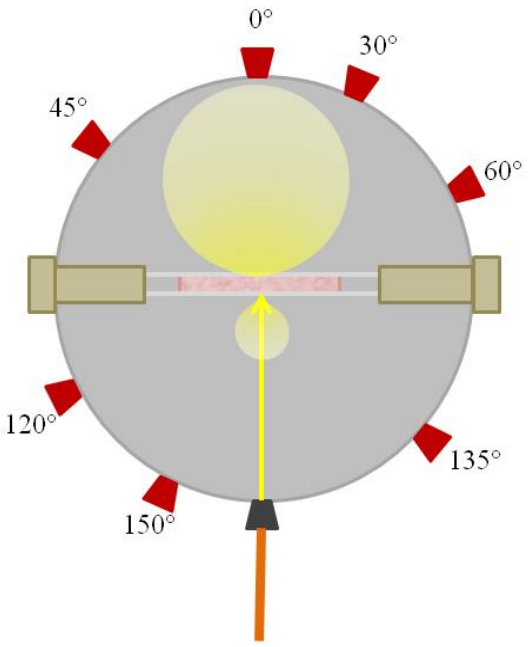

Figure 3.9 Schematic of holder, angular placement of collecting fiber and ideal distribution of forward and back scattered light.

Three liver samples were irradiated, each of them in two different positions: for each investigated region, the probe was fixed between two screws in the holder, and the position of collecting fiber was changed at different angles.

3.5.1.3 Results and discussion

Light intensities, measured at 7 angles, were normalized considering the measurement of light transmitted by the glass slices in absence of tissue. Six measurements were performed, and results are expressed as mean ± standard deviation (Fig. 3.9):

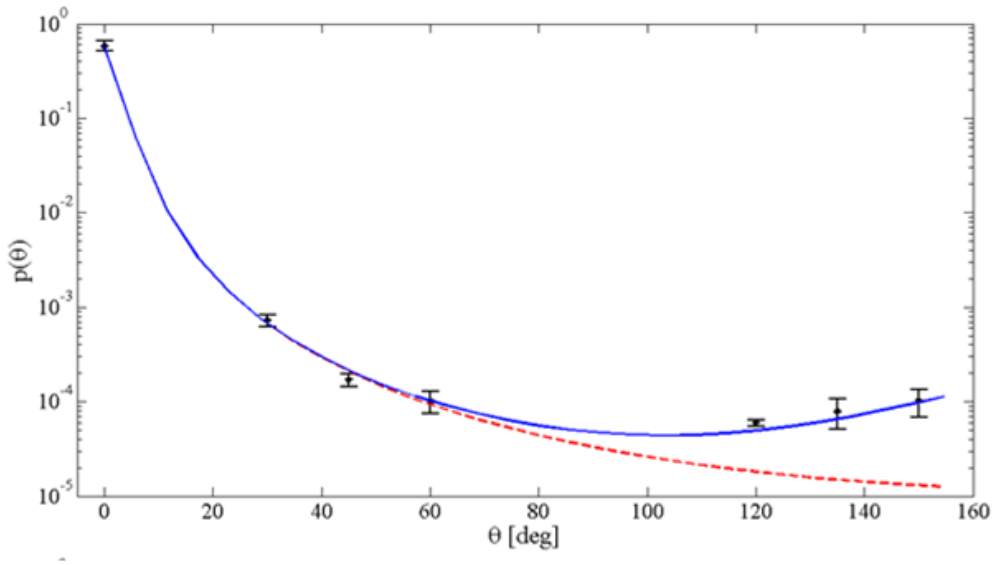

Figure 3.9 Normalized light intensity transmitted and reflected by liver at different angles (black dots), and two different fitting curves: Henvey-Greenstein curve with g=0.947 (red dashed line), and sum of two Henvey-Greenstein curves (blue continue line), one describing the forward scattering (g=0.947), and the other one for the back scattering (g=-0.498).

As explained in paragraph 3.3.1, anisotropy and, consequently, scattering behavior of biological tissue can be described by Equations 3.4 and 3.5. Both models of one-term Henvey-Greenstein (OTHG) and two-terms Henvey-Greenstein (TTHG) phase functions have been used to fit the experimental data, and parameters of the curves are listed in Table I:

Table I. Coefficient and fitting parameters of Equations 3.4 and 3.5 used to fit experimental data in Fig. 3.9.

fitting curve	**a**	**c**	**g_{fs}**	**g_{bs}**	**R^2**

OTHG	0.00084	-	0.947	-	0.99
TTHG	0.00084	0.00003	0.947	-0.498	1

The OTHG phase function (Equation 3.4) used to fit all the normalized light intensity values provides a value of g_{fs}=0.947 (red dashed curve in Fig. 3.9) obtained by the best fitting curve used only for the transmission angles (0°, 30°, 45° and 60°). As observable from the graph in Fig. 3.9, the curve provides an adequate description of forward scattering, but the prediction capability is very poor in correspondence of angles higher than 60°. Therefore I fitted the data also using the TTHG in Equation 3.5, which provides a good description of the phenomena of forward and back scattering. Considering the values of coefficient a and c, it is possible to find the percentage contribution of forward and back scattering, respectively: forward scattering contributes for the 96% of scattering (g=0.947), and the remaining 4% is represented by back scattering (g=-0.498). These results are reasonable, and comparable with theory and experiments already reported in literature. For example, Marchesini *et al* [7] found for liver tissue at 633 nm 86% of forward scattering (g=0.85) and 14% of back scattering (g=-0.34), and, for lungs, 95% of forward scattering (g=0.82) and 5% of back scattering (g=-0.54).

Another important finding from this experiment is the estimation of total attenuation coefficient of liver tissue. I considered the normalized intensity light measured at 0° as the collimated transmission (T_c) of the sample. As explained in Fig. 3.4 and through the simple application of Equation 3.12, a value of μ_t=90±20 cm^{-1} was found. Since it is known that μ_a of a biological tissue in NIR spectrum is about two orders of magnitude smaller than the value of μ_s, in first approximation it can be considered $\mu_s \approx \mu_t$. For example, Ritz *et al* [15] proposed a value of about 60 cm^{-1} for porcine liver at 850 nm. As deeply discussed [2, 3], in the field of optical properties measurement is quite challenging to establish comparisons with previously published data, even about the same tissue, because of many conditions, as the intrinsic variability of biology, the inhomogeneity of tissue (as observable in Fig. 3.7A), the preparation of sample. In particular, Ritz *et al* homogenized the tissue with a pre-cooled mortar. Although Peters *et al* [20] demonstrated, for breast tissue, that homogenization procedure causes a maximum deviation of 3.4% of reduced scattering and of 5.9% of absorption, any manipulation of tissue lead to a variation of its properties. Therefore the results obtained by our method are considered acceptable.

3.5.2 Reflectance and transmittance of human pancreas with double integrating spheres system

A system similar to the one described in Paragraph 3.4.1 and Fig. 3.6 has been used for the optical characterization of human healthy pancreas, in correspondence of wavelength 1064 nm [21, 22, 23].

3.5.2.1 Pancreas samples preparations

Healthy pancreas samples were provided by the Pathological Anatomy Unit of University Campus Biomedico di Roma. After autopsy, organ were stored at -80 °C, and then cut by microtome (HS3060T Jinhua Hisure Scientific) in slices with thickness of 100 µm and 200 µm. Slices were arranged between glass slides and stored at -21 °C for 1 day before performing measurements.

3.5.2.2 Experimental set up

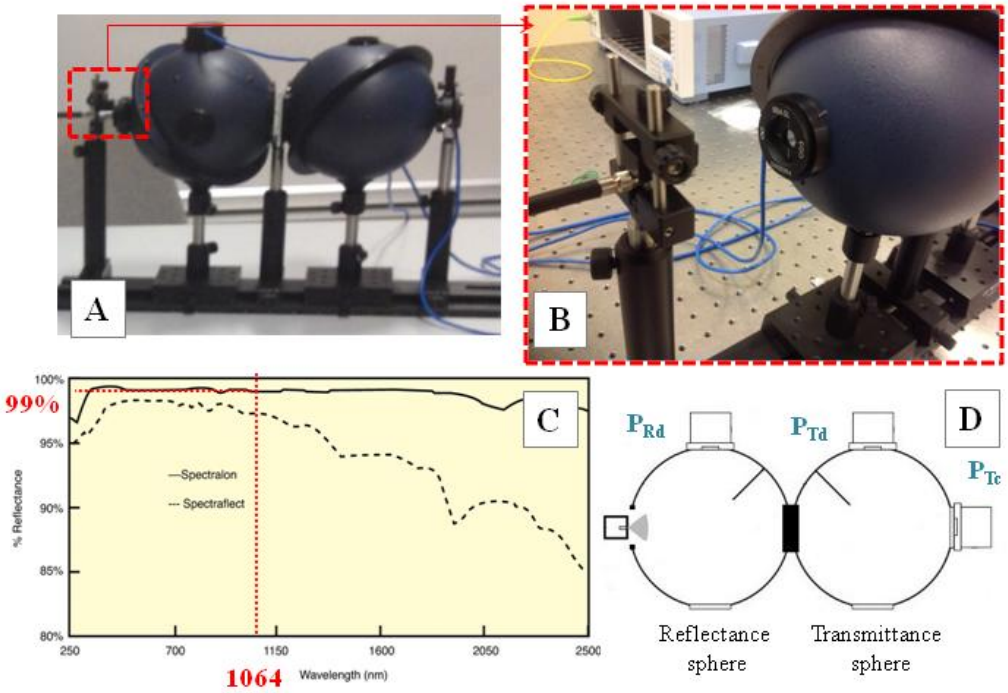

Figure 3.10 Experimental set up adopted for the optical characterization of human pancreas: A) double integrating spheres system, B) detail of the emitting fiber and the entrance port of the laser radiation, C) spectrum of reflectance of the Spectralon®, coating material of internal surface of sphere, providing a reflectance of 99% at 1064 nm, and D) placement of photodetectors (one for reflected diffused power, P_{Rd}, one for transmitted diffused power, P_{Td}, and one for transmitted collimated power, P_{Tc}) on the spheres walls.

- **Integrating spheres system**

Two integrating spheres (Newport 819C-SL-5.3 [24]) were included in the experimental set up (Fig. 3.10A). They are internally coated by a highly reflective material, Spectralon®, which shows a reflectance of 99% at 1064 nm (wavelength of Nd:YAG laser radiation, Fig. 3.10C). The spheres are nominally identical, with an internal diameter of 13.5 cm, ports to house photodetectors with diameter of 2.54 cm, ports for the placement of sample with diameter of 6.35 cm. The reflectance sphere houses the photodetector for the measurement of the power diffusely reflected by the tissue (P_{Rd}) at 90° respect to the emitted light axes; the transmittance sphere houses the photodetector for the measurement of diffused transmitted power (P_{Td}) at 90°, and the photodetector for the measurement of collimated transmitted power (P_{Tc}) at 0° (Fig. 3.10D).

- **Laser radiation**

Samples placed between the two spheres are irradiated by the Nd:YAG laser light guided by an optical fiber. The value of beam power, opportunely attenuated, is 1 mW. Optical fiber (QMMJ-5HP,5HP-IRVIS-365/400-3-3, OZ Optics [25]) has a core (a) of 365 µm, a numerical aperture (NA) of 0.22. Laser beam is collimated by a multimodal collimator for high power light (HPUCO-T,5-1064-M-7.5AS-HP, OZ Optics [25]), guaranteeing NA=0.11 and a focal distance (f) of 7.5 mm. According to the schematic in Fig. 3.11 and the following formula, it is possible to calculate the area of sample region hit by laser beam (Sp, with diameter of d_p) at distance d from the emitting tip of the collimator (corresponding to the transversal area of the laser beam at distance d+f from the applicator tip):

$$\begin{cases} BD[mm] = 2 \cdot f[mm] \cdot NA \\ DA[mrad] = \dfrac{a[mm]}{f[mm]} \end{cases} \tag{3.13}$$

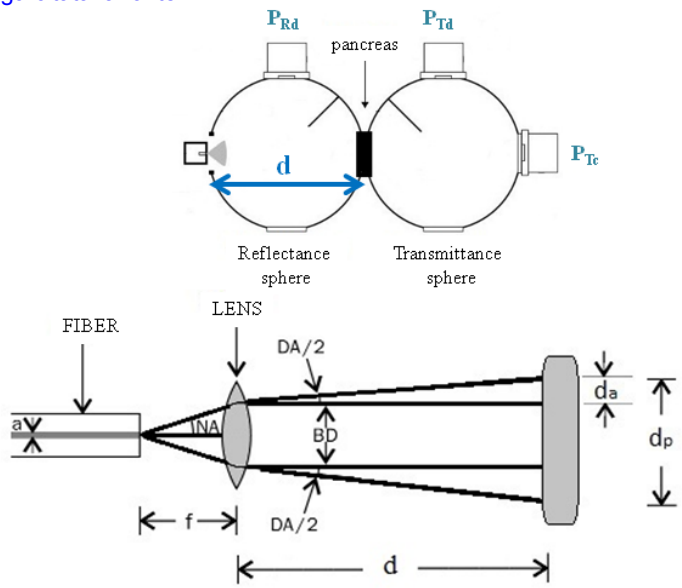

Figure 3.11 Collimation of laser beam and area of the sample surface hit by light.

From Equations 3.13 and geometrical considerations, Sp=0.83 cm^2 is obtained.

This value is crucial, since it is responsible of the averaged measurement on the inhomogeneous tissue surface [22].

- **Photodetectors**

Three photodetectors are nominally identical (818-SL/DB, Newport corporation [24]), with a wavelength measurement range between 400 and 1100 nm. The sensitive surface is made by silicon (Si), and the active area is 1 cm^2. The maximum measurable power is 2 W, and the use of adequate attenuator allows extending the power optical range of three decades. The sensitivity is 1 $A \cdot W^{-1}$, for power ranging from 10^{-12} W to 10^{-2} W. The power values are provided by power meters.

3.5.2.3 Metrological assessment

Before the estimation of optical pancreas properties, efforts have been made for the metrological assessment of the measurement chain, with particular regard to the sample. On one hand, the influence of exposition time on the sample has been taken into account; on the other hand the inhomogeneity of the sample. At the best of my knowledge it is the first study about the evaluation of exposition time, whereas a few authors performed measurement on more regions of the sample surface.

- **Influence of exposition time**

As well known, the laser light entails a thermal damage on the exposed tissue. This is the aim of the LA, and during the treatment all the physical properties of the tissue change because of temperature variation. Some authors investigated the effect of coagulation temperature on tissue optical properties, showing a dependence. For example, Gemert *et al* [13] considered the effect of coagulation on the optical properties of human liver (process of coagulation was obtained dunking the samples into a water bath at 80 °C): from the native state (room temperature) to the coagulated one, at 1064 nm μ_a and g decreased of about 50% and 6% respectively, while μ_s increased of about 18%, entailing a reduction of optical penetration of about 17%.

The aim of this study is to evaluate if the optical response of the tissue changes during the measurement of reflected and transmitted power using a double integrating spheres system, or, in other terms, if the power of incident beam can entail a thermal damage on the tissue.

(In the following, each power value is expressed only with mean value, since the standard deviation is at least three orders of magnitude smaller than the mean value. For example, the diffused reflected power, after an exposure time of 30 s, was $6.1 \cdot 10^{-3} \pm 4.3 \cdot 10^{-6}$ mW)

One pancreas sample with thickness of 200 µm has been irradiated with a laser power of 1 mW for three different exposure times: 30 s, 120 s and 300 s, and three measurements on the same region have been performed. Values are listed in Table II:

Table II. Reflected and transmitted power, diffused and collimated, of human pancreas as function of different exposure time to Nd:YAG radiation (30 s, 120 s, 300 s).

Exposure time [s]	**# measurement**	**P_{Rd} [W]**	**P_{Td} [W]**	**P_{Tc} [W]**	**Figure**
30	1	6.1×10^{-6}	1.4×10^{-5}	2.4×10^{-4}	3.12
	2	6.3×10^{-6}	1.4×10^{-5}	2.4×10^{-4}	
	3	6.2×10^{-6}	1.4×10^{-5}	2.4×10^{-4}	
120	1	5.8×10^{-6}	1.3×10^{-5}	2.4×10^{-4}	3.13
	2	5.8×10^{-6}	1.4×10^{-5}	2.4×10^{-4}	

	3	5.8×10^{-6}	1.3×10^{-5}	2.4×10^{-4}	
300	1	5.8×10^{-6}	1.3×10^{-5}	2.4×10^{-4}	3.14
	2	5.9×10^{-6}	1.4×10^{-5}	2.4×10^{-4}	
	3	5.9×10^{-6}	1.4×10^{-5}	2.4×10^{-4}	

In the following, the graph for each measurement is reported:

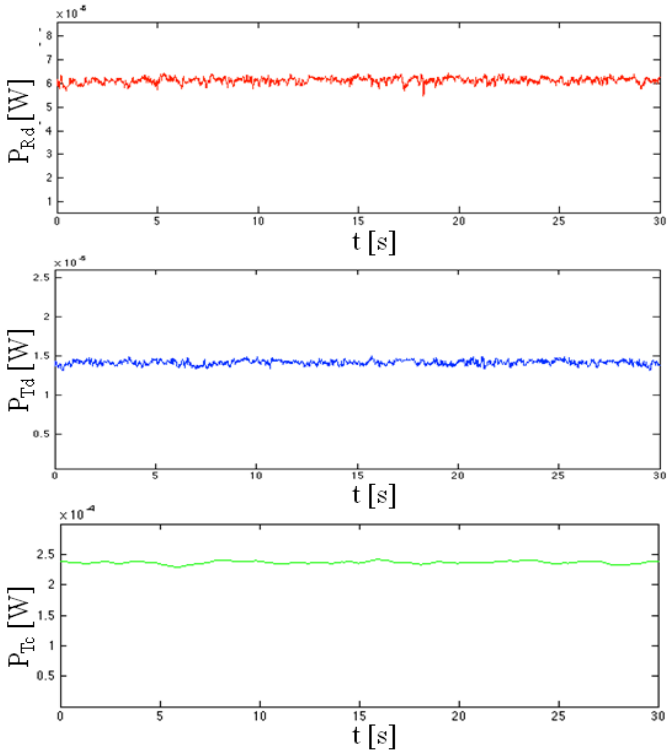

Figure 3.12 Diffused reflected power (P_{Rd}), diffused (P_{Td}) and collimated (P_{Tc}) transmitted power of human pancreas with thickness of 200 µm undergoing Nd:YAG laser (1 mW) for exposure time of 30 s.

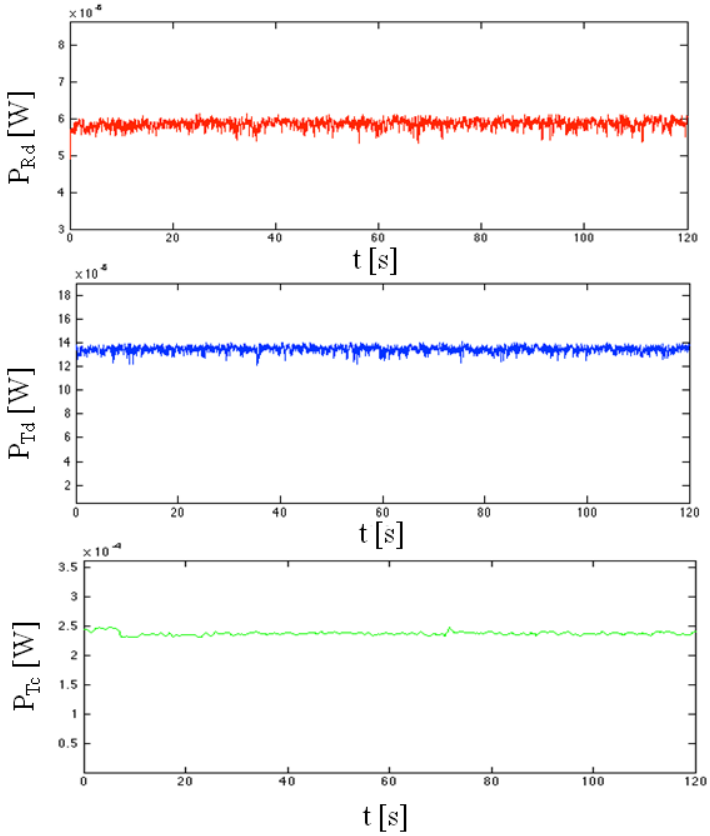

Figure 3.13 Diffused reflected power (P_{Rd}), diffused (P_{Td}) and collimated (P_{Tc}) transmitted power of human pancreas with thickness of 200 µm undergoing Nd:YAG laser (1 mW) for exposure time of 120 s.

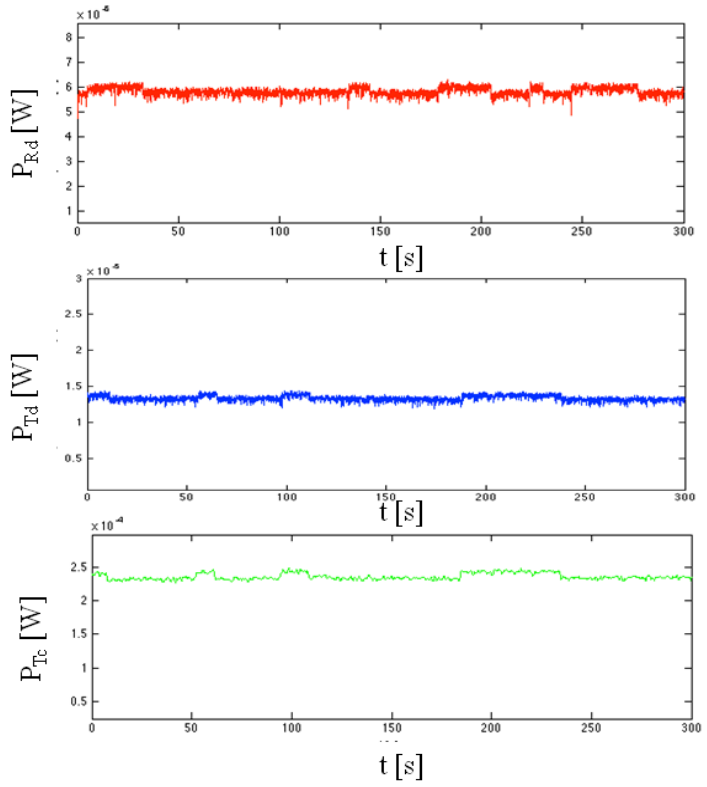

Figure 3.14 Diffused reflected power (P_{Rd}), diffused (P_{Td}) and collimated (P_{Tc}) transmitted power of human pancreas with thickness of 200 µm undergoing Nd:YAG laser (1 mW) for exposure time of 300 s.

The experimental assessment demonstrates the reproducibility of measurements, since the power values do not shown any significant variation during the measurement procedure.

- **Normalization of power values and correction of spheres residual radiation**

As well know, in order to obtain values of diffused and collimated transmittance, and diffused reflectance, power values provided by photodetectors should be normalized, and the diffused radiation, which remains inside the spheres without contributing to the measurement, should be also taken into account. An immediate approach is provided by Yust *et al* [26], who define diffused reflectance (Rd), diffused transmittance (Td) and collimated transmittance (Tc) according to the following relations (equation 3.14):

$$\begin{cases} R_d = \dfrac{P_{Rd} - Y_r}{Z_r - Y_r} \\ T_d = \dfrac{P_{Td} - Y_t}{Z_t - Y_t} \\ T_c = \dfrac{P_{Tc}}{Z_c} \end{cases} \tag{3.14}$$

where:

- ✓ P_{Rd} is the diffused reflected power, Z_r is the power revealed by the same photodetector of P_{Rd} but in absence of the sample (the exit port is closed with a plug made of Spectralon), and Y_r is the correction factor of diffused light, measured by P_{Rd} photodetector without sample;
- ✓ P_{Td} is the diffused transmitted power, Z_t is the power measured by the same photodetector of P_{Td} but in absence of the sample (the photodetector of P_{Tc} is substituted by a plug made of Spectralon), and Y_t is the correction factor of diffused light, measured by P_{Td} photodetector without sample and without Spectralon on the position of photodetector of P_{Tc};
- ✓ P_{Tc} is the collimated transmitted power and Z_c is the power measured by the same photodetector of P_{Tc} but in absence of the sample.

Measured values with respective uncertainty (40 samples, 95% confidence) are reported in Table III:

Table III. Normalization and correction factors for integrating sphere system

Normalization and correction factors	mean value ± uncertainty [W]
$\mathbf{Z_r}$	$1.9 \times 10^{-5} \pm 3.0 \times 10^{-7}$
$\mathbf{Y_r}$	$5.9 \times 10^{-7} \pm 8.6 \times 10^{-9}$
$\mathbf{Z_t}$	$1.9 \times 10^{-5} \pm 3.0 \times 10^{-7}$
$\mathbf{Y_t}$	$8.5 \times 10^{-7} \pm 6.4 \times 10^{-9}$
$\mathbf{Z_c}$	$5.8 \times 10^{-4} \pm 1.8 \times 10^{-6}$

The law of error propagation has been used to calculate the uncertainty of R_d, T_d and T_c.

- **Considering of tissue surface inhomogeneity**

For each sample, reflected and transmitted power values have been measured in 5 different positions, depending on the total surface of the sample, as shown in Fig. 3.15, avoiding the areas overlapping:

Figure 3.15 Selection of different areas on the pancreas samples surface to investigate during the process of measurement.

Measurements performed on one pancreas sample with thickness 100 µm and one pancreas sample with thickness of 200 µm, irradiated for 300 s, are listed following:

Table IV. Optical measurements on human pancreas

Pancreas thickness	Position	P_{Rd} [W]	P_{Td} [W]	P_{Tc} [W]	Rd	Td	Tc
100 µm	#1	$4.5 \cdot 10^{-6}$	$6.5 \cdot 10^{-6}$	$2.4 \cdot 10^{-4}$	0.21 ± 0.06	0.31± 0.01	0.43± 0.03
	#2	$4.4 \cdot 10^{-6}$	$6.4 \cdot 10^{-6}$	$2.6 \cdot 10^{-4}$			
	#3	$4.3 \cdot 10^{-6}$	$6.5 \cdot 10^{-6}$	$2.5 \cdot 10^{-4}$			

	#4	$4.4 \cdot 10^{-6}$	$6.1 \cdot 10^{-6}$	$2.8 \cdot 10^{-4}$			
	#5	$4.4 \cdot 10^{-6}$	$6.5 \cdot 10^{-6}$	$2.4 \cdot 10^{-4}$			
	mean ± uncertainty	$(4.4 \pm 0.1) \cdot 10^{-6}$	$(6.4 \pm 0.2) \cdot 10^{-6}$	$(2.5 \pm 0.2) \cdot 10^{-4}$			
200 µm	#1	$4.2 \cdot 10^{-6}$	9.2×10^{-6}	$1.4 \cdot 10^{-4}$	0.20 ± 0.01	0.45 ± 0.03	0.30 ± 0.09
	#2	$4.3 \cdot 10^{-6}$	9.4×10^{-6}	$1.2 \cdot 10^{-4}$			
	#3	$4.2 \cdot 10^{-6}$	8.6×10^{-6}	$1.9 \cdot 10^{-4}$			
	#4	$4.1 \cdot 10^{-6}$	8.9×10^{-6}	$1.9 \cdot 10^{-4}$			
	#5	$4.2 \cdot 10^{-6}$	8.5×10^{-6}	$2.4 \cdot 10^{-4}$			
	mean ± uncertainty	$(4.2 \pm 0.1) \cdot 10^{-6}$	$(8.9 \pm 0.5) \cdot 10^{-6}$	$(1.8 \pm 0.6) \cdot 10^{-4}$			

As expected, the value of T_d increases with the thickness of the sample while, on the other hand, T_c is strongly reduced. The value of R_d remains mostly constant, since it is more dependent on the first layers of sample.

3.5.2.4 Estimation of pancreas total attenuation and scattering coefficient

From the analysis of these data, it is possible to estimate the total attenuation coefficient of human pancreas, with an approach similar to the one discussed in Paragraph 3.5.1.3 for the liver tissue. Through the Equation 3.12, and considering the thickness of tissue of 100 µm as suggested by Jacques for direct measurement [3] and T_c, I obtain $\mu_t = 88 \pm 5$ cm^{-1}. Since the absorption of tissue within this wavelength range is about two orders of magnitude lower than the value of scattering coefficient, is it possible to consider, in first approximation, $\mu_t \approx \mu_s$.

3.5.2.5 Kubelka-Munk model for preliminary estimation of pancreas optical properties

The simpler model provided by literature to estimate optical properties of tissue is Kubelka-Munk method (KMM). It does not require an iterative algorithm, but the solution of a system of equations. KMM allows separating the light beam attenuation due to absorption from the loss due to scattering. Briefly, KMM assumes that the light incident on tissue can be modeled by two counter-propagating fluxes. The optical flux, which propagates in the same direction of incident flux, is decreased by absorption and forward scattering, and increased by back scattering. The fraction of each flux lost by absorption per unit of path length is denoted by K, and the fraction lost by scattering by S. The main

assumption of KMM is that K and S are constant throughout the tissue thickness [9]. The relationships between optical coefficients and K and S equations are reported:

$$\begin{cases} K = 2 \cdot \mu_a \\ S = \frac{3}{4}(1-g) \cdot \mu_s - \frac{1}{4}\mu_s \end{cases} \tag{3.15}$$

while the dependence of S and K on measured values (R_d, T_d and T_c) is described by the following formula:

$$\begin{cases} K = S(a-1) \\ S = \frac{1}{b \cdot t \cdot T_d} \ln\left[1 - R_d(a-b)\right] \\ a = \frac{1 + R_d{}^2 - T_d{}^2}{2R_d} \\ b = \sqrt{a^2 - 1} \\ -\ln(T_c) = (\mu_a + \mu_s)t \end{cases} \tag{3.16}$$

From averaged measured values listed in Table IV, the optical properties of pancreas according KMM are:

Table V. Pancreas optical properties according Kubelka Munk model.

Pancreas thickness [µm]	**μ_a [cm^{-1}]**	**μ_s [cm^{-1}]**	**g**
100	33	59	0.66
200	20	96	0.56

The influence of tissue inhomogeneity has been considered also in the calculation of optical properties. In correspondence of each position, where the measurements have been performed, KMM provides the following data:

Table VI. Pancreas optical properties (100 µm thickness, 4 positions) according Kubelka Munk model.

Pancreas thickness 100 [µm]	**μ_a [cm^{-1}]**	**μ_s [cm^{-1}]**	**g**
#1	25	67	0.38
#2	32	65	0.40
#3	40	49	0.70
#4	27	61	0.76

Table VII. Pancreas optical properties (200 µm thickness, 5 positions) according Kubelka Munk model.

Pancreas thickness 200 [µm]	**μ_a [cm^{-1}]**	**μ_s [cm^{-1}]**	**g**
#1	21	106	0.59
#2	21	110	0.55
#3	19	96	0.58
#4	21	98	0.47
#5	20	114	0.54

In Table VIII are presented the maximum percentage variations between measured reflectance and transmittances, and the values calculated by KMM, provided by different areas of samples (both thickness are considered):

Table VIII. Comparison between maximum percentage variation of measured powers on different areas of sample, and the related optical coefficients calculated by KMM.

	maximum % variation on measured powers			**maximum % variation on KMM optical properties**		
Pancreas thickness	**P_{Rd}**	**P_{Td}**	**P_{Tc}**	**μ_a**	**μ_s**	**g**
100 µm	20%	15%	8%	36%	8%	50%
200 µm	20%	5%	20%	10%	16%	20%

Measured power values (P_{Rd}, P_{Td} and P_{Tc}) show percentage variation up to 20 % when different areas of sample are investigated. These variations, related to the intrinsic inhomogeneity of biological tissues, lead to a high percentage variation of optical coefficients calculated through Equations 3.15 and 3.16.

As observable in Tables V-VII, values change with tissue thickness, while optical properties are intrinsic properties of material, therefore independent from geometrical characteristics. Moreover, KMM overestimates μ_a and underestimates g, while the value of μ_s is similar to the one determined by direct method (about 88 cm^{-1}, Paragraph 3.5.2.4). Although it is not possible to compare these data with literature, they can be compared in term of order of magnitude.

KMM does not take into account some phenomena, as boundary reflection, or the geometry of double integrating spheres system, therefore the high percentage variation

(Table VIII) is related not only to the inhomogeneities of pancreas, but also to the limits of the model.

Because of its weakness, KMM is commonly used to determine reference values to be employed and corrected in iterative algorithms (e.g., Inverse Monte Carlo), which are not included in this work.

Bibliography Chapter 3

[1] J. T. Walsch, "Basic interaction of light with tissue," in *Optical-thermal response of laser-irradiated tissue*, Welch, A J; van Gemert, M J C;, 2011, pp. 13-26.

[2] M. Niemz, "Light and matter," in *Laser-tissue interactions: fundamental and application*, Springer, 2005, pp. 9-44.

[3] S. L. Jacques, "Optical properties of biological tissues: a review," *Physics in medicine and biology* , vol. 58, no. 11, p. R37, 2013.

[4] M. Xu, T. T. Wu and J. Y. Qu, "Unified Mie and fractal scattering by cells and experimental study on application in optical characterization of cellular and subcellular structures," *Journal of Biomedical Optics,* vol. 13, no. 2, pp. 024015-024015, 2008.

[5] N. Pfeiffer and G. H. Chapman, "Successive order, multiple scattering of two-term Henyey-Greenstein phase functions," *Optics express,* vol. 16, pp. 13637-13642, 2008.

[6] S. L. Jacques, C. A. Alter and S. A. Prahl, "Angular dependence of HeNe laser light scattering by human dermis," *Lasers Life Sci*, vol. 1, pp. 309-333, 1987.

[7] R. Marchesini, A. Bertoni, S. Andreola, E. Melloni and A. E. Sichirollo, "Extinction and absorption coefficients and scattering phase functions of human tissues in vitro," *Applied Optics* , vol. 28, pp. 2318-2324, 1989.

[8] A. Ishimaru, "Diffusion of light in turbid material," *Appl Opt*, vol. 28, no. 12, pp. 2210-2215, Jun. 1989.

[9] V. V. Tuchin, Tissue Optics: Light Scattering Methods and Instruments for Medical Diagnosis, SPIE, 2nd Edition, 2007.

[10] G. J. Derbyshire, D. K. Burger and M. Unger, "Thermally induced optical property changes in myocardium at 1.06 μm," *Lasers in surgery and medicine,* vol. 10, pp. 28-34, 1990.

[11] J. W. Pickering, C. J. Moes, H. J. C. M. Sterenborg, S. A. Prahl and M. J. Van Gemert, "Two integrating sphere with an intervening scattering sample," *JOSA*, vol. 9, pp. 621-31, 1992.

[12] J. W. Pickering, S. A. Prahl, N. Van Wieringen, J. F. Beek, H. J. Sterenborg and M. J. Van Gemert, "Double-integrating-sphere system for measuring the optical properties of tissue," *Applied Optics*, vol. 32, pp. 399-410, 1993.

[13] C. Germer, A. Roggan and J. Ritz, "Optical properties of native and coagulated human liver tissue and liver metastases in the near infrared range," *Laser in Surgery and Medicine*, vol. 23, pp. 194-202, 1998.

[14] J. P. Ritz, A. A. Roggan, C. Germer, C. Isbert, G. Muller and H. J. Buhr, "Continuous Changes in the Optical Properties of Liver Tissue During Laser-Induced Interstitial Thermotherapy," *Lasers in Surgery and Medicine*, vol. 28, pp. 307-312, 2001.

[15] J. P. Ritz, A. Roggan, C. Isbert, G. Müller, H. J. Buhr and C. T. Germer, "Optical properties of native and coagulated porcine liver tissue between 400 and 2400 nm.," *Lasers in surgery and medicine*, vol. 29, pp. 205-212, 2001.

[16] V. Peters, D. Wyman, M. Patterson and G. Frank, "Optical properties of normal and diseased human breast tissues in the visible and near infrared," *Phys. Med. Biol.*, vol. 35, pp. 1317-1334, 1990.

[17] H. J. Wei, D. Xing, J. J. Lu, H. M. Gu, G. Y. Wu and Y. Jin, "Determination of optical properties of normal and adenomatous human colon tissue in vitro using integrating sphere techniques," *World Journal of Gastroenterology*, vol. 11, pp. 2413-2419, 2005.

[18] J. F. Beek, P. Blokland, P. Posthumus, M. Aalders, J. Pickering, H. J. C. M. Sterenborg and M. J. C. van Gemert, "In vitro double-integrating-sphere optical properties of tissues between 630 and 1064nm," *Phys. Med. Biol.*, vol. 42, pp. 2255-2261, 1997.

[19] G. Müller and A. Roggan, "Optical and thermal properties of biological tissue," in *Laser-Induced Interstitial Thermotherapy*, SPIE Press, 1995, pp. 9-82.

[20] V. G. Peters, D. R. Wyman, M. S. Patterson and G. L. Frank, "Optical properties of normal and diseased human breast tissues in the visible and near infrared," *Physics in medicine and biology*, vol. 35, pp. 1317-34, 1990.

[21] E. De Paolis, "Apparato sperimentale per la stima delle proprietà ottiche del pancreas con il metodo monte carlo inverso," M. Sc. Degree Thesis, Università Campus Biomedico di Roma, 2012.

[22] D. Carmina, "Calibrazione di un sistema di misura a doppia sfera integratrice e misure preliinari delle proprietà ottiche di tessuto pancreatico," M. Sc. Degree Thesis, Università Campus Biomedico di Roma, 2013.

[23] E. Caimo, "Misura delle riflettanza e della trasmittanza, diffusa e collimata, di tessuto pencreatico, epatico e renale," M. Sc. Degree Thesis, Università Campus Biomedico di Roma, 2013.

[24] d. d. i. s. system, "Newport. Experience Solutions," [Online]. Available: http://www.newport.com/.

[25] "OZ Optics," [Online]. Available: http://www.ozoptics.com/.

[26] B. G. Yust, L. Mimun and D. K. Sardan, "Optical absorption and scattering of bovine cornea, lens, and retina in the near-infrared region," *Lasers Med Sci*, vol. 27, pp. 413-422, 2012.

Part II. Laser Ablation outcomes: thermometry and ablation volumes

Introduction

Temperature value reached within the tissue plays a crucial role in LA outcome and the spatial temperature distribution defines the volume of coagulation and vaporization thus, the amount of tissue undergoing thermal damage. Therefore, the monitoring of temperature increase during LA provides an useful feedback in order to adjust laser dosimetry, and can result pivotal for effective therapy, aimed to completely remove the neoplastic volume without thermal damage of the surrounding healthy tissue. The research effort devoted to the development of temperature monitoring during thermal therapies, and particularly regarding LA, allowed the introduction of several techniques along the last thirty years. The first invasive approaches were able to monitor temperature only in one or a few points around the fiber applicator, by utilizing temperature sensors, such as, thermocouples [1], and fiber optic sensors [2]; during seventies and eighties, other approaches, based on medical imaging techniques, such as, MRI [3], and CT scan [4], were considered attractive because of their non-invasiveness. In the following, main techniques will be presented according to the schematic reported in Fig. 4:

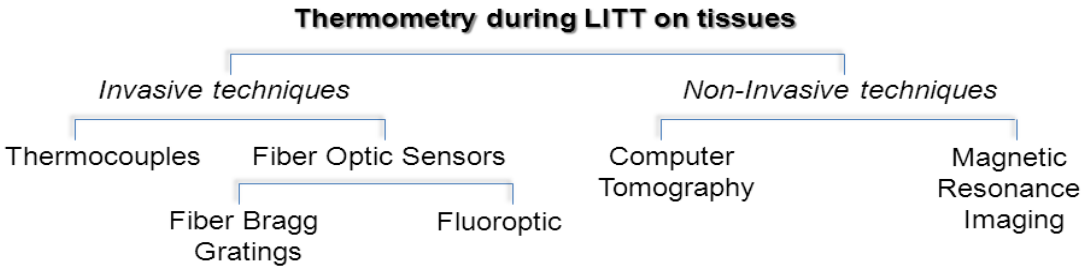

Figure 4. Schematic of thermometry techniques during LA.

Chapter 4. Invasive thermometry techniques during Laser Ablation

In this section three most widely used invasive approaches for temperature monitoring during hyperthermia are described. The need to introduce the sensing element within the organ is the main drawback of these methods, which require a direct contact with the measurement site. Furthermore, since the information about LA outcome are related to the distribution of tissue temperature, a number of sensors is required. The abovementioned features contribute to the classification of these techniques as invasive approaches, even though efforts are dedicated to the minimization of the number of probes necessary to the temperature map estimation.

4.1 Fiber Bragg Grating

4.1.1 Working principle

FBGs are periodical perturbations of refraction index of an optical fiber [5] photo-inscribed within the core of the fiber.

Working principle of FBGs is based on the detection of a wavelength shift ($\Delta\lambda_B$), due to change of temperature or strain. The Bragg wavelength (λ_B) is expressed by:

$$\lambda_B = 2n_{eff} \cdot \Lambda \tag{4.1}$$

where n_{eff} is the effective refractive index of the fiber core, and Λ is the period of index modulation. When a broadband light source propagates within the fiber, a narrowband spectral component centered at λ_B is reflected by the grating. A perturbation of the measurand causes a variation of n_{eff} (Δn_{eff}) and Λ ($\Delta\Lambda$), which entail a $\Delta\lambda_B$, as shown in Equation 4.2 and Fig. 4.1.

$$\frac{\Delta\lambda_B}{\lambda_B} = \frac{\Delta n_{eff}}{n_{eff}} + \frac{\Delta\Lambda}{\Lambda} \tag{4.2}$$

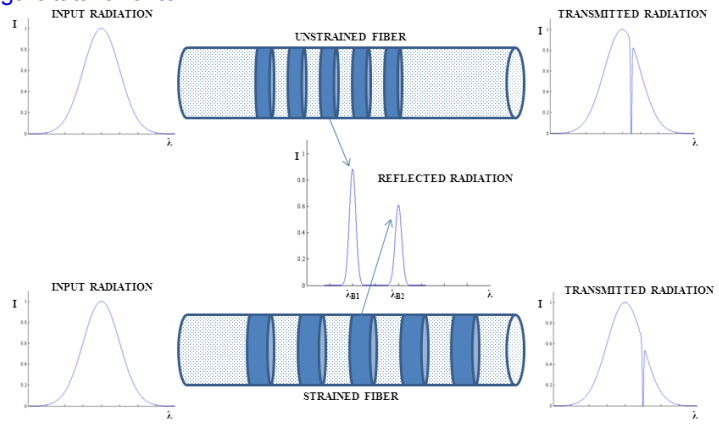

Figure 4.1: Working principle of Fiber Bragg Grating [6].

The shift of λ_B can be considered an indirect measurement of temperature or strain. In particular, $\Delta\lambda_B$ depends on temperature changes (ΔT) because of the thermal expansion of fiber material (changes of Λ), and on the temperature dependence of n_{eff}; whereas, dependence of $\Delta\lambda_B$ on strain (ε) is due to physical elongation of the sensor and the corresponding variation of Λ along with the change in n_{eff} due to photo-elastic effect.

When FBGs are employed as temperature sensor, the contribution of ε changes on $\Delta\lambda_B$ should be negligible with respect to the contribution of ΔT. When the measurand is T, the thermal response of silica fiber is dominated by the changes of n_{eff} with T (about 95% of the observed shift).

4.1.2 Features and state of art

FBGs have been introduced in biomedical field in the last twenty years [7, 8], owing to their appreciate features, such as the electromagnetic inert nature, the small size, the biocompatibility, the non-toxicity and chemical inertness, the capability to be encapsulated into thin and flexible optical fibers. A number of gratings can be easily embedded into a single fiber, since the nominal λ_B is different, and they can be interrogated by the same optical spectrum analyzer. This is an attractive feature, because distributed FBG sensor can be realized by housing an array of multiple gratings within the same fiber.

At least to my knowledge, first *in vivo* study employing FBGs for temperature monitoring during hyperthermia was performed by Rao *et al.* [9], who developed a novel FBG temperature sensor system: the strain free probe was designed by enclosing the FBG sensor array in a protection sleeve (diameter of 0.5 mm). The system showed a resolution of 0.1 °C and an accuracy of 0.2 °C over a temperature range between 30 °C and 60 °C. The same group of researchers tested the performances of a similar FBG-based

temperature sensor inside a NMR machine with static magnetic field of 4.7 T. The probe allowed a resolution of 0.1 °C and an accuracy of 0.5 °C, for temperature ranging from 25 °C to 60 °C [10]. The first *in vivo* trials with this novel probe were carried out by Webb *et al.* on diseased livers and healthy kidneys of rabbit undergoing hyperthermia [11]; a good agreement with temperature measurements performed by a reference fluoroptic probe was found. Other works aimed to perform temperature profile monitoring in *ex vivo* and *in vivo* animal models [12] and human models [13] during hypothermia.

When *in vivo* temperature monitoring is performed, the presence of possible movements can cause measurement errors, hence the encapsulation of FBGs within a protective shield is recommended. Although the use of FBGs in hyperthermia procedures should be further examined, they represent an efficient sensor to be employed in LA-MRI guided, thanks to their immunity to electromagnetic fields, and to perform temperature distribution monitoring, thanks to the feasibility of embedding a number of gratings within a single fiber. The possibility to develop small-sized FBGs allows to perform measurement with high spatial resolution (i.e., 1 mm, Fig. 4.2). Some drawbacks are related to the cost of the optical spectrum analyzer, and to the invasiveness of inserting the fibers into the body district undergoing LA.

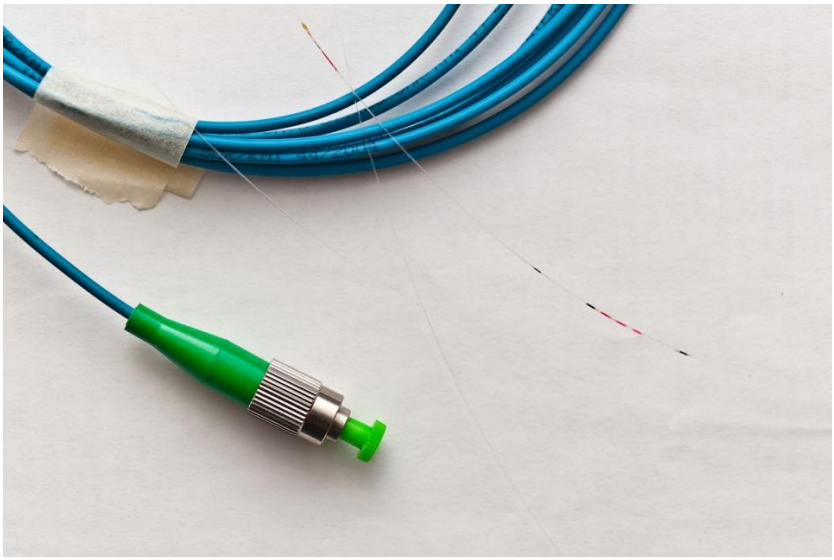

Figure 4.2. Fiber Bragg Gratings, in correspondence of red signs on the fiber (Technica S.A, Beijing Operation, P. R. China).

During my PhD program, the feasibility of inserting FBGs in direct contact with tissue undergoing hyperthermia, without protecting capsule, has been investigated, and then FBG sensors were employed for measurement of temperature distribution in pancreas, in several

configuration, and at different laser settings. The static calibration of FBG has also been performed.

4.1.3 Negligible influence of tissue strain on FBG output

Before performing temperature measurements on pancreas undergoing LA by FBG, a critical step is to verify that FBG sensors do not experience any appreciable mechanical strain. In fact, FBG sensors are sensitive to temperature but also to strain: the relaxation of tissue under its weight might entail a shift in FBG sensor output ($\Delta\lambda_B$) causing an error in temperature measurement accordingly to the relation:

$$\Delta\lambda_B = c_\varepsilon \cdot \varepsilon + c_T \cdot \Delta T \tag{4.3}$$

where c_ε is the strain-optic coefficient, ε is the strain experienced by sensor, c_T is the coefficient of temperature and ΔT is the temperature variation measured by the sensor. $\Delta\lambda_B$ depends on both ε and ΔT and, in order to use the FBG sensor as temperature sensor only, it is necessary to evaluate the negligibility of strain contribution, so that to assume ε=0 in Equation 4.3 and to consider $\Delta\lambda_B$ related to temperature variation only.

A preliminary test aimed to estimate the influence of pancreas strain (ε), caused by the gravitational field, on FBG sensor output. During the experiment, one FBG sensor has been introduced inside the pancreas, and its λ_B has been monitored for a time quite longer than time of laser irradiation, t_l (800 s), without mechanical stress. Also pancreas temperature can be considered constant during the whole experiment, as confirmed by a reference thermistor. Since $\Delta\lambda_B$ measured during the trial can be quantified in a ΔT by less than 0.1 K, the influence of pancreas strain on temperature measurements can be assumed negligible for the aims of our research (Fig. 4.3) [14].

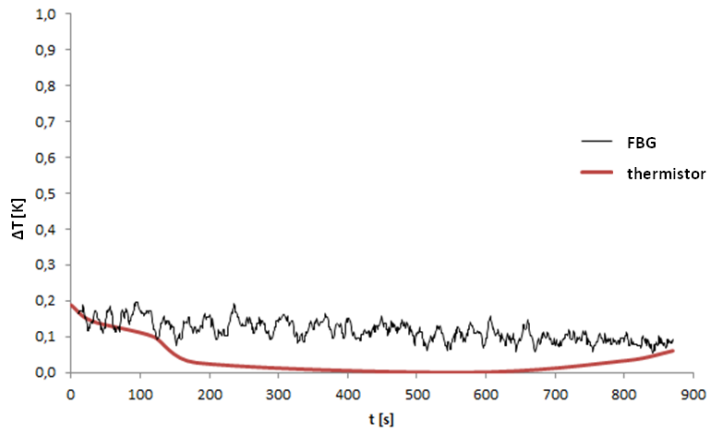

Figure 4.3. Negligible influence of mechanical stress on output of FBG for temperature measurement in pancreas during LA.

4.1.4 FBG with length of 1 cm to measure pancreas temperature distribution during Laser Ablation

Once assumed ε=0, the experimental setup, shown in Fig. 4.4, has been realized to monitor ΔT of *ex vivo* pancreas undergoing LA at different laser settings [14]. It is composed of: laser Nd:YAG with wavelength of 1064 nm operating in CW (Smart 1064 BS, Deka M.E.L.A. Srl, Florence, Italy); 2) a laser applicator quartz bare fiber 300 μm diameter core, and a set of 6 FBG sensors (1 cm grating length); 3) an *ad hoc* designed polymeric mask to contain the pancreases and to control relative distances among sensors and laser tip applicator; 4) an Optical Spectrum Analyzer, OSA, (Optical Sensing Interrogator, sm125, Micron Optics) for $\Delta\lambda_B$ detection; 5) a PC to collect data obtained by the OSA; 6) a NTC thermistor to monitor T_{0t}, because FBG sensors measure shift of λ_B during treatment, thus just ΔT. FBG sensors were already statically calibrated at ENEA Centro Ricerche Frascati (c_T=0.01 nm·°C^{-1}). A schematic representation of sensors placed around the applicator is also shown in Fig. 4.4. Six FBG sensors have been placed at three fixed distances, i.e. 5 mm, 10 mm and 15 mm from the applicator, in a symmetrical configuration, with the same orientation of the bare fiber tip, and realizing the alignment of gratings centers with the fiber tip. Each FBG sensor has been inserted into the pancreas guided with a needle (20 gauge) that has been removed before the treatment. Experimental trials have been performed at P=3 W and P=6 W, because these values appeared to lead interesting results in pancreatic injured volumes: at 1.5 W the laser beam can produce just coagulated lesion; at 10 W the high value of V_v could cause a break of the FBG sensor being T≥100 °C. Pancreas initial temperature in each trial was 20 ± 1 °C.

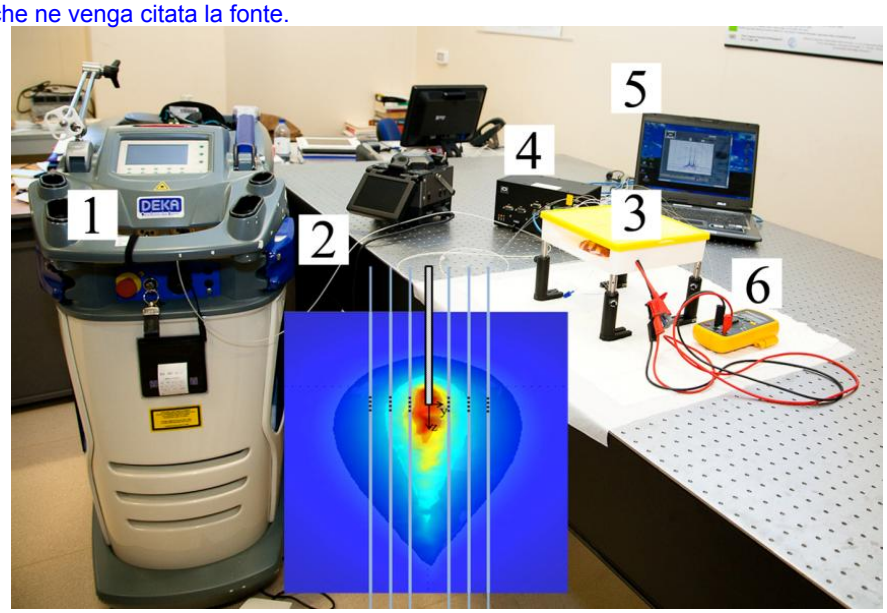

Figure 4.4. Experimental set up realized for temperature measurements of porcine *ex vivo* pancreas undergoing LA: 1) laser Nd:YAG, 2) laser fiber, 3) mask containing pancreas and FBG sensors, 4) OSA, 5) pc for data collection, 6) NTC thermistor. A schematic representation of FBG sensors placed inside the pancreas is reported.

The spatial FBG configuration allows to monitor T(x,y,z,t) in *ex vivo* pancreas undergoing LA. Experiments show that the longer is the distance between sensor and applicator, the lower is the local temperature increase. For example, at the end of the procedure with P=3 W, for y=5 mm, FBG sensors measured ΔT is about 25 °C. On the other hand, at y=10 mm the measured ΔT is about 10 °C, and at y=15 mm ΔT is about 6 °C. If P=6 W, at y=5 mm we measured ΔT of about 50 °C, at y=10 mm of about 7 °C, and at y=15 mm of about 2 °C.

Experimental results were compared with theoretical ones, obtained by the physical model described in Par. 2.2: results are reported as ΔT and then compared as function of time (Fig. 4.5). Some preliminary considerations about the extraction of T(x,y,z,t) values are necessary to compare theoretical results with experimental ones. Since FBG sensors have 1 cm grating length, they do not measure punctual T, but average out T(x,y,z,t) on the whole sensitive length. Hence, physical dimension of FBG sensors must be also considered in theoretical evaluation of T: theoretical punctual T(x,y,z,t) values have been averaged out on 1 cm length, and these results have been compared with FBG outcomes.

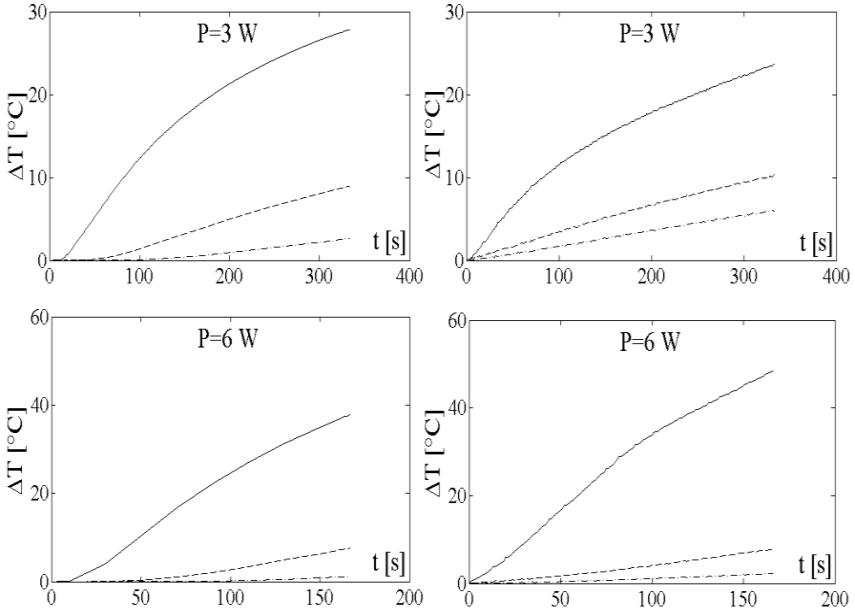

Figure 4.5. Comparison between theoretical (left side) and experimental (right side) temperature in *ex vivo* pancreatic tissue at distances of 5 mm (continuous line), 10 mm (dashed line) and 15 mm (dash-dotted line) from the applicator with 3 W and 6 W laser power as a function of time.

A relevant evidence from experimental data is the effect of treatment duration (t_1) on thermal pancreas response: at P=6 W, the experimental ΔT at 5 mm is higher than ΔT at 3 W (50 °C vs 25 °C), but at high distance ΔT at 6 W are lower than the ones at 3 W (e.g., 7 °C vs 10 °C at 10 mm, 2 °C vs 7 °C at 15 mm), in agreement with theoretical prediction. This phenomenon may be explained by considering that, the higher is P, the lower is the time of laser irradiation (t_l) at constant energy (1000 J) - Table I-, therefore, at high power values, time is too short to let heat conduction in sites quite distant from the laser application point, but the local effect close to the fiber tip produces a significant increase of temperature.

The comparison between theoretical and experimental data is expressed by percentage variations of T(x,y,z,t) between the distances of 5 mm and 10 mm, and between 10 mm and 15 mm, as reported in Table I:

$$\Delta T\%(d_1 \rightarrow d_2) = \frac{|T(d_1) - T(d_2)|}{T(d_1)} \cdot 100 \tag{4.4}$$

Where $T(d_1)$ and $T(d_2)$ are temperatures reached at the end of the procedure at distance of d_1 and d_2 from the applicator respectively.

Table I: Comparison between theoretical and experimental ΔT% at different distances from the applicator at 3 W and 6 W

P	E	t_l	Theoretical values	Experimental values
3 W	1000 J	333 s	ΔT%(5 mm→10 mm)=68 %	ΔT%(5 mm→10 mm)=60 %
3 W	1000 J	333 s	ΔT%(10 mm→15 mm)=66 %	ΔT%(10 mm→15 mm)=42 %
6 W	1000 J	167 s	ΔT%(5 mm→10 mm)=80 %	ΔT%(5 mm→10 mm)=84 %
6 W	1000 J	167 s	ΔT%(10 mm→15 mm)=87 %	ΔT%(10 mm→15 mm)=74 %

Table I shows a quite good agreement between theoretical and experimental data (e.g., the percentage variation between 5 mm and 10 mm is 68 % and 60 % at 3 W, and 80 % and 84 % at 6 W for theoretical and experimental values respectively). In both cases, experimental and theoretical results are in agreement with t_l value on the thermal profile: ΔT%(5 mm→10 mm) and ΔT%(5 mm→10 mm) at 6 W are higher than the corresponding variations at 3 W: the high value of P produces a considerable heating in the small volume closest to the fiber tip, but t_l is not long enough to let surrounding volumes heat as the treatment with 3 W.

Previous studies present the assessment of temperature profile in tissues undergoing LA, using FBG sensors [15] and thermocouples [16], although none in pancreatic tissue. FBG sensors [15] are used to monitor a treatment with laser source of 532 nm on fresh porcine liver at P=1 W: after 93 s a T of about 63 °C has been measured close to the applicator tip, but the exact distance is not reported.

Thermal effects of Nd:YAG on tissue (i.e., tongue) have been measured by Lippert *et al.* [16] using thermocouples: temperature increases have been measured at four distances from the applicator tip (from 6 mm up to 15 mm), and at a single P value (i.e., 5 W). They measured ΔT values in quite good agreement with our results, even if thermocouples can introduce some heat sinking due to thermal conduction and artifacts (cfr Paragraph 4.2). For example their results at 6 mm and P=5 W are comparable with the values obtained in the present study at 5 mm and 6 W (44 °C vs 50 °C).

The small difference between data obtained in present study and the ones reported in literature can be considered acceptable, regarding that different tissues have been investigated, and ΔT has been measured at different distances from the heating source and power settings.

4.1.5 FBG with length of 1 mm: static calibration

The static calibration of twelve FBGs was performed in order to obtain the value of coefficient c_T, and to express the relationship between $\Delta\lambda_B$ and ΔT, according to equation (3), where $\varepsilon=0$.

The temperature was adjusted and changed in the range 20 - 80 °C inside a thermostatic chamber (B.E. 77, BICASA), and two silicon band-gap sensors were used as temperature references (LASCAR ELECTRONICS EL USB-2-LCD, accuracy of ±0.5 °C).

$\Delta\lambda_B$ as a function of ΔT between 0 and 60 °C for the FBGs is shown in Fig. 4.6.

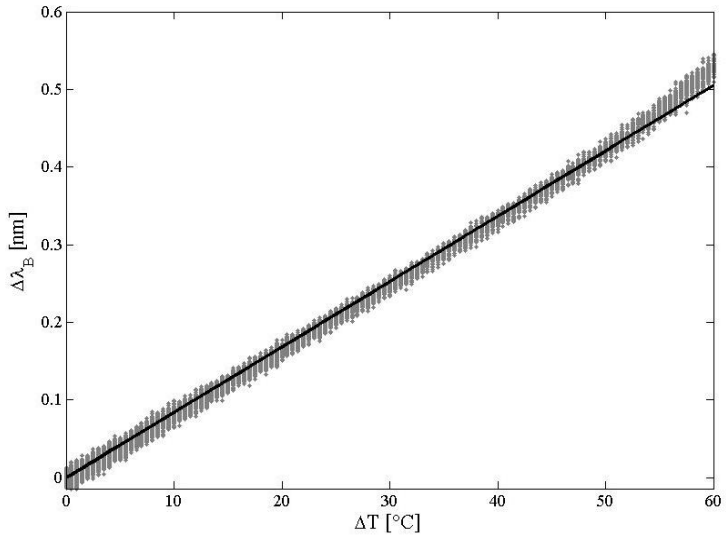

Figure 4.6: Static calibration of FBGs. The figure shows the linear trend of experimental $\Delta\lambda_B$ as a function of ΔT (gray circles) and the linear calibration curves (black line).

The calibration curve is obtained by a linear fit of the data using the least mean squares error algorithm. The range of $c_{\Delta T}$ values, estimated by fitting the experimental data with a level of confidence of 95%, is $c_{\Delta T}= 0.008417 \pm 0.000004$ nm·°C^{-1}.

4.1.6 FBG with length of 1 mm to measure pancreas temperature distribution during Laser Ablation

This study presents the temperature monitoring in an *ex-vivo* porcine pancreas undergoing double-applicator LA, and the comparison with theoretical predictions [17].

A continuous-wave radiation (λ = 1064 nm), emitted by means of a Nd:YAG laser, is conveyed within two bare fiber-optic applicators consisting of a quartz optical fiber with a 300-µm core diameter. The tips of the two applicators are placed parallel to each other inside the *ex vivo* healthy porcine pancreas, at a distance of 4 mm between their centers (Fig. 4.7A and 4.7B).

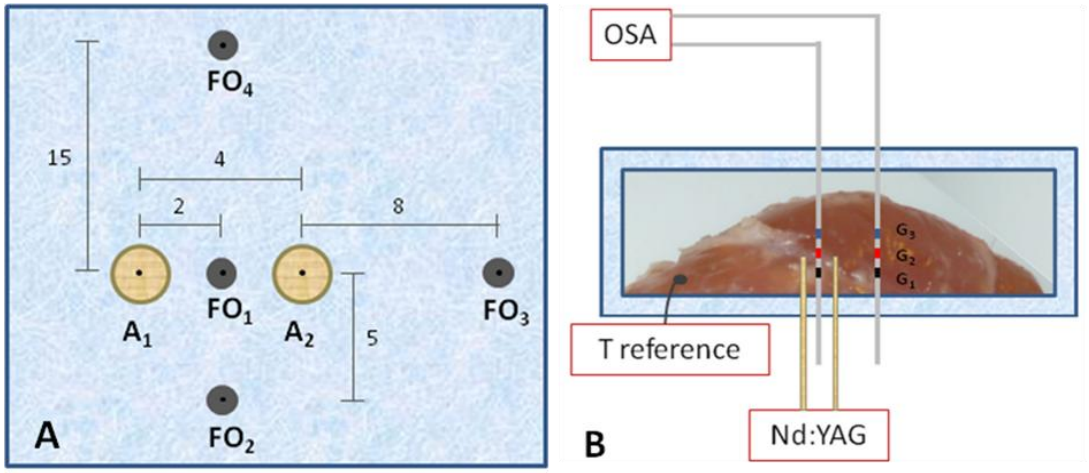

Figure 4.7. Schematic representation of the relative position between the two applicators A_1 and A_2 and the fiber where the FBG sensors are mounted. A) Top view: configuration and relative distances (expressed in mm) among A_1, A_2 and the four optical fibers FO_1, FO_2, FO_3 and FO_4, housing temperature sensors; B) Position of the three FBG mounted on each fiber: one is positioned 2 mm upward from applicators tip (black), one is aligned with tips (red), and one is placed 2 mm downward from the tips (blue). Reference temperature sensor is shown.

The adopted experimental set up is similar to the one presented in Fig. 4.4. $\Delta\lambda_B$ is detected by an Optical Spectrum Analyzer, OSA, (Optical Sensing Interrogator, sm125, Micron Optics) with four channels, each of them connected to one fiber. To distinguish the output of each Bragg grating equipped in one fiber, they are characterized by three different λ_B, i.d., 1533 nm, 1541 nm and 1549 nm, at 23 °C (Technica SA, Beijing Operation, P.R. China, Fig. 4.2). Experimental data acquired by the OSA, with a sampling frequency of 250 Hz, are sent to a PC. Finally, an NTC thermistor, with output picked up by a multimeter (Fluke 179, Digital Multimeter) is used to monitor the pancreas temperature before starting treatment (20 ± 1 °C).

Fig. 4.7A schematically reports the experimental configuration. The four fiber-optics (FO) with three FBG sensors each (G_1, G_2 and G_3) are set at four fixed distances from the two applicators A_1 and A_2: FO_1 is placed between A_1 and A_2, at a distance of 2.0 mm, FO_2 is set equidistant from A_1 and A_2 at a distance of about 5.4 mm, FO_3 is placed at 8.0 mm

from A_2 and FO_4 is set equidistant from the two applicators at a distance of about 15.1 mm. The centers of FO_1, FO_2 and FO_4 are aligned with each another, as are the centers of A_1, A_2, FO_1 and FO_3. Figure 4.7B represents the positions of the gratings within the same fiber, and their depth inside the pancreas. All G_1 of each fiber-optic line are placed 2 mm upward from the A_1 and A_2 tips (Fig. 4.7B, black color), all G_2 are placed at the same level of the A_1 and A_2 tips (Fig. 4.7B, red color), and all G_3 are positioned 2 mm downward from the A_1 and A_2 tips (Fig. 4.7B, blue color).

Experimental data have been compared to predictions from numerical simulations, based on the theoretical model reported in Paragraph 2.2. Experimental trials are performed during LA (500 s) and after stopping treatment (between 500 s and 1800 s) in order to monitor the temperature rise and tissue cooling phenomena in twelve sites around the applicators. Since the experimental tissue temperature is averaged on the whole FBGs length (i.e., 1 mm), the predicted temperature is calculated by averaging out the theoretical temperatures on 1 mm.

The adimensional parameter:

$$\tilde{T} = \frac{\Delta T}{\Delta T_{\max}} \tag{4.5}$$

where ΔT is the temperature increase calculated in the four mentioned time points, and ΔT_{max} is the maximum ΔT reached during the whole treatment between A_1 and A_2 (in correspondence of G_3 of the fiber FO_1, Fig. 4.7), is introduced.

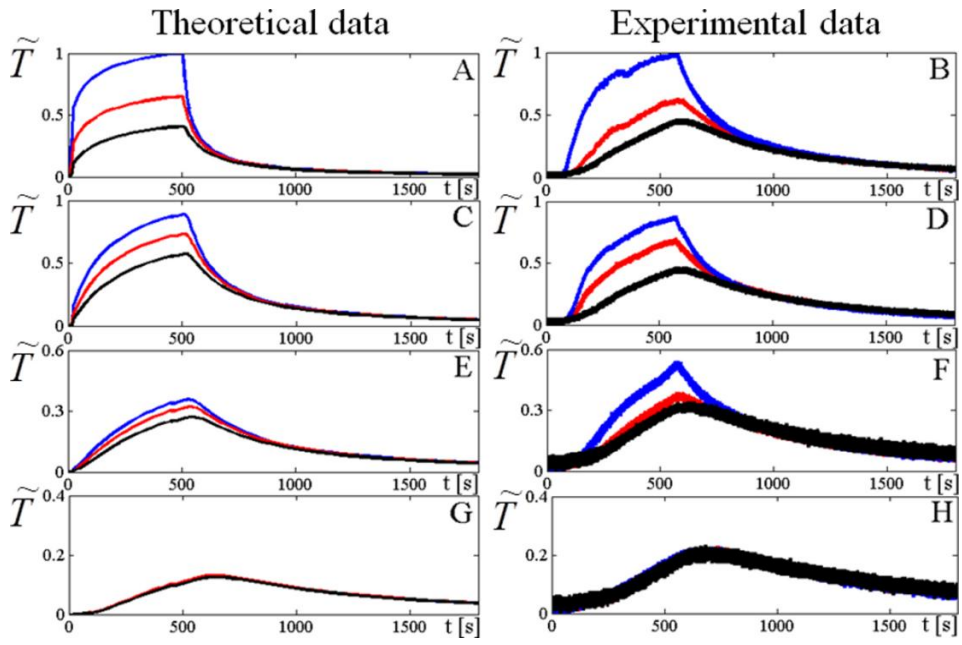

Figure 4.8. Distribution of $\tilde{T}$ in an ex vivo pancreas where the location of the FBG sensors correspond with the fiber positions FO1, FO2, FO3 and FO4: A, C, E, G) theoretically predicted; B, D, F, H) experimentally evaluated. Blue, red and black lines respectively represent the temperature calculated 2 mm downward, at the same level and 2 mm upward from the applicators.

Fig. 4.8A, C, E, G and 4.8B, D, F, H respectively illustrate the theoretical and experimental trends of $\tilde{T}$ within the pancreas in the regions where the FBG sensors are placed, during both the heating and cooling phases.

The ΔT_{max} measured by the twelve sensors are reported in Table II.

Table II. ΔT_{max} measured by the twelve sensors.

	FO_1 (d≈2 mm)			FO_2 (d≈5 mm)			FO_3 (d≈8 mm)			FO_4 (d≈15 mm)		
	G_1	G_2	G_3	G_1	G_2	G_3	G_1	G_2	G_3	G_1	G_2	G_3
ΔT_{max} [°C]	25	35	60	26	40	50	18	21	30	12	12	12

The maximum ΔT (ΔT_{max}) measured by G_3 placed on FO_2 is 50 °C, showing a good agreement with the results presented in [18], where a ΔT of 60 °C is measured at 6 mm in porcine *ex vivo* tongue undergoing LA. ΔT_{max} also agrees with the results reported in [14] where a slightly lower value is obtained at a distance of 5 mm with similar laser settings and using one applicator. This underestimation could be related to the different length of the FBGs used in the two studies. FBGs with length of 10 mm are employed in previous study (cfr. Paragraph 4.1.4), therefore the measured temperature are averaged out on 10 mm; indeed, the FBGs with length of 1 mm, employed in this study, allow to measure temperature with higher spatial resolution. This solution is particularly useful close to the applicator, where the thermal gradient is high (investigated in Paragraph 4.1.7). In the present study, values measured upward the applicators (by G_1) are lower than the values measured by the grating placed at the same level of the applicators (i.e., G_2) during the entire trial; the maximum values reached by ΔT in the experiments are respectively 35 °C versus 25 °C. A further increase is observable in temperatures monitored downward the applicators (by G_3). Furthermore, the trends obtained by the sensors placed on FO_2, FO_3 and FO_4 agree with the numerical results. The grating placed downward the applicators measured higher temperatures (blue lines in Fig. 4.8B) than the grating placed upward the applicators (black lines in Fig. 4.8B) as theoretically predicted (Fig. 4.8A). These differences increased when the distance from the applicators decreased.

As far as it concerns the correlation between theoretical and experimental data, the maximum temperature reached at the end of laser procedure can be considered. In particular, a linear regression between maximum variations of temperature (ΔT_{max}) obtained from both simulations and experiments have been performed. Figure 4.9 shows the relationship between experimental ΔT_{max} and theoretical ΔT_{max}.

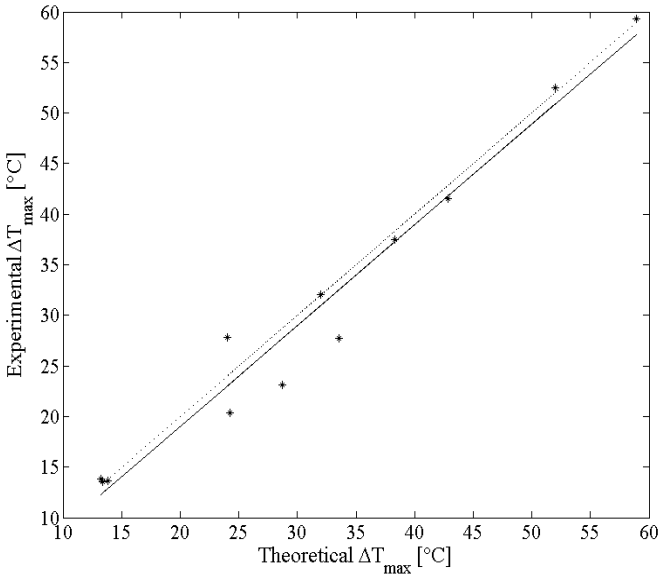

Figure 4.9. Agreement between theoretical and experimental data: the best fitting line (continuous line) is compared to the line of equality (dashed line).

The good agreement between theoretical and experimental data is confirmed by: 1) the high value of R^2=0.98 and 2) by the closeness of the best fitting line (continuous line) to the line of equality (dashed line) reported in figure. In fact, the slope of the best fitting line is close to 1 (i.e., 0.996).

4.1.7 Assessment of influence of FBG length on measurement of temperature

This study aims to assess the difference in T(x,y,z,t) measure and prediction due to different sensor length, and the advantage to employ small sensors (ideally punctual) [19].

T(x,y,z,t) measurement inside two *ex vivo* swine pancreases undergoing LA are performed as presented in Fig. 4.10, by means of twelve FBGs (Technica SA, Beijing Operation, P.R. China, Fig. 4.2). The polymeric mask houses sensors at known distances from the applicator tip (2 mm, 5 mm and 10 mm, for both experiments, Fig. 4.11). Applicator and sensors are parallel each other. Temperature has been measured with two modalities:

1) three FBGs with 10 mm of length placed at different distances from the laser fiber applicator tip (2 mm, 5 mm and 10 mm) -Fig. 4.10, left side;

2) nine FBGs 1 mm-long (three embedded in three different fibers) placed at the same distances from tip, but at different quotes (0 mm, and 2 mm and 4 mm downward the applicator) -Fig. 4.10, right side.

Experimental set up is similar to the one displayed in Fig. 4.4, and the theoretical data have been extracted from simulations performed according to the model described in Paragraph 2.2.

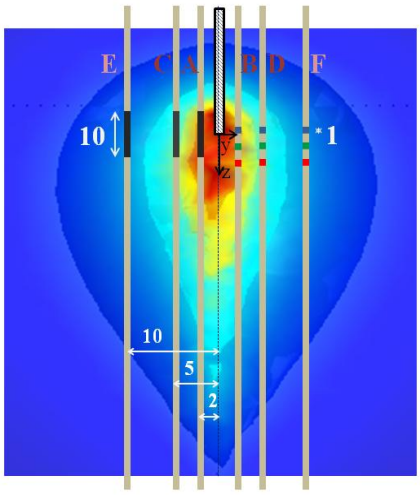

Figure 4.10. Schematic of FBGs arrangement in pancreas: FBGs 10 mm-long (left side) and FBGs 1 mm-long (right side). Lengths are expressed in mm.

Theoretical results: Theoretical T(x,y,z,t) provided by the numerical model is obtained by averaging out on 10 mm and 1 mm the theoretical temperatures in correspondence of gratings position in experiments. Results are reported in Fig. 4.11. As expected, ΔT predicted by averaging the theoretical T(x,y,z,t) on 10 mm is lower than the one obtained by averaging on 1 mm. It happens because the temperature gradient inside a tissue undergoing LA is high. In fact, the tissue can experience a steep variation of ΔT along 10 mm as demonstrated by temperature modeling on 1 mm. At 2 mm from the applicator, theoretical maximum ΔT (ΔTmax) registered at the end of irradiation are the following: predicted value on length of 10 mm (Fig. 4.11A) reaches about 145 °C, ΔTmax predicted on length of 1 mm ranges from 118 °C to 200 °C (Fig. 4.11B). The difference between the two configurations drops with the increase of the distance between the tip and the sensors, because temperature gradient decreases. As a matter of fact, at 5 mm the estimated ΔTmax averaged out on 10 mm (Fig. 4.11C) reaches 50 °C, whereas other

configuration shows ΔTmax ranging from 46 °C to 63 °C (Fig. 4.11D). At 10 mm distance from the tip, the difference is equal to a few degrees (8 °C *vs* a range of 9-11 °C, Fig. 4.11E-F).

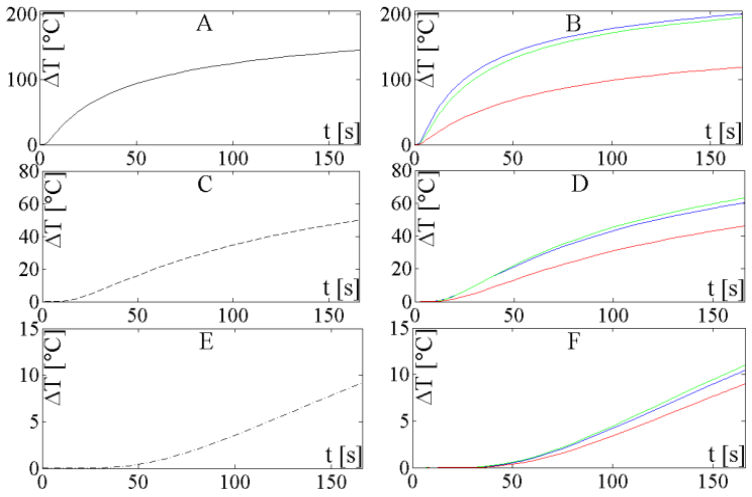

Figure 4.11. Theoretical ΔT in *ex vivo* pancreas during LA. ΔT averaged out on 10 mm of length at 2 mm (A), 5 mm (C) and 10 mm (E) from applicator tip; ΔT averaged out on 1 mm of length at 2 mm (B), 5 mm (D) and 10 mm (F) from applicator tip, at three quotes: 0 mm (blue line), 2 mm (green) and 4 mm (red).

Experimental results: Theoretical trends are confirmed by experimental data (Fig. 4.12). FBG 10 mm-long at 2 mm from the applicator measures a ΔTmax of 62 °C (Fig. 4.12A), whereas ΔTmax monitored by three FBGs 1 mm-long ranges from 40 °C to about 74 °C (Fig. 4.12B). At 5 mm, FBG 10 mm-long records 48 °C (Fig. 4.12C) *vs* the range 35-48 °C showed by smaller sensors (Fig. 4.12D). Lastly, at 10 mm from the applicator tip, in configuration 1 (Fig. 4.10, left side) sensor measures less than 8 °C (Fig. 4.12E), whereas in configuration 2 (Fig. 4.10, right side) FBGs record ΔTmax ranging from about 4 °C up to 8 °C (Fig. 4.12F).

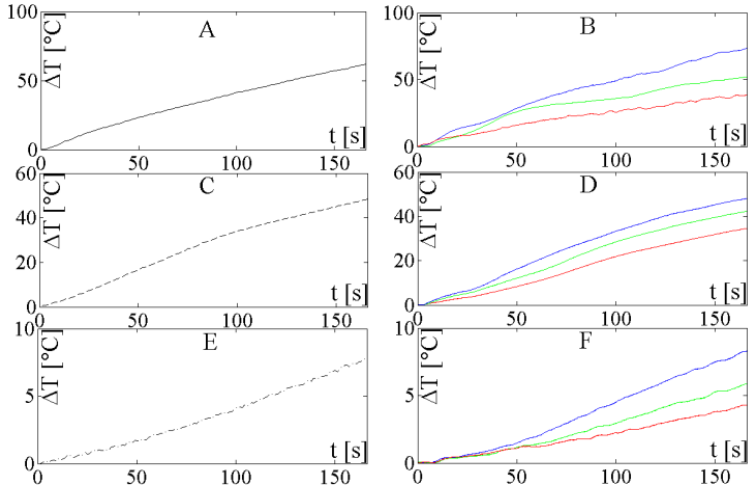

Figure 4.12. Experimental ΔT in *ex vivo* pancreas during LA. ΔT averaged out on 10 mm of length at 2 mm (A), 5 mm (C) and 10 mm (E) from applicator tip; ΔT averaged out on 1 mm of length at 2 mm (B), 5 mm (D) and 10 mm (F) from applicator tip, at three quotes: 0 mm (blue line), 2 mm (green) and 4 mm (red).

Since a laser-irradiated tissue presents a high spatial temperature gradient in a limited region surrounding the applicator (diameter up to 3 cm [20]), the ideal sensor for temperature estimation should be punctual. This study demonstrates that a small sensor (i.e., FBG 1 mm-long) is more suitable when the region of interest is close to the applicator tip (e.g., 2 mm). As a matter of fact, differences between sensors with length of 10 mm and 1 mm reduce at higher distance (e.g., at 10 mm, both FBGs measure ΔTmax up to 8 °C), as also predicted by the theoretical model. The difference between measurements and predictions close to applicator (Fig. 4.11A and B, and Fig. 4.12A and B) is higher than the other data at 5 mm and 10 mm. This is probably due to the weakness of the model in the description of real physical and chemical transformations occurring within the tissue when the temperature reaches and overcomes 100 °C. As a matter of fact, the model considers the phenomenon of evaporation (Equations 2.8-2.9), but other phenomena like carbonization and melting of the tissue should be taken into account to perform a more accurate prediction.

At the best of my knowledge, this is the first study which theoretically and experimentally assesses the influence of sensors size on temperature measurements during LA.

FBGs have been used during my PhD Program also as reference thermometers during images-based thermometry (cfr Chapter 5).

4.2 Thermocouples

4.2.1 Working principle

A thermocouple is composed by two different metal wires spot welded in two junctions, where an electromotive force is generated. One junction is placed at known reference temperature, whereas the other is used to measure the unknown temperature. Its principle of working is based on the Seebeck effect: in a closed loop configuration, the current flowing within the loop is proportional to the difference of temperature between two junctions. In open loop configuration, it is possible to measure the voltage, which is a non-linear function of the temperature difference between the two junctions.

Thermocouples are moderately accurate (up to 2 °C), and their small size results in a rapid response time, varying from tens of microseconds to tens of milliseconds. Moreover, thermocouple are mostly cost-effective, which makes them one attractive and widely used thermometer. Upon all the type of thermocouples, based on the couple of metals used, the most common is the K-type, whose conductors are Nickel-Chrome and Nickel-Aluminum. The operation range varies from producers but generally is comprehended in the range from -100°C to 300°C. The sensitivity of this sensor is about 41μV/°C, therefore amplification and noise filtering are required.

4.2.2 Artifact removal for application in Laser Ablation: state of the art

The issues related to temperature monitoring by thermocouples, during hyperthermia induced by RF and microwaves, were investigated since seventies by Christensen [21] and, afterwards, by Manns [22]. During LA, the two conductors, usually embedded in a thin needle, strongly absorb the laser radiation, inducing an error in the temperature measurement. In addition to the invasiveness, the main concern in the use of thermocouple during LA is the mentioned measurement error, resulting in a significant overestimation of the actual surrounding tissue temperature [23].

A deep investigation of the overestimation caused by the strong absorption of laser light by thermocouple was carried out by Anvari *et al.*, who showed that the increase of temperature due to the direct absorption of laser radiation by thermocouple is almost instantaneous [24]. The magnitude of the artifact was considered to be the rise, or drop, of the temperature when the laser was turned on, or off. In order to better evaluate the artifact amplitude the laser was continually turned on and off and then an average on its value on several trials was performed, as shown in Figure 4.13A.

A later study reports a technique to quantify and correct the artifact. The temperature rise has been split in two different phenomena: one due to light absorption by the thermocouple and the other one due to the light absorption by the tissue. The resulting equation for temperature rise assumed the form:

$$T_m(t) = A\left(1 - e^{-\frac{t}{\tau}}\right) + B \cdot t \qquad (4.6)$$

Where T_m is the temperature measured and A, B and τ are constant which assume a different value for each thermocouple. The exponential term represent light absorption by thermocouple and the linear term represent light absorption by the tissue. From this study it

emerges that the thermocouple artifact can reach value up to 18°C, so its correction is crucial. Few years later, Manns *et al.* analyzed the overestimation of temperature caused by the direct radiation absorption of the thermocouple in water, intralipid, and porcine tissue at different distances from the optical fiber applicator [22]. Reid *et al.* [25] analyzed temperature differences measured by thermocouples and fluoroptic probes at different distances from a cylindrical applicator emitting laser radiation at 810 nm. They applied laser light to different materials (i.e., air, water, and agar-albumin phantom) and in the agar-albumin phantom recorded a maximum temperature difference between the values measured by thermocouple and flouroptic sensor during the laser application of about 10°C. Recently, van Nimwegen *et al.* also performed temperature monitoring with thermocouples during Nd:YAG laser treatment on canine prostate (Fig. 4.13B). They also showed a relevant artifact due to the direct absorption and erased the temperature increase with short response time to correct it [26]. The correction was applied only to the tissue cooling curve: since the response time for laser-induced temperature change is much faster for the small thermocouple probes compared to tissue, they separated the thermocouple response from the tissue response; the resulting temperature has been assumed to be an exponential function, as in equation

$$T_m(t) = A+Be^{-Ct} + De^{-Et} \tag{4.7}$$

being A, B, C, D, E constant parameters. The corrected tissue cooling curve was obtained removing the exponential referred to the thermocouple.

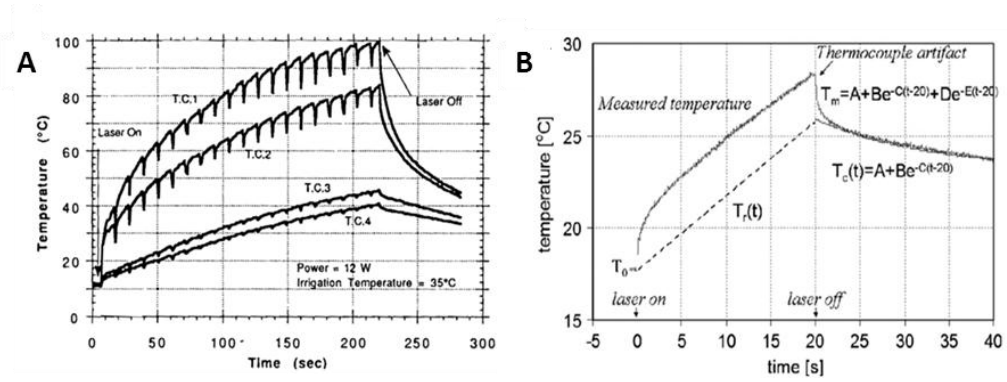

Figure 4.13. Temperature measured during LA by thermocouples: A) thermocouple artifact when laser is turned on and turned off [26]; B) temperature increase measured by thermocouples (T.C.) at different distances from the applicator: T.C.1 at 2 mm, T.C.2 at 4 mm, T.C.3 at 6 mm, and T.C.4 at 10 mm [24].

4.2.2 Experimental trials

Some experimental trials have been performed to quantify the artifact on thermocouples during LA on pancreas. Preliminarily, the tissue has been irradiated with laser power of 2 W for 150 s, and three thermocouples (K-type) were placed at controlled and different distances from the applicator tip (at 3 mm on the same axis, and at 0, 2 and 4 mm from the axis, with a quote of 3 mm, Fig. 4.14B). Results are shown in Fig. 4.14A:

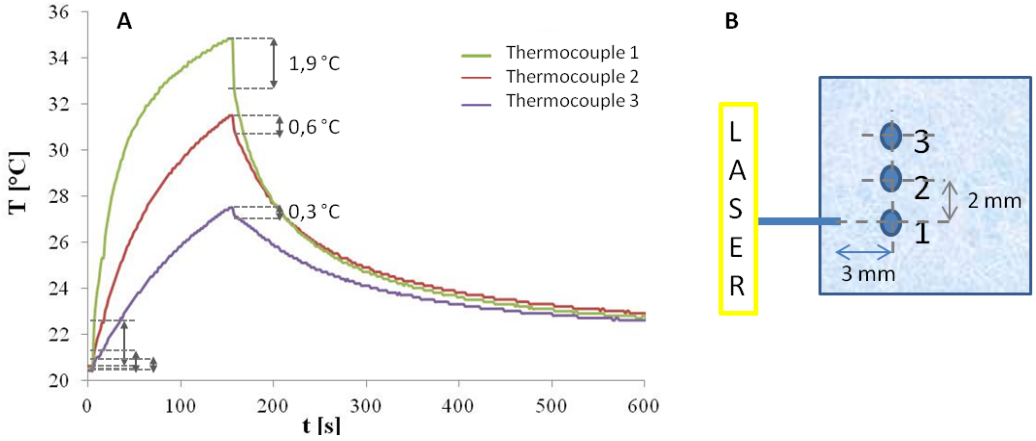

Figure 4.14. A) Trends of temperature in pancreas undergoing LA. Artifacts on thermocouples measurements are present both in correspondence of laser-on and laser-off. B) Placement of thermocouples.

In correspondence of laser-on (t=0 s), all the thermocouples show an immediate increment of temperature, due to the direct absorption of laser light. Obviously, the value of the artifact is function of distance between applicator and sensors: the higher the distance, the lower the artifact. It happens because the number of photons absorbed by the tissue increases with the distance from light source therefore, at higher distances (depending also on the laser power), the thermocouple is not hit significantly. Furthermore, at high distances, the phenomenon of thermal conduction is dominant on the light absorption of thermocouple.

A set of measurements on swine pancreatic tissue have been carried out to evaluate the abovementioned artifact [27]. Experimental set up included the Nd:YAG laser system (1064 nm), three K-type thermocouples, a PMMA (poly methyl methacrylate) mask to control the distances between thermocouples and applicator (Fig. 4.15A), a 4-channel data acquisition system (FX100, Yokogawa, sample frequency of 0.5 Hz, Fig. 4.15B) to convert, visualize and store the output of thermocouples, and surgical needles to insert sensors within pancreas. The laser has been turned on for 10 s and the turned off for 30 to 60 s, in order to keep the temperature under 55 °C and to minimize tissue vaporization.

Two power values (1.6 W and 2.0 W) have been set in order to assess the influence of the laser power on the magnitude artefact, and experiments have been carried out positioning thermocouples at various distances and angles due to the significant variation of the error magnitude (Fig. 4.15C).

Figure 4.15. A) Swine pancreas in PMMA mask and inserted thermocouples and applicator; B) Thermocouples acquisition module; C) Schematic of positioning of thermocouples.

The Table III summarizes values of distances, d, and angle, θ, between applicator tip and thermocouples:

Table III. Values of d and θ for the 18 positions.

	Distance d (mm)	Angle θ (°)
Positions 1-5	5.0	53.1
Positions 2-4	3.6	33.7
Position 3	3.0	0
Positions 6-10	6.4	38.7
Positions 7-9	5.4	21.8
Position 8	5.0	0
Positions 11-15	8.1	29.7
Positions 12-14	7.3	15.9
Position 13	7.0	0
Position 16	10.0	0
Position 17	12.0	0
Position 18	15.0	0

The following Fig. 4.16 presents trends of temperature measured by thermocouples in position 3, 8 and 13 (Fig. 4.15C). As previously explained, in order to better evaluate the artifact amplitude the laser was continuously turned on and off and, then, an average on its value on several trials was performed.

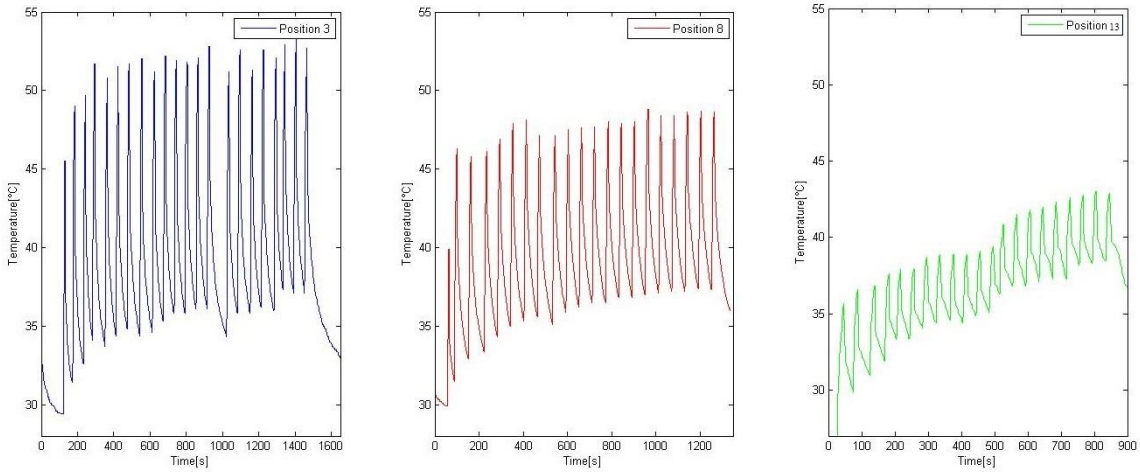

Figure 4.16. Trends of temperatures and artifacts on thermocouples in position 3, 8 and 13 during LA on swine pancreas, at P=1.6 W.

Table IV reports experimental data at several distance and angle, and two laser power. Position of thermocouples substantially influences the magnitude of the artefact. Values from symmetrical positions have been considered as one position in order to mediate the differences due to the tissue anisotropy.

Table IV. Mean and standard deviation (SD) for the artifact at P=1,6W and P=2,0W.

	Distance d [mm]	Angle θ [°]	Mean [°C] 1.6 W	SD [°C] 1.6 W	Mean [°C] 2.0 W	SD [°C] 2.0 W
Position 1-5	5.0	53.1	1.0	0.1	1.9	0.3
Position 2-4	3.6	33.7	4.0	0.6	4.4	0.6
Position 3	3.0	0	9.1	0.8	14.0	2.0
Position 6-10	6.4	38.7	1.0	0.1	2.5	0.3
Position 7-9	5.4	21.8	2.0	0.2	3.0	0.4
Position 8	5.0	0	5.5	0.7	8.7	1.3
Position 11-15	8.1	29.7	0	/	0.9	0.2
Position 12-14	7.3	15.9	0.5	0.1	1.9	0.2
Position 13	7.0	0	3.0	0.3	4.0	0.4
Position 16	10.0	0	0	/	1.5	0.2
Position 17	12.0	0	0	/	0	/
Position 18	15.0	0	0	/	0	/

The relationship between the artifact magnitude and the distance has been experimentally assessed. Result of the fitting is shown in Figure 4.17 for P=1.6 W.

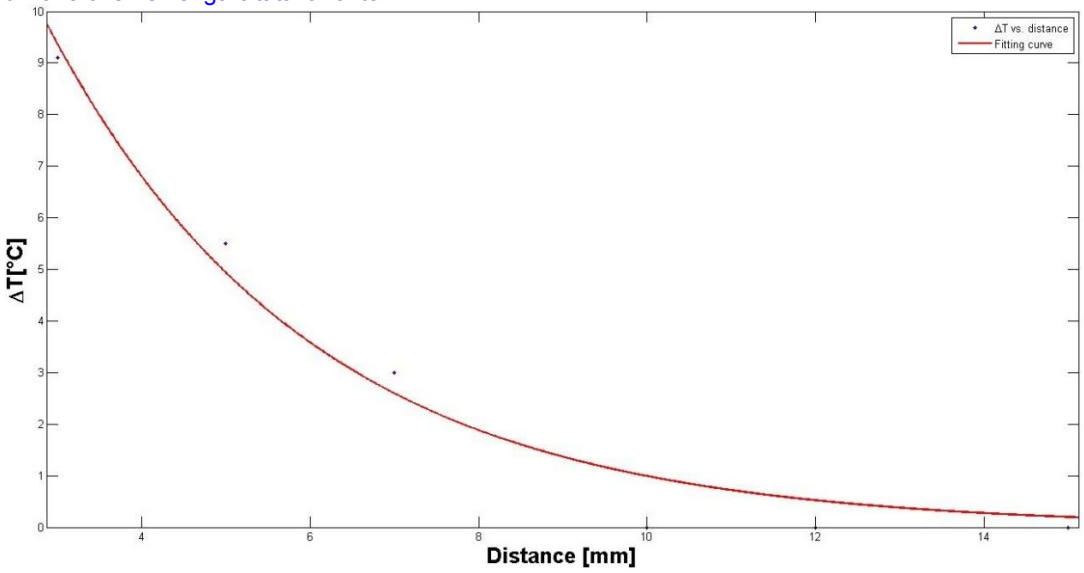

Figure 4.17. Fitting curve at P=1.6 W.

Experimental data have been fitted by the fitting curve:

$$\Delta T(d) = a \cdot e^{-b \cdot d} \tag{4.8}$$

where: a=24.5 °C, b=0.32 mm^{-1} for P=1.6 W (R^2=0.974) and a=36.0 °C, b=0.31 mm^{-1} for P=2.0 W (R^2=0.990).

Aiming to take into account also the influence of angle, a two-variable fitting has been calculated. Result of the fitting is shown in Fig. 4.18 for laser power of 1.6 W.

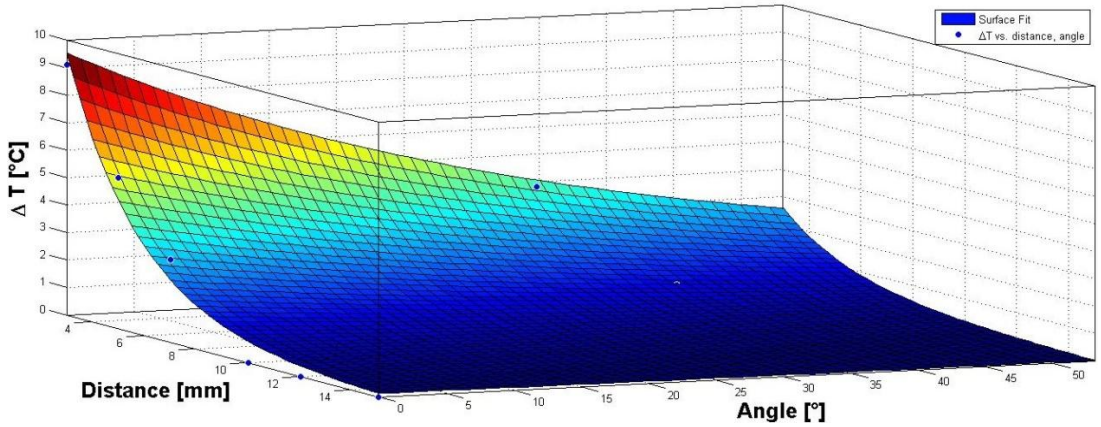

Figure 4.18. Surface Fitting at P=1,6W.

The curves that best approximate experimental data have the following form:

$$\Delta T(d) = a \cdot e^{-b \cdot d} \cdot e^{-c \cdot \theta} \tag{4.9}$$

Table V shows the values of the parameters, as well as the coefficients of determination (R^2) and the maximum error, considered as the absolute value of the maximum difference between the fitting function and the experimental data).

Table V. Parameters, R^2 and max. error values.

	a [°C]	b [mm^{-1}]	c [$°^{-1}$]	R^2	Max. Error [°C]
P=1.6 W	28.2	0.36	0.02	0.952	1.0
P=2.0 W	39.8	0.34	0.02	0.981	1.5

The correction significantly reduces the overestimation caused by the thermocouples' artifact. The comparisons between the error magnitudes before and after the correction at P=1.6 W and P=2.0 W are shown in Fig. 4.21 and 4.22, respectively.

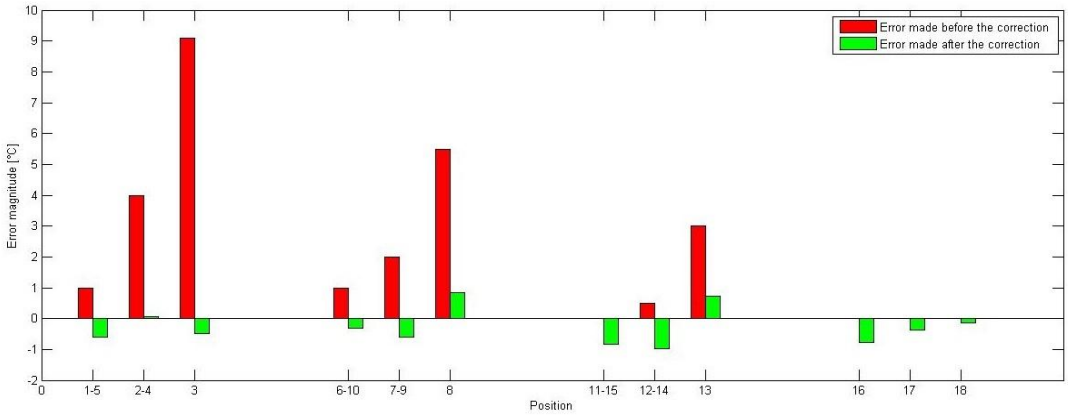

Figure 4.21. Error magnitude before (red) and after the correction (green) at P=1.6 W.

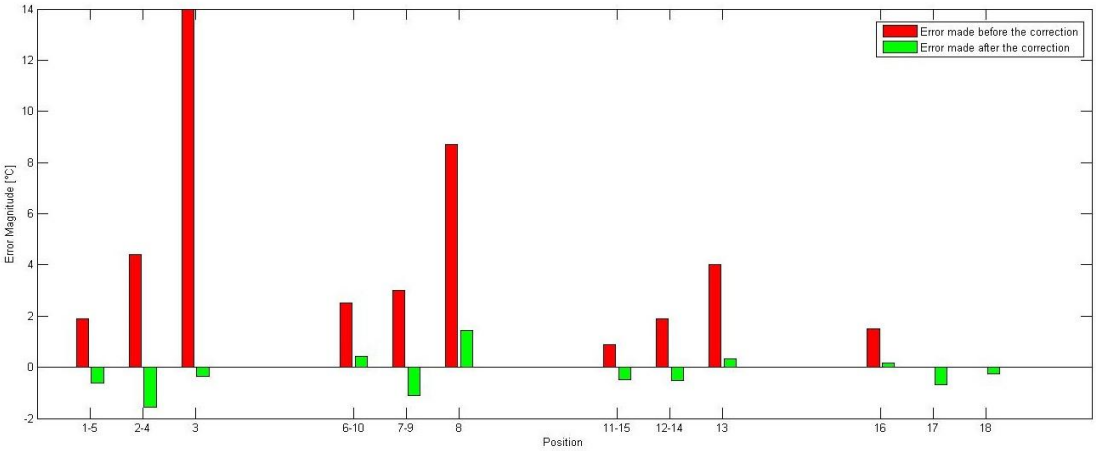

Figure 4.22. Error magnitude before (red) and after the correction (green) at P=2,0 W.

Means of the measurement errors have been calculated before and after the correction, in order to have another parameter that could express the goodness of the correction. The results are reported in Table VI.

Table VI. Means of the artifacts' magnitude before and after the correction.

	Mean (before the correction) [°C]	Mean (after the correction) [°C]
P=1.6 W	2.2	0.5
P=2.0 W	3.5	0.6

4.3 Fluoroptic probes

4.3.1 Working principle

Fluoroptic sensor technology, patented by Luxtron, now LumaSense Technologies (Fig. 4.23), is based on the fluorescence decay time of a special thermo-sensitive rare-earth phosphor (such as magnesium fluorogermanate activated with tetravalent manganese), located at the end of a fiber optic cable [28].

Figure 4.23 Luxtron Fluoroptic Thermometer: interrogation and acquisition module, and optical cable.

The decay time of the phosphor is function of temperature of the phosphor itself. An excitation light pulse generated by a Xenon flash lamp propagates through the fiber, and excites the phosphor layer at its extremity. The fluorescent signal produced by the exciting phosphor is sent back within the same fiber. After the excitation, the fluorescent signal decays with an exponential law, which depends on the temperature of the phosphor. The correlation between the decay time and the temperature of the phosphor estimates the temperature at the end of the fiber [29], Fig. 4.24.

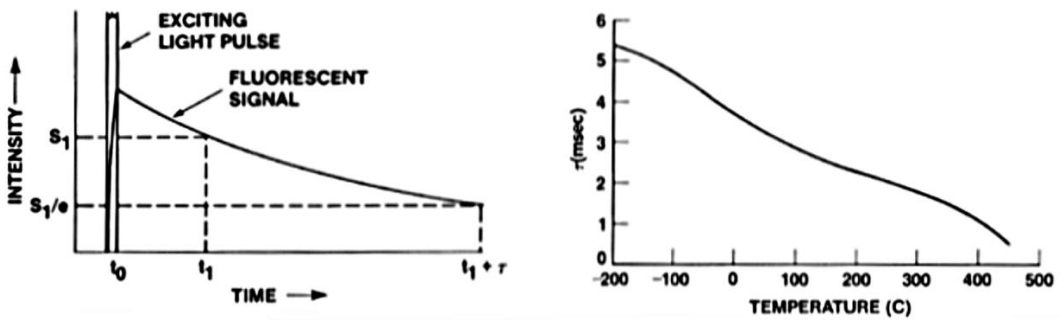

Figure 4.24 Left side: Fluorescent decay time of Phosphor sensor; decay time is the time between the initial measurement of signal level S1 and the signal level S1/e. Right side: phosphor temperature as function of temperature [28].

The valuable features of fluoroptic sensors are the following: 1) the wide range of measurement, typically from -25 °C to 300 °C; 2) the accuracy of 0.2 °C; 3) the immunity to electromagnetic interferences; 4) the inertness and biological compatibility; 5) the chance to realize a multi-sensors system by sharing the pulsed excitation source among several channels.

The characteristics of the phosphor do not depend on the intensity of excitation, therefore this typology of sensor is versatile to many applications and sensor designs. Furthermore, since the excitation light signal and the fluorescent decay signal travel along the same optical path, the size of the fiber optic probe and sensing tip can be reduced: diameter less than 0.5 mm can be an attractive feature in medical research applications.

4.3.2 Artifacts

Fluoroptic temperature sensors are widely used in LA, especially in MRI-guided hyperthermia. This is mainly due to MRI-compatibility. Since the estimation of temperature distribution within a tissue undergoing LA can be performed also by MR imaging, fluoroptic probes are also employed to provide the reference temperature in MRI thermometry calibration [30, 31]. Nevertheless, efforts are made to characterize the performances of fluoroptic sensors in thermometry during laser irradiation, because of the presence of measurement error, caused by the self-heating of fluoroptic sensors [30]. This artifact mainly depends on the black pigments in the coating of fluoroptic probe [32]. Reid *et al.* assessed that measurement error induced by self-heating of the fluoroptic probe in presence of laser irradiation (810 nm) cannot be neglected if the distance between the laser applicator and the sensor is less than 4 mm [25].

Hübner *et al.* [30] studied the influence of Nd:YAG (1064 nm) on Fluoroptic probes, comparing the temperature measurements performed by means of thermocouples and MRI thermometry. Experiments were carried out on *ex vivo* porcine liver and gel phantom liver mimic, undergoing LA with laser power of 30.8 W, guided within the media through diffuser tip, cooled applicator. Probes in the liver were placed at distances ranging from 6.8 mm to 14 mm from the applicator. Results are reported in the Fig. 4.25:

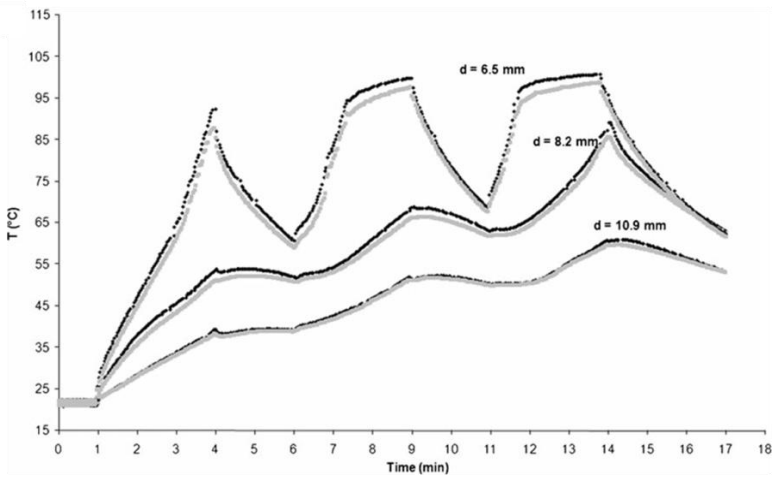

Figure 4.25. Temperature measurements in pig liver by fiber optics (black) and thermocouples (gray) at different distances from laser applicator [30].

The main difference between the measurements was found at 6.5 mm from the applicator, and of about 5 °C, in correspondence of the first laser-off (after 3 minutes from the start of irradiation), and decreases in correspondence of the following switching on and off, because of thermal effects of tissue. At 10.9 mm the difference between temperature measured by thermocouple and Fluoroptic is about 1 °C, and at 14 mm (not shown in Figure 4.25) the difference is almost negligible. Therefore, authors recommend to use Fluoroptic probes placed at distance of at least 1 cm from the applicator, so that the measurements are not affected by artifacts. The use of Fluoroptic sensor during LA performed with Nd:YAG laser source (1064 nm) was motivated by the excitation spectrum of magnesium fluorogermanate phosphor, that ranges from 200 nm to 50 nm, and by its emission spectrum, ranging from 600 nm to 700 nm. Nevertheless, the influence of black pigments in the coating of fluoroptic probe at 1064 nm was not investigated.

In my research, Fluoroptic probes have been employed as reference thermometers during CT-scan thermometry. Experiments are carried out in Universitäts Klinikum,

Goethe-Universität Frankfurt am Main, under the supervision of Prof. Vogl, Dr. Bazrafshan, Dr. Paul and Eng. Hübner (cfr. Chapter 5).

Bibliography Chapter 4

[1] C. Cain and A. Welch, "Thin-film temperature sensors for biological measurements," *IEEE T Biomed Eng*, vol. 21, pp. 421-423, 1974.

[2] D. Christensen, "A new nonperturbing temperature probe using semiconductor band edge shift," *J Bioeng*, vol. 1, pp. 541-545, 1977.

[3] D. L. Parker, "Applications of NMR Imaging in Hyperthermia: An Evaluation of the Potential for Localized Tissue Heating and Noninvasive Temperature Monitoring," *IEEE T Biomed Eng*, vol. 31, pp. 161-167, 1984.

[4] B. G. Fellone, P. R. Moran and E. B. Podgorsak, "Noninvasive thermometry with a clinical x-ray CT scanner," *Med Phys*, vol. 9, pp. 715-721, 1982.

[5] Y. Rao, "In-fiber Bragg grating sensors," *Meas Sci Technol*, vol. 8, pp. 355-375, 1997.

[6] S. Silvestri and E. Schena, "Optical-Fiber Measurement Systems for Medical Applications," in *Optoelectronics- Devices and Applications*, InTech, Predeep P, eds, 2011, pp. 205-224.

[7] V. Mishra, N. Singh, U. Tiwari and P. Kapur, "Fiber grating sensors in medicine: Current and emerging applications," *Sensor Actuat A-Phys*, vol. 167, pp. 279-90, 2011.

[8] Y. J. Rao, "Recent progress in applications of in-fibre Bragg grating sensors," *Opt Laser Eng*, vol. 31, pp. 297-324, 1999.

[9] Y. J. Rao, B. Hurle, D. J. Webb, D. A. Jackson, L. Zhang and I. Bennion, "In-situ temperature monitoring in NMR machines with a prototype in-fibre Bragg grating sensor system.," in *Conf Proc OSA Optical Fibre Sensors*, 1997.

[10] Y. J. Rao, D. J. Webb, D. A. Jackson, L. Zhang and I. Bennion, "Optical in-fibre Bragg Grating Sensor System for Medical Applications," *J Biomed Opt*, vol. 31, pp. 38-44, 1998.

[11] D. J. Webb, M. W. Hathaway, D. A. Jackson, S. Jones, L. Zhang and I. Bennion, "First in vivo trails of a fiber Bragg grating based temperature profiling system," *J Biomed Opt*, vol. 5, pp. 45-50, 2000.

[12] E. Samset, T. Mala, R. Ellingsen, I. Gladhaug, O. Søreide and E. Fosse, "Temperature measurement in soft tissue using a distributed fiber Bragg grating sensor system," *Minim Invasiv Ther*, vol. 10, pp. 89-93, 2001.

[13] B. Gowardhan and D. Greene, "Cryotherapy for the prostate: an in vitro and clinical study of two new developments; advanced cryoneedles and a temperature monitoring system," *BJU Int*, vol. 100, pp. 295-302, 2007.

[14] P. Saccomandi, E. Schena, M. A. Caponero, F. M. Di Matteo, M. Martino, M. Pandolfi and S. Silvestri, "Theoretical analysis and experimental evaluation of laser induced interstitial thermotherapy in ex vivo porcine pancreas," *IEEE Transactions on Biomedical Engineering*, vol. 59, no. 10, pp. 2958-64, 2012.

[15] C. Li, N. Chen, Z. Chen and T. Wang, "Fully distributed chirped FBG sensor and application in laser-induced interstitial thermotherapy," *Proc. Spie*, vol. 7634, pp. 1-6, Nov. 2009.

[16] B. M. Lippert, A. Teymoortash, B. J. Folz and J. A. Werner, "Coagulation and temperature distribution in Nd:YAG interstitial laser thermotherapy: an in vivo animal study," *Lasers Med Sci*, vol. 18, no. 1, pp. 19-24, 2003.

[17] P. Saccomandi, E. Schena, F. Giurazza, R. Del Vescovo, M. A. Caponero, L. Mortato, F. Panzera, R. L. Cazzato, F. R. Grasso, F. M. Di Matteo, S. Silvestri and B. Beomonte Zobel, "Temperature monitoring and lesion volume stimatio during double-applicator laser induced thermotherapy in ex vivo pancreas: a preliminary study," *Laser Med Scie*, pp. 1-8, 2013.

[18] Y. Ding, N. Chen, Z. Chen, F. Pang, X. Zeng and T. Wang, "Dynamic temperature monitoring and control with fully distributed fiber Bragg grating sensor," *Proc SPIE*, vol. 7634, pp. 1-6, 2010.

[19] P. Saccomandi, G. Lupi, E. Schena, A. Polimadei, M. A. Caponero, F. Panzera, M. Martino, F. M. Di Matteo, S. Sciuto and S. Silvestri, "Influence of FBG sensors length on temperature measures in laser-irradiated pancreas: Theoretical and experimental evaluation," in *Proc. of Eng Med Biol Soc, EMBC*, Osaka, 2013.

[20] R. J. Stafford, D. Fuentes, A. A. Elliott, J. S. Weinberg and K. Ahrar, "Laser-Induced Thermal Therapy for tumor ablation," *Crit. Rev. Biomed. Eng.*, vol. 38, no. 1, pp. 79-100, 2010.

[21] D. A. Christensen., "Thermal dosimetry and temperature measurements," *Cancer Res*, vol. 39, pp. 2325-2327., 1979.

[22] F. Manns , P. J. Milne , X. Gonzales-Cirre, D. B. Denham, J. M. Parel and D. S. Robinson, "In situ temperature measurements with thermocouple probes during laser interstitial thermotherapy (LITT): quantification and correction of a measurement artifact. ;," *Laser Surg Med*, 1998.

[23] C. P. Cain and A. J. Welch, "Thin-film temperature sensors for biological measurements," *IEEE T Biomed Eng*, vol. 21, pp. 421-423, 1974.

[24] B. Anvari , M. Motamedi, J. H. Torres , S. Rastegar and E. Orihuela, "Effects of surface irrigation on the thermal response of tissue during laser irradiation," *Laser Surg Med*, vol. 14, pp. 386-395, 1994.

[25] A. D. Reid, M. R. Gertner and M. D. Sherar, "Temperature measurement artefacts of thermocouples and fluoroptic probes during laser irradiation at 810 nm," *Phys Med Biol*, vol. 46, pp. N149-N157, 2001.

[26] S. A. Van Nimwegen, H. F. L'Eplattenier, A. I. Rem, J. J. van der Lugt and J. Kirpensteijn, "Nd:YAG surgical effects in canine prostate tissue: temperature and damage distribution," *Phys Med Biol*, vol. 54, pp. 29-44, 2009.

[27] L. Majocchi, "Analysis of temperature distribution by thermocouple in porcine pancreas during laser thermotherapy: estimation and correction of measurement error," Roma, 2013.

[28] K. A. Wickersheim and M. H. Sun, "FiberOptic Thermometry and its Applications," *J Microwave Power*, vol. 22, pp. 85-94, 1987.

[29] K. T. Grattan and Z. Y. Zhang ZY, "FiberOptic Fluorescence Thermometry: An Introduction," in *FiberOptic Fluorescence Thermometry*, St. Edmundsbury Press (GB), 1995, pp. 1-34.

[30] F. Hübner, B. Bazrafshan, J. Roland, A. Kickhefel and T. J. Vogl, "The influence of Nd:YAG laser irradiation on Fluoroptic(R) temperature measurement: an experimental evaluation," *Laser Med Sci*, vol. 28, pp. 487-496, 2013.

[31] S. Puccini, N. K. Bär, M. Bublat, T. Kahn and H. Busse , "Simulation of Thermal Tissue Coagulation and Their Value for the Planning and Monitoring of Laser-Induced Interstitial Thermotherapy (LITT)," *Magnet Reson Med*, vol. 49, pp. 351-362, 2003.

[32] S. R. Davidson, I. A. Vitkin, M. D. Sherar and W. M. Whelan, "Characterization of measurement Artefacts in Fluoroptic Temperature Sensors: Implications for Laser Thermal Therapy at 810 nm," *Laser Surg Med*, vol. 36, pp. 297-306, 2005.

Chapter 5. Non-invasive images-based thermometry during Laser Ablation

5.1 Computed Tomography Thermometry

5.1.1 Physical basis

An image obtained by CT scan is composed by pixels (picture elements), which display the average x-ray attenuation properties of the tissue in the corresponding voxel (volume elements). A series of x-ray passes through the patient, and the transmitted rays reach the detectors after modulation. The intensity of transmitted x-ray depends on the linear attenuation coefficient, μ. A single image is obtained by the reconstruction of transmitted x-rays passing through the patient at a large number of orientations, called projections or views. At each pixel corresponds a raw data, representing the linear attenuation coefficient, which is processed and, finally, converted in CT number, also called Hounsfield Unit (HU). The CT number is obtained by the following relationship:

$$CT(x,y) = 1000 \cdot \frac{\mu(x,y) - \mu_W}{\mu_W} \tag{5.1}$$

where μ_W is the attenuation coefficient of water, and μ(x,y) is the average linear attenuation coefficient in the (x,y) voxel (Fig. 5.1).

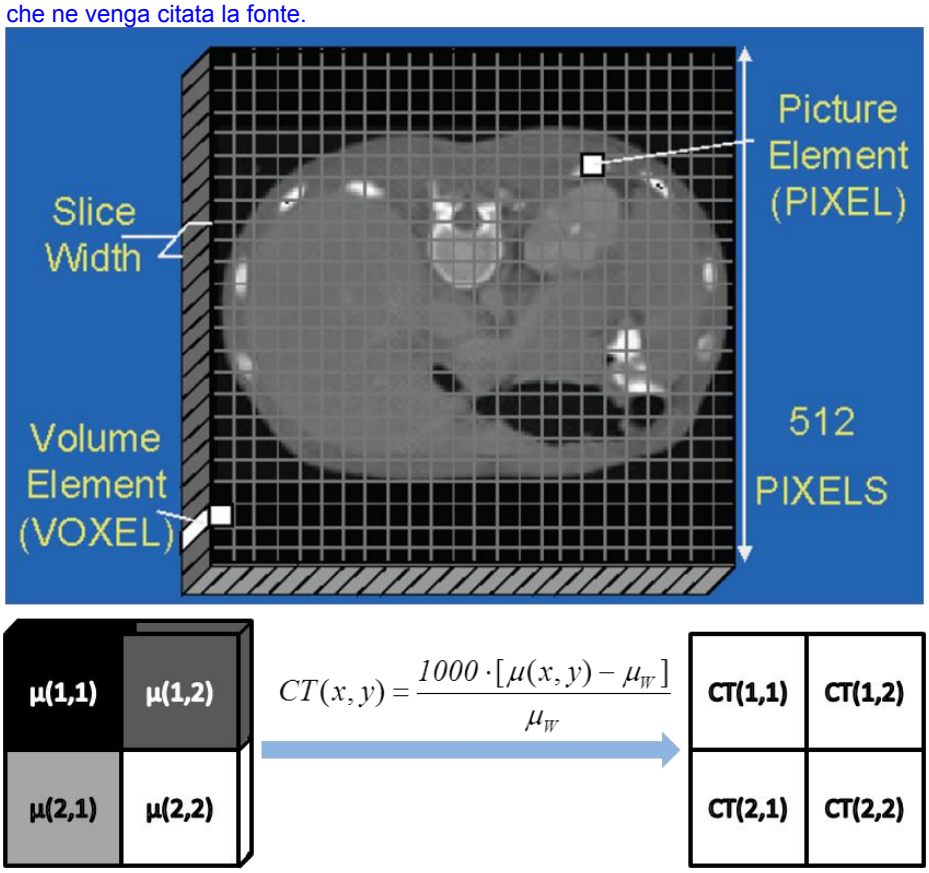

Figure 5.1: Computed Tomography image: features and definition of CT number as function of attenuation coefficient of tissue.

The μ(x,y) value depends on the phenomenon of interaction between tissue and x-ray. During CT scans this phenomenon is mainly due to the Compton scattering because of the high photon energy used. Therefore, the temperature dependence of physical parameters which influence the phenomenon of Compton scattering is the basis of the CT thermometry. A simplified description of the temperature influence on CT can be performed by considering that μ tracks linearly with the tissue physical density (ρ). Therefore, as schematically reported in Fig. 5.2, the phenomenon of thermal expansion explains the decrease of density when temperature increases, thus, the CT decrease with temperature.

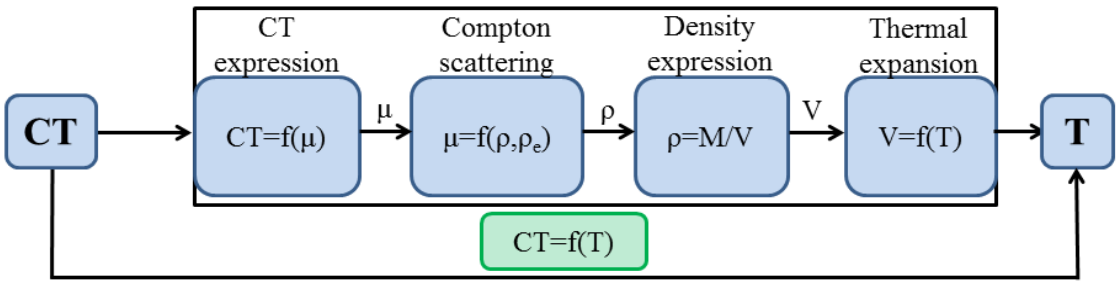

Figure 5.2: Principles of dependence of CT-number on temperature, because of the change of tissue density with temperature.

By following the schematic reported in Fig. 5.2, the change of μ depends on the phenomenon of thermal expansion; in fact, the density of a material, at a generic temperature, T, can be expressed as:

$$\rho(T) = \frac{\rho(T_0)}{1 + \alpha \cdot \Delta T} \tag{5.2}$$

being $\rho(T_0)$ the material density at a reference temperature (T_0), α the volumetric expansion coefficient, and $\Delta T = T - T_0$.

Since the mass attenuation coefficient (μ/ρ) does not depend on density, the dependence of μ with density, and, consequently with temperature, can be expressed as following:

$$\mu(T) = \left(\frac{\mu}{\rho}\right) \cdot \rho(T) \tag{5.3}$$

Considering the linear relationship between CT and μ, Equation 5.2 and Equation 5.3, and after performing a linearization based on Taylor series expansion in $\alpha\Delta T$ [1], it is obtained:

$$\Delta CT \approx -[1000 + CT(T_0)] \cdot \alpha \cdot \Delta T \tag{5.4}$$

where $\Delta CT = CT(T) - CT(T_0)$ is the difference between the CT variation, when temperature changes from T_0 to T.

The final outcome of the process should be the superimposition of temperature map on the CT images, as shown in Fig. 5.3:

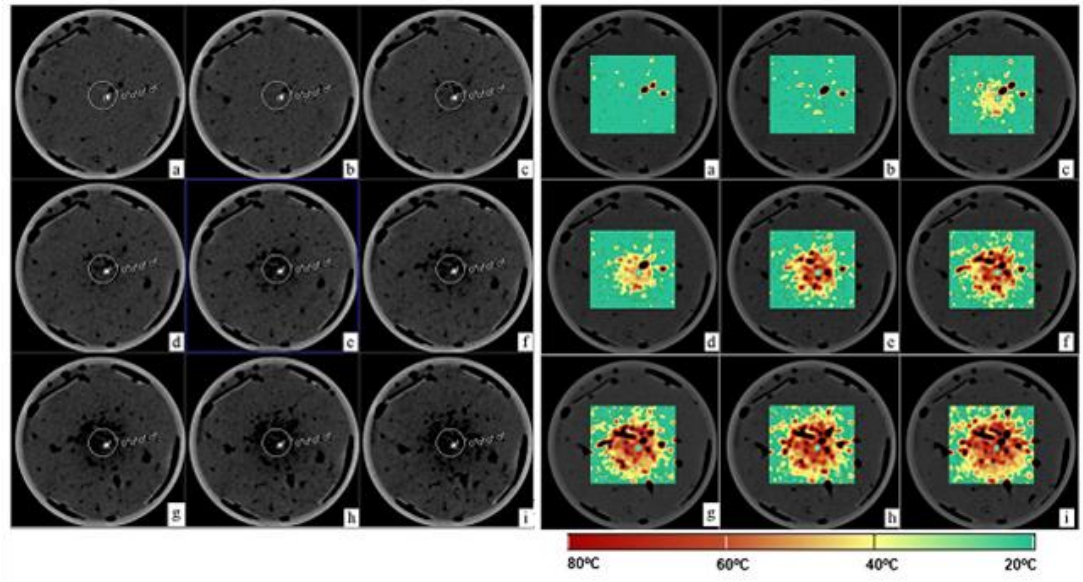

Figure 5.3: CT scan during Radiofrequency ablation in bovine liver (left side), and superimposition of evolving temperature distribution on images (right side) [2].

5.1.2 State of the art

During the last years a big research effort has been devoted in the development of CT-based thermometry for monitoring tissue temperature during hyperthermic treatment [3]. In the late seventies, Bydder and Kreel conducted a study regarding the influence of temperature on the calibration procedure of CT scanner, and the changes in water CT number with temperature were experimentally assessed [4]. A few years later, Fallone *et al.* [5] used the CT scanner to perform a non-invasive temperature estimation and proposed the introduction of this technique during hyperthermic treatments. Despite of the valuable characteristic of non-invasiveness, technical difficulties, mainly related to the reproducibility and spatial resolution of CT scanner, discouraged the widespread use of this technique except for calibration purpose [6]. Therefore, the CT-based thermometry sank in the oblivion, and only recent improvements of CT scanner performances have encouraged investigations on feasibility of this method to provide a feedback in hyperthermia dosimetry and some *ex vivo* and *in vivo* studies have been performed [7]. Undoubtedly, the patient's exposure to x-ray radiation is the most important issue in the use of a CT scanner. On the other hand, it is important to remark that the mostly palliative character of hyperthermia treatment in patients with limited life expectancy and the acceptable radiation exposure of healthy organs which are adjacent to the organ

undergoing LA needs also to be considered in the analysis of feasibility of CT-based thermometry, as also reported by Bruners *et al.* [8]. These characteristics with the non-invasiveness make attractive the use of CT-based thermometry during LA in some particular cases.

Some investigations have been carried out on the feasibility of the CT thermometry in temperature monitoring during hyperthermia. In the early 1980s, Fallone *et al.* [5] published for the first time the CT decrease with temperature of biological tissue (i.e., muscle). The temperature changes of muscle were induced by an external water bath in a range from 20 °C to 60 °C, and the thermal sensitivity was about -0.45 $HU \cdot °C^{-1}$. It also showed that the reproducibility of the area averaged CT number decreases with the area of the selected region of interest (ROI), and finally they predicted that, CT thermometry was able to discriminate fraction of Celsius degree with spatial resolution in the order of a centimeter. About 30 years later, Bruners *et al.* performed temperature mapping during RF hyperthermia on *ex vivo* swine livers, and they obtained a thermal sensitivity ranging from -0.35 $HU \cdot °C^{-1}$ to -0.44 $HU \cdot °C^{-1}$; they also reported results on *in vivo* trials, showing concerns related to artifacts, which distort the measurement of CT number [3]. Pandeya *et al.* studied the CT thermal sensitivity in *ex vivo* swine livers, by heating the tissue with a hot air flux from 20 °C to 95 °C. They measured a sensitivity of about -0.54 $HU \cdot °C^{-1}$ [9]. Pandeya *et al.* also studied the CT thermal sensitivity in *ex vivo* bovine livers during RF ablation from 20 °C to 98 °C. They measured a sensitivity of about -0.60 $HU \cdot °C^{-1}$ [2]. The same research group assessed the feasibility of CT Thermometry during LA by performing experiments on *ex vivo* bovine liver. They reported a thermal sensitivity of -0.65 $HU \cdot °C^{-1}$ in a range of temperature from 18 °C to 85 °C [10]. Among recent studies, the most detailed analysis of the influencing factors on the performances of CT thermometry were performed by Bruners *et al.* on phantoms [11]. They heated the phantoms by using a water temperature controlled bath. By analyzing the influence of some CT scan parameters on the standard deviation of CT numbers, they found that the standard deviation decreased with the increase of tube current-time product, tube voltage and slice thickness, and with the decrease of collimation thickness. They also assessed the thermal sensitivity of water, sunflower oil and contrast agent dilutions, an almost linear relationship between CT and temperature for the different fluid samples.

The ideal requirements for non-invasive temperature monitoring during hyperthermic ablation therapies include an accuracy of 1-2 °C, a spatial resolution of 1-2 mm, and an

acquisition time lower than 10 s - 30 s [12]. Furthermore, a CT scanner does not need special devices compared to non-invasive thermometry performed by MRI, and when used to monitor temperature during LA, the concerns related to the artifacts due to metallic objects are overcome; on the other hand, further studies are needed to assess the feasibility of this technique, in particular *in vivo* trials should increase the standard deviation of averaged CT number on a ROI, moreover the dose must be taken into account.

5.1.3 Experimental trials: thermal dependence of pancreas CT number

In the present study [13], the assessment of pancreas CT number changes during LA was performed, and twelve FBG sensors (cfr Paragraph 4.1) were employed as reference thermometers.

5.1.3.1 Negligible influence of CT table movement on FBG output

Before proceeding with temperature evaluation and CT scan, a preliminary assessment of effects of CT table movement was performed. As previously assessed (cfr Paragraphs 4.1.1 and 4.1.3), FBG sensors are sensible to both temperature change and strain (ε). In order to employ them only as thermometers, the measurement error due to the contribution of ε on the output signals of FBGs should be assessed, both in presence and absence of the RX irradiation. The acceleration of the table could cause a force acting on the gratings, or on the tissue, entailing a strain (ε) that contributes to $\Delta\lambda_B$. An experimental trial was performed arranging the four fiber optics inside the pancreatic tissue, and the table was translated in absence of any temperature variation. The maximum $\Delta\lambda_B$ measured by FBGs both in the absence and presence of RX irradiation corresponds to a ΔT of about 0.3 °C (Fig. 5.4) that, for the aim of our study, has been considered negligible, with respect to the maximum temperature values reached within the tissue during LA.

The negligibility of the strain due to the gravitational field on the pancreas (ΔT of 0.1 °C) was investigated in a previous study, as discussed in Paragraph 4.1.3 [14].

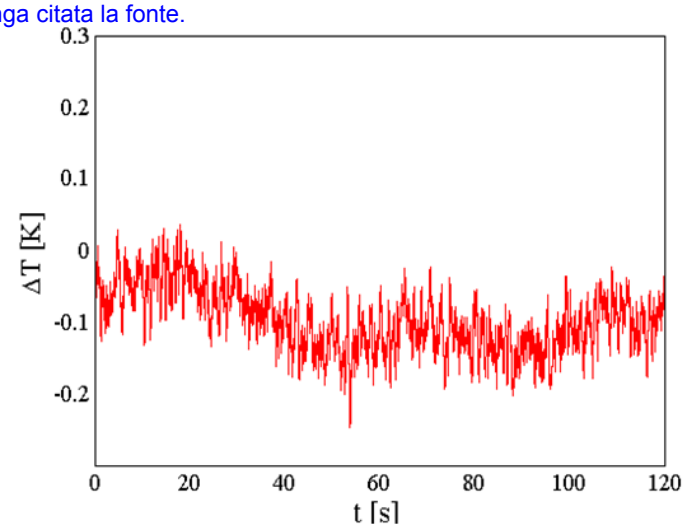

Figure 5.4: Experimental set up employed for CT-scan thermometry during LA on pancreas: A) negligible measurement error due to CT table movement, in presence of RX irradiation.

5.1.3.2 Laser settings and FBG sensors placement

An *ex vivo* healthy swine pancreas underwent LA, with a laser power of 3 W emitted by a Nd:YAG source in continuous mode (Fig. 5.5A.2), for 120 s (energy of 360 J). The laser light was guided within the fresh organ by means of a quartz bare fiber, with diameter of 300 µm. The pancreas was housed in an *ad hoc* designed polymeric mask, used to accurately control the relative distances between laser applicator and FBG sensors (Fig. 5.5A.1). CT images were acquired by the CT scanner Siemens Somatom Sensation 64 (Fig. 5.5A.2).

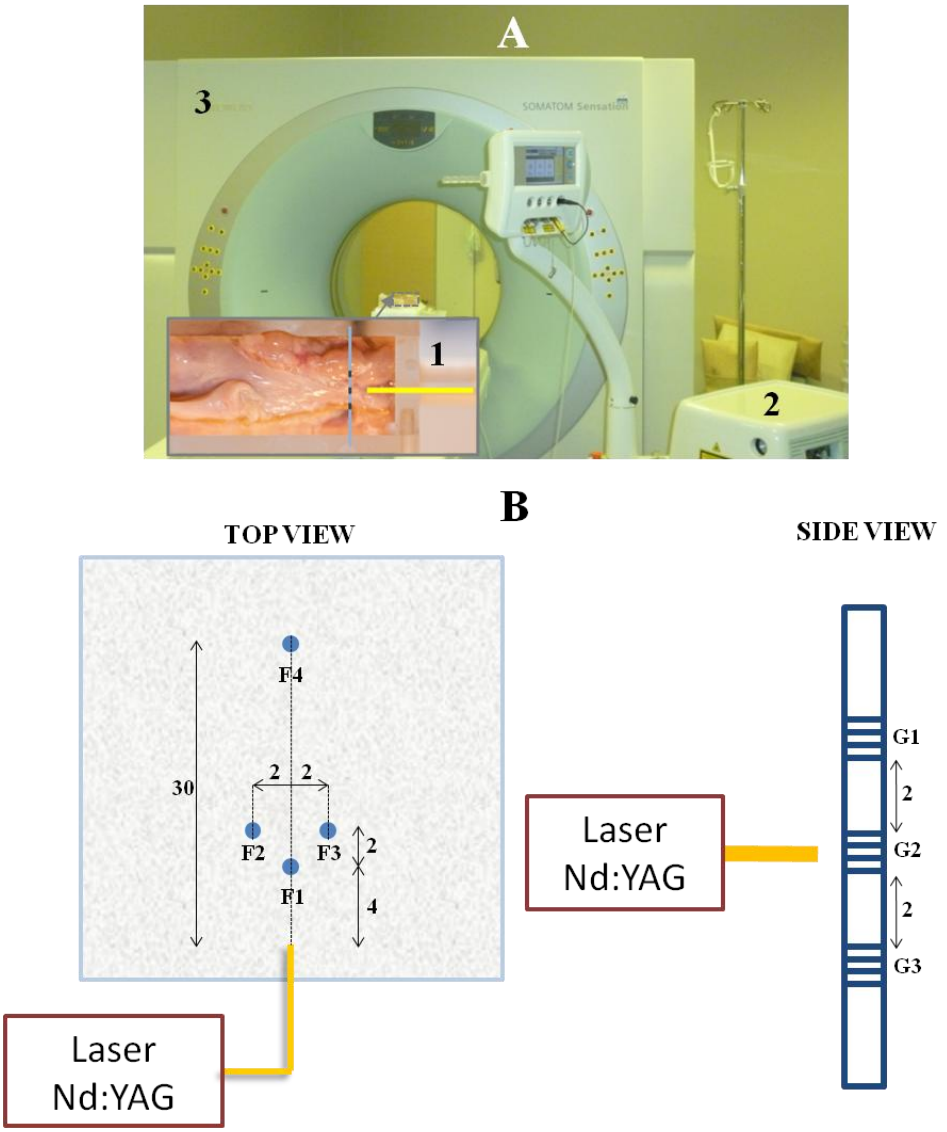

Figure 5.5: A) Experimental set up employed for CT-scan thermometry during LA on pancreas: 1) pancreas in had doc designed polymeric mask, with schematic of FBG sensors (black signs) and applicator (yellow), 2) Nd:YAG laser source, and 3) CT scanner Siemens Somatom 64 slices; B) Schematic representation of the relative distances between FBG sensors and the optical fiber applicator.

Twelve previously calibrated FBGs (cfr. Paragraph 4.1.5) were used in the present work for monitoring the temperature during laser irradiation of *ex vivo* pancreas, in order to measure temperature in 12 sites at different distances from the laser applicator. Gratings are 1-mm long and have been *ad hoc* fabricated for this application (SMF, TechnicaSA). Each optical fiber houses an array of three gratings (indicated as G1, G2 and G3), for a total of four fibers (F1, F2, F3 and F4, with a diameter of 250 µm). Gratings on the same fiber are spaced 2 mm from each other. λ_B of the gratings on the same fiber are 1533, 1541 and 1549 nm, for G1, G2 and G3, respectively. This configuration is shown in Fig. 5.5B. Considering that the plane of the applicator is perpendicular to the plane of F1, F2, F3 and

F4, the three FBGs of each fiber are arranged as follows: the central FBG, i.e., G2, is placed at the same quote of the applicator tip (z = 0), while G1 and G3 are located 2 mm upward (z = +2 mm) and 2 mm downward (z = −2 mm). Furthermore, F1, F2, F3 and F4 are placed within the tissue at distances ranging from d = 4 mm to d = 30 mm from the applicator.

5.1.3.3 Temperature measurement performed by FBGs

Figure 5.6 displays trends of ΔT monitored by the twelve FBGs placed inside the pancreatic tissue during LA, as a function of time (t). F1 is the fiber closest to the applicator (d = 4 mm) and, therefore, presents the highest ΔT values. The maximum ΔT, measured when the laser has been stopped (ΔT_{max}), is registered by G2, and has a value of about 45 °C, whereas G1 and G3 show a ΔT_{max} of about 30 °C and 28 °C, respectively. The fibers, arranged at a distance of about 6 mm from the applicator tip (F2 and F3), should be expected to measure the same T in a homogeneous tissue. Indeed, in both fibers, G2 measures a ΔT_{max} of about 25 °C, whereas G1 and G3 show ΔT_{max} ranging between 15 and 18 °C. F4 is placed at 30 mm from the applicator, and its gratings do not detect any significant temperature increment. The relevant fact resulting from these experimental trials is that for all four fibers, G2 measures temperature higher than that detected by G1 and G3. This happens because G2 is placed in front of the applicator tip, which is in the direction of the main heat conduction.

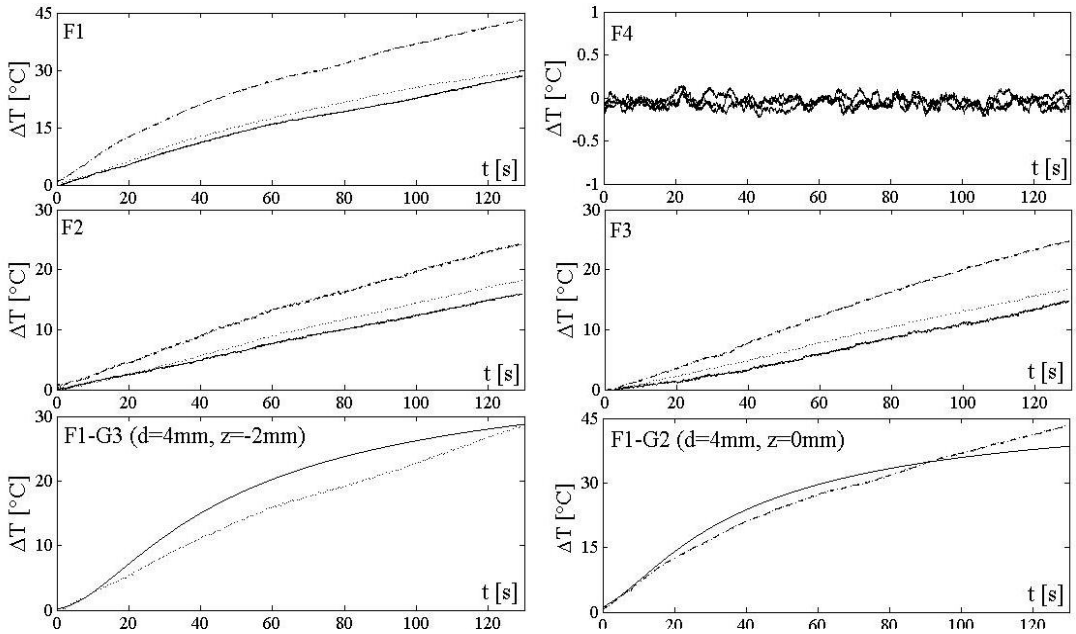

Figure 5.6: Trend of ΔT monitored by FBGs within a pancreas undergoing Nd:YAG LA at different distances from the applicator: 4 mm (F1), 6 mm (F2 and F3) and 30 mm (F4). The trends of ΔT experienced

by G2 (dash-dotted line), by G1 (dotted line), and by G3 (continuous line) are shown; the comparison between ΔT measured by G1 placed on F1 and G2 placed on F1 (dotted lines) with the theoretical predictions (continuous lines) obtained by Equation 5.5 are also reported.

F1, F2, F3 and F4 are placed at 4 mm, 6 mm, 6 mm and 30 mm from the applicator, respectively. For each fiber, ΔT monitored by G2 (dash-dotted line), G1 (dotted line) and G3 (continuous line) are plotted.

The two graphics reported in the lower part of Fig. 5.6 show that ΔT can be well described by the following relationship:

$$\Delta T(t) = \beta_1 \cdot \frac{1}{d} \cdot \left(1 - erf\left(\frac{d}{\sqrt{4 \cdot \delta \cdot t}}\right)\right) \qquad (5.5)$$

where *erf* indicates the error function, d is the distance between applicator and sensor, β_1 is a constant depending on some tissue properties and on the laser power, and δ=0.1391 mm^2/s is the thermal diffusivity of the pancreas [15]. This relationship is obtained by considering the laser as a heat point source [16]. This model can be applied under the hypothesis that the distance d is larger than the spot size: in our case, the laser fiber tip has a diameter of 300 µm, and it is in contact with the tissue, therefore no laser beam divergence occurs, and the minimal value of d is 4 mm.

5.1.3.4 Temperature measurement performed by CT scan

During LA, CT scans were acquired by a CT scanner (Siemens Somatom Sensation 64). CT scan settings were the following:

- tube current-time product: 150 mAs
- tube voltage: 120 kVp
- slice thickness: 0.6 mm
- scan time: 7 s
- region of interest (ROI): 0.02 cm^2 (circular shape)
- about 52 pixel per ROI

The averaged area CT number was monitored in twelve sites of the pancreas undergoing LA on ROIs centered where the FBG sensors were placed. An image obtained by CT scan

is reported in Fig. 5.7B, whereas the exact positions of FBG sensors in the polymeric mask is shown in Fig. 5.7A.

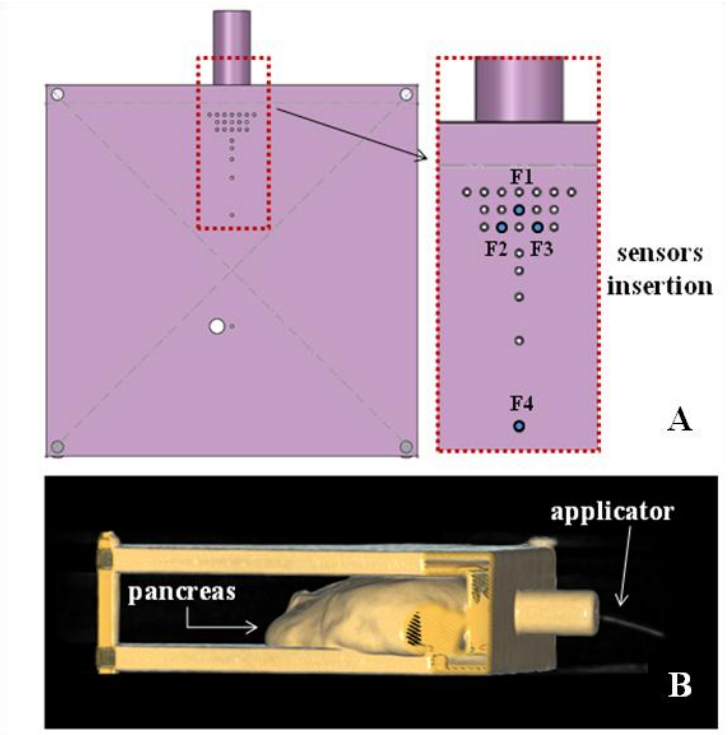

Figure 5.7: A) Arrangement of the four fibers inside the pancreas by means of the PMMA mask (top view of the mask); B) CT scan image of the pancreas undergoing treatment.

The CT number does not present a decreasing trend at d = 30 mm; moreover, it shows a similar trend in the ROI placed at the same distance from the applicator upward and downward the applicator. The variation of CT numbers *(*ΔCT) of tissue undergoing LA for five ROI (at d = 4 mm and z = 2 mm, at d = 4 mm and z = 0, at d = 6 mm and z = 2 mm, at d = 6 mm and z = 0 mm, and at d = 30 mm and z = 0) as a function of time, t, are reported in Fig. 5.8.

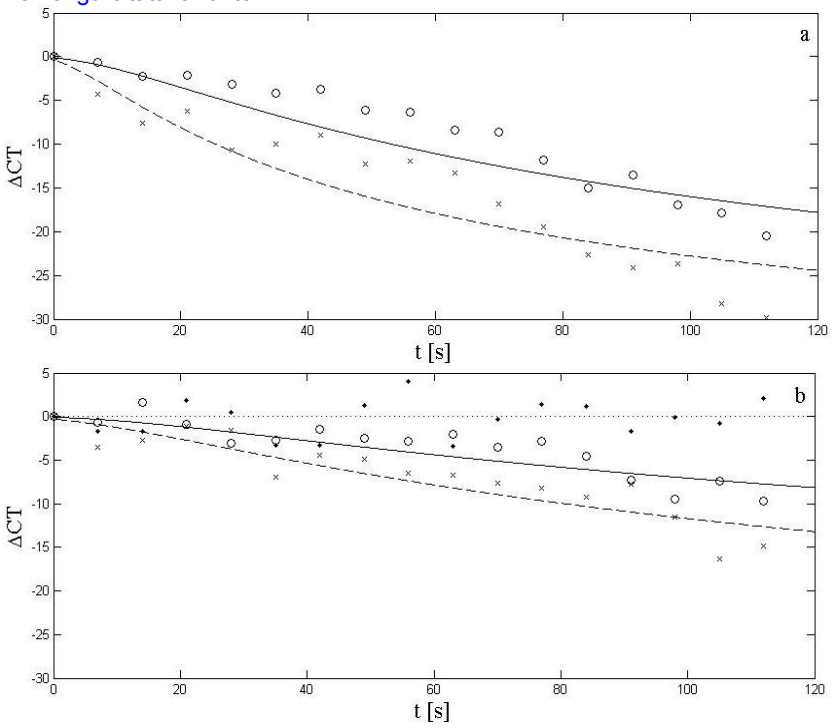

Figure 5.8. Trend of ΔCT(t) in the pancreas during LA: A) ΔCT values of a ROI placed at d = 4 mm, z = 0 (squares) and z = 2 mm (circles), also their fittings using the model expressed in Equation (6) are reported; B) ΔCT values of a ROI placed at d = 6 mm, z = 0 (squares) and z = 2 mm (circles), and at d = 30 mm and z = 0 (dots); also their fitting by Equation 5.6 are reported.

The trends of $\Delta CT=f(t)$ are fit by the following equation:

$$\Delta CT(t) = \beta_2 \cdot \left(1 - erf\left(\frac{d}{\sqrt{4 \cdot \delta \cdot t}}\right)\right) \tag{5.6}$$

where β_2 is a constant. Equation 5.6 is obtained by considering a ΔT during LA described by Equation 5.5 and a linear relationship between ΔCT and ΔT, as reported in Equation 5.4.

The experimental data reported in Fig. 5.8 could be fitted also with a linear model, according to the experience of the large part of the studies reported in literature which uses a linear relationship between ΔCT and ΔT. In Table I, the equations of the best fitting line, $\Delta CT=f(t)$, the correlation coefficient, and the maximum temperature increase measured by the FBG sensors in the five ROIs are reported. The linear model strongly simplifies the phenomenon, because it assumes the tissue temperature increase during LA as linear.

Table I. Equation of the best fitting lines and correlation coefficients obtained by linear regression of experimental data, ΔCT *vs*. t, in different ROI. Maximum temperature increase during LA is also reported.

ROI	ΔT_{max} [°C]	Equation	R^2

d = 4 mm, z = 0	44 °C	$\Delta CT = -0.2565 \cdot t$	0.95
d = 4 mm, z = ±2 mm	30 °C	$\Delta CT = -0.1568 \cdot t$	0.93
d = 6 mm, z = 0	25 °C	$\Delta CT = -0.1194 \cdot t$	0.85
d = 6 mm, z = ±2 mm	17 °C	$\Delta CT = -0.0676 \cdot t$	0.76
d = 30 mm, z = 0	≈0 °C	$\Delta CT = -0.0003 \cdot t$	/

Regarding the equation of the best fitting line (Table I), a higher value of the slope is associated with a greater variation in CT number with time. The decrease in time of the CT number is caused by the temperature increase during the treatment; a higher slope is associated with a greater temperature increase, as predicted by Equation 5.6. The values of the slope (Table I) agree with the highest temperature increase (ΔT_{max}) observed during the treatment and measured by the FBG sensors (Fig. 5.6). The slope increases as the distance from the applicator of the considered ROI decreases (e.g., considering the ROI placed at z = 0, at d = 4 mm the slope is −0.2565 HU·s^{-1}, at d = 6 mm is −0.1194 HU·s^{-1}, and at d = 30 mm is almost null because the temperature increase is negligible); this behavior agrees with the trend obtained by Equation 5.6 and reported in Figure 5.8.

In order to obtain the relationship between ΔCT and ΔT, as expressed by Equation 5.4, the HU values monitored during CT-scans (Fig. 5.8) have been synchronized with the temperature values measured by FBGs (Fig 5.6).

This trend, and both its best fitting line and the quadratic fitting are reported in Fig. 5.9.

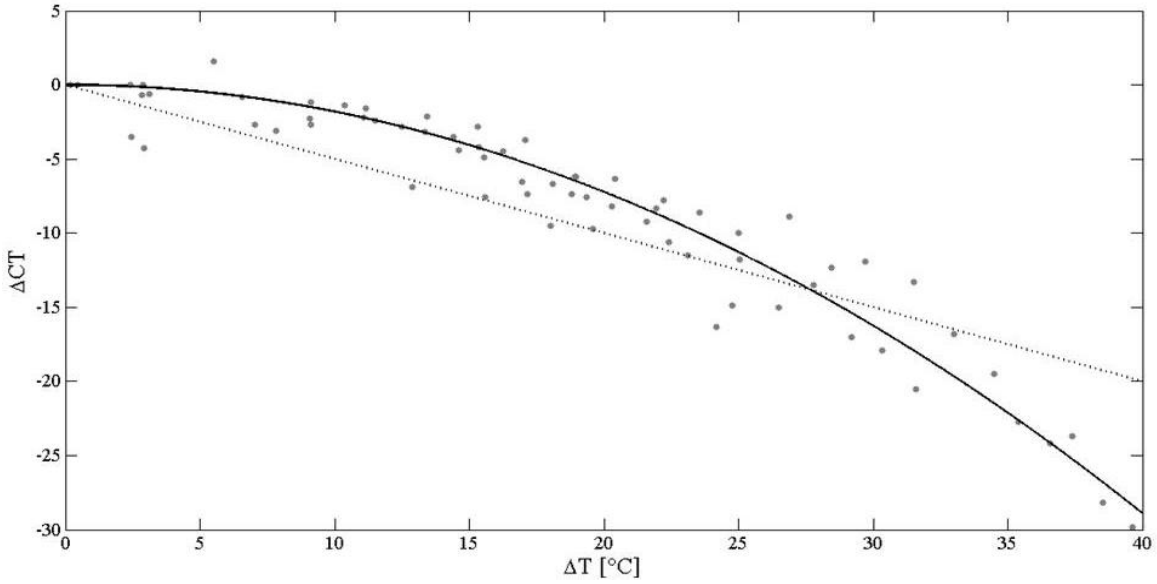

Figure 5.9. Trend of ΔCT as function of ΔT (dots), with best fitting line (dotted line), and the quadratic model (continuous line).

The slope of the best fitting line considering the whole range of ΔT represents the thermal sensitivity of CT pancreatic tissue, and its value is -0.50 HU·°C^{-1}. Although linear model quite agrees with the experimental data (R^2=0.79), a quadratic fitting was also performed: the parabola, whose equation is $\Delta CT=-0.0181\cdot\Delta T^2$, better fits the data than the linear model, as confirmed by the increase of R^2 values (i.e., 0.93).

5.1.3.5 Discussion of results

The results presented in this work confirm that a smaller temperature increase, associated with a greater distance from the applicator, is measured at 30 mm, as confirmed by the negligible ΔCT at 30 mm after 120 s, in agreement with results reported in [17]. Furthermore, the ΔT values obtained at 6 mm are slightly higher than the data presented in [14], where swine *ex vivo* pancreases were treated with Nd:YAG laser (energy equal to 1000 J and P equal to 3 W). This observation could be explained by considering the different arrangement of sensors with respect to the laser applicator, and the smaller length of the FBGs used in this work (1 mm *vs.* 10 mm in [14]), allowing for a quasi-punctual measurement. Regarding the measurement errors, FBGs are not affected by errors due to light absorption presented by thermocouples; furthermore, the errors introduced by the FBG strain, which could be caused by tissue relaxation and CT table translation, have been experimentally investigated and found negligible (about 0.3 °C). These results indicate that temperature measurements performed with FBGs can be considered reliable for evaluating the temperature dependence of CT from an experimental standpoint.

Results obtained with CT scan thermometry show that the mean thermal sensitivity of pancreatic CT in the whole range of T (i.e., from 20 °C to 60 °C) presents a value similar to data published by several authors. Indeed, Pandeya *et al.* [9] report a mean thermal sensitivity of −0.54 HU·°C^{-1} during heating of *ex vivo* porcine liver between 20 °C and 90 °C, considering a ROI of 0.21 cm^2, and the reference temperatures were measured with thermocouples. On the same tissue, Bruners *et al.* [3] report a sensitivity ranging from −0.44 HU·°C^{-1} to −0.37 HU·°C^{-1}, explaining the difficulties in the monitoring of the CT number near the RF probe hampered by metal artefacts. In [10], authors determine a slightly different sensitivity (i.e., −0.60 HU·°C^{-1}) during RF ablation on *ex vivo* bovine liver, considering a ROI of 1 cm^2.

Nevertheless, this study shows that the relationship between ΔCT and ΔT (Fig. 5.9) does not present a constant sensitivity if the tissue temperature experiences wide changes,

as also reported by Fallone *et al.* [5] on *ex vivo* porcine muscle undergoing hyperthermic treatments. In fact, the quadratic fitting better agrees with experimental data than the linear model, as shown in Figure 5.9 The second order relationship between ΔCT and ΔT can be explained by considering also a second order term in the denominator of Equation 5.2. Therefore, when ΔT ranges from 20 °C to 40 °C, the mean thermal sensitivity, calculated by the equation of the parabola, was -1.08 $HU \cdot °C^{-1}$, whose absolute value is about three times higher than the absolute value of the sensitivity found for ΔT ranging from 0 °C to 20 °C (i.e., -0.36 $HU \cdot °C^{-1}$).

To the best of my knowledge, CT scan thermometry has never been applied to monitor the temperature of pancreatic tissue during LA. As theoretically predicted and experimentally assessed, the CT number decreases during laser irradiation. Because the increase of tissue temperature is more marked close to the applicator (Fig. 5.6), the CT number decreases as the distance from the applicator shortens. This is clearly shown in Table I, which displays the slope of the best fitting line of ΔCT at different distances from the applicator versus treatment time. At distances ranging from 4 mm to 6 mm, the absolute value of the slope decreases from about 0.26 $HU \cdot s^{-1}$ to 0.068 $HU \cdot s^{-1}$, and at 30 mm it can be considered null during treatment, as tissue temperature increase does. This is also clear in Fig. 5.8, which shows the experimental ΔHU vs time, and its fitting with a model in Equation 5.6 more accurate than a linear one.

Finally, for the first time, the CT sensitivity with temperature in the pancreas has been experimentally evaluated: the mean sensitivity was $-0.50\ HU \cdot °C^{-1}$ in the whole range of temperature experienced by tissue (i.e., from 20 °C to 60 °C); it is also evident (Fig. 5.9) that the sensitivity increases with T (g., its mean value is about $-0.36\ HU \cdot °C^{-1}$ from 20 °C to 40 °C *vs* $-1.08\ HU \cdot °C^{-1}$ when T ranges from 40 °C to 60 °C), according to [5].

The issues related to the radiation dose received by patients when CT scan-based thermometry is adopted must be also analyzed. In the above described experiments the total dose length product (TDLP) was about 600 mGy·cm; this value is comparable to the value reported in a previous study on liver [11], and it is also comparable to other CT-guided procedures. Further studies should be performed to assess potential side effects due to the additional radiation exposure of organs adjacent the target undergoing LA. On the other hand, it must be considered that hyperthermia is mostly applied as palliative treatment on some organs (e.g., pancreas and liver), in oncology patients with limited life expectancy.

5.1.4 Experimental trials: thermal dependence of liver CT number with Dual Source CT scan

In Universitätsklinikum of Goethe University of Frankfurt am Main, I performed some experiments of CT-scan thermometry, using a Dual Source CT-scanner.

5.1.4.1 Dual Source CT scanner: working principle and features

The first realization of a Dual Source CT scanner was made in 2006 by Siemens [18]. It consists in a double pair of source-detector, mounted into the gantry with an angular offset of 90°, which rotate simultaneously around the object to be scanned, as shown in Fig. 5.10:

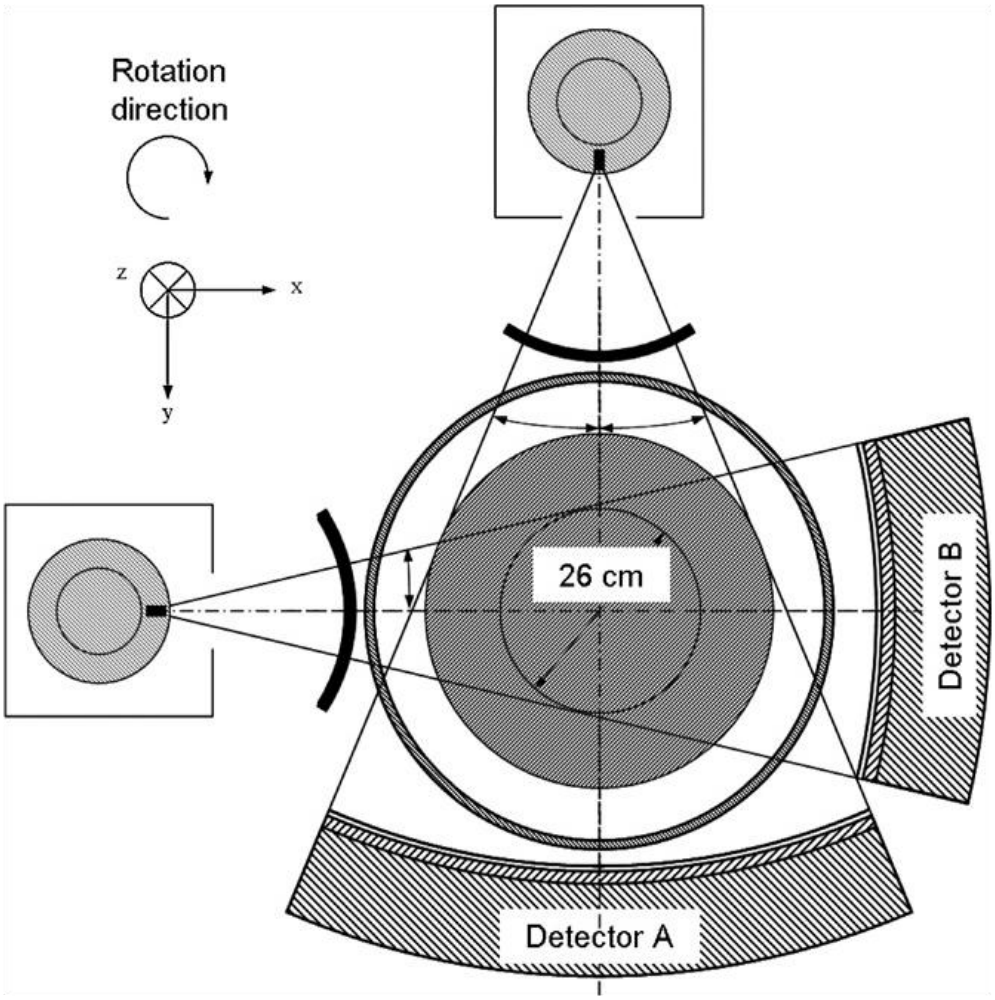

Figure 5.10. Illustration of the dual source acquisition geometry using two tubes and two corresponding detectors, mounted into the gantry with an angular offset of 90° [18].

Both tubes can operate independently in terms of tube current and voltage settings. The advantages of this novel configuration are the flexible modes of operation, and the feasibility to combine the resulting acquisition data. Another strong points are the

capability to improve the temporal resolution of scan (minimum value of 82 ms), useful in field of cardiac scan, and a maximum power reserve of 160 kW, since each tube is characterized by tube power of 80 kW.

Since each pair source-detector can be set with proper characteristics, from a single data set of images it is possible to obtain several image features. In particular, the SOMATOM Definition (Siemens Healthcare, Forchheim, Germany) scanner allows a combination of tube voltage of 140 kV on tube A, and of 80 kV on tube B. For smaller objects, spiral scan modes with collimations of 32mm×0.6mm and 10mm×0.6mm are recommended. The data delivered by detector A and detector B is reconstructed separately. The dual energy analysis is based on a so-called "three-material decomposition" of the resulting images. Two different CT numbers can be assigned for each voxel inside the common scan field of the A and the B detector: the first value results from an "illumination" with the 140 kV tube, the second value results from the 80 kV tube. Each pair of CT numbers is represented by a point in a coordinate system, which is defined by the CT numbers generated at each particular tube voltages. Consider diagram in Fig. 5.11:

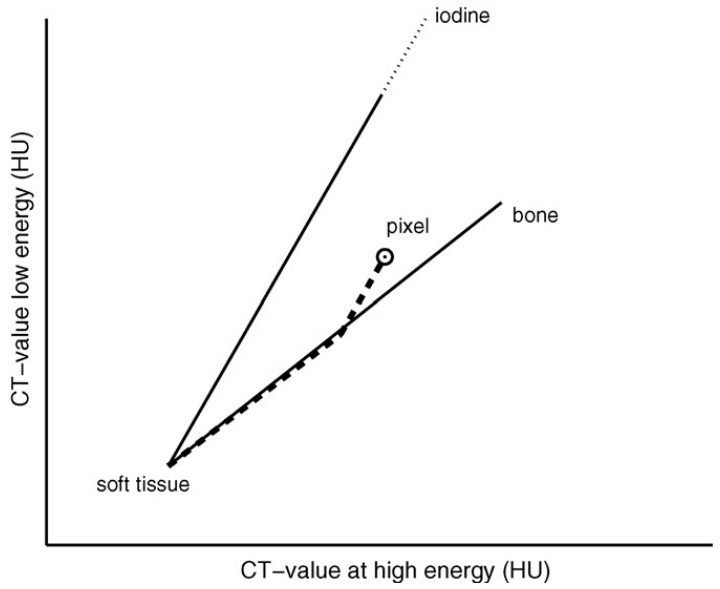

Figure 5.11. Principle of three-material decomposition. Materials (e.g. soft tissue, iodine and bone) are connected by two vectors in a diagram that maps CT values obtained at low energy versus CT values obtained at high energy. Any pixel coordinate in this diagram can be represented in terms of the two vectors. The pixel values along the line connecting "soft tissue" and "iodine" represent different mixtures of iodine and soft tissue. Values located further to the right-hand side of the line connecting soft tissue and iodine correspond to higher iodine fractions within the voxel of interest. Pixels along the line between soft tissue and bone represent different bone densities without iodine content. The pixel shown between the two ideal

lines contains both iodine and bone, quantified by the length of the respective dashed lines. In this example, the bone content dominates over the iodine content [18].

The introduction of three points in this diagram which represent the HU values of three idealized materials (e.g. soft tissue, bone, iodine), allows for definition of two ideal vectors originating from a common start point (e.g. at soft tissue) and ending at two different points (e.g. one vector from soft tissue to bone, one vector from soft tissue to iodine). These two vectors define a new coordinate system. The proportions of each of the three idealized materials which are contained in a given voxel of interest are given by the coordinates of this voxel within the new coordinate system (Fig. 5.11). Based on this coordinate transformation, a material separation and a subsequent segmentation can be performed for every voxel (e.g. bone versus iodine for bone removal segmentation).

The weakness of this system is the scattered radiation: as a matter of fact, during the scanning of an object, the presence of a second tube induces scattering in the first one, and *vice versa*. Nevertheless, this issue can be overcome by dedicated correction algorithm which prevents the image degradation and restores the image contrast. Furthermore, the problem of data truncation can occur: since, to preserve system compactness, the detector B covers a smaller measurement field of 26 cm, when larger objects are scanned some data can be truncated, and a post-processing extrapolation should be performed.

In phase of imaging reconstruction, the dedicated software of the machine works as follows: once images by 140 kV tube and 80 kV tube have been acquired by respective detectors, a weighting factor should be chosen to select the amount of information to extract from each image. For example, a weighting factor of 0.2 means that the 20% of information content is extracted from 80 kV image, and the remaining 80% from 140 kV image. Weighting factor can assume 11 values, ranging from 0.0 (information extracted only from 140 kV image) to 1.0 (information extracted only from 80 kV image). Different weighting factors have effects on the signal to noise ratio (SNR) and on the contrast to noise ratio (CNR). A study about the performances of Dual Source CT scan technique (DSCT) has been recently performed by Paul *et al.* [19] on forty patients undergoing a CT scan of the neck. They found that for the detection of anatomical structures like aorta and thyroid gland, the increasing weighting factors provided an increased value of CT number, but the higher values of SNR and CNR were obtained with weighing factor of 0.6. It is evident that the optimal weighing factor should be investigated for each anatomical structure.

At the best of my knowledge, studies about DSCT-scan thermometry are absent in the current literature. Bruners *et al* [11, 8] utilized the same DSCT scanner employed for this study, during hepatic RF ablation, but they did not considered the thermal dependence of CT number for different weighting factors; they used the system as a standard CT scanner. The application of such technique to the thermometry could easily lead to the identification of the optimal data fusion to obtain the highest thermal sensitivity of CT number variation.

5.1.4.2 Experimental set up

- **Laser settings and water cooled applicator**

Experimental set up is shown in Fig. 5.12.

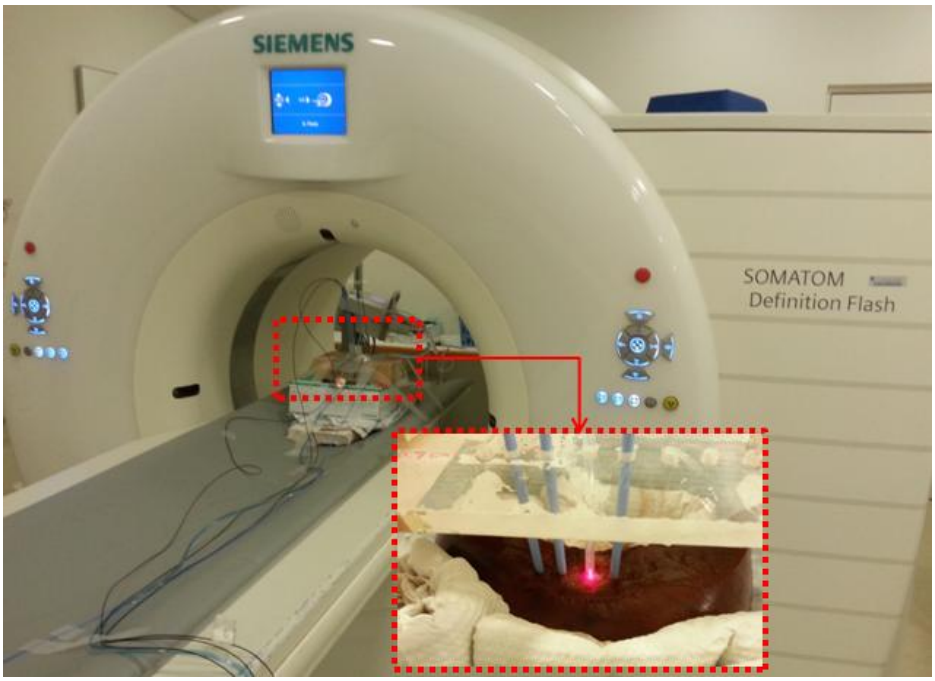

Figure 5.12. Experimental set up for DECT images based thermometry.

The radiation of a Nd:YAG laser (1064 nm, MY30 Martin Richard Medizintechnik, GmbH, Tutlingen; Germany) is conveyed into a water cooled applicator (Power Laser Set 602120, Somatex Medical Technologies), with a power of 30 W delivered for 200 s, to perform LA on *ex vivo* porcine livers.

A water pump (GF1200E, Dornier Medizintechik, GmbH) circulates saline solution (0.9 NaCl) through a plastic pipe at 60 ml·min^{-1}.

The applicator has been designed in 1997, and experimentally validated on 127 patients with colorectal liver tumor during the following years [20]. The applicator integrates the scattering properties of the surface (25 mm of length) of an optical fiber with diameter of 400 µm, with the cooling effects of a saline solution that flows at room temperature within

a double-tube PTFE catheter. The catheter material is flexible and transparent to near infrared radiation, and stable for temperature up to 400 °C. The features of the water cooling applicator are listened in Table II:

Table II. Features of water cooled applicator for LA [20].

Part	Property	Value
PTFE catheter	outer diameter	3.0 mm (9 Fr)
	length	420 mm
	cooling medium	saline solution
	cooling temperature	0-25 °C
Scattering applicator	fiber length	12 m
	fiber core diameter	400 µm
	fiber type	HCS
	fiber connector	SMA 905
	fiber numerical aperture	0.37
	outer diameter	0.95 mm
	active scattering length	25 mm

The main advantage in the use of water cooled applicator is to prevent fiber surface from melting, and to modulate the temperature reached within the tissue during LA treatment. Moreover, the radial temperature distribution is modified, and this system allows obtaining increased ablation volumes, with respect to the traditional bare fiber.

- **Temperature probes placement**

Three fluoroptic sensors (cfr Paragraph 4.3) are used to monitor temperature during LA. Two probes are placed at distance of 1 cm from the laser applicator through a mask (symmetrical configuration), the third one at 2 cm, as shown in following figure:

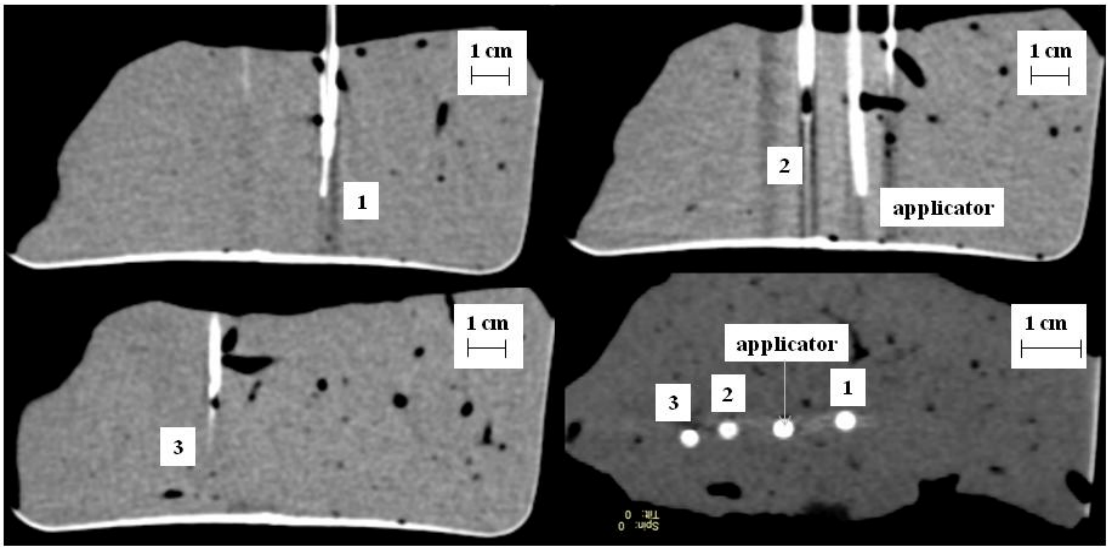

Figure 5.13. CT scan image of water cooled applicator and fluoroptic sensors placed inside *ex vivo* porcine liver.

- **CT settings**

- Dual Energy CT (DECT) under SOMATOM Definition flash Dual Source CT scanner (Siemens, Forchheim, Germany) is employed to obtain the CT images during LA procedure on *ex vivo* porcine livers. The following parameters have been set to obtain the desired data fusion:

- 80 kV- Sn 140 kV
- weighting factors: 0.0, 0.5, 1.0
- 200 mAs
- slice thickness: 0.6 mm
- collimation: 2x32x0.6 mm
- pitch: 0.9
- rotation frequency: 2 Hz
- time for scanning the whole organ: as short as possible (about 15 s), according to the dimensions of tissue, the automatic stop of the patient's table and the time required to carry back the table at the initial position
- reconstruction kernel: D31f (suitable for soft tissues)

The images from the liver have been acquired with a Field of View (FOV) of 200 mm x 200 mm, and the CT number variation have been evaluated within ROI of 0.04 cm^2 (about 24 pixels in each ROI).

5.1.4.3 Results and discussion

Treatment was performed until a temperature of about 100 °C was reached. Temperature trends measured by three fluoroptic sensors are shown in Fig. 5.14:

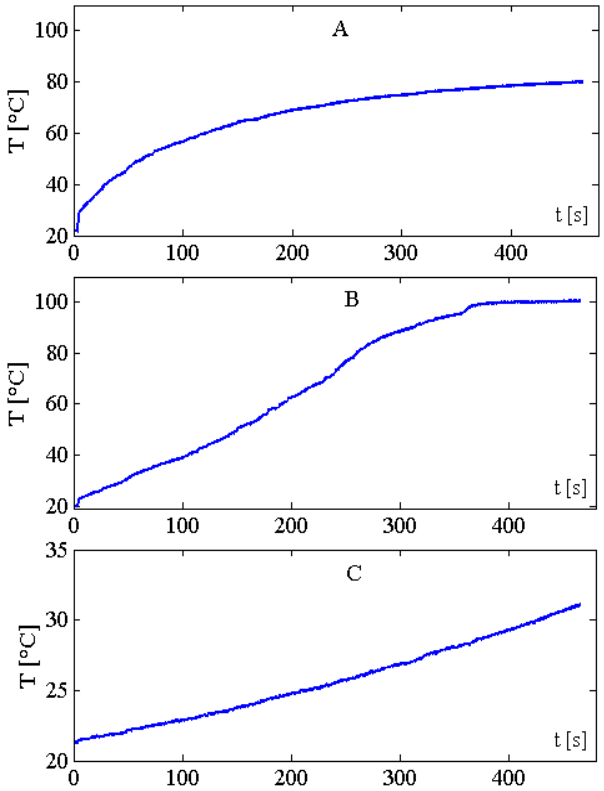

Figure 5.14. Temperature trends in liver undergoing laser thermotherapy, measured by A) fluoroptic sensor 1 (in Fig. 5.13A), B) fluoroptic sensor 2 (in Fig. 5.13B) and C) fluoroptic sensor 3 (in Fig. 5.13C)

Fluoroptic 1 and 2 are placed in symmetrical configuration with respect to the applicator (plane x-y, Fig. 5.13D), but their sensitive tip are not at the same depth (plane x-z, Fig. 5.13A and B), therefore they measure different temperatures (Fig. 5.14A and Fig. 5.14B), with a maximum difference of about 20 °C at the end of the treatment. As expected, fluoroptic 3 measures a smaller temperature increase (about 10 °C, Fig. 5.14C).

The biggest issue showed by fluoroptic probes is the presence of artifact on CT images, particularly visible on the x-z plane (Fig. 5.13). In order to avoid artifacts influence on the measurements, ROI were considered 2 slices after the slices where sensor tip was visible, considering the isothermal distribution (Fig. 5.15 shows the case for fluoroptic 1). Since

the slice thickness is 0.6 mm, the ROI was taken at 1.2 mm from the tip, but on the same isothermal surface, supposing the ideal circular symmetry of temperature distribution on x-y plane.

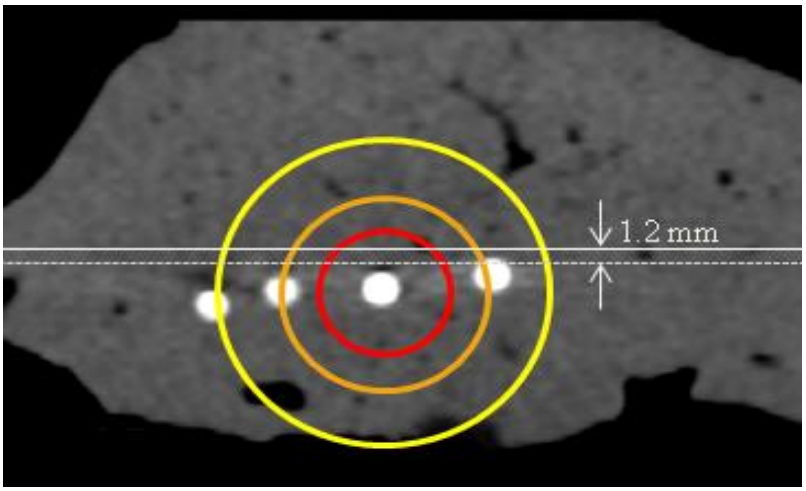

Figure 5.15. Isothermal boundaries and ideal circular-shape temperature distribution on x-y plane, and choice of slice to select ROI, in order to avoid artifacts caused by fluoroptic material on CT image.

The synchronization of variation of temperature (ΔT) with variation of CT number (ΔCT) leads to the relationships ΔCT=f(ΔT), shown in Fig. 5.16 for three different weighting factors:

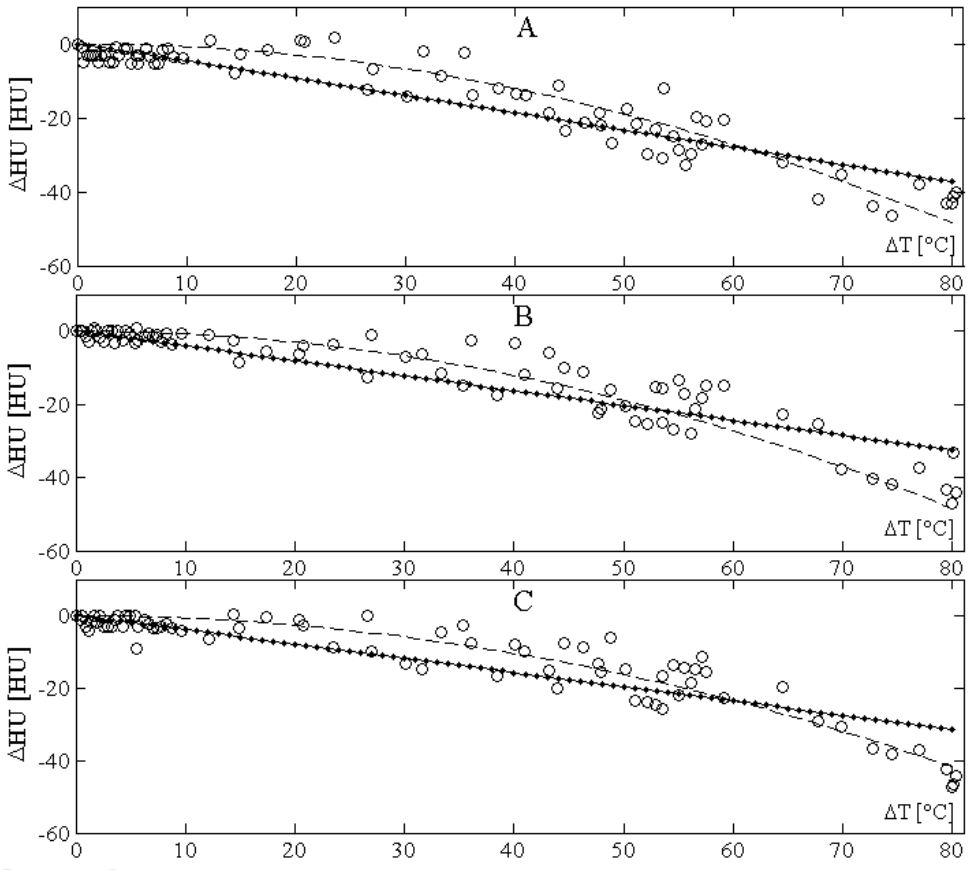

Figure 5.16. Liver CT number as function of temperature variation, for weighting factors A) 0, B) 0.5 and C) 1. For each trend are plotted the best fitting parabolic curve (dashed line) and the sensitivity (continuous line).

Table III summarizes the angular coefficient m (or mean sensitivity) of relationship $\Delta CT=m\cdot\Delta T$, and the coefficient γ of the parabolic curve $\Delta CT= \gamma\cdot\Delta T^2$ (uncertainty has been calculated considering the 95% of confidence of interval):

Table III. Mean sensitivity (m) and coefficient γ of the parabolic curve $\Delta CT= \gamma\cdot\Delta T^2$, R^2 for different weighting factors of images acquired during thermotherapy on swine liver.

weighting factor	linear fitting		parabolic fitting	
	m [HU·°C^{-1}]	R^2	γ [HU·°C^{-2}]	R^2
0.0	-(0.56±0.04)	0.78	-(0.0085±0.0007)	0.58
0.5	-(0.39±0.03)	0.76	-(0.0063±0.0005)	0.78
1.0	-(0.36±0.04)	0.65	-(0.0059±0.0006)	0.68

The increase of weighting factor entails the decrease of absolute value of sensitivity, the decrease of γ. The increase of weighting factors corresponds to the decrease of voltage tube value responsible for the formation of image.

Images with weighting factor 0.0 (corresponding to voltage tube of 140 kV) show the highest thermal sensitivity (-0.56 HU·°C^{-1}), the highest value of γ (-0.0085 HU·°C^{-2}). Values of mean sensitivity are comparable with the ones reported by the literature for liver. For example, Pandeya *et al* [9] report a mean sensitivity of -0.54 HU·°C^{-1} for swine liver in the range 20 °C-90 °C, with voltage tube of 120 kV and slice thickness of 1.2 mm, and -0.60 HU·°C^{-1} for bovine liver [2]. On the other hand, Bruners *et al* published values ranging from -0.35 to -0.44 HU·°C^{-1} for swine liver at 140 kV, 300 mAs with the same DECT used in my study [3].

For weighting factors of 0.5 and 1.0 (voltage tube of 80 kV), m and γ decrease with respect to images at 0.0, but both values are not discrepant.

Another important finding of this study is the assessment of conspicuity of the thermal lesion (LC). It is referred to the extent of treated lesion which can be distinguished from

the normal parenchyma, and has a clinical relevance, since it visually guides the clinicians to assess if all the desired lesion has been treated.

When the treatment is finished, around 7 s after the end of laser ablation, CT number values were measured in three positions of the images, for the three weighting factor: at 1 cm from the laser applicator, at 2 cm from it, and on the normal liver parenchyma, i.e., around 6 cm from the laser applicator, where is supposed that temperature did not increase during the treatment.

For each position, Signal to Noise Ratio (SNR), defined as ratio between mean CT number in the selected ROI, and the standard deviation (sd) has been calculated. Furthermore, the LC was calculated as difference between CT number in normal parenchyma and CT number in ROI at 1 cm far from applicator and 2 cm far from applicator, respectively. For each position, 10 ROIs were selected and mean values have been calculated.

Values are reported in Table IV:

Table IV. For normal liver parenchyma, and at distances of 1 cm and 2 cm from applicator, are displayed CT number, standard deviation of ROI (sd), Signal to Noise Ratio (SNR), and the conspicuity of lesion (LC). Each value has been assessed for the three weighting factors, i.e., 0.0, 0.5 and 1.0.

	weighting factor	**0 (140 kV)**	**0.5**	**1 (80 kV)**
normal parenchyma	CT number [HU]	66±3	69±1	75±3
	sd [HU]	7±2	5±2	9±2
	SNR	10±3	14±3	9±2
0.7 cm from applicator	CT number [HU]	25±3	27±5	29±3
	sd [HU]	10±1	9±2	14±3
	SNR	2.6±0.4	3±1	2.2±0.6
	LC [HU]	41±2	42±5	46±5

1 cm from applicator	CT number [HU]	48±2	52±2	56±2
	sd [HU]	9±2	9±2	10±2
	SNR	5±1	6±1	6±1
	LC [HU]	18±3	17±2	19±3
2 cm from applicator	CT number [HU]	59±3	63±5	66±4
	sd [HU]	8±2	5±1	10±3
	SNR	7±2	11±3	6±2
	LC [HU]	12±5	12±5	15±4

Table IV shows that CT number increases from 0.7 cm-distance from applicator to the parenchyma, and this is due to the increase of temperature during treatment. Moreover, sd decreases with distance to applicator. This phenomenon is also due to the spatial gradient of temperature distribution, which affects the homogeneity of selected ROI. As consequence of the increase of CT number and decrease of sd, the SNR increases when distance from applicator increase. Furthermore, LC increases when the distance from applicator decreases. For example, LC at 0.7 cm from applicator is 41±2 HU for weighting factor 0.0, 42±2 HU for 0.5 and increases at 46.5 HU for 1.0; LC at 2 cm assumes values of 12±5 HU at 0.0 and 0.5, and 15±4 HU at 1.0.

The main drawback has been demonstrated to be the use of fluoroptic sensors for the monitoring of reference temperature, that, nevertheless has never been mentioned by other authors employing the same sensors. Although they are suitable to be employed in MRI, the artifact on CT images entail a low value of SNR.

Therefore, considering the study presented in Paragraph 5.1.3, FBG result to be the most performing sensors for tissue temperature monitoring, also as reference sensors during CT-based thermometry.

5.2 Magnetic Resonance Images-based Thermometry

5.2.1 Hints of MRI

Protons in a medium undergoing an external magnetic field are characterized by a net magnetization (i.e., a specific orientation into the space). An external radiofrequency pulse at the same precession frequency of protons (Larmor frequency, 63.855 MHz) can rotate the net magnetization vector. The angle to which the net magnetization is rotated relative to the main magnetic field direction via the application of an RF excitation pulse at the Larmor frequency is known as Flip Angle (FA). A phenomenon of protons relaxation follows, in order that protons can recover the initial position and direction imposed by the external magnetic field. The phenomenon of relaxation is described by two parameters: T1 and T2 relaxation times. During the relaxation, protons release part of their energy, in form of radiofrequency signal, which is used to build the image. The volumetric information are achieved thanks to gradient coil, which, when opportunely switched, are able to code the region of the body from where the RF echo is generated.

In the practice, the RF signal can be transmitted with several timing and duration.

A pulse sequence is a sequence of RF pulse, gradient switches and collecting RF echoes.

It is useful at this step of the dissertation to explain the physical meaning of the MR parameter used for thermometry purpose, with regard to the two sequences employed in this experimental study, i.e., Saturation Recovery (SR) and Inversion Recovery (IR).

Saturation Recovery sequence: is characterized by a train of excitation pulses at 90°, repeated with a repetition time of TR, so that T2<TR<T1. Longitudinal magnetization that develops during the TR period after the dephasing gradient is rotated into the transverse plane by another 90° pulse. A gradient echo is acquired immediately after each pulse. The signal will reflect T1 differences in tissues because of different amounts of longitudinal recovery during the TR period.

Inversion Recovery sequence: applies pulses of 180°—90°—180°. The longitudinal magnetization is first flipped (inverted) by the excitation pulse at 180° in the opposite direction. The transverse magnetization is therefore zero and no MR signal is received. The interval between the 180° pulse and the 90° stimulation pulse is known as inversion time TI. During this time period, the longitudinal magnetization recovers. The stimulating 90° pulse converts the current longitudinal magnetization into transverse magnetization.

Echo time (TE) is the time between the application of the 90° pulse and the peak of the echo signal (Fig. 5.17).

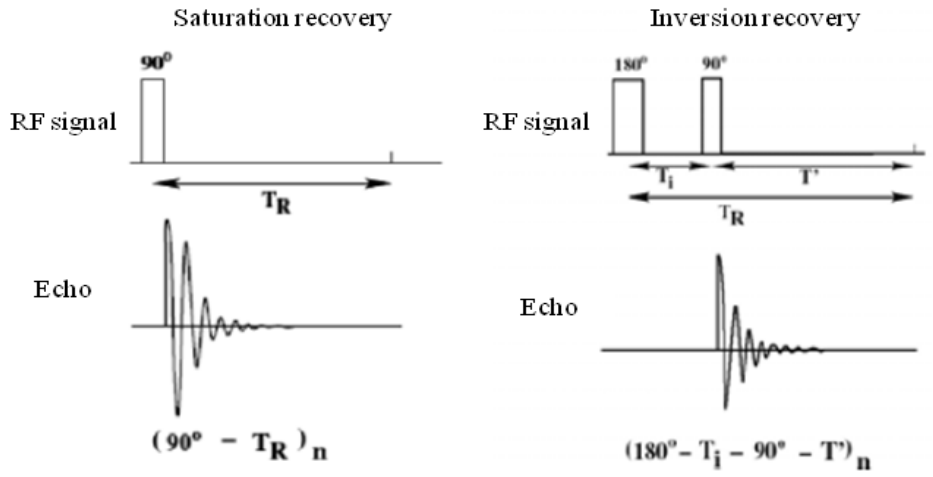

Figure 5.17. Saturation Recovery and Inversion Recovery sequences.

5.2.2 Temperature dependence of T1 relaxation time of water protons: background and application in Laser Ablation

As it is well known, after the transmission, and the successive interruption, of a radio frequency signal to the medium, proton spin recovers the initial position and direction.

Two temporal parameters, i.e., spin-lattice relaxation time T1 and the transversal relaxation time T2, quantify the mechanism of relaxation of the spin proton to recover the equilibrium status, and give information about the structure of the tissue. T2 relaxation time is less attractive than T1 one because its temperature dependence is reduced respect to T1 [21] and can be masked by other factors [22]. Therefore, only the description of T1-based MRI thermometry is reported in detail.

Spin-lattice relaxation in biologic tissues results from dipolar interactions of macromolecules and water molecules, which is due to their translational and rotational motion. The temperature dependence of this motion causes changes to T1, which increases with temperature. The relationship between T1 of water protons and temperature is described by the following equation [23]:

$$T1 \propto \exp\left(-\frac{E_a(T1)}{k \cdot T}\right) \tag{5.7}$$

where $E_a(T1)$ is the activation energy of the relaxation process, k is the Boltzmann constant and T is the absolute temperature. Within a certain temperature range of interest

for hyperthermia purposes (i.e., 30 °C-70 °C), the relationship between T1 and temperature can be considered mostly linear, leading to the following relationship:

$$T_{cur} = \frac{1}{\beta} \cdot \left[T1(T_{cur}) - T1(T_{ref}) \right] + T_{ref} \tag{5.8}$$

being T_{cur} the current temperature value, β^{-1} the slope of the curve, and T_{ref} the reference temperature. The quality of T1-based thermal mapping depends on the accuracy in measuring T1. Lipid suppression should be used because the presence of lipids, which have a different T1 change with temperature, is a potential source of artifacts. Non-linear effects can occur if the tissue properties change, e.g., due to coagulation. Furthermore, since the T1 change due to temperature depends on the tissue type (e.g., 1–2 $\%\cdot°C^{-1}$ in liver, 1.4 $\%\cdot°C^{-1}$ in bovine muscle, and 0.97 $\%\cdot°C^{-1}$ in fat), the previous knowledge of the thermal coefficient of each tissue is essential. Because of these issues, T1 changes are often used to get a qualitative measurement of the temperature distribution [24]. Nevertheless, the above described technique is easily implemented, exhibits high sensitivity to low external magnetic field and low sensitivity to motion.

5.2.3 State of the art

The first study about the relationship of MR parameters with temperature was carried out by Bloembergen *et al.* [25] in 1948, and since 1983 the MRI-based thermometry has been considered as non invasive approach to internal temperature estimation, when Parker *et al.* [23] observed variations in local temperature within water and blood samples. Few years later, Jolesz *et al.* [26] developed the technique of MRI-guided LA, and investigated the capability of MR images to visualize and distinguish the region of tissue damaged by laser energy deposition. MRI-based thermometry emerged as a natural consequence of the LA development, because of the use of MRI-compatible instrumentation (i.e., optical fibers guiding laser beam).

The big research effort to assess the feasibility of temperature monitoring through changes of some MRI parameters has shown that T1 relaxation time and the proton resonance frequency (PRF) are the most attractive ones [27]. The T1 relaxation time dependence on temperature shows the main advantage of high sensitivity at low field; however, it is strongly tissue dependent and the presence of lipid can cause significant artifacts, which can be minimized by lipid suppression techniques [24]. PRF shift method overcomes the strongly dependence on tissue; a further valuable characteristic is the

linearity of its relationship with temperature and the feasibility to be acquired by means of fast sequence (i.e., Echo Planar Imaging, EPI); its main concern is due to motion artifacts [24, 28, 29].

For deeper analyses, the reviews of Plewes and Kucharczyk [30] about the physics of MR, and the one by Rieke and Pauly about MR Thermometry [24] are recommended among others.

5.2.4 Experimental trials: thermal dependence of pancreas T1

In order to obtain the relation in Equation 5.8 for pancreatic tissue, some experiments have been carried out. The method has been preliminary tested on *ex vivo* swine tissue, to verify the suitability of approach, in comparison with published data.

5.2.4.1 Experimental set up

LA was performed by a Nd: YAG laser (1064 nm, Smart 1064, DEKA M.E.L.A s.r.l, Florence, Italy) that conveyed the radiation into an MR-compatible fiber applicator (Thorlabs, core of 300 μm of diameter). It operated with a power of 2 W for 4 minutes on each of the three *ex vivo* healthy porcine livers and two pancreases undergoing LA. The approach is similar to the one employed to perform CT-based thermometry (cfr. Paragraph 5.1.3.2).

The experimental set up and the positions of FBGs is reported in Fig. 5.18:

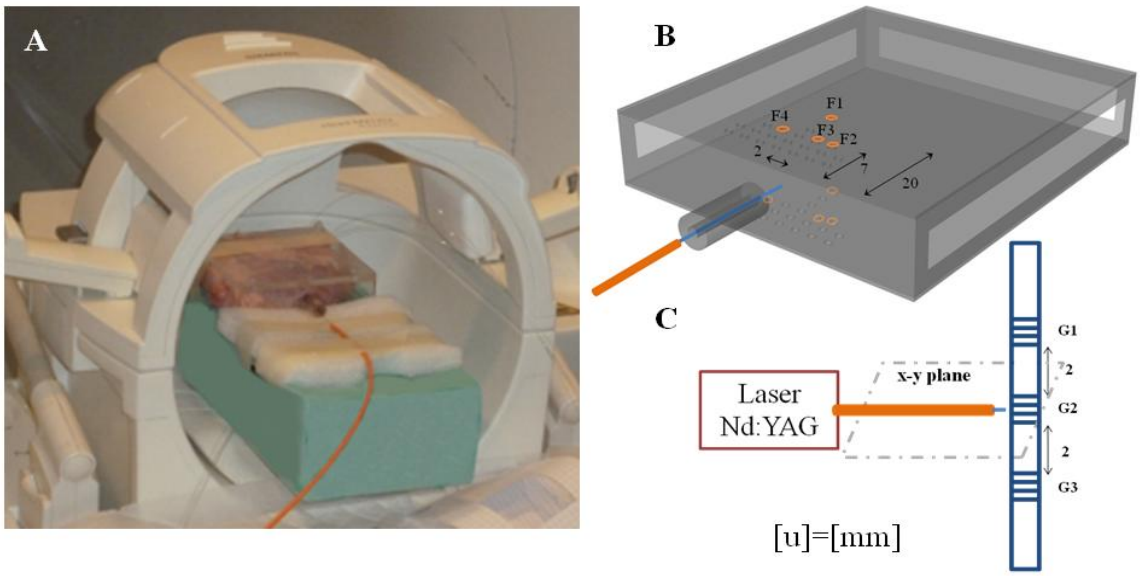

Figure 5.18. A) Experimental set-up: pancreatic tissue inside polymeric mask used to arrange laser applicator and FBGs, placed within MR coils; B) relative distances, guaranteed by the polymeric mask,

between laser applicator and optical fibers housing FBG; C) quotes of each FBG with respect to the x-y plane of the laser applicator.

Each of four fibers F1, F2, F3, F4, is equipped with 3 FBG sensors with length of 1 mm. The laser applicator was inserted into the tissue at a depth of 2 mm and exactly at the center of the box. Three FBGs, G1, G2 and G3, housed in each optical fiber, are placed at a distance of 2 mm each other; considering that the x-y plane of the applicator is perpendicular to the plane of the optical fibers, the central FBG, i.e., G2, is placed at the same quote of the applicator (Fig. 5.18C). The four fibers were placed at the same four positions in all the tests corresponding to the center of the four ROIs which were selected to analyze the images.

The heating process was monitored by the 1.5-T MR scanner (Siemens Avanto), utilizing two different T_1-weighted sequences: inversion recovery turbo flash (IRTF) and saturation recovery turbo flash (SRTF). The sequences parameters are listed in Table V.

Table V. SRFT and IRFT sequence parameters used for MR-thermometry during LA on porcine pancreases and livers.

parameters	IRFT	SFRT
TR [ms]	820	820
TE [ms]	1.6	1.6
TI [ms]	520	520
FA [°]	20	20
FOV [mm]	280x280	280x280
ST [mm]	4	4
Matrix [pixel]	128x128	128x128
Bandwidth [Hz/pixel]	399	399
TA [s]	820	820

These parameters were chosen in order to obtain a high image quality and signal to noise ratio within a reasonable acquisition time (TA<3s) [28]. The two sequences were alternately repeated 8 times during the whole ablation procedure (treatment time of 4 min).

Definitively, 8 IRTF and 8 SRTF images were obtained for each porcine liver and pancreas.

Four ROIs centered in the same positions of the 4 FBG fibers, were selected for each MR image using the Radiant Dicom Viewer software. The averaged pixel value of each ROI, with a circular shape of 0.1 cm^2 (3 pixels), was read out. The data were elaborated in Matlab® environment.

5.2.4.2 Results in liver tissue: temperature trends and MR-based thermometry

5.2.4.2.1 Temperature monitoring

Figure 5.19 shows the temperature increases, ΔT, monitored by F1, F2, F3 and F4 during LA, as a function of time, t. These data were obtained within one of the three porcine livers; the same experimental setup and the LA parameters, were used for the other two healthy porcine livers.

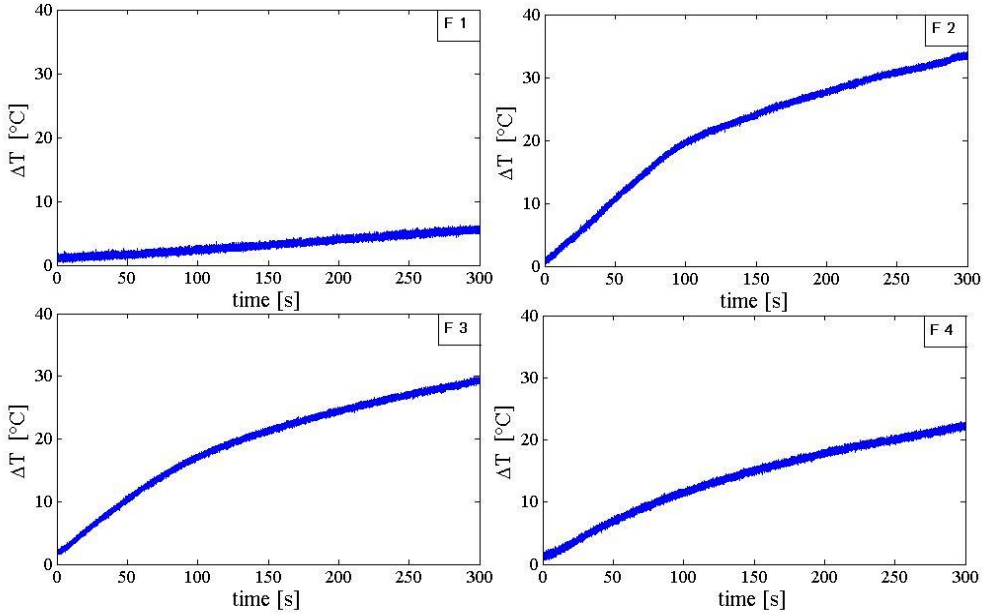

Figure 5.19. Temperature increases, ΔT, as a function of time, t, monitored by F1, F2, F3 and F4 in porcine liver undergoing LA.

5.2.4.2.2 Temperature measurement with MR T_1-weighted images

Figure 5.20 shows the signal intensity trend (pixel value) as a function of time during the whole LA procedure, for the same porcine liver considered in Fig. 5.19.

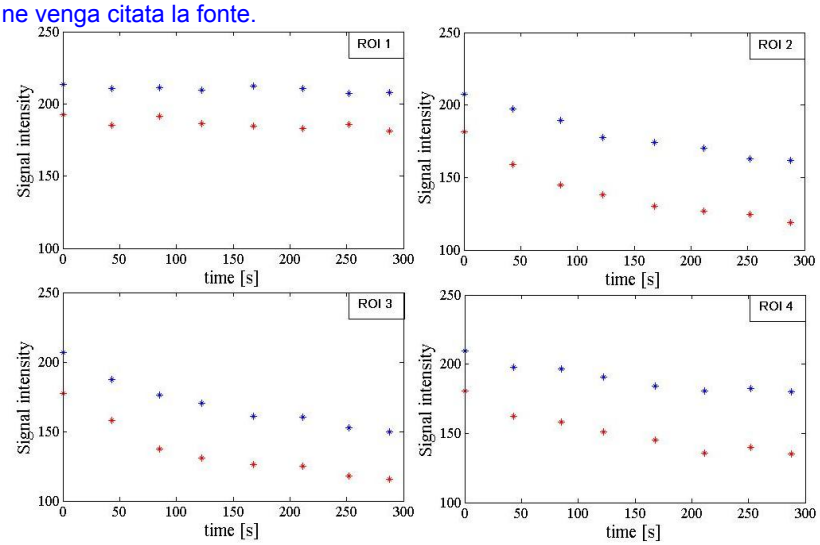

Figure 5.20. Intensity variations within the four ROIs during LA on liver: image obtained with SRTF (blue dots) and IRTF (red dots) .

The image signal intensity of the three porcine livers presents a decreasing trend during the ablation procedure in the ROIs 2, 3 and 4, due to the high temperature increment; on the other hand, the averaged signal intensity of ROI 1 is characterized by an almost constant trend due to the higher distance from the laser applicator.

In order to obtain the relationship between the signal intensity variation, ΔS, and the temperature increase, ΔT, the averaged intensity of each ROI of the three livers was correlated and synchronized with the temperature values monitored by the related FBGs. In particular, ΔS is the ROI value difference between the current and the reference image acquired at the beginning of the trial.

Finally, data of ROIs 2, 3 and 4 of each liver were matched for a global assessment of the experiment, obtaining $\Delta S = f(\Delta T)$ for the IRTF and SRTF images. ROI 1 data were considered as reference. The trend and the best fitting line are shown in Fig. 5.21.

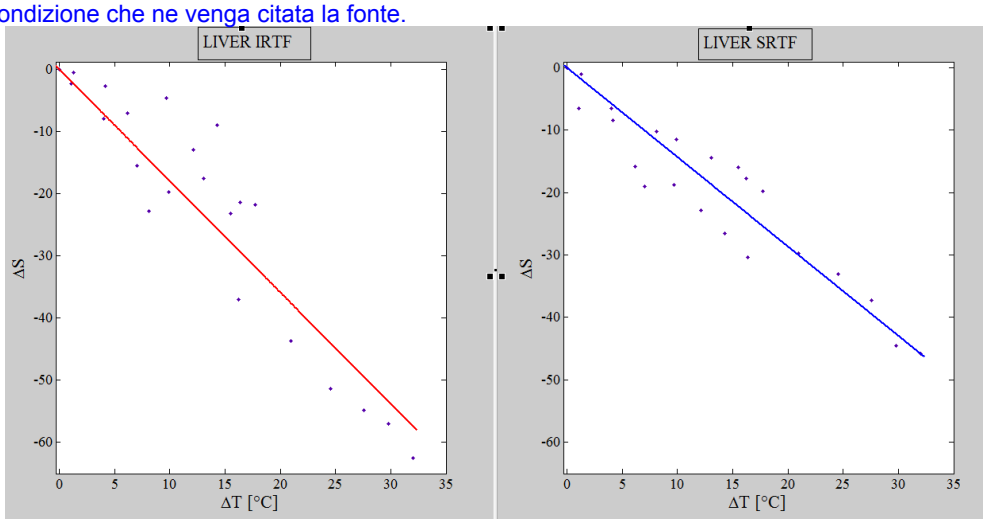

Figure 5.21. Intensity variations (ΔS) vs temperature increase in liver undergoing LA: experimental data (dots) and best fitting lines (continuous lines).

Considering Equation (5.8), the slope of the fitting lines in Figure 5.21 represents the thermal coefficient β, corresponding to the temperature sensitivity of the MR sequence. Table VI shows the thermal coefficient β, the Pearson correlation coefficient R, and the significance of the linear fitting.

Table VI. Thermal coefficient, β, Pearson correlation coefficient, R, and the significance, p-value, of the linear fitting in liver tissue.

	β [°C^{-1}]	R	p-value
IRFT	[-1.8 ±0.2]	-0.94	<0.001
SRFT	[-1.4 ±0.1]	-0.94	<0.001

In order to analyze the difference between the MR-based temperature measurements and the reference ones (measured by FBGs) the Bland-Altman analysis for both IRTF and SRTF data was carried out and it is shown in Figure 5.22. The MR-based temperature measurements were calculated through the thermal coefficient of the sequence and the signal intensity variation. In Table VII are reported the Mean Of Difference (MOD) and Limits Of Agreement (LOA) values for the two sequences.

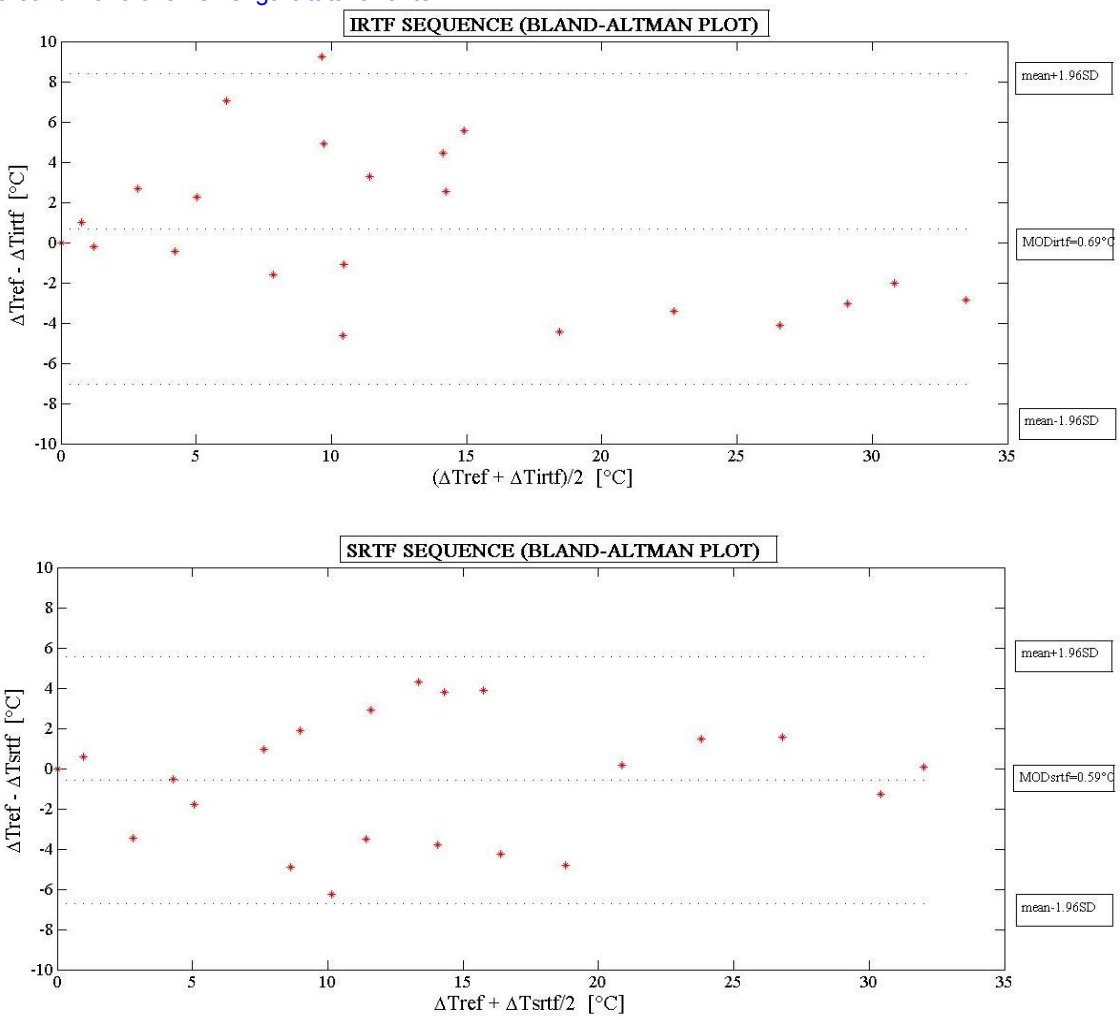

Figure 5.22. Band-Altman plot for measurements performed on livers with the two sequences. The limits of agreement and the mean of difference are reported with dotted lines.

Table VII. Mean of difference (MOD) and limits of agreement (LOA) values for the two sequences used for MR-thermometry in liver.

	MOD [°C]	LOA [°C]
IRFT	-0.7	9.1/ -9.4
SRFT	-0.6	2.1/ -2.3

MOD values provide information on the accuracy of the temperature measurements and on the systematic mean bias. LOA values evaluate the data dispersion with a confidence level of 95%.

5.2.4.3 Results in pancreatic tissue: temperature trends and MR-based thermometry

5.2.4.3.1 Temperature measurement with FBGs

Figure 5.23 reports the temperature monitored by the FBGs during LA for one sample of the two porcine pancreas. Similar trends were obtained for the other pancreas sample. In particular, F1, i.e. the most distant fiber from the laser applicator (d=2 cm), recorded a maximum temperature increase of ΔT=2 °C. F2, F3 and F4 showed, instead, a significant increase in temperature. The maximum ΔT, measured by F4, has a value of about 25 °C.

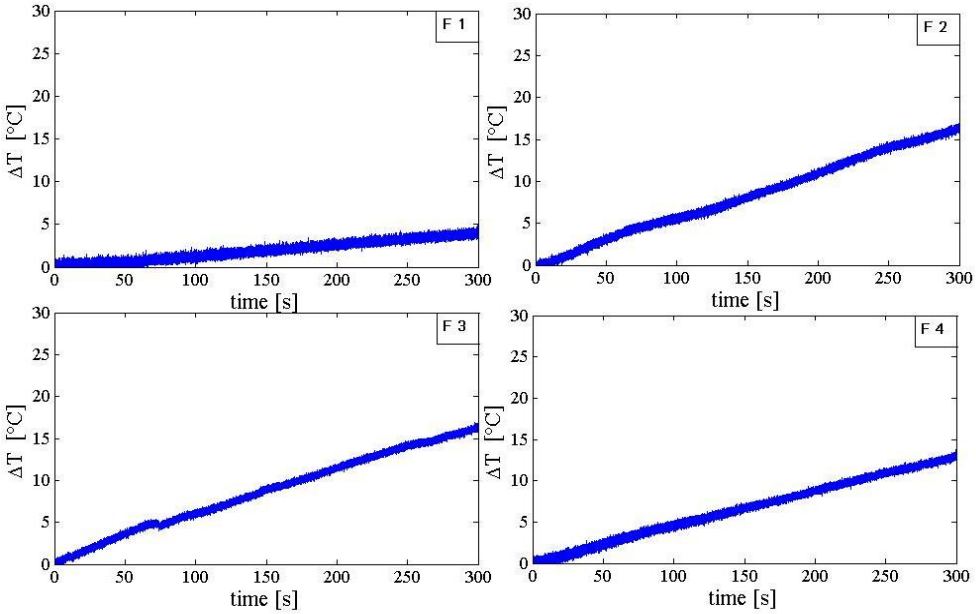

Figure 5.23. Temperature increases, ΔT, as a function of time, t, monitored by F1, F2, F3 and F4 in porcine pancreas undergoing LA.

5.2.4.3.2 Temperature measurement with MR T_1-weighted images

Figure 5.24 shows the signal intensity trend with time during the ablation procedure for the same pancreas considered in Figure 5.23.

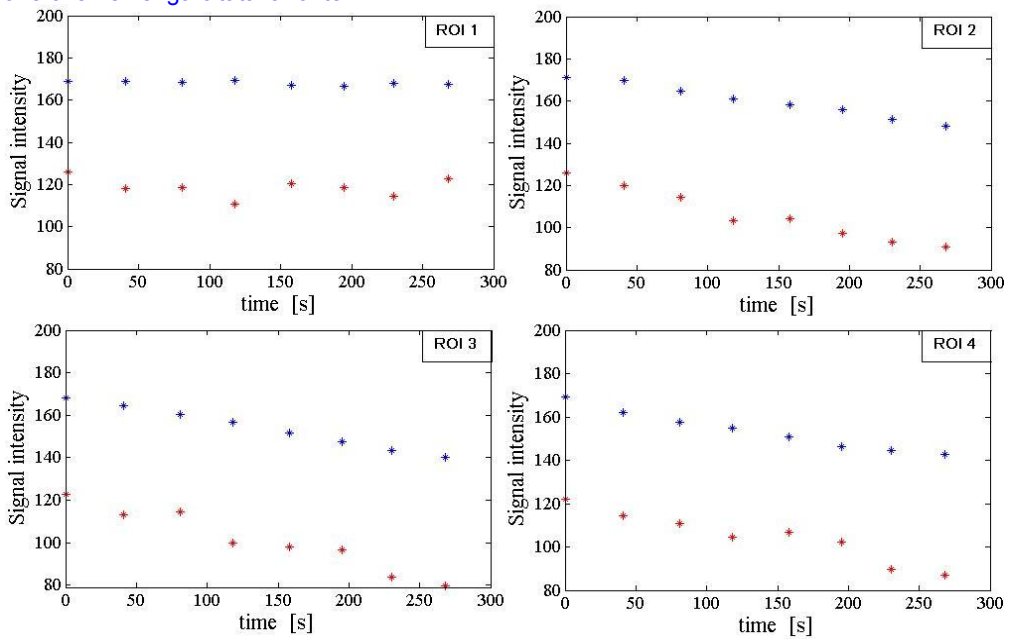

Figure 5.24. Intensity variations within the four ROIs during LA on pancreas: image obtained with SRTF (blue dots) and IRTF (red dots).

As seen for liver trials, the relationship between the ROI signal intensity and time shows a decreasing trend in ROI 2, 3 and 4, confirming the temperature trend. ROI 1, instead, shows a negligible temperature dependence.

Finally, ROIs 2, 3 and 4 data of each pancreas were correlated to the respective FBGs temperature. ROI 1 was considered as reference. For a global assessment of the experimental test, the signal intensity trend of each trial was matched, obtaining $\Delta S=f(\Delta T)$ for IRTF and SRTF sequences (Fig. 5.25).

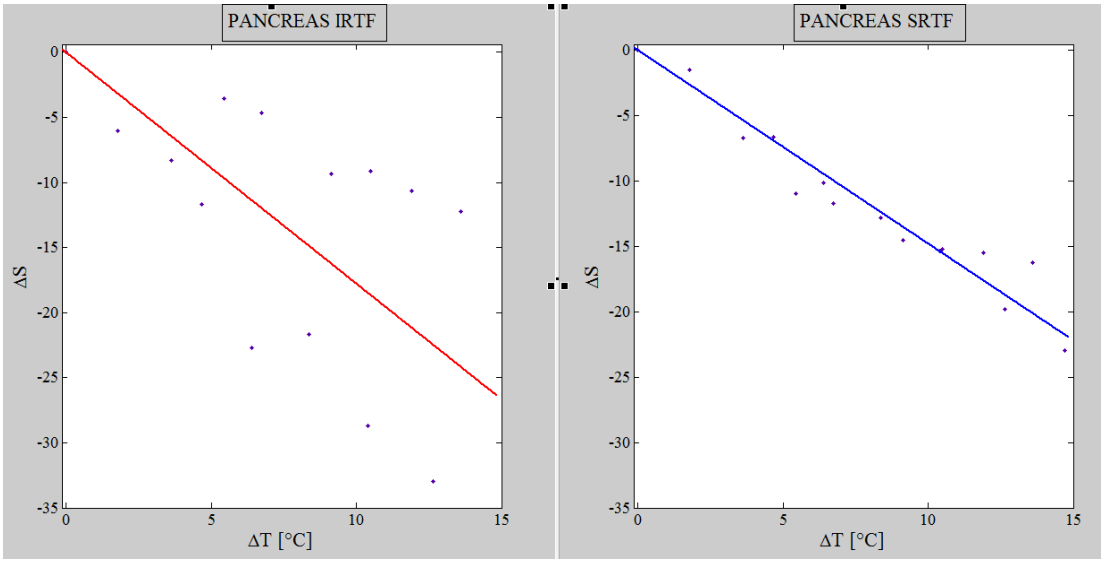

Figure 9. Intensity variations (ΔS) vs temperature increase in pancreas undergoing LA: experimental data (dots) and best fitting lines (continuous lines).

In Table VIII, the same parameters evaluated for the livers are listed: the thermal coefficient β, the Pearson correlation coefficient R and the p-value. These parameters allow evaluating the temperature sensitivity of each sequence, the correlation between the reference temperature and the signal intensity variation read out from the MR-images and the trial significance.

Table VIII. Thermal coefficient, β, Pearson correlation coefficient, R, and the significance, p-value, of the linear fitting in pancreatic tissue.

	β [°C^{-1}]	R	p-value
IRFT	[-1.8 ±0.5]	-0.66	<0.001
SRFT	[-1.5 ±0.1]	-0.97	<0.001

In order to compare the temperature obtained from the signal intensity trend and the FBGs temperature, the Bland Altman analysis for the IRTF and SRTF data was carried out (Figure 5.26). The MOD and LOA values of each sequences are listed in Table IX.

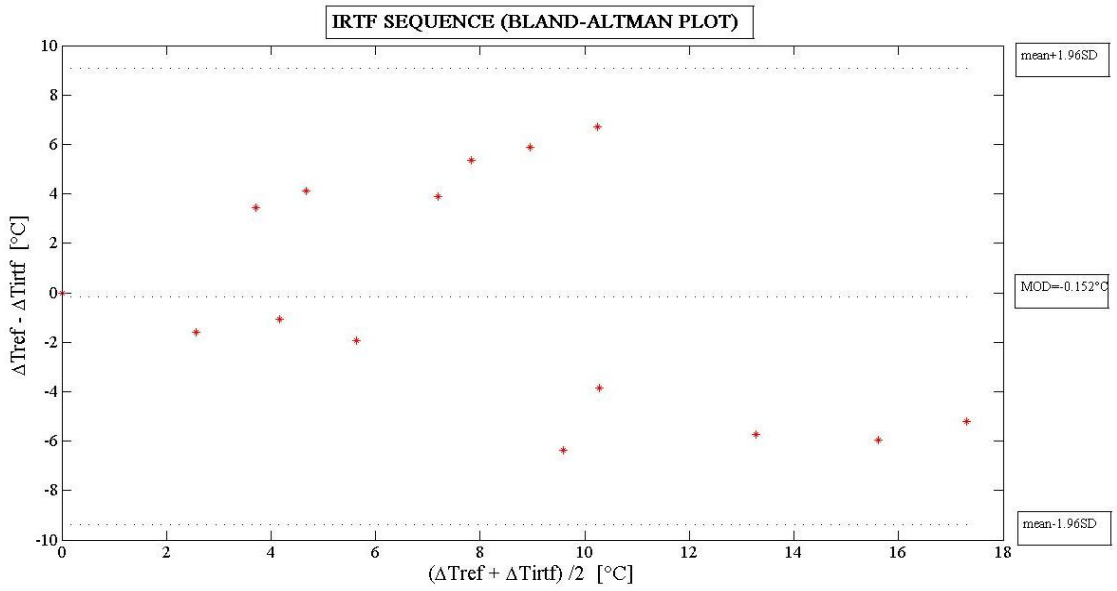

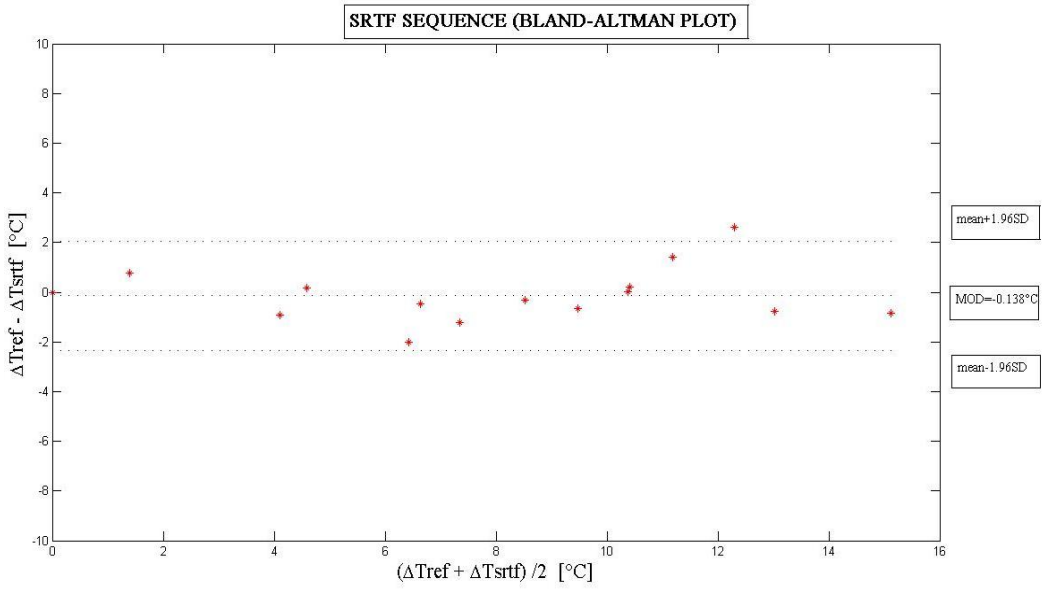

Figure 5.26. Band-Altman plot for measurements performed on pancreases with the two sequences. The limits of agreement and the mean of difference are reported with dotted lines.

Table IX. Mean of difference (MOD) and limits of agreement (LOA) values for the two sequences used for MR-thermometry in pancreas.

	MOD [°C]	LOA [°C]
IRFT	-0.1	9.1/ -9.4
SRFT	-0.1	2.1/ -2.3

6. Discussion and Conclusion

In this study, the temperature accuracy, sensitivity and precision during LA on healthy porcine pancreas and liver of two different T_1-weighted sequences, i.e. IRTF and SRTF, have been evaluated. FBGs have been used to measure the temperature during the treatment. The main advantage of the use of FBGs is the absence of measurement artifacts, due to radiation absorption, as in case of thermocouples; such artifacts can cause overestimation of up to 20 °C [31]. Moreover, the errors introduced by the FBG strain (less than 1 °C) have been investigated in our previous work and found negligible (cfr. Paragraph 5.1.3.1 and [13]).

Furthermore, the sequence parameters have been chosen in order to obtain a high image quality and signal to noise ratio within a reasonable acquisition time. They were set identical in the two sequences in order to provide the acquisition consistency.

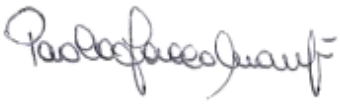

The results obtained on the livers agree with those already reported in literature, in particular the IRTF sequence resulted more temperature sensitive than the SRTF: [-1.8±0.2] $°C^{-1}$ IRTF sequence, [-1.4 ±0.1] $°C^{-1}$ SRTF sequence. These data correspond, to some extent, with the results reported by Bazrafshan *et al.* [28] for a liver-mimicking gel phantom. Furthermore, it has been analyzed for the first time the temperature sensitivity of the same MR-sequences on porcine pancreas. Like the liver tests, IRTF sequence was more sensitive than the SRTF sequence: [-1.8±0.5] $°C^{-1}$ IRTF sequence, [-1.5±0.1] $°C^{-1}$ SRTF sequence.

The SRTF sequence was in both cases less sensitive but more accurate and precise. Moreover, a stronger correlation between the liver reference value, ΔT, and the liver signal intensity variation, ΔS, has been obtained compared to the pancreas correlation; it is highlighted by the pancreas data significance, lower than the p-value calculated for trials on liver. This discrepancy may be linked to the different characteristics of the two tissues, in particular to the greater inhomogeneity of the pancreas compared to the liver. In this case the PRF tissue-independent sequence appears to be more suitable. Although these trials have never been carried out in an *ex vivo* pancreas, the results are comparable with those present in literature, obtained from other tissues.

In terms of accuracy, represented by MOD, for both the liver and the pancreas sequences, a MOD value lower than 1 °C has been obtained: for the liver MOD_{SFRT}=0.6 °C and MOD_{IFRT} =-0.7 °C , for the pancreas MOD_{SFRT}= -0.1 °C and MOD_{IFRT}= -0.1 °C. These data are lower than those reported in previous studies [32]: for the liver MOD_{SFRT} =1.57 °C and MOD_{IFRT}=1.65 °C.

LOA gives information related to the data dispersion with a level of confidence of 95%. For the IRTF sequence it has been obtained a confidence interval greater than the SRTF sequence one, for both the liver and the pancreas, in agreement with results reported by Bazrafshan *et al.* [32].

Bibliography Chapter 5

[1] P. Homolka, A. Gahleitner and R. Nowotny, "Temperature dependence of HU values for various water equivalent phantom materials," *Phys Med Biol*, vol. 47, pp. 2917-2923, 2002.

[2] G. D. Pandeya, D. Ganga, M. J. Greuter, K. P. De Jong, B. Schmidt, T. Flohr and O. M., "Feasibility of Noninvasive Temperature Assessment During Radiofrequency Liver Ablation on Computed Tomography," *J Comput Assist Tomo*, vol. 35, pp. 356-360, 2011.

[3] P. Bruners, G. D. Pandeya, E. Levit, E. Roesch, T. Penzkofer et al, "CT-based temperature monitoring during hepatic RF ablation: Feasibility in an animal model," *Int J Hyperther*, vol. 28, pp. :55-61, 2012.

[4] G. M. Bydder and L. Kreel, "The temperature dependence of Computed tomography attenuation values," *J Comput Assist Tomo*, vol. 3, pp. 506-510, 1979.

[5] B. G. Fallone, P. R. Moran and E. B. Podgorsak, "Noninvasive thermometry with a clinical x-ray CT scanner," *Med Phys*, vol. 9, pp. 715-721, 1982.

[6] T. C. Cetas, "Will Thermometric Tomography Become Practical for Hyperthermia Treatment Monitoring?," *Cancer Res*, vol. 44, pp. 4805s-4808s, 1984.

[7] A. H. Mahnken and P. Bruners, "CT thermometry: will it ever become Ready For Use?," *Int J Clin Pract*, vol. 65, no. s171, pp. 1-2, 2011.

[8] P. Bruners, G. D. Pandeya, E. Levit, E. Roesch, T. Penzkofer, P. Isfort et al, "CT-based temperature monitoring during hepatic RF ablation: Feasibility in an animal model," *Int J Hyperther*, vol. 28, pp. 55-61, 2012.

[9] G. D. Pandeya, M. J. Greuter, B. Schmidt, T. Flohr et al, "Assessment of thermal sensitivity of CT during heating of liver: an ex vivo study," *Brit J Radiol*, vol. 85, pp. e661-e665, 2012.

[10] G. D. Pandeya, J. H. G. M. Klaessens, M. J. W. Greuter, B. Schmidt, T. Flohr, R. Van Hillegersberg and M. Oudkerk, "Feasibility of computed tomography based thermometry during interstitial laser heating in bovine liver," *Eur Radiol*, vol. 21, pp. 1733-1738, 2011.

[11] P. Bruners, E. Levit, T. Penzkofer, P. Isfort, C. Ocklenburg, B. Schmidt et al., "Multi-slice computed tomography: A tool for non-invasive temperature measurement?," *Int J Hyperther*, vol. 26, pp. 359-365, 2010.

[12] L. Frich, "Non-invasive thermometry for monitoring hepatic radiofrequency ablation," *Minim Invasiv Ther*, vol. 15, pp. 18-25, 2006.

[13] E. Schena, P. Saccomandi, F. Giurazza, M. A. M A Caponero, L. Mortato, F. M. Di Matteo, F. Panzera, R. Del Vescovo, B. Beomonte Zobel and S. S Silvestri, "Experimental assessment of CT-based thermometry during laser ablation of porcine pancreas," *Phys Med Biol*, vol. 5075, p. 58, 2013.

[14] P. Saccomandi, E. Schena, M. A. Caponero, F. M. Di Matteo, M. Martino, M. Pandolfi and S. Silvestri, "Theoretical analysis and experimental evaluation of laser induced interstitial thermotherapy in ex vivo porcine pancreas," *IEEE Transactions on Biomedical Engineering*, vol. 59, no. 10, pp. 2958-64, 2012.

[15] J. W. Valvano, J. R. Cochran and D. K. R, "Thermal conductivity and diffusivity of biomaterials measured with self-heated thermistors," *International Journal of Thermophysics*, vol. 6, pp. 301-311, 1985.

[16] R. Poprawe, "Tailored Light 2: Laser Application Technology, 1st edn," Berlin, Germany, Springer, 2011 .

[17] S. C. Gnyawali, Y. Chen, F. Wu, K. E. Bartels, J. P. Wicksted, H. Liu, C. K. Sen and W. R. Chen, "Temperature measurement on tissue surface during laser irradiation," *Med. Biol. Eng. Comput.* , vol. 46, pp. 159-68, 2008.

[18] T. Flohr, C. Mc Collough, H. Bruder and al, "First performance evaluation of a dual-source CT (DSCT) system.," *Eur Radiol*, vol. 16, p. 256–68, 2006.

[19] J. Paul, R. W. Bauer, W. Maentele and T. J. Vogl, "Image fusion in dual energy computed tomography for detection of various anatomic structures –

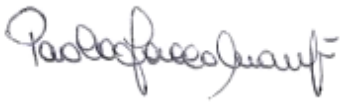

Effect on contrast enhancement, contrast-to-noise ratio,signal-to-noise ratio and image qualitiy," *European Journal of Radiology*, vol. 80, pp. 612-19, 2011.

[20] A. Roggan, V. Knappe, M. G. Mack, T. J. Vogl, D. Albrecht, C. T. Germer, J. P. Ritz, F. Knieppe and G. Müller, "Experimental study and first clinical results with a cooled applicator system for interstitial laser coagulation (LITT)," *Proc SPIE*, vol. 3249, pp. 85-93, 1998.

[21] D. L. Parker, "Applications of NMR Imaging in Hyperthermia: An Evaluation of the Potential for Localized Tissue Heating and Noninvasive Temperature Monitoring," *IEEE T Biomed Eng*, vol. 31, pp. 161-167, 1984.

[22] S. J. Graham, M. J. Bronskill and R. M. Henkelman, "Time and temperature dependence of MR parameters during thermal coagulation of ex vivo rabbit muscle," *Magn Reson Med*, vol. 39, pp. 198-203, 1998.

[23] D. L. Parker, V. Smith, P. Sheldon, L. E. Crooks and L. Fussell, "Temperature distribution measurements in two-dimensional NMR imaging," *Med Phys* , vol. 10, pp. 321-325, 1983.

[24] V. Rieke and K. B. Pauly, "MR Thermometry," *J Magn Reson Imaging* , vol. 27, pp. 376-390, 2008.

[25] N. Bloembergen, E. M. Purcell and R. V. Pound, "Relaxation effects in nuclear magnetic resonance absorption," *Phys Rev*, vol. 73, pp. 679-712, 1948.

[26] F. A. Jolesz, A. R. Bleier, P. Jakab, P. W. Ruenzel, K. Huttl and G. J. Jako, "MR imaging of laser-tissue interactions," *Radiology*, vol. 168, pp. 249-53, 1988.

[27] N. McDannold, "Quantitative MRI-based temperature mapping based on the proton resonant frequency shift: Review of validation studies," *Int J Hyperther*, vol. 21, pp. 533-546, 2005.

[28] B. Bazrafshan, F. Hübner, F. P, R. Hammerstingl, J. Paul, V. Vogel, W. Mäntele and T. J. Vogl, "Temperature imaging of laser-induced thermotherapy (LITT) by MRI: evaluation of different sequences in phantom," *Laser Med Sci* , pp. 1-11 , 2013.

[29] T. J. Vogl, R. Straub, S. Zangos, M. G. Mack and K. Eichler, "MR-guided

laser-induced thermotherapy (LITT) of liver tumours: experimental and clinical data," *Int J Hyperthermia*, vol. 20, pp. 713-724, 2004.

[30] D. B. Plewes and W. Kucharczyk, "Physics of MRI: a Primer," *J Magn Reson Imaging* , vol. 35, pp. 1038-54, 2012.

[31] F. Manns, P. J. Milne, X. Gonzalez-Cirre, D. B. Denham, J. M. Parel and D. S. Robinson, "In Situ Temperature Measurement With Thermocouple Probes During Laser Interstitial Thermotherapy (LITT): Quantification and Correction of a Measurement Artifact," *Laser Surg Med*, vol. 23, pp. 94-103, 1998.

[32] B. Bazrafshan, F. Hübner, P. Farshid, R. Hammerstingl, J. Paul, V. Vogel, W. Mäntele and T. J. Vogl, "Magnetic resonance temperature imaging of laser-induced thermotherapy: assessment of fast sequences in ex vivo porcine liver," *Future Oncol*, vol. 9, pp. 1039-1050, 2013.

Chapter 6. Ablation volumes

Temperature distribution within laser irradiated tissue is responsible of the ablation volumes. Theoretical predictions of coagulated and vaporized volumes have been performed as explained in Paragraph 2.2.2 and, in the following, the experimental assessment is illustrated. Volumes have been measured with two methods: histological technique and MR image.

6.1 Histological method

Experimental trials have been carried out on *ex vivo* animal models: 40 porcine healthy pancreases underwent LA after being excised [1]. A Nd:YAG laser (Echolaser X4, Elesta s.r.l., Florence, Italy) was utilized and the treatment was performed using a bare fiber applicator consisting of a quartz optical fiber with 300 µm core diameter. Four power (P) values have been utilized, namely 1.5 W, 3 W, 6 W and 10 W, to deliver always the same energy (E) amount (1000 J). After performing LA, animal organs were immediately placed in formalin and underwent histological examination in order to analyze and measure the size of injured volumes due to hyperthermia. Each organ was cut in slices and the three abovementioned regions were identified: the vaporized (V), the coagulated (C), and the unaffected (H) one.

For each slice, the lesion area (Fig. 6.1A) was calculated using Nikon System Software Arkon (Nikon Instruments S.p.A., Calenzano Florence, Italy); then it was multiplied for the thickness of the slice. By summing the volumes of each slice the whole vaporized volume (V_v) was calculated (Fig. 6.1B).

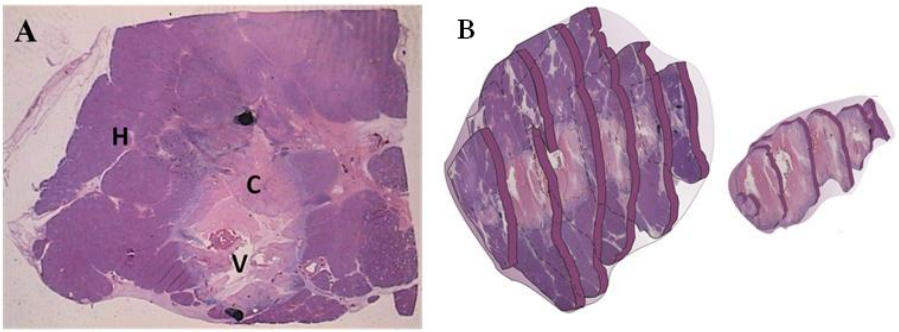

Figure 6.1. A) Specimen of pancreatic tissue undergone laser thermotherapy: coagulated (C), vaporized (V) and healthy (H) regions are distinguished in samples after the LA treatment; B) reconstructions of slices of treated pancreas cut by microtome.

Same procedure has been performed to estimate the coagulated region. During the preparation of specimens, the fibre applicator was left in the treated tissue, in order to cut slices parallel to the applicator axis.

Briefly, V_v has been simply theoretically calculated considering the region of tissue where T >100 °C, whereas the volume where the condition 60 °C<T<100 °C has been reached is indicated as V_c.

Experimental V_v and V_c, reported in Table I, are expressed as mean value ± expanded uncertainty. The same laser power value has been set on 10 samples, so the expanded uncertainty is estimated by multiplying the standard deviation of the 10 measurements with a coverage factor of 2.26, obtained considering a Student's distribution with 9 degrees of freedom and a level of confidence of 95 % [2].

Table I. laser settings and experimental results

N	P [W]	E [J]	t_l [s]	V_v [mm^3]	V_c [mm^3]
10	1.5	1000	667	0	415±73
10	3	1000	333	40±30	1750±190
10	6	1000	167	77±24	1964±400
10	10	1000	100	96±20	2205±392

Both V_v and V_c values increase with P up to 10 W. In particular, V_v is absent at P=1.5 W for all treated pancreas samples thus, at low power values, only the coagulated region is present. V_c values obtained by simulation results, as a function of laser power, have been compared with experimental values and are reported in Fig. 6.2A.

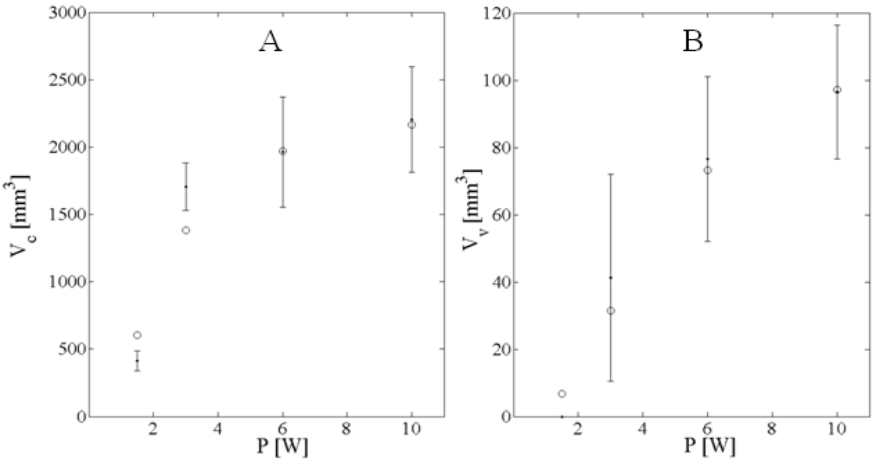

Fig. 6.2. A) Comparison between theoretical *ex vivo* V_c values (circles) and experimental ones (dots) as function of P; B) Comparison between theoretical *ex vivo* V_v values (circles) and experimental ones (dots) as function of P.

Theoretical V_c values non-linearly increase with P, showing a trend in good agreement with the experimental data. The comparison between theoretical and experimental data of V_c and V_v as a function of P can be expressed by the percentage variation, according to the following formula:

$$\Delta V\%(P_1 \to P_2) = \frac{\left|\bar{V}(P_1) - \bar{V}(P_2)\right|}{\bar{V}(P_1)} \cdot 100 \tag{6.1}$$

where $\bar{V}(P)$ is the mean value of V_c or V_v at a particular P.

The agreement between experimental and theoretical V_c values is evaluated by the following results calculated with Equation 6.1: e.g., from 3 W to 6 W, the measured $\Delta V_c\%$=15%, whereas the theoretical one is 43 %; the agreement improves from 6 W to 10 W, where both tests and simulations show an increase of 12 %.

Similar results have been found if theoretical and experimental V_v values are compared (Fig. 6.2B). If P increases from 3 W to 6 W experimental results show an increase of 86 %, versus a theoretical increment of 132 %; lastly, from 6 W to 10 W, measurements increase of 26 % versus a theoretical 32 %.

Therefore, a quite good agreement is found between the trends of experimental results and simulated ones. Generally speaking, treated volumes increase with P, whereas the volume increment decreases with P.

6.2 MR image

Paragraph 4.1.6 reports a double applicator laser thermotherapy on *ex vivo* swine pancreas. In this study, V_v has been experimentally estimated through MR image [3].

The theoretical results of the ablated tissue volume, calculated as the volume of the region where T reaches 100 °C, is 0.95 cm^3. This value agrees with the experimental value obtained by means of measurements based on MR images. In particular, the best results are obtained with T1-weighted gradient-echo (3D flash) sequences with fat saturation in the axial plane, where the lesion appeared as a hypointense area in the parenchyma with a thin peripheral hyperintense margin; to be sure that no artifacts influenced our analysis, the ablated cavity is filled with gadolinium (Dotarem Gadoteric Acid, Guerbet®, Ireland), a

paramagnetic contrast agent commonly used in MR imaging which appears hyperintense in T1-weighted images (Fig. 6.3A).

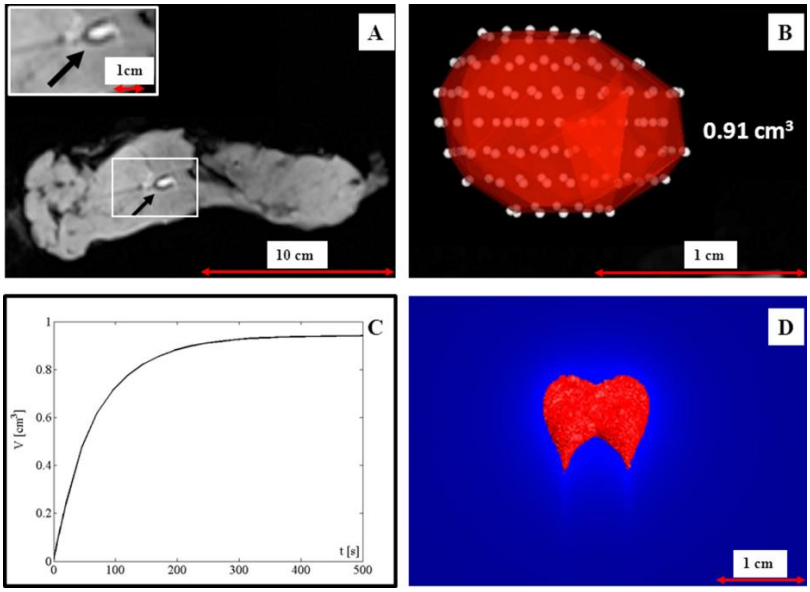

Fig. 6.3. MR image of the pancreas: A) after laser treatment where the ablated tissue volume appears as a hypointense area, B) 3D volume rendering post-processing reconstruction of the ablated tissue, C) ablated volume as a function of treatment time obtained by the simulation, and D) predicted ablated volume at the end of the treatment

The post-processing image software used to quantify the ablation is Osirix (Apple Inc.®, Cupertino, California, USA); a three-dimensional representation of the lesion is obtained and the volume has been semi-automatically computed (Fig. 6.3B). The ablated volume as a function of treatment time obtained by simulation and the predicted ablated volume at the end of the procedure are shown in Fig. 6.3C and 6.3D, respectively.

The volume calculations by post-processing the images are repeated seven times in order to examine the repeatability of the method; the result is expressed as mean volume ± the expanded uncertainty: 0.91 ± 0.09 cm^3. The expanded uncertainty is estimated by multiplying the standard deviation of the seven measurements with a coverage factor of 2.45, which is obtained considering a Student's distribution with six degrees of freedom and a level of confidence of 95% [2].

Bibliography Chapter 6

[1] P. Saccomandi, E. Schena, M. A. Caponero, F. M. Di Matteo, M. Martino, M. Pandolfi and S. Silvestri, "Theoretical analysis and experimental evaluation of laser induced interstitial thermotherapy in ex vivo porcine pancreas," *IEEE Transactions on Biomedical Engineering,* vol. 59, n. 10, pp. 2958-64, 2012.

[2] Guide to the Expression of Uncertainty in Measurement, JCGM 100, 2008.

[3] P. Saccomandi, E. Schena, F. Giurazza, R. Del Vescovo, M. A. Caponero, L. Mortato, F. Panzera, R. L. Cazzato, F. R. Grasso, F. M. Di Matteo, S. Silvestri and B. Beomonte Zobel, "Temperature monitoring and lesion volume stimatio during double-applicator laser induced thermotherapy in ex vivo pancreas: a preliminary study," *Laser Med Sci,* pp. 1-8, 2013.

Conclusions

The preset PhD research project regarded the study of interaction between laser light and pancreatic tissue. The aim was the assessment of Nd:YAG effects on pancreas, in order to evaluate the feasibility of Laser Ablation (LA) on this organ.

Aiming to provide a tool to predict Nd:YAG effects on pancreas, the study was organized into three parts: 1) the implementation of a mathematical model to describe the effects of laser light on tissue, and to predict the effects of different laser settings (i.e., power, energy and time) on organ; 2) the assessment of causes of laser-tissue interaction, i.e, tissue optical properties, as well as 3) the measurement of effects, in terms of temperature distribution and ablation volumes. In both cases 2) and 3), experimental trials have been performed, and results compared with previous published data, when possible. This issue was related to the lack about optical and thermal response of pancreas, since no studies about LA on pancreas have been performed since now, at the best of my knowledge.

Theoretical model was based on the Pennes Bioheat equation, describing the conduction phenomenon on biological tissue, and coupled with different methods for modeling laser-tissue interaction: the first one describes the laser beam as a Gaussian beam, whereas the second one is based on Monte Carlo simulation, for the description of photon trajectory within the tissue. The first method is the simplest one, requires the use of a unique software to be implemented, and it is preferred to simulate the temperature effects of LA induced by bare fiber applicator; the second one is suitable to simulate the outcomes induced by laser applicator with diffusing surfaces. Theoretical results, in terms of temperature distribution and ablation volumes, provided by the first model are in agreement with experimental data on *ex vivo* pancreatic swine tissues.

As far as it concerns the assessment of tissue optical properties, an experimental set up based on double integrating spheres has been assembled. The measurement of power light reflected and transmitted by human pancreas slices with thickness of 100 μm was used to estimate the total attenuation coefficient, equal to 88±5 cm^{-1} for a laser source of 1064 nm. This a reasonable value for fresh tissue at this wavelength, in comparison with previously investigated tissues.

Another experimental set up, based on goniometric and spectroscopic techniques has been employed to perform the direct measurement of anisotropy coefficient of tissue. It was originally designed for the investigation of clear solution, but at the department of Biophysics of Goethe University of Frankfurt a preliminary trial on highly scattering media, like biologic tissue, was carried out. In particular, three swine liver samples with thickness of 60 μm and LED source of 850 nm were employed in the study. Through sum of two Henvey-Greenstein curves, the anisotropy forward-scattering coefficient was found to be 0.947, whereas the anisotropy backward-scattering coefficient was -0.498, with probability of 96% and 4%, respectively. These data are in agreement with values already published for liver tissue at 850 nm. Furthermore, the total attenuation coefficient of liver was calculated, and the value of μ_t=90±20 cm^{-1} is in accord with published data for porcine liver at 850 nm. Promising results obtained with the goniometric and spectroscopic techniques encourage to employ the set up also for the measurement of anisotropy coefficient of pancreatic tissue.

Assessment of effects of Nd:YAG on pancreas was performed in terms of temperature distribution monitoring and ablated volumes measurement.

Temperature distribution is the result of LA, and ablation volume depends on it; therefore, the monitoring of temperature has a crucial impact on the optimal outcome of LA during *in vivo* treatments.

Temperature distribution has been monitored with several techniques, distinguished into invasive and non invasive ones. Invasive techniques require the contact between tissue and sensible elements, and for this purpose Fiber Bragg Grating (FBG) sensors and thermocouples were used. Temperature in pancreases undergoing LA was measured at several distances from applicator, also at different laser settings (power and energy). FBGs revealed to be the most performing thermometer for LA monitoring, since they are unaffected from artifact due to the direct absorption of laser light by sensors, and their small dimensions (1 mm of length and 125 μm of diameter) and the feasibility to house three and more on the same fiber make them suitable for quasi-punctual measurements in several positions.

Thermocouples and fluoroptic thermometers are the most commonly used sensors during LA experiments, but they present the drawback of artifacts (up to 20 °C) caused by direct absorption of laser light. In particular, artifacts affecting thermocouples have been

measured at different distances from applicator, during LA on *ex vivo* pancreases, and mathematically corrected.

The non-invasive techniques regard the images-based thermometry. CT images and MRI-based thermometry have been included in this research program. Advantages of images-base thermometry are the absence of sensors inside the organ, the feasibility to obtain a volumetric distribution of temperature from many images, and the use of the same imaging tool used during treatment by clinician for the positioning of laser applicator.

CT-based thermometry during LA has been performed on *ex vivo* swine pancreas, and a Double Energy CT (DECT) scanner was used to perform thermometry trial on *ex vivo* porcine liver. CT number variation with temperature of pancreatic tissue showed a mean sensitivity of -0.50 $HU \cdot °C^{-1}$ in temperature range from 20 °C to 60 °C; reference temperature has been measured by FBG sensors. Liver tissue showed a mean sensitivity ranging from -0.56 $HU \cdot °C^{-1}$ to -0.36 $HU \cdot °C^{-1}$, for different weighting factors of DECT (corresponding to different voltage tube values, i.e., from 80 kV to 140 kV), and in the temperature range between 20 °C and 100 °C. This experiment, performed at Radiology Department of Goethe University of Frankfurt am Main, employed fluoroptic probes as temperature reference. Artifact of metallic part of these sensors affect the CT images, decreasing their quality, although the decreasing trend of CT number with temperature is measurable and results are confirmed by literature. Nevertheless, this issue confirmed the selection of FBG as the most performing sensors in LA experiments: CT images are not affected by any artifacts because FBG sensors do not include any metallic part.

Furthermore the first trial of CT-based thermometry on pancreatic tissue has been carried out, and results are comparable with data published by some authors for other tissue, as, for example, liver.

Experiments about MRI-based thermometry have also been carried out on *ex vivo* pancreas and liver. The thermal sensibility of T1 relaxation time of tissues has been evaluated with two sequences, the inversion recovery turbo flash (IRTF) and saturation recovery turbo flash (SRTF), during LA procedures. On both organs, SRFT was less sensitive to temperature than IRTF, but more accurate and precise. A further step should be consider other methods in MRI thermometry, such as Proton Resonance Frequency.

Lastly, two methods for measurement of ablation volumes have been assessed: the first one was based on histological sections of pancreas undergoing LA, and the second one

employed MRI. In both cases predictions from theoretical model were in agreement with measurements.

In conclusion, this research project demonstrate the feasibility of LA on pancreatic tissue, although *in vivo* trials should be performed. The most relevant findings are the evaluation of performances of FBGs in this application, in comparison with other sensors historically used for LA purposes, the implementation of a predictable theoretical model, the determination of images-based thermometry sensitivity for pancreas and the preliminary study about the optical coefficients of human pancreas.

Appendix 1

A novel target type low pressure-drop bidirectional optoelectronic air flow sensor for infant artificial ventilation: measurement principle and static calibration.

Paola Saccomandi, Emiliano Schena and Sergio Silvestri

Published in review of Scientific Instruments, vol 82, no. 10, pp. 024301 - 024301, 2011.

Abstract

An optoelectronic target type volumetric air flow rate transducer for bidirectional measurements is presented. The sensor is composed by a T-shaped target and two nominally identical LED-photodiode couples, which are operated in differential mode. The sensitive surfaces of the photodiodes are differentially shadowed by the deflection of the target, which in turn depends on the gas flow rate.

The principle of operation is described in mathematical terms and the design parameters have been optimized in order to obtain the highest sensitivity along with minimal pressure-drop and reduced dimensions. The sensor is placed in a 20 mm diameter hose and was tested with air flow rate in the typical temperature range of mechanical ventilation between 20 °C and 40 °C. The theoretical model was validated through experiments carried out in the volumetric flow range of ±7.0 $L \cdot min^{-1}$. The nonlinear behavior allows sensitivities from 0.6 $V \cdot L^{-1} \cdot min$ when flow rates ranging from -2.0 $L \cdot min^{-1}$ to +2.0 $L \cdot min^{-1}$, to 2.0 $V \cdot L^{-1} \cdot min$, at flow rates ranging from -3.0 $L \cdot min^{-1}$ to -2.0 $L \cdot min^{-1}$ and from +2.0 $L \cdot min^{-1}$ to +3.0 $L \cdot min^{-1}$, up to 5.7 $V \cdot L^{-1} \cdot min$, at higher flow rates ranging from -7.0 $L \cdot min^{-1}$ to -3.0 $L \cdot min^{-1}$ and from +3.0 $L \cdot min^{-1}$ to +7.0 $L \cdot min^{-1}$. The linear range extends from 3.0 $L \cdot min^{-1}$ to 7.0 $L \cdot min^{-1}$, with constant sensitivity equal to 5.7 $V \cdot L^{-1} \cdot min$. The sensor is able to detect a flow rate equal to 1.0 $L \cdot min^{-1}$ with a sensitivity of about 400 $mV \cdot L^{-1} \cdot min$. The differential nature of the output minimizes the influence of the LEDs' power supply variations and allows to obtain a repeatability in the order of 3% of full scale output. The small pressure drop produced by the sensor placed inline the fluid stream, of about 2.4 Pa

at 7 L/min, corresponds to a negligible fluid dynamic resistance lower than 0.34 Pa·L^{-1}·min.

Nomenclature

Latin symbols

B [mm] half length of "T" horizontal beam;

E [GPa] Young modulus of "T" sensing element;

h [mm] height of "T" vertical beam;

I [m^4] "T" sensing element second moment of area;

I_0 [A] internal current generated by the photodiode;

I_r [W·m^{-2}] light power density (irradiance);

I_{r0} [W·m^{-2}] irradiance reaching photodiode sensitive surface when LED beam path is free (12.1 W·m^{-2});

k drag coefficient, adimensional, experimentally determined constant;

l [mm] side of total photodiode sensitive surface (2.3 mm);

L_t [mm] cantilever width;

$M(r)$ [N·m] bending moment acting on "T" sensing element;

$F(r)$, $F(r')$ [N·m^{-1}] force per unit length acting on the cantilever;

$P(r)$ [Pa] pressure acting on the cantilever as a function of the radial coordinate;

P_R [W] light power incident on the sensitive surface of the photodiode;

Q [L·min^{-1}] volumetric flow-rate;

r [mm] radial coordinate with origin on the pipe wall;

r' [mm] radial coordinate with origin in the centerline of the pipe, $r'=r-R$;

$r_{Ph}(\lambda)$ [A·W^{-1}] photodiode responsivity as a function of incident light wavelength;

R [mm] pipeline radius;

R_f [MΩ] photodiode feedback resistance (1 MΩ);

s [mm] cantilever thickness (0.2 mm);

S [mm^2] cantilever surface;

S_f [mm^2] photodiode sensitive surface exposed to radiation;

S_h [mm^2] half photodiode sensitive surface (2.6 mm^2);

S_p [mm^2] photodiode entire sensitive surface (5.3 mm^2);

$u(r)$, $u(r')$ [$m \cdot s^{-1}$] air velocity as a function of the radial coordinate;

U [$m \cdot s^{-1}$] average fluid velocity in the pipe;

V_0 [V] photodiode output;

$w(r)$ [mm] cantilever displacement as a function of radial coordinate.

Greek symbols

ΔI_r [$W \cdot m^{-2}$] irradiance difference investing the two photodiodes;

ΔP [Pa] pressure drop across the sensor;

Δx [mm] cantilever edge displacement along the x-direction;

ΔV_0 [V] transducer output voltage;

γ [$m^2 \cdot A^{-1}$] photodiode constant depending on R_f.

λ [nm] incident light wavelength;

λ_p [nm] LED light wavelength peak (660 nm);

ρ [$kg \cdot m^{-3}$] air density (from 1.14 $kg \cdot m^{-3}$ to 1.20 $kg \cdot m^{-3}$);

$\tau(r)$ [N] shear force acting on "T" sensing element;

μ [Pa·s] air viscosity (from $1.83 \cdot 10^{-5}$ Pa·s to $1.93 \cdot 10^{-5}$ Pa·s).

1. Introduction

Continuous and accurate measurement of gas flow in newborns requiring artificial ventilatory support is essential to improve ventilator control, monitoring of vital parameters and safety during mechanical ventilation. Ventilator induced lung injury is an important cause of morbidity and mortality in infant patients [1], e.g. the term *volutrauma* indicates a pathological situation due to an excessive breathing volume (Tidal Volume - V_T) [2], and the so called "volume-targeted ventilation" is increasingly used in neonatal ventilation to reduce the risks of hyperventilation and high pulmonary volume and peak pressure [3].

Generally speaking, the flow sensor of a mechanical ventilator dedicated to infant respiratory support should be placed at the Y-piece, between the ventilator circuit and endotracheal tube, in order to minimize the difference between the V_T measured by the sensor and the V_T actually delivered to the patient's lung [4]. Proximal volumetric flow (i.e. measured at the patient's airway) can be considerably different from volumetric flow measured at the ventilator level, due to the gas compression in the breathing circuit. This is particularly critical for neonates and preterm infants, due to the relatively small V_T, in the range of 2 mL to 10 mL with flows in the range of ±7.0 $L \cdot min^{-1}$, and to the potentially significant contribution of the breathing circuit fluid dynamic resistance and compliance [5].

Thus, a flow transducer for neonatal ventilation should measure flow accurately, with an accuracy better than 3% [6], have a small volume and an adequate measurement range (at least ±7.0 $L \cdot min^{-1}$), should show a high sensitivity, due to the relatively small flows to be measured, should determine a low pressure drop to gas passage and should be robust [7].

During past years, several researchers have focused on the design and realization of flow-meters suitable for application in mechanical ventilation. As described below, each operating principle shows advantages and drawbacks, thus the ideal solution for continuously and accurately measuring delivered gas flows in artificial ventilation has not yet completely achieved. Currently, flow transducers used in neonatal ventilation are, mainly, linear pneumotachographs, pressure drop flow-meters with fixed or variable orifice, and hot wire anemometers [8].

Pneumotachographs measure a pressure drop across a linear resistance, or across a fine wire mesh. They are robust and show good accuracy, on the other hand the measurement is influenced by composition and thermo-hygrometric characteristics of the gas delivered [8,9]. Moreover, the sensitivity is proportional to fluid dynamic resistance, and therefore typical fluid dynamic resistance values [10] are in the range of 3 $Pa \cdot L^{-1} \cdot min$ to 4 $Pa \cdot L^{-1} \cdot min$.

Orifice flow transducers allow to measure a pressure drop across a fixed or a dynamically opening orifice. The advantages and drawbacks are mostly the same as for the pneumotachographs, although orifice transducers show a non linear response and quite a high fluid dynamic resistance, in the order of about 18 $Pa \cdot L^{-1} \cdot min$ [11].

Hot wire anemometers show good sensitivity, a negligible fluid dynamic resistance and high measurement range, the main drawback is their fragility. The sensitive element, a very thin and fragile platinum wire with a diameter ranging from 10 µm to 20 µm, is easily broken by the movement of the infant.

This paper presents a novel optoelectronic target type volumetric flow rate transducer, whose innovative aspect is the use of two nominally identical LED-photodiode couples operated in differential mode. Each LED emits a light intensity which is collected on the sensitive surface of the corresponding photodiode. The sensitive surfaces of the photodiodes are differentially shadowed by the deflection of the target which depends on gas flow.

The sensor has been designed with a symmetric geometry in order to obtain a symmetric response to bidirectional flows. The differential measurement method allows to obtain high sensitivity and to minimize the influence of light intensity variations of the environment and of the LEDs. The differential nature of the output, although slightly decreasing sensor's measurement range, still allows a full scale span wide enough to cover typical air flow values in neonatal ventilation.

Experimental trials, presented in Section 4, show a very high sensitivity to low gas flows, a good repeatability in overall range of calibration (about 3 %), a negligible fluid-dynamic resistance to gas flows (pressure drop across the target is smaller than the pressure drop across an entire breathing circuit [12]) and a good symmetry of the calibration curve. The principle of operation and the physical model is presented in the following sections.

2. Sensor design and theory of operation

The flow sensing element is constituted by a T-shaped cantilever with rectangular cross section embedded in the pipe wall, perpendicularly to the axis of the pipe line, as shown in figure 1.

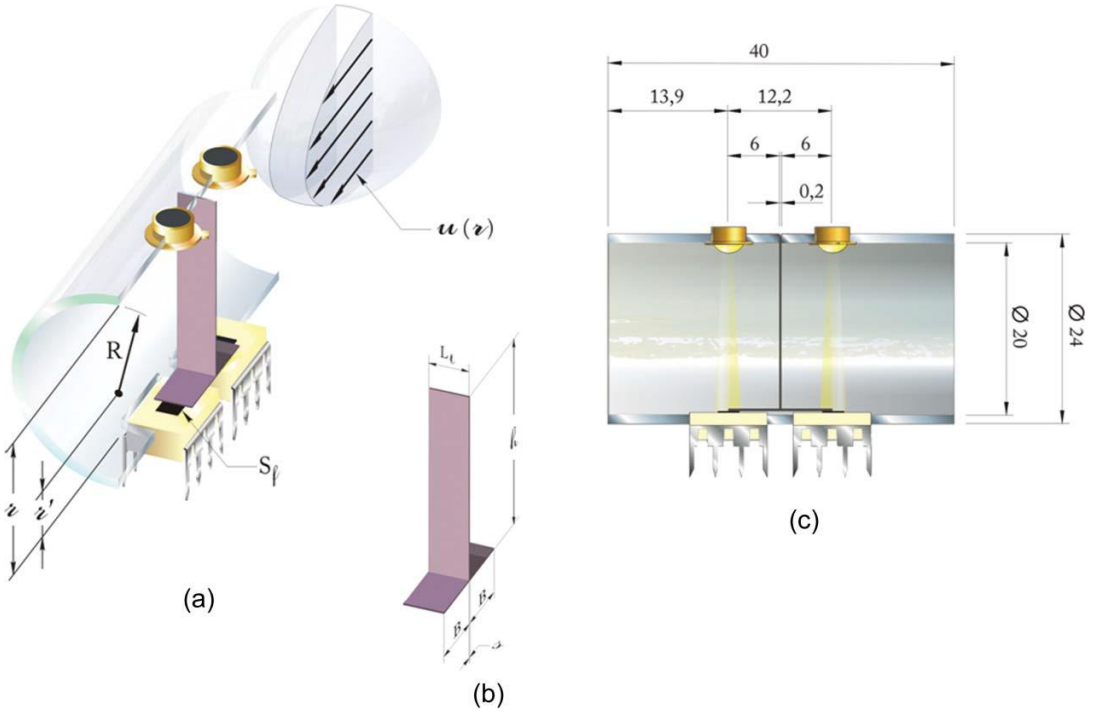

Figure 1.Schematic representation of the flow sensor. Flow sensor structure placed in-line a hose with radius R, the gas velocity profile, u(r), is represented along with the radial coordinates r and r_L (a). T-shaped flow sensing element (b). Frontal view of the sensor with quotes (c).

The T-shaped cantilever is placed between two nominally identical LED-photodiode couples, flush with the inner conduct surface. Each photodiode collects the radiation produced by the opposite LED. The internal current (I_0) generated by the photodiode depends on the incident light power, according to the following relation [13]:

$$I_0 = P_R \cdot r_{Ph}(\lambda) = I_r \cdot S_f \cdot r_{Ph}(\lambda) \qquad (1)$$

where P_R is the incident light power and λ its wavelength, r_{Ph} the photodiode responsivity, I_r the irradiance, i.e. the light power density, and S_f is the photodiode sensitive surface exposed to the radiation.

In absence of flow, the force acting on the cantilever is null and the "T" covers half of the sensitive surfaces of both photodiodes, so that they collect an equal incident light power. An operational amplifier, operated in differential mode, provides the output voltage of the sensor, which in this case in null.

When the gas flow passes through the sensor distributed forces act on the cantilever inducing a bending moment deflecting the "T". Thus, the photodiodes collect different light power, due to the different sensitive surface percentage reached by the radiation, and allow a differential output signal.

2.1 Theory of operation

In order to optimize the sensor design, aimed to obtain the highest sensitivity along with the lower pressure drop, a mathematical model of the sensor was developed. Also, a few assumptions and simplifying hypotheses must be put forward.

When flow passes through the sensor a force per unit length acts on the cantilever. This can be expressed as:

$$F(r) = L_t P(r) \tag{2}$$

where *P(r)* is the pressure, due to air flow rate, acting on the vertical cantilever, L_t is the horizontal width of the cantilever, as shown in figure 1.B. The deflection of the "T" is calculated by considering the expression of *F(r)* as obtained under the simplifying hypotheses that *P(r)* acts only on the vertical cantilever, since this surface is much greater than the thickness of the horizontal beam. Moreover, *P(r)* has been considered uniformly distributed on the horizontal coordinate of the vertical cantilever, i.e. it has been assumed uniform over L_t.

Under the hypothesis of ideal and incompressible steady flow, and considering air as the flowing gas, *P(r)* has the following expression [14]:

$$P(r) = \frac{k \cdot \rho \cdot u(r)^2}{2} \tag{3}$$

where *u(r)* is the air velocity parallel to the axis of the pipe line at distance *r* from the pipe wall, ρ is the air density (1.14 kg·m^{-3} to 1.20 kg·m^{-3} in the typical temperature range of mechanical ventilation 20 °C to 40 °C), *k* is the drag coefficient which depends on the shape of the body obstructing the flow and which must be determined experimentally.

Under laminar flow conditions (Reynolds number < 2000) the gas velocity as a function of the distance from the central axis of the pipe can be expressed as:

$$u(r') = 2 \cdot U \cdot \left[1 - \left(\frac{r'}{R}\right)^2\right] = 2 \cdot \frac{Q}{\pi \cdot R^2} \cdot \left[1 - \left(\frac{r'}{R}\right)^2\right] \quad (4)$$

where R is the pipeline radius, r' is the radial coordinate with origin in the centerline of the pipe, $r'=r-R$ (see figure 1.A), U is the average fluid velocity in the pipe and Q is the volumetric flow-rate.

Introducing Eq. (4) in Eq. (3) and then in Eq. (2) it is deduced that:

$$F(r') = \frac{2 \cdot k \cdot \rho}{\pi^2 \cdot R^4} \cdot Q^2 L_t \left[1 - \left(\frac{r'}{R}\right)^2\right]^2 \quad (5)$$

The deflection of the T-shaped sensing element caused by the applied force is transformed into optical information, causing a differential output from the photodiodes. In fact, Eq. (5) shows that $F(r')$ depends on the volumetric flow-rate (Q) by means of a quadratic function therefore the differential output of the photodiodes gives an indication related to the volumetric flow-rate.

The T deflection can therefore be obtained by:

$$\begin{cases} M(r) = -EIw''(r) \\ \dfrac{dM(r)}{dr} = T(r) \\ \dfrac{dT(r)}{dr} = -F(r) = -L_t P(r) \end{cases} \quad (6)$$

where $M(r)$ is the bending moment, E is the Young modulus of the T sensing element, I is the T second moment of area, i.e. $I=L_t s^3/12$, $w''(r)$ is the second order derivative of the T displacement ($w(r)$), $T(r)$ is the shear force, $F(r)$ is the force per unit of length acting on the cantilever surface, as defined above.

Boundary conditions are $w'(r=0)=0$ and $w(r=0)=0$, because the cantilever is fixed into the pipe wall where $r=0$ thus, it is deduced that $T(0) = \frac{32}{15} \cdot \frac{\rho \cdot Lt \cdot k \cdot Q^2}{\pi^2 \cdot R^3}$ and $M(0) = \frac{32}{15} \cdot \frac{\rho \cdot Lt \cdot k \cdot Q^2}{\pi^2 \cdot R^2}$.

By solving Eq. (6), the cantilever displacement *w(r)* as a function of the flow rate and the radial coordinate is given by:

$$w(r)=\frac{2\cdot\rho\cdot k\cdot L_t}{\pi^2\cdot E\cdot I\cdot R^8}\left[\frac{h^6 r^2}{60}+\frac{r^8}{1680}-\frac{R^2\cdot h^4\cdot r^2}{6}+\frac{R^2\cdot r^6}{90}+\frac{R\cdot h^5\cdot r^2}{10}-\frac{R\cdot r^7}{210}\right]Q^2 \quad (7)$$

where *h* is the cantilever height.

The displacement of the cantilever extremity can be obtained by posing *r=h* in Eq. (7) and thus obtaining:

$$w(h)=\frac{2\cdot\rho\cdot k\cdot L_t}{\pi^2\cdot E\cdot I\cdot R^8}\left[\frac{29\cdot h^8}{1680}-\frac{7\cdot R^2\cdot h^6}{45}+\frac{2\cdot R\cdot h^7}{21}\right]Q^2 \quad (8)$$

The T deflection parallel to the axis of the pipe line (x-direction) is shown in figure 2, which reports only one half of the T in virtue of its symmetry.

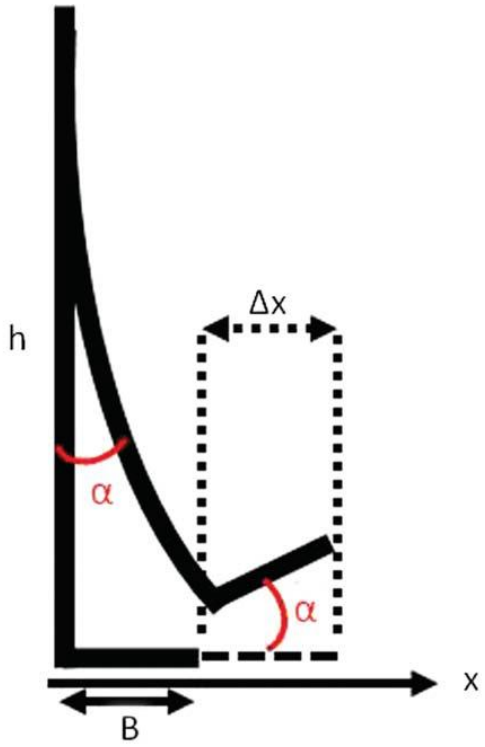

Figure 2. Deflection of one half the T-shaped sensing element.

As in small deformations, like those obtained with flow rates lower than 10 L·min^{-1}, $\alpha\rightarrow 0$, $tg\alpha=-w'(h)\cong\alpha$. By deriving Eq. (8) it is found that:

$$\alpha=\frac{2\cdot\rho\cdot k\cdot L_t}{\pi^2\cdot E\cdot I\cdot R^8}\left[\frac{h^6\cdot R}{6}-\frac{4\cdot R^2\cdot h^5}{15}-\frac{h^7}{35}\right]Q^2 \quad (9)$$

Cantilever edge displacement (Δx), as shown in figure 2, is the T edge displacement, caused by the sensing element deflection, along the pipeline axis. It can be expressed as follows:

$$\Delta x = w(h) + B(\cos\alpha - 1) = w(h) + \eta(h) \qquad (10)$$

where B is half the horizontal beam length. Eq. (10) shows that the displacement Δx is the sum of two terms where $w(h)$ increases with Q and $\eta(h)$, which is always negative, decreases with Q.

The sensor sensitivity depends on the value of Δx which, in turn, mainly depends on the value of h. A greater Δx can be obtained at the same flow rate by increasing the cantilever height (h) rather than by increasing L_t, as shown by Eq. (8).

Simulations were carried out in order to evaluate the sensitivity of the sensor as a function of h and the contribution of the cosinusoidal term $\eta(h)$. The simulations were performed by considering four different values for the drag coefficient [15] (k=0.9, k=1.0, k=1.1 and k=1.2) in Eq. (10). Figure 3 shows the two terms $w(h)$ and $\eta(h)=B(\cos\alpha-1)$ as a function of Q, ranging from 0.0 to 8.0 L/min, for three values of cantilever height h (10 mm, 15 mm, 20 mm) and the above reported k values.

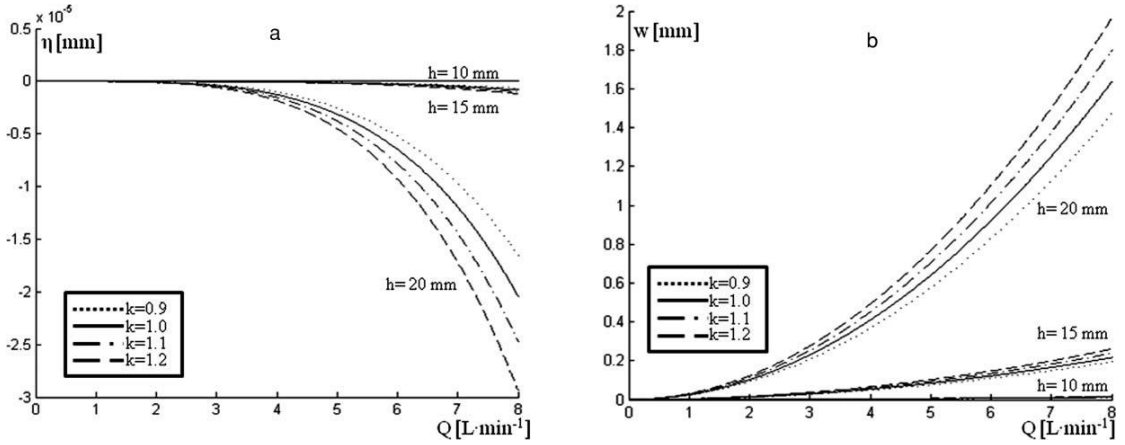

Figure 3. Contributions to the total displacement _x by the terms $\eta(h)$ (a), and $w(h)$ (b) as a function of volumetric flow-rate Q, for three values of h: dotted line (k = 0.9), continuous line (k = 1.0), dash-dotted line (k = 1.1), and dashed line (k = 1.2).

Simulations show that $w(h)$ is much greater than $\eta(h)$ in the whole flow rate range (e.g. for Q=4.0 L·min^{-1}, h=20 mm and k=1.0, we obtain η = -1.2·10^{-6} mm and w = 0.41 mm, for Q=8.0 L·min^{-1}, h=20 mm and k=1.0, we obtain η = -2.0·10^{-5} mm and w=1.6 mm). Thus, the contribution of $\eta(h)$ to the overall sensitivity is negligible, and Eq. (10) can be rewritten as:

$$\Delta x = w(h) + \eta(h) \cong w(h) = \frac{2 \cdot \rho \cdot k \cdot L_t}{\pi^2 \cdot E \cdot I \cdot R^8} \left[\frac{29 \cdot h^8}{1680} - \frac{7 \cdot R^2 \cdot h^6}{45} + \frac{2 \cdot R \cdot h^7}{21} \right] Q^2 \qquad (11)$$

Moreover, simulations reported in Figure 3 show that the sensor must be designed with *h* slightly lower than 20 mm (2*R*) in order to maximize the sensitivity and to avoid possible friction force caused by low clearance between the T and the pipe wall. We realized the "T" with a height (h) of 19.9 mm, this causes a negligible variation of the sensor displacement obtained using h=20 mm (about 1%), as calculated by further simulations. We were able to increase Δx of about 800 %, from 0.2 mm up to 1.7 mm, for the maximum flow rate by increasing *h* of 30 %, from 15 mm to 20 mm, whichever k value was chosen. Therefore, by assuming $h=2R$, Eq. (11) can be written as:

$$\Delta x = \frac{4192 \cdot \rho \cdot k \cdot L_t}{315 \cdot \pi^2 \cdot E \cdot I} Q^2 \qquad (12)$$

It can be seen that the sensing element displacement is a quadratic function of volumetric flow-rate.

2.2 Sensor design and construction

The T was made of black-coloured PVC ($E \cong 3$ GPa) and, according to the above reported considerations, it was realized with *h* slightly smaller than the pipe diameter (19.9 mm) in order to maximize the sensor sensitivity and to avoid friction between the T and the pipe wall. The following geometric features were chosen in the simulations reported in figure 3: $B \cong 6$ mm, $L_t \cong 4$ mm, $s \cong 0.2$ mm (see figure 1.C). The 20 mm diameter hose allows to validate the laminar flow hypothesis for the typical volumetric flow rate used in neonatal ventilation: Q<10 L·min^{-1} for which Re≤1000. The following values have been considered: ρ is comprised in the range of 1.14 kg·m^{-3} to 1.20 kg·m^{-3} and μ in the range of $1.83 \cdot 10^{-5}$ Pa·s to $1.93 \cdot 10^{-5}$ Pa·s considering the typical gas temperature range in mechanical ventilation (20 °C to 40 °C).

Considering the application field, the issue of fatigue-crack must be considered because the sensor is subject to cyclic loading. The maximum load acting on the T can be expressed as $\sigma_{Max} = 6 \cdot \frac{M(0)}{L_t \cdot s^2}$; in the worst condition (maximum value of flowrate equal to 10 L·min^{-1}) and considering k=1 (as shown in the section 4) $\sigma_{Max} \approx 1.1 \cdot 10^4 \, Pa$. This value is much

lower than 1% of static failure load of PVC (60 Mpa) and allows to avoid fatigue crack [16]

Two photodiodes (Texas Instruments OPT 101) were used as photodetectors, operated under constant regulated voltage (15.00±0.01 V) supplied by a constant voltage generator. The OPT 101 is a monolithic photodiode with on-chip transimpedance amplifier, its output voltage (V_0) increases linearly with light intensity. Photodiode total sensitive surface ($S_p \cong 5.3$ mm^2) is a square of side l=2.3 mm. Two LEDs (Osram SFH 464) were chosen in order to obtain light with wavelength peak emission in accordance with high photodiode responsivity: wavelength peak emission [17] is λ_p=660 nm corresponding to a normalized spectral photodiode absorption [18] of about 75%. The two LED-photodiode couples are placed symmetrically at a 6 mm distance from the vertical cantilever in order to shield half of the area of the photodiodes (S_h) in absence of air flow-rate (Q=0 L·min^{-1}). The electrical scheme of the device is shown in figure 4.

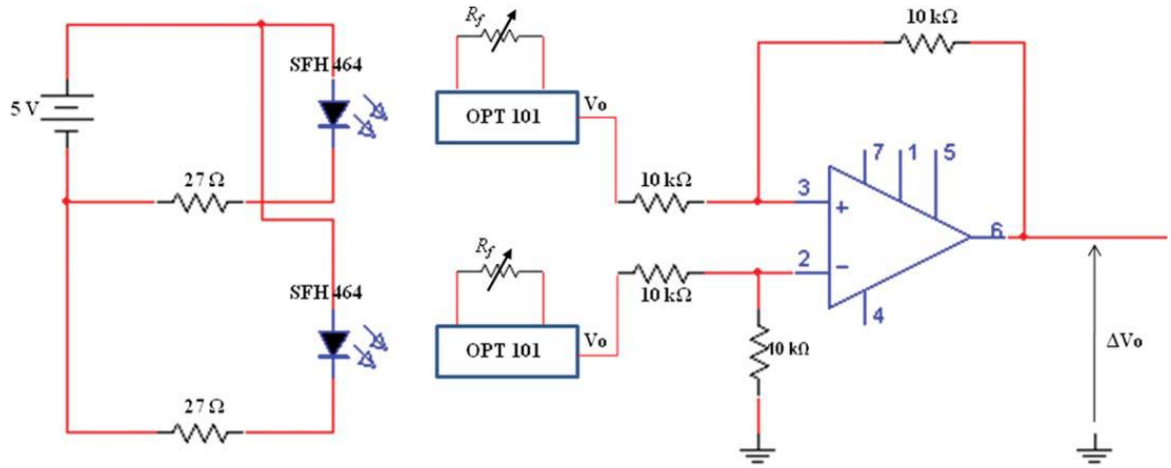

Figure 4. Electronics schematic of the realized sensor.

When air flows through the pipe ($Q \neq 0$ and $\Delta x \neq 0$) the photodiode sensitive area, which is not shadowed by the horizontal beam of the T, increases for one photodiode and decreases for the other. Consequently, the light emitted by the LEDs which reaches the two photodiodes is proportional to the exposed sensitive surfaces, which are respectively:

$$\begin{cases} S_{f1} = S_h + \Delta x \cdot l = \frac{1}{2} l^2 + \Delta x \cdot l \\ S_{f2} = S_h - \Delta x \cdot l = \frac{1}{2} l^2 - \Delta x \cdot l \end{cases} \quad (13)$$

where S_{f1} is the first photodiode sensitive surface exposed to radiation and S_{f2} is the second photodiode sensitive surface exposed to radiation. Both photodiodes are reached by

irradiance equal to $I_r = I_{r0}\frac{S_f}{l^2}$, where I_{r0} is the irradiance which reaches the photodiode if the path between the LED and the photodiode is free. The photodiode output voltage (V_0) can then be expressed as a linear function of irradiance:

$$V_0 = \gamma \cdot I_r = \gamma \cdot I_{r0}\frac{S_f}{l^2} \qquad (14)$$

where γ is a constant depending on the internal feedback impedance utilized[16].

Two variable resistors were utilized as internal feedback impedance, in order to compensate little difference between the two LED-photodiode couples due to a non-perfect reproducibility, or due to different deterioration with time. Small manufacturing differences between the LEDs, or between the photodiodes, can cause variations of I_r or γ respectively, and therefore a variation of V_0, see Eq. (14). A fine trimming of internal feedback impedance (R_f) allows to easily set a null output for null flow rate.

The irradiance difference received by the two photodiodes can be expressed by the following equation:

$$\Delta I_r = I_{r1} - I_{r2} = \frac{I_{r0}}{l^2}\left(S_{f1} - S_{f2}\right) = \frac{2 \cdot I_{r0} \cdot \Delta x}{l} \qquad (15)$$

By introducing Eq. (12) in Eq. (15), the following equation can be obtained:

$$\Delta I_r = \frac{8384 \cdot I_{r0} \cdot \rho \cdot k \cdot L_t}{315 \cdot l \cdot \pi^2 \cdot E \cdot I} Q^2 \qquad (16)$$

Then, by substituting the Eq. (16) in Eq. (14) the following relationship between the two photodiode voltage outputs difference ΔV_0 and the volumetric flow rate can be obtained:

$$\Delta V_0 = \gamma \cdot \Delta I_r = \gamma \cdot \beta \cdot Q^2 \qquad (17)$$

where $\beta = \frac{8384 \cdot I_{r0} \cdot \rho \cdot k \cdot L_t}{315 \cdot l \cdot \pi^2 \cdot E \cdot I}$.

Thus, transducer output ΔV_0 depends on the volumetric gas flow rate according to a quadratic law, expressed by Eq. (17), which represents the device calibration curve.

3. Sensor static calibration setup

Experimental trials were performed in order to calibrate the sensor and to verify the mathematical model expressed by Eq. (17), and thus the validity of the formulated simplifying hypotheses. Figure 5 shows the experimental setup adopted.

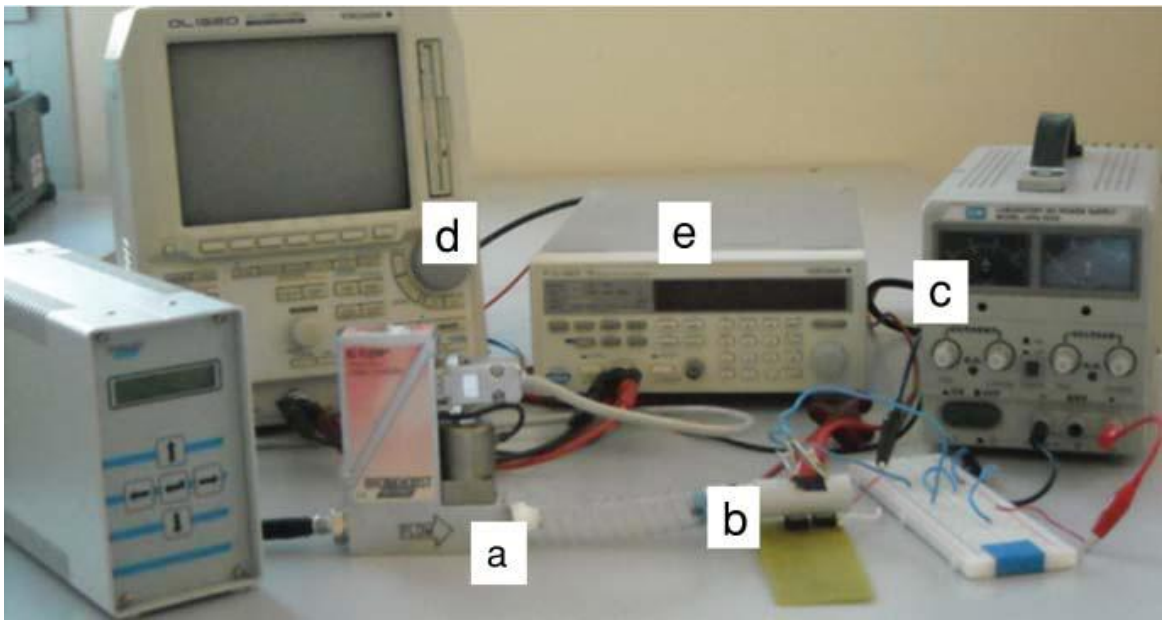

Figure 5. Picture of the experimental setup utilized for calibration:(a) air flow controller, (b) transducer under calibration, (c) power supply, (d) oscilloscope for output visualization, and (e) two channel function generator.

The experimental setup consists of an air flow controller, figure 5.A (Bronkhorst El-Flow, range of 0.05 $L \cdot min^{-1}$ to 10.00 $L \cdot min^{-1}$, accuracy 0.2 % of the set-point value), in order to generate a controlled air flow rate ranging from 1 to 7 $L \cdot min^{-1}$ in steps of 1 $L \cdot min^{-1}$.

The output signal ΔV_0 was obtained by an operational amplifier (Burr-Brown OPA604AP, FET-Input, Low Distortion Operational Amplifier) in differential configuration (see figure 4). ΔV_0 corresponds to the difference between the two photodiode voltage outputs and was displayed on a digital oscilloscope (1540, Yokogawa, figure 5.D).

A power supply unit (DC ISO-TECH IPS2302A, figure 5.C) was used to power the two LEDs (V_{al}=5.00±0.01 V) and the two photodiodes ($V_{al\ photodiode}$=15.00±0.01 V). The flow sensor was designed for bidirectional use, therefore a bidirectional flow rate was generated.

4. Experimental results and discussion

Preliminary trials were carried out in order to assess the value of I_{r0}. The entire sensitive surface of both photodiodes was reached by the light emitted by LEDs, operated at 5.00±0.01 V. The photodiode transimpedance was set as R_f =1 MΩ in order to obtain a V_0 linearly related to I_r [18]. Thus, I_{r0}≅12.1 W·m^{-2} was obtained.

The experiments were repeated five times in different days in order to realize trials under different gas and environmental conditions (e.g. gas and environmental temperature, external light, *et cetera*). From this point onward, all the results are reported as mean ± the expanded uncertainty, which was calculated by multiplying the combined standard uncertainty by a coverage factor of 2.8. The coverage factor was obtained considering a Student's distribution with 4 degrees of freedom and a confidence of 95 % [19]. Sensor output variations during repeated trials are mainly caused by the "T" oscillations. This phenomenon can be explained considering the "T" oscillations caused by vortex created when the airflow hit the cantilever (vortex shedding phenomenon) [20].

Calibration curves represented by Eq. (17), using four different values for the drag factor (k=0.9, k=1.0, k=1.1 and k=1.2), are shown in figure 6 along with the experimental data obtained. The curve obtained with k=1.0 shows the best agreement with experimental data, as compared with other three curves. This is also confirmed by the value of the mean squared error (MSE) value equal to 1.0 V^2 for k=1.0 (MSE=3.4V^2 for k=0.9, MSE=2.2V^2 for k=1.1 and MSE=7.1V^2 for k=1.2). The lowest MSE was obtained for k=1.01 (MSE=0.98 V^2), which confirms drag force coefficient value reported in literature for similar cases [15].

Experimental data, compared with the results obtained by the simulations shown in Figure 6 indicate an excellent agreement over the entire flow rate range.

The sensor shows a mean repeatability value in the whole range of calibration equal to 3% of full scale output (FSO). As predicted by the model, the sensor shows a non linear function curve: sensitivity varies from about 2.0 V·L^{-1}·min (at flow rates in the range of 2.0 L·min^{-1} to 3.0 L·min^{-1}) up to about 5.7 V·L^{-1}·min (at flow rates higher than 3.0 L·min^{-1}), it is equal to about 0.6 V·L^{-1}·min at lower flowrates (in the range of -2 L·min^{-1} to +2.0 L·min^{-1}) showing a discrimination threshold lower than 1 L·min^{-1}.

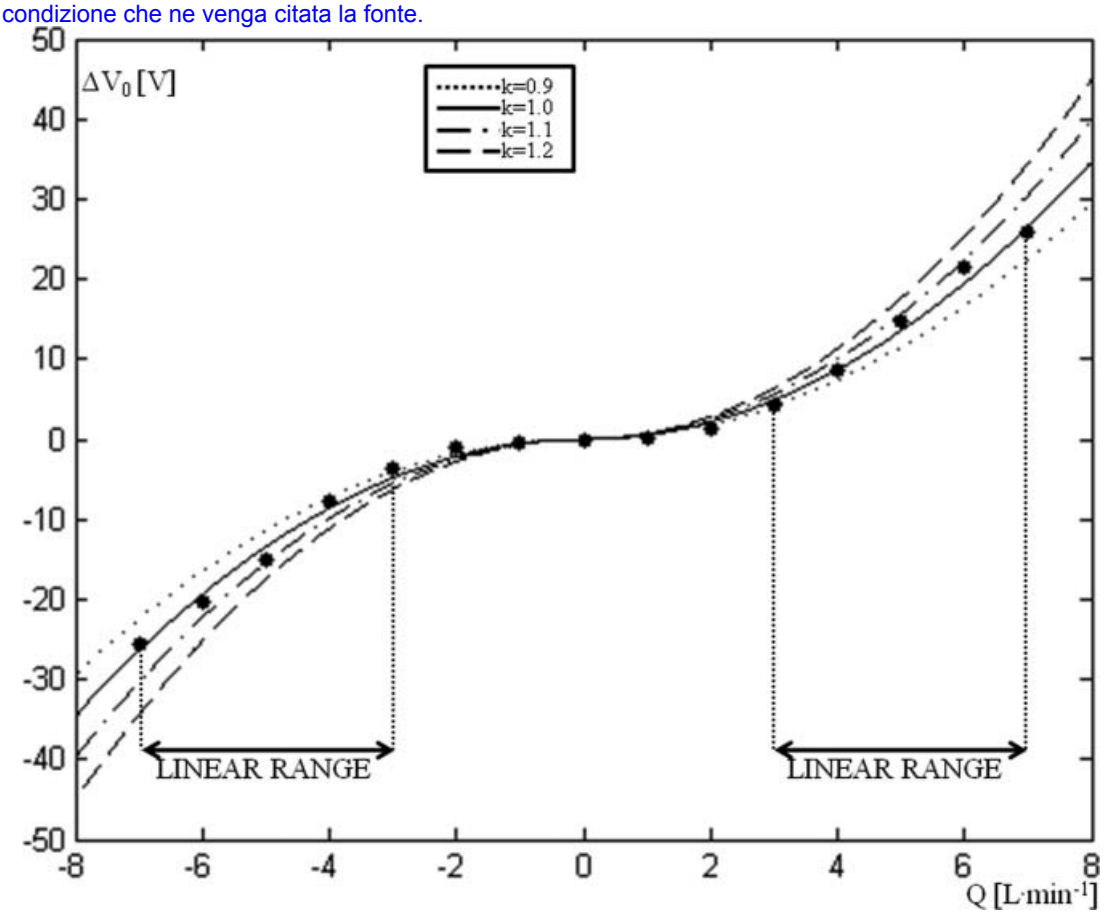

Figure 6. Experimental data obtained by calibration and continuous curve obtained by the mathematical model reported in Eq. (17), with drag force coefficient k = 0.9 (dotted line), k = 1.0 (continuous line), k = 1.1 (dash-dotted line), and k = 1.2 (dashed line). The linear range is also indicated.

Sensor response was found almost symmetric as far as flow direction is concerned. Therefore experimental data have been fitted with a symmetric function.

The sensor shows a linear behavior from 3.0 L·min^{-1} to 7.0 L·min^{-1} and from -7.0 L·min^{-1} to -3.0 L·min^{-1} (R^2>0.99 in both cases), where the sensitivity is constant and equal to 5.7 V·L^{-1}·min. The sensitivity value is greater than a bidirectional flow-meter for designed and realized pulmonary ventilation[i] with a large measurement range (±60 L·min^{-1}). In fact, its sensitivity is lower than 100 mV·L^{-1}·min in the typical neonatal flow range (±10 L·min^{-1}).

The presented sensor was designed with a differential output. This allows to maximize sensitivity and, at the same time, to minimize the influence of environmental light radiation, which could induce a zero drift with consequent measurement errors. Usually, a differential output also causes a decrease of the measurement range however, the measurement range of the presented sensor (-7.0 L·min^{-1} to +7.0 L·min^{-1}) covers flow range typically used in neonatal ventilation. Furthermore, the differential output also

allows to minimize the influence of voltage supply instability. Therefore, experiments were carried out in order to verify the differential output stability (ΔV_0) in dependence of environmental light and LED power supply variations and to compare this value with single photodiode outputs (V_{01}, V_{02}).

LED radiation intensities were modulated by varying supply voltages. A function generator (Yokogawa FG120 with fully independent two output channels, figure 4.E) supplied each LED with a sine wave voltage with 4 V amplitude, 0.5 Hz frequency and 750 mV offset.

Results are reported in figure 7, where the sensor output (ΔV_0) and the two photodiode outputs (V_{01}, V_{02}) as a function of time are shown. Output signals were sampled for about five periods (10 s) of the sine wave function supplying the LEDs. During the whole acquisition time ΔV_0 shows a variation equal to 24 mV, calculated as a difference between the maximum value and the minimum value. The output variations of the photodiodes were as high as 4 V. Therefore, the differential output allows a stability of ΔV_0 in the order of 0.6% when LED voltage supply varies sinusoidally with an amplitude equal to 4 V and the supply voltage variations are synchronized.

The influence of environmental light variations on sensor output was found negligible.

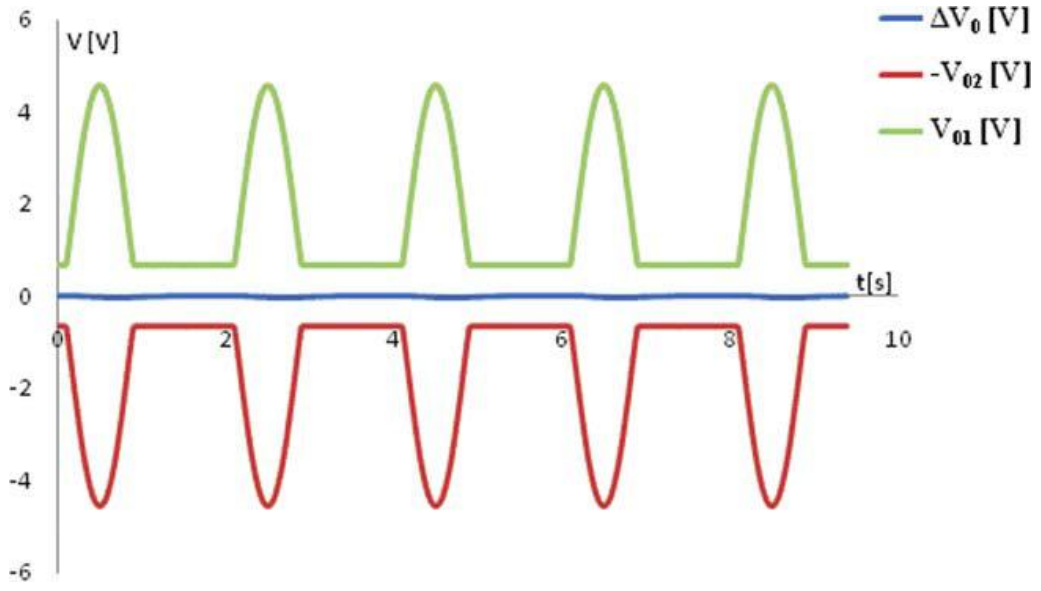

Figure 7. Influence of LEDs voltage supply variation. Sensor output (*V*0) and photodiodes output (*V*01, *V*02) as a function of time.

Experimental tests were performed also in order to evaluate the fluid dynamic resistance introduced by the presence of the sensor placed in-line the fluid stream. The air flow

controller was used to generate a controlled air flow rate ranging from 1 to 7 L·min^{-1}, in 2 L·min^{-1} steps. The pressure drop produced by the flow rate (ΔP) was measured across the sensor by a 163PC01D75 pressure transducer (Honeywell, range ±623 Pa, repeatability ±0.25 % FSO). Each measurement was repeated six times in different conditions and the results are reported in Table I along with the values of the sensor voltage output, repeatability and sensitivity obtained in correspondence of the flow rate value.

Table I. Values of pressure drop, sensor output, repeatability and sensitivity obtained at different volumetric flow rates in the calibration range.

Flow rate Q [L·min^{-1}]	Pressure drop ΔP [Pa]	Sensor Output ΔV_0 [V]	Repeatability $\delta\Delta V_0$ [V]	Sensitivity S [V·L^{-1}·min]
1.0	0 to 0.7	0.39	0.04	0.39
3.0	0.2 to 1.0	1.36	0.08	0.68
5.0	0.2 to 1.7	8.66	0.11	2.16
7.0	0.3 to 2.4	25.9	0.15	3.70

Table I shows very small pressure drop values in the overall flow rate range of calibration. The maximum value obtained, about 2.4 Pa at 7.0 L/min, corresponds to a fluid dynamic resistance, calculated as ΔP/Q, lower than 0.34 Pa·L^{-1}·min. This value is about one order of magnitude lower than the typical fluid dynamic resistance values of linear resistance pneumotacographs (3 Pa·L^{-1}·min to 4 Pa·L^{-1}·min), and about two orders of magnitude lower than the fluid dynamic resistance of orifice flow sensors: a research [11] reports a flow sensor with constant resistance and pressure drop of about 37 Pa at typical flow rates of neonatal ventilation (10 L·min^{-1}); this value is slightly lower than that of a Fleisch no. 0 pneumotachograph (about 42 Pa). Other researches describe flow transducers with a pressure drop at 10 L/min equal to 450 Pa [10] or larger than 300 Pa [21]. For the here described sensor, the pressure drop obtained at the maximum flow rate value is comparable with the pressure drop produced by the entire breathing circuit at the same

flow rate [13]. One of the design goals for a flow sensor placed in-line with the breathing circuit is to minimize the resistance to flow rate.

However, pressure drop values for the realized transducer, reported in table I, are greater than the ones produced by thermal flow sensors and fiber optic-based flow-meters based on Fiber Bragg Grating (FBG) technology [22,23,24].

Thermal flow sensors such as hot-wire and hot-film anemometers, which perform fluid velocity measurements based on convective heat loss, are also well known [25]. Although hot-element sensors show many advantages, such as a negligible pressure drop, they presents some issues such as flow direction detection, dependence on gas temperature [26] and pressure, and presence of dust particles in the vicinity of the sensor may cause concerns for applications in the biomedical field [27]. Moreover, these sensors are subject to failure due to the fragile nature of the sensing element: a thin platinum wire (a few micrometers of diameter) at high temperature (above 400 °C).

FBG-based flow sensors generally show a wide measurement range, but small sensitivity and immunity to temperature, and also, they normally require the additional presence of expensive devices, e.g. optical spectrum analyzer.

5. Conclusions

In conclusion, a new optoelectronic flow sensor to detect bidirectional volumetric air flow rate has been designed and realized. Its sensing element is based on the use of two LED-photodiode couples. The excellent agreement between static calibration experimental data and the mathematical model (MSE=1.0 V^2) confirms the underlying theory described.

The main advantages of the presented sensor are: its ability to bi-directionally measure the flow rate; a quite high sensitivity (from about 0.6 $V \cdot L^{-1} \cdot min$ to about 5.7 $V \cdot L^{-1} \cdot min$); a low discrimination threshold (lower than 1 $L \cdot min^{-1}$); very low fluid dynamic resistance (lower than 0.34 $Pa \cdot L^{-1} \cdot min$); and, finally, a measuring range (-7.0 $L \cdot min^{-1}$ to +7.0 $L \cdot min^{-1}$) containing typical air flow rates for neonatal ventilation. The differential measurement method allows to maximize the sensitivity and to minimize the influence of environmental light and LED light intensity variations due to power supply instability. Moreover, the advantages of the working principle include simple construction, robustness and no need to use expensive devices to detect sensor output.

Bibliography

[1] S.M. Donn, S.K. Sinha, Arch Dis Child Fetal Neonatal, **91**, F226 (2006).

[2] R.L. Auten, M. Vozzelli, R.H. Clark, Clinics in Perinatology , **28**, 505 (2001).

[3] N. Claure, E. Bancalari, Curr Opin Pediatr, **20**, 125 (2008).

[4] M.L. Cannon, J. Cornell, D.S. Tripp-Hamel, M.A. Gentile, C.L. Hubble, J.N. Meliones, I.M. Cheifetz, American Journal of Respiratory and Critical Care Medicine, **162**, 2109 (2000).

[5] S. Silvestri, Physiological Measurement, **27**, 23 (2006).

[6] M.R. Miller, J. Hankinson, V. Brusasco, F. Burgos, R. Casaburi, A. Coates, R. Crapo, P. Enright, C.P.M. Van der Grinten, P. Gustafsson, R. Jensen, D.C. Johnson, N. MacIntyre, R. McKay, D. Navajas, O.F. Pedersen, R. Pellegrino, G. Viegi, J. Wanger, European Respiratory Journal, **26**, 319 (2005).

[7] J.H.T. Bates, M.J. Turner, C.J. Lanteri, B. Jonson, P.D. Sly, Infant respiratory function testing, Wiley-Liss Inc, (1996).

[8] K. Roske, B. Foitzik, R.R. Wauer, G. Schmalisch, Journal of Clinical Monitoring and Computing, **14**, 413 (1998).

[9] E. Schena, G. M. P. Masselli, S. Silvestri Proc. of 31st Int Conf IEEE Engineering in Medicine and Biology Society, 1226 (2009).

[9] P. Vallinis, G.M. Davis, L. Coates, Journal of applied physiology, **69**, 1542 (1990).

[10] Manual service of Respironics Novametrix flow sensor.

[11] D.G. Martin, K.L. Kong, G.T.R. Lewis, British Journal of Anaesthesia, **62**, 456 (1989).

[12] M. Johnson, Photodetection and measurement, MCGraw-Hill (2003).

[13] W.T. Clark, Encyclopedia of fluid mechanics, Gulf Publishing Company, 1408 (1986).

[14] J. Mireles Jr, Sensor Review, **25**, 33 (2005).

[15] M Burman. Fatigue-crack initiation and propagation in sandwich structures. PhD theses, KTH department of aeronautics.

[16] Datasheet SFH 464, Osram Opto Semiconductors.

[17] Datasheet OPT101, Burr-Brown product from Texas Instrument.

[18] Guide to the Expression of Uncertainty in Measurement, JCGM 100 (2008).

[19] T von Karman, Aerodynamics, McGraw-Hill (1963)

[20] M.J.A.M. van Putten, M.H.P.M. van Putten, A.F.P. van Putten, J.C. Pompe, H.A. Bruining, IEEE Transactions on Biomedical Engineering, **44**, 205 (1997).

[21] J.P. Brady, D.D. Deming, E.M. McCann, Journal of Applied Physiology, **58**, 1023 (1985).

[22]Y. Zhao, K. Chen, J. Yang, Measurement, **38**, 230 (2005).

[23] J. Lim, Q.P. Yang, B.E. Jones, P.R. Jackson, Sensors and Actuators:A, **92**, 102 (2001).

[24] P. Lu, Q. Chen, Measurement Science and Technology, **19**, 125302 (2008).

[25] A. Al-Salaymeh, J. Jovanovi, F. Durst, Medical Engineering & Physics, **26**, 623 (2004).

[26] E. Schena, S. Silvestri, Review of Scientific Instruments, **79**, 104301 (2008).

[27] M.A. Ardekani, M. Masoudi Motlagh, Measurement, **43**, 31 (2010).

Appendix 2

A high sensitivity fiber optic macro-bend based gas flow rate transducer for low flow rates: theory, working principle and static calibration.

Emiliano Schena, Paola Saccomandi and Sergio Silvestri

Published in Review of Scientific Instruments, vol. 84, no. 2, pp. 024301 - 024301-7, 2013.

ABSTRACT

A novel fiber optic macro-bend based gas flowmeter for low flow rates is presented. Theoretical analysis of the sensor working principle, design, and static calibration were performed. The measuring system consists of: an optical fiber, an LED, a Quadrant position sensitive Detector (QD), and an analog electronic circuit for signal processing. The fiber tip undergoes a deflection in the flow, acting like a cantilever. The consequent displacement of light spot center is monitored by the QD generating four unbalanced photocurrents which are function of fiber tip position. The analog electronic circuit processes the photocurrents providing voltage signal proportional to light spot position. A circular target was placed on the fiber in order to increase the sensing surface. Sensor, tested in the measurement range up to 10 $L \cdot min^{-1}$, shows: a discrimination threshold of 2 $L \cdot min^{-1}$, extremely low fluid dynamic resistance (0.17 $Pa \cdot min \cdot L^{-1}$), and high sensitivity, also at low flow rates (i.e., 33 $mV \cdot min \cdot L^{-1}$ up to 4 $L \cdot min^{-1}$ and 98 $mV \cdot min \cdot L^{-1}$ from 4 $L \cdot min^{-1}$ up to 10 $L \cdot min^{-1}$). Experimental results agree with the theoretical predictions. The high sensitivity, along with the reduced dimension and negligible pressure drop, make the proposed transducer suitable for medical applications in neonatal ventilation.

1. Introduction

Optical fibers are currently involved in several industrial fields, including, among others, chemical industry, structural health monitoring, and medicine. In medical engineering an intensive growth is taking place in use of fiber optic-based sensors (FOS) to monitor physical variables of physiological interest [1]. Recent market expansion is

encouraged by the cost reduction of key optical components and by some valuable characteristics of FOS, such as good accuracy and sensitivity, large bandwidth, and immunity from electromagnetic field, among others; moreover, the chance of FOS miniaturization makes these sensors suitable also for invasive measurements.

FOS are usually divided into two groups [1]: 1) intrinsic sensors, where the sensing element is the fiber optic itself; 2) extrinsic sensors, where the fiber is used to transport the radiation. Both intrinsic and extrinsic FOS can be designed using the optical fiber as element subjected to deformation.

Working principles based on optical fiber macro-bend have been proposed for fluid flow measurements. They are based on bending, that modifies the light guiding properties of optical fiber (e.g., flow rate varies the bending curvature and modulates the bending loss [2,3]).

Fiber Bragg gratings (FBGs) are also employed to fabricate sensing element of fiber optic-based flowmeters. Lim *et al*. developed an FBG-based differential pressure flow sensor constituted of two FBGs mounted on a diaphragm surface monitoring the pressure drop across an orifice, which is caused by fluid flow in pipeline [4]. Zhao *et al.* proposed to combine the idea of target type flowmeter with FBG technology. A target disk mounted on a cantilever is subjected to the force applied by fluid flowing into a pipeline. The deflection of cantilever is monitored by two FBG sensors stuck on either side of cantilever: this configuration allows to compensate temperature effects [5]. An FBG cantilever sensor, able to discriminate flow direction, was also proposed by Lu *et al.* [6]. FBG sensors show advantages such as high sensitivity and large dynamic range; however, the need of expensive components to monitor sensor's output (i.e., optical spectrum analyzer), still constitutes the main drawback to market expansion.

As presented by current literature, the use of cantilever as sensing element in flow transducers is common. Similar approaches have been employed to design optoelectronic transducers, although without using an optical fiber as sensing element. Liao *et al.* realized a force sensor employing a cantilever combined with a microspherical reflecting mirror on its tip: a laser beam hits the mirror and, as result of cantilever deflection, the mirror induces changes of optical beam displacement. Reflected laser beam displacement is monitored by a QD [7]. In a previous work, a bidirectional target-type flowmeter has been developed: a T-shaped target is deflected by the air flowing in the duct and differentially shadows two photodiodes surface hit by two correspondent LEDs [8].

Employment of optical fiber cantilever has been recently described: the displacement of fiber tip induced by flow rate results in the photocurrent produced by a QD [9,10]; transducer proposed by Ganguly *et al*. was based on the coupled light between two fibers modulated by flow velocity [11].

In this paper an extrinsic FOS with a fiber cantilever as sensing element is designed and realized. Working principle, based on the fiber optic transporting light to a QD, makes the sensor able to measure physical variables causing a displacement of fiber optic tip. The sensor response with fiber tip displacement is theoretically predicted and experimentally validated. Moreover, a particular configuration is adopted to realize a target type flowmeter. The fiber is placed in a duct where it is hit and deflected by the gas flow passing through it. The consequent displacement of light spot center is monitored by the QD and can be considered as an indirect measurement of flow rate.

Comparing with above described works, the main novelty introduced by present paper is the use of a QD and the positioning of a circular target on the fiber tip, in order to improve sensor sensitivity. Employment of the QD reduces transducer sensitivity to fiber displacement perpendicular to fluid flow direction (e.g., vibrations caused by von Karman vortex shedding phenomenon). Furthermore, the sensor has been tested with airflow values up to 10 $L \cdot min^{-1}$, that is a typical range used in mechanical ventilation.

2. Working principle and theoretical model

The light emitted by an LED is conveyed, through an *ad hoc* designed connector, within a fiber optic, whose distal tip is perpendicular to the surface of the QD. Since, at rest condition, the light fiber tip is aligned to the center of the QD, the four photodiodes generate identical photocurrents. When a displacement is applied, photodiodes generate unbalanced photocurrents, which can represent an indirect measurement of the displacement along one (x or y) or both directions.

The above described principle is employed to develop a target type flowmeter, where the fiber is used as a target placed in a duct perpendicular to the stream line of flow rate. A schematic representation of the flow transducer and a block diagram of its principle of work are shown in Fig. 1.

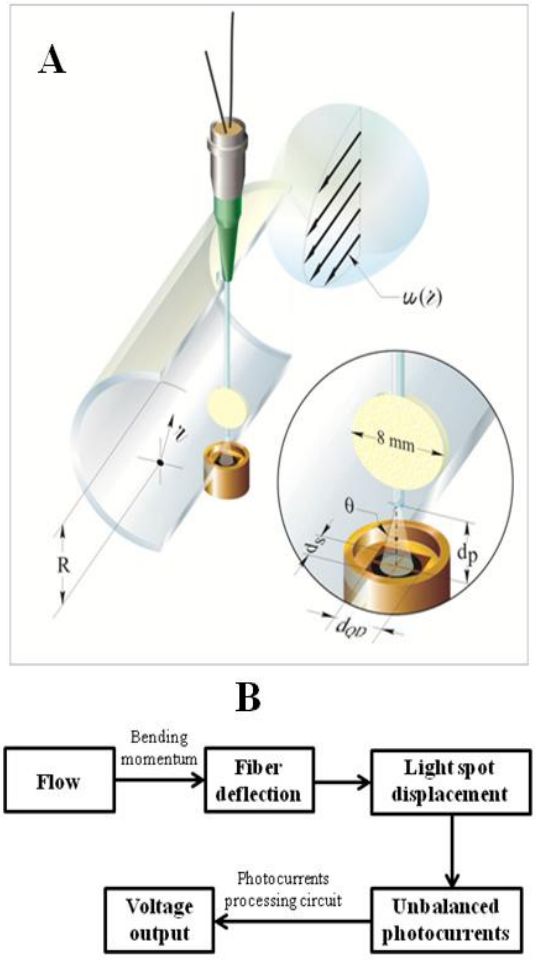

Figure 1. A) Schematic representation of the flow transducer sensing element. B) Block diagram of the measurement principle.

Sensor response is theoretically described through the following two steps: the former aims to provide the relation between the light spot position on the QD and the photocurrents generated by the four photodiodes; the second step gives a relation between flow and light spot position.

As it well known, the internal photocurrent (I_P), generated by each photodiode of the QD, can be expressed as a function of its responsivity (r_p). Photocurrent value strongly depends on the wavelength (λ) of incident light and on the radiant flux (Φ), expressed by the product between the light power density (I_r) and the photodiode sensitive surface exposed to radiation (S_p) [12]:

$$I_P = r_p(\lambda) \cdot \Phi = r_p(\lambda) \cdot I_r \cdot S_p \qquad 1$$

Therefore, the position of the light spot center $P_c=(x_c;y_c)$ can be expressed as a function of the four photocurrents ($I_{A/B/C/D}$): since the S_p size of each photodiode depends on P_c,

also the photocurrents will depend on P_c. For example, when the light spot center corresponds to the QD center, i.e., $P_c=(0;0)$ as shown in Fig. 2B, the four photodiodes generate equal currents; on the other hand, when the two centers do not correspond each other, the photodiodes are hit by different radiant flux and will generate different photocurrents (Fig. 2B).

The sensing element has been used to design a target type flow transducer. When passing through a duct, and under the hypothesis of ideal and incompressible steady flow, the gas flow rate produces a pressure $P(r)$ on the optical fiber cantilever

$$P(r)=\frac{1}{2}\cdot k\cdot \rho\cdot u(r)^2 \qquad 2$$

where k is the drag coefficient (≈ 1), ρ is the air density (≈ 1.29 kg·m^{-3}), $u(r)$ is the gas velocity and r is the distance from the center of the pipe.

Being the sensing element placed in a hose of 2 cm of diameter, the laminar flow condition (Reynolds number < 2000) is largely respected in the whole airflow range considered, as described in detail in Section 4. Therefore, $u(r)$ is expressed as

$$u(r)=2\cdot\frac{Q}{\pi\cdot R^2}\cdot\left[1-\left(\frac{r}{R}\right)^2\right] \qquad 3$$

where Q is the gas flow rate, R is the pipe radius, r is the radial coordinate with origin in pipe center.

The optical fiber is deflected along the flow direction. The fiber tip deflection can be approximately considered a mono-directional displacement of the light spot center and, by considering the Euler-Bernoulli bending theory for a cantilever, the displacement of the light spot can be expressed as follows:

$$x_c=\frac{4192\cdot k\cdot\rho\cdot d_f}{315\cdot E\cdot I\cdot\pi^2}\cdot Q^2 \qquad 4$$

where d_f is the external fiber diameter, equal to 730 µm, E is the fiber Young modulus, approximately equal to 2 GPa, and I is the second moment of area, calculated as $I=d_f^4/12$. The theoretical model developed to obtain the relation between Q and x_c is described in detail in a previous work [9], where the simplifying hypothesis considering the fiber as a square-section cantilever, with edge width equal to d_f, is assumed.

3. Sensor design and signal processing

With reference to Fig. 1A, the transducer is composed of an LED (SFH480-2, Osram), a custom made connector that conveys the light emitted by LED within a multimode fiber optic (BFH48-400, Thorlabs) with external diameter of 730 µm and core diameter, d_c, of 400 µm. The distal tip of the fiber is placed at a distance d_p=*1.5* mm above the surface of the QD (QD7-5T, Centronic) having an active circular area of 7 mm^2 (diameter d_{QD}=3.0 mm), with four nominally identical photodiodes with responsivity peak close to 0.5 A/W in proximity of the LED emission peak at 880 nm.

The distance (d_p) between the fiber tip and QD sensitive surface has been optimized, with the aim to obtain the light spot diameter (d_s) larger than d_c; d_s is calculated by the following equation (Fig. 2A):

$$d_s = 2 \cdot r_s = 2 \cdot \left(\frac{d_c}{2} + d_p \cdot \tan(\theta) \right) \approx 1.5\, mm \qquad 5$$

being $\theta = n \cdot arcsin(NA) \approx 28.7°$, where n is the refractive index of air ($n \approx 1$), and NA=*0.48* is the numerical aperture of the fiber. The value of d_p has been chosen in order to have $d_{QD} = 2 \cdot d_s$ when $x_c = d_{QD}/4$ ($x_c = -d_{QD}/4$), therefore, in this case, the whole spot light is included in one half of QD surface.

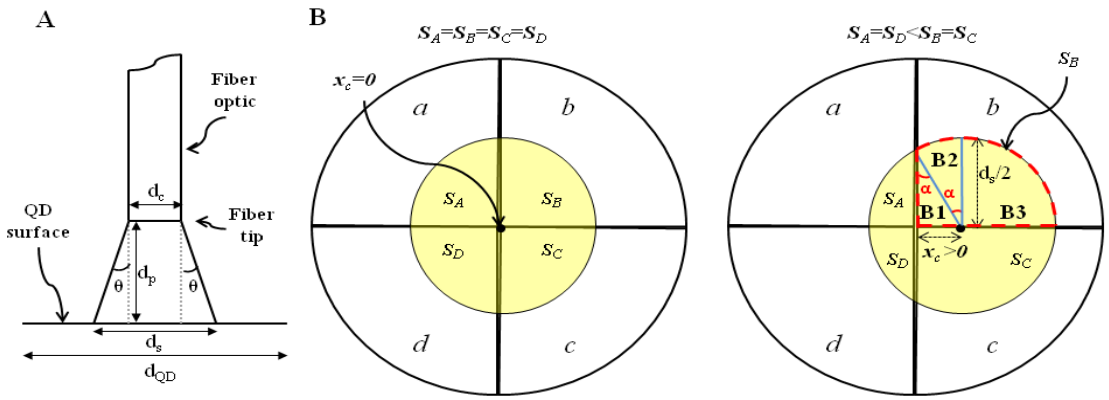

Figure 2. A) Schematic representation of the gap between the fiber tip and the QD to calculate the light spot diameter (d_s), as reported in Eq. (3). B) Photodiodes sensitive surfaces hit by light as function of the light spot position (x_c).

Considering mono-axial displacement of light spot along x direction, the surfaces of photodiodes hit by light depend on light spot center coordinates (x_c;y_c=0). As shown in Fig. 2B, it is evident the increase of the hit surface for the photodiodes b and c (S_B=S_C) and the decrease for a and d surfaces (S_A=S_D) when x_c is positive. With reference to Fig. 2B, and

expressing $\alpha = \arcsin\left(2 \cdot x_c / d_s\right)$, S_B (red dotted outline) can be calculated as sum of three terms B1, B2 and B3, and the surfaces are expressed as follows:

$$\begin{cases} S_B = S_C = B1 + B2 + B3 = \frac{1}{4} d_s \cdot x_c \cdot \cos(\alpha) + \frac{1}{8} d_s^2 \cdot \alpha + \frac{\pi d_s^2}{16} \\ S_A = S_D = \frac{\pi d_s^2}{8} - S_B = \frac{\pi d_s^2}{16} - \frac{1}{4} d_s \cdot x_c \cdot \cos(\alpha) - \frac{1}{8} d_s^2 \cdot \alpha \end{cases} \quad 6$$

Finally, introducing Eq. (6) in Eq. (1) we obtain the photocurrents as a function of x_c:

$$\begin{cases} I_B = I_C = r(\lambda) \cdot I_r \cdot \left[\frac{\pi d_s^2}{16} + \frac{1}{4} d_s \cdot x_c \cdot \cos(\alpha) + \frac{1}{8} d_s^2 \cdot \alpha \right] \\ I_A = I_D = r(\lambda) \cdot I_r \cdot \left[\frac{\pi d_s^2}{16} - \frac{1}{4} d_s \cdot x_c \cdot \cos(\alpha) - \frac{1}{8} d_s^2 \cdot \alpha \right] \end{cases} \quad 7$$

The graphs of I_B (supposed equal to I_C) and I_A (supposed equal to I_D) as function of x_c and normalized respect to I_r are shown in Fig. 3.

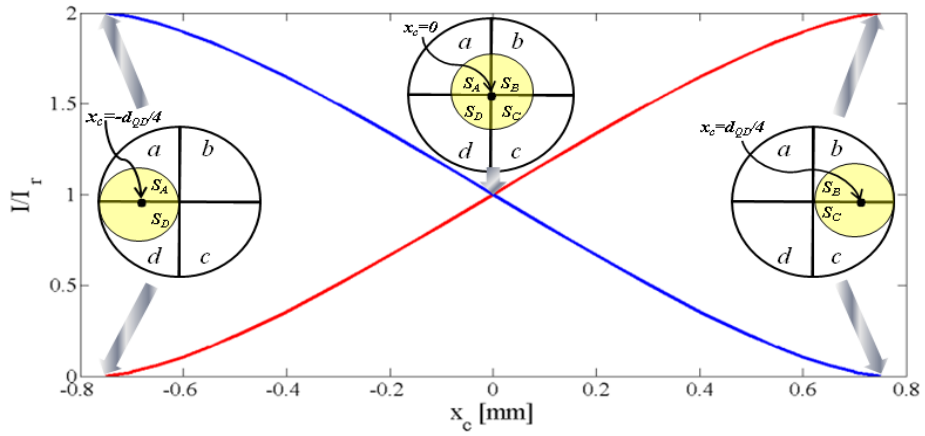

Figure. 3. Trend of the photocurrent I_B (equal to I_C, red curve) and of the photocurrent I_A (equal to I_D, blue curve) as a function of light spot position (x_c) and normalized respect the light power density (I_r).

At rest condition, the spot light is centered in $x_c=0$: under this condition the photodiodes *a*, *b*, *c* and *d* are equally hit, resulting in $S_A=S_B=S_C=S_D$, therefore, photocurrents are balanced ($I_A=I_B=I_C=I_D$), as described in Eq. (7). If the optical fiber is deflected by flow rate, the spot light undergoes displacement according to flow direction. When spot light center moves from $x_c=0$ to $x_c=d_{QD}/4$, S_B and S_C increase, while S_A and S_D decrease, resulting in an increase of I_B and I_C versus a decrement of I_A and I_D, as shown in Fig. 3. When centered in $x_c=d_{QD}/4$, the whole spot light is included in photodiodes *b* and *c*: since S_B and S_C reach the maximum value while $S_A=S_D=0$, this configuration entails $I_B=I_C$

maximum and $I_A=I_D=0$ (right side of Fig. 3). On the other hand, if the flow direction reverses respect the above described configuration, photocurrents invert their trends: when spot light center moves from $x_c=0$ to $x_c=-d_{QD}/4$, S_A and S_D increase, while S_B and S_C decrease, resulting in an increase of I_A and I_D versus a decrement of I_B and I_C. Finally, spot light centered in $x_c=-d_{QD}/4$ results in a maximum value of S_A and S_D, while $S_B=S_C=0$. This configuration determines maximum values of I_A and I_D and $I_B=I_C=0$, as shown in left side of Fig. 3.

The sensor's output voltage is obtained through an analog circuit that converts into a voltage (V_{out}) the sum and difference of photocurrents, $(I_A+I_D)-(I_B+I_C)$, as follows:

$$V_{out} = R \cdot \left\{ r(\lambda) \cdot I_r \cdot \left[d_s \cdot x_c \cdot \cos(\alpha) + \frac{1}{2} d_s^2 \cdot \alpha \right] \right\} \qquad 8$$

where R=100 kΩ is the gain of the current to voltage conversion.

Equation (8) represents the voltage sensor output as a function of the displacement of light spot center x_c.

Under the simplifying hypothesis of small displacements, we can consider $\alpha \to 0$ and $\cos(\alpha) \to 1$, therefore, Eq. (8) provides a linear relationship between V_{out} and x_c:

$$V_{out} = \eta \cdot x_c \qquad 9$$

Where $\eta = R \cdot r(\lambda) \cdot I_r \cdot d_s$.

The calibration curve of the target type flowmeter can be obtained by introducing Eq. (4) in Eq. (8):

$$V_{out} = \gamma \cdot \left[d_s \cdot \beta \cdot Q^2 \cdot \cos(\alpha) + \frac{1}{2} d_s^2 \cdot \alpha \right] \qquad 10$$

where $\gamma = R \cdot r(\lambda) \cdot I_r$ and $\alpha = \arcsin\left(\frac{2 \cdot \beta \cdot Q^2}{d_s} \right)$.

Under the hypothesis of small displacements Eq. (10) becomes:

$$V_{out} = \gamma \cdot Q^2 \qquad 11$$

The quadratic relation between V_{out} and Q in Eq. (11) represents the calibration curve of the flowmeter when the abovementioned hypothesis is valid.

4. Experimental trials, results and discussion

Experimental trials have been carried out in order to verify the relation between V_{out} and x_c in Eq. (8) through the measurement of V_{out} when displacements of light spot center from $x_c=0$ up to $x_c=600\ \mu m$ are applied. Experimental setup consists of: the sensing element and the analog circuit described in Section 3. A micropositioning kit, composed of a travel stage (TSGNF5/M, Thorlabs), a piezo driver (TPZ001, Thorlabs) and a strain gauge reader (TSG001, Thorlabs), has been used to move the QD in order to obtain x_c values ranging from 5 µm up to 600 µm. A voltage supply unit (DC ISO-TECH IPS 2302A) is used to power the LED at a constant voltage supply (V_s) with quite good stability (≤ 0.5 mV_{rms}).

Three sets of measurements are carried out by using three different V_s (3 V, 4 V, and 5 V). Since LED irradiance increases with V_s, sensitivity of V_{out} as a function of x_c increases with V_s, as shown in the experimental curves presented in Fig. 4. The experimental data are reported as mean ± expanded uncertainty estimated considering a student reference distribution with 2 degrees of freedom and a level of confidence of 95 % [13].

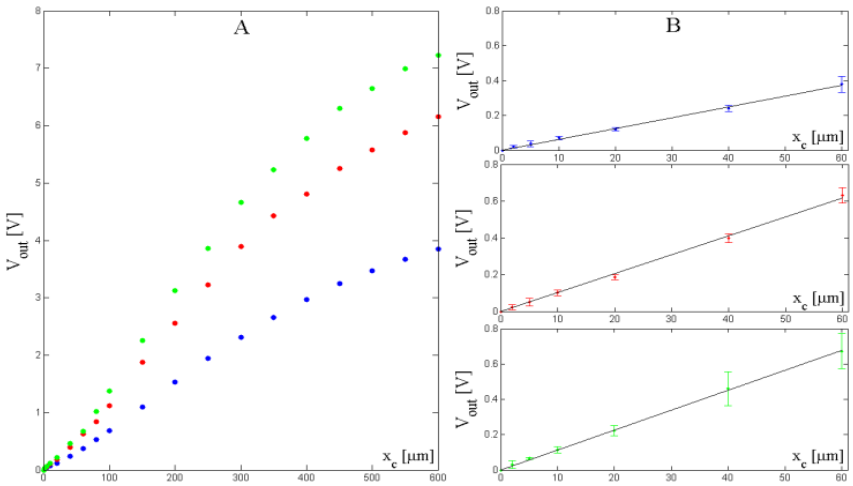

Figure 4. A) Voltage output (V_{out}) as a function of light spot position (x_c) at different LED voltage supply values (V_s): 3 V (blue dot), 4 V (red dot), and 5 V (black dot); B) theoretical -Eq. (10)- and experimental response for small displacements (up to 60 µm).

Experimental data confirm the increase of sensitivity with V_s maintaining constant the resistance R=100 kΩ, as reported in Eq. (8): sensitivity is about 11 $mV \cdot \mu m^{-1}$ with V_s= 5 V, 10 $mV \cdot \mu m^{-1}$ with V_s= 4 V, and 6.2 $mV \cdot \mu m^{-1}$ with V_s= 3 V. Figure 4 also shows the system ability to discriminate small displacements (e.g., a displacement of 5 µm is discriminated at all three voltage supplies). In Fig. 4B the hypothesis of small displacements in Eq. (9) is validated up to 60 µm: the linear fitting, Eq. (9), gives high correlation coefficient

($R^2 \approx 0.99$ at all three voltage supplies). Also in the linear range, sensitivity increases with V_s, as shown in Table I.

TABLE I. Sensitivity and R^2 values in the linear range at different voltage supply values.

	Range of x_c	S [mV·µm^{-1}]	R^2 value
V_s=3 V	up to 60 µm	6.22	0.99
V_s=4 V	up to 60 µm	10.3	0.99
V_s=5 V	up to 60 µm	11.3	0.99

A volumetric flow controller -Bronkhorst, El-Flow F201C, accuracy = ± (0.5% read value + 0.1% FS)- has been utilized to generate volumetric flow rate up to 10 L·min^{-1} in steps of 2 L·min^{-1}. With the aim to increase the transducer sensitivity, the LED has been supplied at the maximum value (V_s= *5 V*).

Preliminary trials were performed using a sensing element without the circular target. In this configuration the fiber displacement at air flow up to 10 L·min^{-1} was negligible and, consequently, the sensor was not able to measure flow in the range of interest. Therefore, we adopted the solution of the circular target of PVC (8 mm of diameter) fixed at the fiber tip, in order to increase the fiber deflection with flow rate. Experimental results and theoretical trend are reported in Fig. 5.

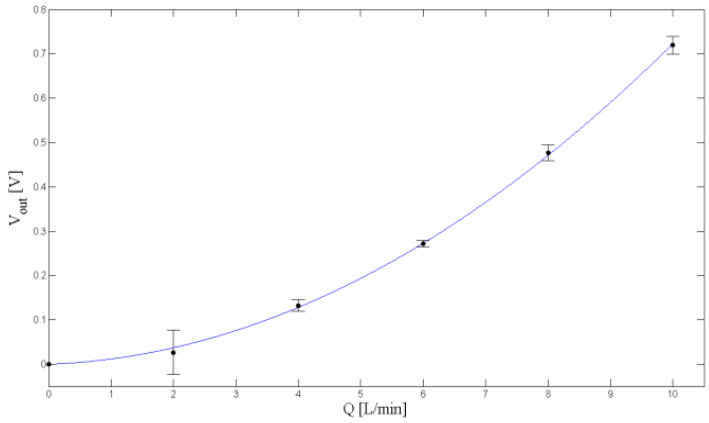

Figure 5. Calibration of flowmeter: experimental data (dots) and numerical simulation (line).

Experimental data show that the introduction of the target makes the sensor able to discriminate flow rates from 2 L·min^{-1}. Through a comparison between Fig. 4 and Fig. 5, it

is evident that V_{out} can be considered caused by small displacements: its highest value (at Q=10 L·min^{-1}) corresponds to a light spot displacement of 60 µm. Therefore, calibration curve has been obtained by fitting experimental data considering the small displacement hypothesis in Eq. (11), using the Curve Fitting Tool in Matlab environment. It shows an increase of sensor sensitivity with Q (e.g., for Q lower than 4 L·min^{-1} the mean sensitivity is about 33 mV·min·L^{-1}, on the other hand when Q ranges from 4 L·min^{-1} up to 10 L·min^{-1} the mean sensitivity increases at about 98 mV·min·L^{-1}). Fitting curve and experimental data show a good agreement as confirmed by the low value of MSE ($1.1\cdot10^{-4}$ V^2).

Finally, being the stability of the sensor dependent on the drift of the light power -V_{out} is a function of I_r, Eq. (8)-, we want to spotlight that data reported in Fig. 5 have been obtained from ten trials carried out during 12 hours when the LED has been always on. Data dispersion, reported in Fig. 5, appears to show quite reproducible results during such a period also using cost effective electronic components. However, longer trials should be performed to analyze this aspect which, obviously, is also dependent on the power supply stability.

Experimental trials were also performed to measure the fluid dynamic resistance (R_f) due to the presence of the target in the pipe. R_f is defined as $R_f=\Delta P/Q$, where ΔP [Pa] is the pressure drop produced by Q across the sensing element. The volumetric flow controller has been used to generate volumetric flow rate ranging from 2 L·min^{-1} to 10 L·min^{-1}. ΔP has been measured by a differential pressure transducer (163PC01D48 Honeywell, measurement range from -196 Pa up to 11760 Pa) placed across the fiber. Four sets of measurements were carried out for each flow rate value. Values of measured ΔP, R_f, and sensitivity are shown in Table II.

Data are reported as mean ± expanded uncertainty, estimated with different approaches depending to the quantity: δQ was estimated considering the accuracy declared by the manufacturer, accuracy = ± (0.5% read value + 0.1% FS); $\delta\Delta P$ was estimated considering a student reference distribution with 3 degrees of freedom and a level of confidence of 95 % [14]; the estimation of δR_f was carried out with the propagation of uncertainty, as recommended by [14], under the hypothesis of uncorrelated input quantities:

$$\delta R_f = \sqrt{\left(\frac{\partial R_f}{\partial Q}\cdot\delta\Delta P\right)^2+\left(\frac{\partial R_f}{\partial \Delta P}\cdot\delta Q\right)^2} = \sqrt{\left(\frac{1}{Q}\cdot\delta\Delta P\right)^2+\left(-\frac{\Delta P}{Q^2}\cdot\delta Q\right)^2} \qquad 12$$

TABLE II. Pressure drop, fluid dynamic resistance, and sensitivity in calibration flow range.

$Q \pm \delta Q$ [L·min^{-1}]	$\Delta P \pm \delta \Delta P$ [Pa]	$R_f \pm \delta R_f$ [Pa·min·L^{-1}]	*Range of Q* [L·min^{-1}]	*Mean Sensitivity* [mV·L^{-1}·min]
2.00 ± 0.02	0.2 ± 0.2	0.1 ± 0.1	from 0 up to 2	13
4.00 ± 0.03	1.0 ± 0.2	0.24 ± 0.06	from 2 up to 4	33
6.00 ± 0.04	1.2 ± 0.4	0.19 ± 0.07	from 4 up to 6	70
10.00 ± 0.06	1.3 ± 0.4	0.13 ± 0.04	from 6 up to 10	121

Experimental tests show very small ΔP values in the whole range of calibration. In particular, the maximum ΔP is 1.3±0.4 Pa at 10 L·min^{-1}. The average value of R_f in the whole flow rate range is 0.17 Pa·min·L^{-1}.

These results are similar to data obtained with a cantilever transducer [10] and voltage obtained are slightly lower than experimental results reported in a previous study with T-shaped target (i.e., ΔP was about 2.4 Pa at 7 L·min^{-1}) [9]. They also confirm the good choice of the circular target diameter (i.e., 8 mm). In fact, both the sensitivity and R_f increase with target diameter; an 8 mm diameter allows to obtain a good compromise between high sensitivity and low R_f.

Respect to previous studies presenting FOS transducers with FBG sensors, the main advantage is the not necessity of optical spectrum analyzer, but it is not the only one. As a matter of fact, the measurement range of the presented sensor reaches 10 L·min^{-1}: mostly doubling the FBG transducer range for measurement of water flow rate and direction (5.4 L·min^{-1}) described in [7]. Furthermore, the discrimination threshold of the here presented transducer (2 L·min^{-1}) is significantly lower than the one of an FBG based differential pressure flow sensor for liquid (12 L·min^{-1}), that is also calibrated in a water flow range up to 48 L·min^{-1} and presents high R_f because of high ΔP (80 kPa) measured across an orifice [5]. The discrimination threshold of 2 L·min^{-1} is also better than the one, equal to 3 L·min^{-1}, shown by target type flowmeter for liquid [6], that, moreover, lacks of bidirectional discrimination ability.

In order to employ this kind of sensor as flow transducer in neonatal ventilation, measurement range, sensitivity and fluid dynamic resistance are crucial points. A flow

sensor based on fiber macro-bending intended to be used in applications with air flow up to 10 L·min^{-1}, has been presented [4]. However, its sensitivity is significantly lower than sensitivity of the proposed transducer. As a matter of fact, the air flow sensor with hinge joint reported in [4], shows average sensitivity of about 2 mV·min·L^{-1} for *Q* ranging from 0.2 L·min^{-1} to 4.5 L·min^{-1}, *versus* the 33 mV·min·L^{-1} at *Q* from 0 L·min^{-1} to 4 L·min^{-1} of the here presented sensor. Both sensors show an increasing average sensitivity when *Q* increases from about 4 L·min^{-1} up to 10 L·min^{-1}, but the compared sensor [4], in the same range, has a sensitivity value of about 13 mV·min·L^{-1}, versus 98 mV·min·L^{-1}. Since sensitivity is a fundamental metrological characteristic for a neonatal flow transducer, especially at low *Q* values, the results obtained appear to make the sensor suitable for this medical application.

Furthermore, the discrimination threshold (lower than 2 L·min^{-1}) presented by our flow sensor is comparable with data presented in previous papers [9,10,11], designed for the same medical application.

Features of the presented sensor are compared with characteristics of other flow transducers presented in literature. The comparison is reported in Table III.

TABLE III. Features of present sensor in comparison with characteristic of other optical flow sensors described in literature.

Principle of sensing	Measurement range	Bidirectionality	Threshold [L·min^{-1}]	Sensitivity	Dynamic resistance [Pa·min·L^{-1}]	References
Cantilever optical fiber transducer	From -10 L·min^{-1} to 10 L·min^{-1}	Yes	- 2 to + 2 (dead zone)	72 mV·min·L^{-1} (mean sensitivity)	0.17	Presented sensor
Cantilever optical fiber transducer	From -8 L·min^{-1} to 8 L·min^{-1}	Yes	- 1 to + 1 (dead zone)	0.12 V·min·L^{-1} (mean sensitivity)	0.48	Schena *et al.* [10]
T-shaped target	From -7 L·min^{-1} to 7 L·min^{-1}	Yes	- 1 to + 1 (dead zone)	2.8 V·min·L^{-1} (mean sensitivity)	0.34	Saccomandi *et al.* [9]
FBG transducer of water flow rate	From -5.4 L·min^{-1} to 5.4 L·min^{-1}	Yes	- 1.2 to + 1.2 (dead zone) (spring steel, forward flow)	153 nm·min·L^{-1} (spring steel, forward flow)	-	Lu *et al.* [7]
Target-type flowmeter based on FBG	From 0 L·min^{-1} to 60 L·min^{-1}	No	3	-	-	Zhao *et al.* [6]
Optical fiber macrobending-based with hinge	From 1 L·min^{-1} to 10 L·min^{-1}	No	1	2 mV·min·L^{-1} (higher sensitivity,	-	Vijayan *et al.* [4]

joint				from 0 L·min^{-1} to 4 L·min^{-1})		
Optical fiber cantilever	From 0 L·min^{-1} to 18 L·min^{-1}	No	2	-	-	Battista *et al.* [11]

5. Conclusions

In conclusion, the design and realization of an extrinsic FOS with sensing element based on the use of commercially available fiber optic, circular target, LED, and QD is presented. The sensing element can be used to develop a target type flowmeter with a quadratic calibration curve: good agreement between experimental calibration and mathematical model is shown ($R^2 \approx 0.99$).

The use of QD makes the principle of measurement intrinsically able to discriminate flow direction.

The mean sensitivity (72 mV·min·L^{-1} in the whole range of calibration) and the discrimination threshold (lower than 2 L·min^{-1}) combined with the measurement range (up to 10 L·min^{-1}) make the sensor attractive for some medical applications (e.g., neonatal ventilation). Further advantages are the use of cost effective electronic components and robustness.

Bibliography

[1] S. Silvestri, E. Schena, "Optical-fiber measurement systems for medical applications," in Optoelectronics – Devices and Applications, P. Predeep, InTech, 2011, pp. 205-224.

[2] E. Udd, "Fiber optic sensors," John Wiley & Sons, Hoboken, New Jersey, 2006.

[3] R. P. Hu and X. G. Huang, "A simple fiber-optic flowmeter based on bending loss," IEEE Sensors Journal, vol. 9, no. 12, 2009, pp. 1052-1955.

[4] A. Vijayan, V. Thakare, R. N. Karekar and R. C. Aiyer "Optical fiber-based macrobend free air flow sensor using a hinge joint: a preliminary report," Microwave and optical technology letters, vol. 50, no. 10, 2008, pp. 2543-2546.

[5] J. Lim, Q. P. Yang, B. E. Jones, P. R. Jackson, "DP flow sensor using optical fibre Bragg grating," Sensors and Actuators A, vol. 92, n. 1-3, 2001, pp. 102-108.

[6] Y. Zhao, K. Chen and J. Yang, "Novel target flowmeter based on differential fiber Bragg grating sensor," Measurement, vol. 38, n. ?, 2005, pp. 230-235.

[7] P. Lu and Q. Chen, "Fiber Bragg grating sensor for simultaneous measurement of flow rate and direction," Measurement Science and Technology, vol. 19, n. 12, 2008, pp. 102-108.

[8] C. Liao and J. Tsai, "A cantilever force sensor combined with a spherical reflecting mirror for sensitivity enhancement of an optical detection system," IEEE Journal of Selected Topics in Quantum Electronics, vol. 15, no. 5, 2009, pp. 1463-1468.

[9] P. Saccomandi, E. Schena, and S. Silvestri, "A novel target type low pressure-drop bidirectional optoelectronic air flow sensor for infant artificial ventilation: measurement principle and static calibration," Review of Scientific Instruments, vol. 82, n.2 (024301), 2011.

[10] E. Schena, P. Saccomandi, M. Mastrapasqua, and S. Silvestri, "An optical fiber based flow transducer for infant ventilation: measurement principle and calibration," in Proc. 6th Annual IEEE International Symposium on Medical Measurements and Applications, Bari (Italy), 2011, pp. 311-314.

[11] L. Battista, S. A. Sciuto and A. Scorza, "Preliminary evaluation of a fiber-optic sensor for flow measurements in pulmonary ventilators," in Proc. 6th Annual IEEE International Symposium on Medical Measurements and Applications, Bari (Italy), 2011, pp. 29-34.

[12] A. K. Ganguly and B. Mondal, "Fluid flow measurement using optical fiber cantilever" National Conference on Electronics, Communication and Signal Processing, NCECS-2011, 19th September 2011, Siliguri Institute of Technology, Siliguri, Darjeeling, West Bengal: 734009.

[13] M. Johnson, Photodetection and Measurement: maximizing performance in optical systems. New York: McGraw-Hill, 2003.

[14] Evaluation of measurement data- Guide to the expression of uncertainty in measurement, JCGM 100:2008.

Curriculum Publications

JOURNAL PAPERS

1) 2013. Taffoni F, Formica D, Saccomandi P, Di Pino G, Schena E. Optical Fiber-Based MR-Compatible Sensors for Medical Applications: An Overview. SENSORS, 13.10: 14105-14120.

2) 2013. Schena E, Saccomandi P, Giurazza F, Mortato L, Caponero A, Di Matteo FM, Martino M, Panzera F, Del Vescovo R, Beomonte Zobel B, Silvestri S. Experimental assessment of CT-based thermometry during laser ablation of porcine pancreas. PHYSICS IN MEDICINE AND BIOLOGY, 58.16: 5705.

3) 2013. Saccomandi P, Schena E, Silvestri S. Techniques for temperature monitoring during Laser Induced ThermoTherapy: an overview. INTERNATIONAL JOURNAL OF HYPERTHERMIA, 29.7: 609-619.

4) 2013. Saccomandi P et al. Temperature monitoring and lesion volume estimation during double-applicator laser-induced thermotherapy in ex vivo swine pancreas: a preliminary study. LASERS IN MEDICAL SCIENCE, 1-8.

5) 2013. Schena E, Saccomandi P, Cappelli S, Silvestri S (2013) Mechanical ventilation with heated humidifiers: measurements of condensed water mass within the breathing circuit according to ventilatory settings. PHYSIOLOGICAL MEASUREMENTS, 34.7: 813.

6) 2013. Di Matteo FM, Pandolfi M, Martino M, Panzera F, Saccomandi P, Schena E, Silvestri S, Pacella CM, Costamagna G US-guided application of ND:YAG laser in porcine pancreatic tissue: an ex vivo study and numerical simulation. GASTROINTENSTINAL ENDOSCOPY, 78.5:750-755.

7) 2013. Schena E, Saccomandi P, Silvestri S. A high sensitivity fiber optic macro-bend based gas flow rate transducer for low flow rates: theory, working principle and static calibration. REVIEW OF SCIENTIFIC INSTRUMENTS, 84.2: 024301-024301.

8) 2012. Saccomandi P, Schena E, Caponero MA, Di Matteo FM, Martino M, Pandolfi M, Silvestri S. Theoretical analysis and experimental evaluation of laser induced interstitial thermotherapy in ex vivo porcine pancreas. IEEE TRANSACTION ON BIOMEDICAL ENGINEERING, 59.10:2958-64.

9) 2012. Schena E, Saccomandi P, Ramandi C, Silvestri S. A novel control strategy to improve performances of heated wire humidifiers in artificial neonatal ventilation. PHYSIOLOGICAL MEASUREMENTS, 33.7: 1199.

10) 2011. Saccomandi P, Schena E, Silvestri S. A novel target type low pressure-drop bidirectional optoelectronic air flow sensor for infant artificial ventilation: measurement principle and static calibration. REVIEW OF SCIENTIFIC INSTRUMENTS, 82.2: 024301-024301.

CONFERENCES PAPERS

1) Giurazza F, Frauenfelder G, Del Vescovo R, Schena E, Saccomandi P, Allegretti G, Siano F, Beomonte Zobel B. (2014) MR thermometry feasibility during LITT in ex-vivo porcine pancreas, EUROPEAN CONGRESS OF RADIOLOGY (ECR) , Vienna, Austria, Mar.6-10,2014.

2) Giurazza F, Del Vescovo R, Schena E, Saccomandi P, Cazzato RL, Mortato L, Di Matteo FM, Grazzo FR, Beomonte Zobel B. (2014) Experimental assessment of temperature distribution on pancreas during laser interstitial thermotherapy (LITT) through CT scan evaluation, EUROPEAN CONGRESS OF RADIOLOGY (ECR), Vienna, Austria, Mar. 6-10, 2014.

3) Saccomandi P, Schena E, Silvestri S. (2013) Design of fiber optics applicators for laser thermotherapy: theoretical evaluation of thermal outcomes. PROC. OF 35th ANNUAL INTERNATIONAL CONFERENCE OF THE IEEE ENGINEERING IN MEDICINE AND BIOLOGY SOCIETY (EMBS), Osaka, Jul. 3- 7, 2013

4) Saccomandi P et al. Influence of FBG sensors length on temperature measures in laser-irradiated pancreas: theoretical and experimental evaluation. PROC. OF 35th ANNUAL INTERNATIONAL CONFERENCE OF THE IEEE ENGINEERING IN MEDICINE AND BIOLOGY SOCIETY (EMBS), Osaka, Jul. 3- 7, 2013

5) Schena E, Cecchini S, Saccomandi P, Leuzzi M, Silvestri S (2013) A solution to improve the outcome of a non-invasive approach for cardiac output monitoring: a preliminary study. PROC. OF 35th ANNUAL INTERNATIONAL CONFERENCE OF THE IEEE ENGINEERING IN MEDICINE AND BIOLOGY SOCIETY (EMBS), Osaka, Jul. 3- 7, 2013

6) Giurazza F, Schena E, Del Vescovo R, Cazzato RL, Mortato L, Saccomandi P, Paternostro F, Onofri L, Beomonte Zobel B (2013) Sex determination from scapular length measurements by CT scans images in a Caucasian population. PROC. OF 35th ANNUAL

INTERNATIONAL CONFERENCE OF THE IEEE ENGINEERING IN MEDICINE AND BIOLOGY SOCIETY (EMBS), Osaka, Jul. 3- 7, 2013

7) Accoto D, Cidda M, Schena E, Francomano M, Saccomandi P, Guglielmelli E, Silvestri S (2013) A micro opto-mechanical displacement sensor based on micro-diffraction gratings: design and characterization. PROC. OF 35th ANNUAL INTERNATIONAL CONFERENCE OF THE IEEE ENGINEERING IN MEDICINE AND BIOLOGY SOCIETY (EMBS), Osaka, Jul. 3- 7, 2013

8) Schena E, Quaranta A, Saccomandi P, Silvestri S (2013) Performances of heated humidifiers in mechanical ventilation: a preliminary intra-breath analysis. PROC. OF 35th ANNUAL INTERNATIONAL CONFERENCE OF THE IEEE ENGINEERING IN MEDICINE AND BIOLOGY SOCIETY (EMBS), Osaka, Jul. 3- 7, 2013

9) Schena E, Saccomandi P, Giurazza F, Del Vescovo R, Mortato L, Martino M, Panzera F, Di Matteo FM, Beomonte Zobel B, Silvestri S (2013) Monitoring of temperature increase and tissue vaporization during laser interstitial thermotherapy of ex vivo swine liver by computed tomography. PROC. OF 35th ANNUAL INTERNATIONAL CONFERENCE OF THE IEEE ENGINEERING IN MEDICINE AND BIOLOGY SOCIETY (EMBS), Osaka, Jul. 3- 7, 2013

10) Bastianini F, Schena E, Saccomandi P, Silvestri S. (2013). Accuracy evaluation of dynamic volume measurements performed by opto-electronic plethysmograph, by using a pulmonary simulator. PROC. OF 35th ANNUAL INTERNATIONAL CONFERENCE OF THE IEEE ENGINEERING IN MEDICINE AND BIOLOGY SOCIETY (EMBS), Osaka, Jul. 3- 7, 2013

11) Giurazza F, Del Vescovo R, E. Schena, P Saccomandi, R. L. Cazzato, L. Mortato, F. M. Di Matteo, R. F. Grasso, B. B. Zobel (2013). Temperature monitoring and lesion volume estimation during double applicator laser-induced thermotherapy in ex vivo pancreas: a preliminary study. EUROPEAN CONGRESS OF RADIOLOGY (ECR), Vienna, Austria, Mar. 7-11, 2013.

12) Giurazza F, Del Vescovo R, Schena E, Saccomandi P, Cazzato RL, Mortato L, Di Matteo FM, Grasso RF, Beomonte Zobel B (2013). Experimental assessment of temperature distribution on pancreas during laser interstitial thermotherapy (LITT) through CT scan evaluation. EUROPEAN CONGRESS OF RADIOLOGY (ECR), Vienna, Austria, Mar. 7-11, 2013.

13) Martino M, Di Matteo FM, Rea R, Pandolfi M, Breschi L, Panzera F, Saccomandi P, Schena E, Silvestri S, Costamagna G (2013) Nd:Yag Laser Application On Normal

Biliary Duct: An Ex-Vivo Pilot Study In Porcine Model. DIGESTIVE DISEASE WEEK, Orlando, Florida, May 18-21, 2013.

14) Di Matteo FM, Pacella CM, Martino M, Pandolfi M, Grasso RF, Panzera F, Rea R, Picconi F, Saccomandi P, Schena E, Silvestri S (2013) EUS-guide Nd:YAG laser ablation of hepatocellular carcinoma of the caudate lobe: Case series. DIGESTIVE DISEASE WEEK, Orlando, Florida, May 18-21, 2013.

15) Schena E, Di Matteo FM, Silvestri S, Saccomandi P, Martino M, Panzera F, Pandolfi M, Costamagna G (2012). Temperature distribution monitoring during ND:YAG laser ablation of porcine pancreatic tissue. Digestive and Liver Disease, Vol. 44, Supplement 2, pp. S144, ABSTRACT OF 18th NATIONAL CONGRESS OF DIGESTIVE DISEASES, ITALIAN FEDERATION OF SOCIETIES OF DIGESTIVE DISEASES-FISMAD, Napoli, Mar. 28-31, 2012.

16) Di Matteo FM, Martino M, Panzera F, Pandolfi M, Rea R, Silvestri S, Saccomandi P, Schena E, Stigliano E, Breschi L, Costamagna G (2012). Us-guided Nd:YAG laser ablation in porcine pancreatic tissue: an ex vivo study and numerical simulation. GASTROINTESTINAL ENDOSCOPY, Vol. 75, Issue 4S, pp. AB187, ABSTRACT OF 18th DIGESTIVE DISEASES WEEK 2012, San Diego, California, May 20-22, 2012.

17) Saccomandi P, Schena E, Di Matteo FM, Pandolfi M, Martino M, Rea R, Silvestri S (2012). Theoretical assessment of principal factors influencing laser interstitial thermotherapy outcomes on pancreas. PROC. OF 34th ANNUAL INTERNATIONAL CONFERENCE OF THE IEEE ENGINEERING IN MEDICINE AND BIOLOGY SOCIETY (EMBS), San Diego, Aug. 28- Sept. 1, 2012.

18) Cecchini S, Schena E, Saccomandi P, Polisca F, Di Cecca I, Notaro M, Carassiti M, Silvestri S (2012). Cardiac output estimation in mechanically ventilated patients: a comparison between prolonged expiration method and thermodilution. PROC. OF 34th ANNUAL INTERNATIONAL CONFERENCE OF THE IEEE ENGINEERING IN MEDICINE AND BIOLOGY SOCIETY (EMBS), San Diego, Aug. 28- Sept. 1, 2012.

19) Moscato M, Schena E, Saccomandi P, Francomano MT, Accoto D, Guglielmelli E, Silvestri S (2012). A micromachined intensity-modulated fiber optic sensor for strain measurements: working principle and static calibration. PROC. OF 34th ANNUAL INTERNATIONAL CONFERENCE OF THE IEEE ENGINEERING IN MEDICINE AND BIOLOGY SOCIETY (EMBS), San Diego, Aug. 28- Sept. 1, 2012.

20) Schena E, Saccomandi P, Mastrapasqua M, Silvestri S (2011). An optical fiber based flow transducer for infant ventilation: measurement principle and calibration. PROC.

OF 2011 INTERNATIONAL SYMPOSIUM ON MEDICAL MEASUREMENTS AND APPLICATIONS, THE IEEE MEASUREMENT AND INSTRUMENTATION SOCIETY, ISBN: 978-1-4244-9337-1, Bari, pp. 311-315, 30 – 31 May, 2011.

21) Saccomandi P, Schena E, Di Matteo FM, Pandolfi M, Martino M, Rea R, Silvestri S (2011). Laser Interstitial Thermotherapy for Pancreatic Tumor Ablation: Theoretical Model and Experimental Validation. PROC. OF 33rd ANNUAL INTERNATIONAL CONFERENCE OF THE IEEE ENGINEERING IN MEDICINE AND BIOLOGY SOCIETY (EMBS), Boston, pp. 5585-5588, Aug. 30- Sept. 3, 2011.

ORAL PRESENTATIONS AT INTERNATIONAL CONFERENCES

1) Giurazza F, Schena E, Del Vescovo R, Cazzato RL, Mortato L, Saccomandi P, Paternostro F, Onofri L, Beomonte Zobel B (2013) Sex determination from scapular length measurements by CT scans images in a Caucasian population. PROC. OF 35th ANNUAL INTERNATIONAL CONFERENCE OF THE IEEE ENGINEERING IN MEDICINE AND BIOLOGY SOCIETY (EMBS), Osaka, Jul. 3- 7, 2013

2) Schena E, Saccomandi P, Giurazza F, Del Vescovo R, Mortato L, Martino M, Panzera F, Di Matteo FM, Beomonte Zobel B, Silvestri S (2013) Monitoring of temperature increase and tissue vaporization during laser interstitial thermotherapy of ex vivo swine liver by computed tomography. PROC. OF 35th ANNUAL INTERNATIONAL CONFERENCE OF THE IEEE ENGINEERING IN MEDICINE AND BIOLOGY SOCIETY (EMBS), Osaka, Jul. 3- 7, 2013

3) Cecchini S, Schena E, Saccomandi P, Polisca F, Di Cecca I, Notaro M, Carassiti M, Silvestri S (2012). Cardiac output estimation in mechanically ventilated patients: a comparison between prolonged expiration method and thermodilution. PROC. OF 34th ANNUAL INTERNATIONAL CONFERENCE OF THE IEEE ENGINEERING IN MEDICINE AND BIOLOGY SOCIETY (EMBS), San Diego, Aug. 28- Sept. 1, 2012.